

NUMERICAL SIMULATION AND FLOW ANALYSIS OF AN ELBOW DIFFUSER

THÈSE N° 2527 (2002)

PRÉSENTÉE À LA FACULTÉ STI SECTION DE GÉNIE MÉCANIQUE

ÉCOLE POLYTECHNIQUE FÉDÉRALE DE LAUSANNE

POUR L'OBTENTION DU GRADE DE DOCTEUR ÈS SCIENCES TECHNIQUES

PAR

Sebastiano MAURI

Dipl. Masch. Ing. ETH

de nationalité suisse et originaire de Chiasso (TI)

acceptée sur proposition du jury:

Prof. F. Avellan, directeur de thèse
Prof. M. Deville, rapporteur
Prof. C. Hirsch, rapporteur
Dr H. Keck, rapporteur
Prof. J.-L. Kueny, rapporteur
Dr A. Ruprecht, rapporteur

Lausanne, EPFL
2002

Abstract

Numerical simulation of the unsteady turbulent flow in a three-dimensional elbow diffuser is performed. The investigation is carried out with a commercial finite volume solver implementing the Reynolds averaged Navier-Stokes equations. Against the background of current research in DNS and LES, the modeling of most practically relevant turbulent flows continues to be based on this system of equations. For this reason it is important to evaluate the limitations of the Reynolds averaging approach with the associated turbulence modeling, in particular for the prediction of time-dependent flows. Verification and validation are presented; detailed measurements are compared with computations. While a great deal of research has focused on draft tube design, relatively little is known about the complex flow features present. The flow is analyzed over a wide range of operating conditions including part load. Topological changes in the flow patterns with the global characteristics of the diffuser are presented. Visualization provides extra insight into the complex flow. Forced and self-sustained time-dependent flow phenomena are captured. Falling into these categories are flow field fluctuations introduced by the runner, self-sustained vortex shedding phenomena, and the typical rotating helical vortex observed at part load. Additionally, the linear stability of measured inlet profiles is investigated, providing a fuller understanding of the basic instability mechanism.

Résumé

Une simulation numérique de l'écoulement turbulent instationnaire dans un diffuseur coudé tridimensionnel est effectuée. L'étude est menée avec un code commercial résolvant les équations de Navier Stokes moyennées en formulation volume fini. Beaucoup des recherches actuelles sont axées sur la DNS et la LES, néanmoins la modélisation de la plupart des écoulements turbulents rencontrés en pratique continue à être basée sur ce système d'équations. Pour cette raison, il est important d'évaluer les limitations de cette approche, en particulier pour la prédiction des écoulements instationnaires. Des vérification et validation sont présentées; des mesures détaillées sont comparées aux calculs. Alors qu'une grande partie de la recherche était concentrée sur le design du diffuseur, peu de connaissance sur les caractéristiques complexes de l'écoulement qui y est présent a été acquis. L'écoulement est analysé sur une large bande de points de fonctionnement incluant des points à charges partielles. Les changements de la topologie de l'écoulement et des caractéristiques globales du diffuseur sont présentés. La visualisation permet une vision supplémentaire de l'écoulement complexe. Des phénomènes instationnaires sont capturés. Parmi ces catégories, on peut citer les fluctuations introduites par la roue, le phénomène de détachement tourbillonnaire auto-entretenu et le tourbillon hélicoidal observé à charge partielle. De plus, la stabilité linéaire du profil de vitesse mesuré en sortie de roue a été étudiée, permettant une compréhension du mécanisme de base de l'instabilité.

Acknowledgments

This work was established during my stay as assistant at the Laboratory for Hydraulic Machines of the EPFL, and is also part of the FLINDT project whose participants are the EPFL, Electricité de France, Alstom Power, General Electric Canada, VA Tech Hydro, Voith Hydro who are gratefully acknowledged. The project was also supported by the Swiss Federal Commission for Technology and Innovation (PSEL) and the German Ministry of Science and Technology (BMBF). I wish to thank Prof. Dr. Jean-Louis Kueny for the scientific supervision of the work and Prof. Dr. François Avellan for the thesis direction. The experimental results presented in this work were carried out by Jorge Arpe and Gabriel Ciocan, coordinated by Jean-Eustache Prénat, to whom I am very thankful. I should also like to acknowledge the following colleagues who have been working on the FLINDT project: Laurent Gros, Kevin Kaupert, Florent Longatte, Isabelle Lurault, Jérôme Saulnier, Bartu Ugurtas, Fabrice Vonnez and as well the members of the FLINDT technical committee. Bartu Ugurtas is particularly acknowledged for the collaboration on the linear stability analysis. The staff of the Laboratory for Hydraulic Machines is gratefully acknowledged for his help in the experimental, numerical and supporting work. I am indebted to the members on my thesis committee for their questions and comments on the work. Many thanks also to the assistants and students of the laboratory. A particular thanks to my family and Simone.

Contents

Abstract	i
Acknowledgment	iii
I Introduction	1
1 Motivation	2
2 Hydraulic turbomachinery	4
3 Numerical flow simulation in a draft tube, state-of-the-art	8
4 Thesis focus and document organization	10
II Modeling and numerical approach	13
1 Governing equations	14
2 Flow solver	19
III Reference cases	23
1 Piston reciprocating in simple harmonic motion	24
2 Vortex shedding past a square obstacle	28
3 Steady swirling flow in a pipe	39
4 Steady swirling flow in a diffuser	44
5 Summary	49
IV Case study	51
1 Investigated geometry	52

2	Measurements	54
3	Machine characteristics	56
V	Modeling and discretization	65
1	Introduction	66
2	Mesh	68
3	Grid convergence	70
4	Outlet boundary condition	73
5	Inlet radial velocity component	75
6	Near wall velocity profile	77
7	Inlet turbulent dissipation	79
8	Inlet turbulent kinetic energy	81
9	Advection scheme	82
10	Turbulence modeling	84
11	Summary and conclusions	86
VI	Steady flow computation	89
1	Introduction	90
2	Comparison with experimental data	91
3	Flow analysis: flow rate and specific energy balance	100
4	Flow analysis: velocity field	104
VII	Time-dependent flow computation with steady boundary conditions	121
1	Introduction	122
2	Operating point in the efficiency drop at $\varphi^* = 1.021$	124
3	Operating point at the highest flow rate $\varphi^* = 1.108$	134

4	Conclusion	139
VIII	Time-dependent flow computation with unsteady inlet boundary conditions	141
1	Phase averaged inlet velocity profile	142
2	Rotating helical vortex	147
3	Conclusion	163
4	Linear stability of the time averaged inlet profiles	164
IX	Summary and perspectives	171
	Bibliography	177
	Nomenclature	187
	Curriculum vitae of the author	190

I

Introduction

1

Motivation

The purpose of the study is the modeling, simulation and characterization of a complex three-dimensional unsteady flow and an evaluation of the prediction capacity of the numerical simulations. The modeling of most practically relevant turbulent flows continues to be based on the Reynolds averaged Navier-Stokes equations. For this reason it is important to evaluate the limitations of this approach with the associated turbulence modeling, in particular for the prediction of time-dependent flows. This work is also strongly related to an industrial application, the understanding of the turbulent flow in a compact draft tube for low head hydraulic turbines. Attention is focused in particular on fluid losses associated with hydraulic efficiency penalties and to the unsteady phenomena in the flow.

Scientific motivation The swirl introduced at the runner outlet sets complex inlet boundary conditions for the draft tube. Greater complexity follows from the draft tube flow streamline curvature and the adverse pressure gradient caused by the diffusion due to the geometrical configuration and from the change of cross sectional shape. Each of these characteristics is known to be difficult to predict with numerical computations. A clear comparison with detailed measurements over a wide range of operating conditions, which would allow an estimation of the influence of modeling parameters, is still missing. Various forms of unsteadiness characterize the flow of hydraulic turbines. In the draft tube, in particular for part load operating conditions, strong flow fluctuations are observed. Relatively little is known about time-dependent phenomena. The application of the two-equation turbulence models quasi-steady approach for the simulation of unsteady flows is questionable, and the limitations are still not well defined. In particular the time scales associated with the runner rotation could invalidate the basic assumption that the turbulence has characteristic time scales that are significantly smaller than those associated with the periodic fluctuation. The conventional closure assumptions have been derived for and calibrated by reference to steady flow and are carried over to unsteady conditions. The likelihood of this being an adequate framework decreases with increasing frequency of the coherent motion. It is expected that when the transient term becomes important everywhere and the temporal variation of the Reynolds stresses is significant, the law of the wall no longer

applies and turbulence models that account only partially for history effects, e.g. only through the total derivative of the turbulent kinetic energy and of the dissipation, are likely to misrepresent the turbulence structure. Visualization of scientific data plays an important role in understanding complex phenomena. Data mining becomes indispensable with the acquisition of high-resolution time-dependent data by means of the numerical simulation. The simulation, visualization and analysis of the flow in the draft tube represent a challenge.

Industrial motivation A large number of hydraulic turbomachinery installations are ageing. This gives rise to the potential for the refurbishment to implementing changes in the design for improved efficiency and associated power output as well as greater operating stability. Usually the runner and guide vanes are focused upon in the refurbishment process. Due to capital constructional costs the spiral casing and the draft tube are seldom redesigned. Unfavorable flow behavior occurs when the runner and the draft tube are unsuitably matched. This can sacrifice flow stability and reduce the optimal operating range of the machine. The modern energy market dictates that energy consortiums operate their hydraulic machines at off-design conditions due to rapidly changing user load conditions. Off design performance of hydraulic turbomachinery is accompanied by strong flow field fluctuations in the draft tube. Modern hydraulic turbomachines are reasonably efficient (up to 95%). Nevertheless it must be recognized that efficiency improvements of only a few tenths of a percent generate substantially increased profits. In Switzerland alone minor improvements in draft tube design for medium head power plants could improve the electrical production by several millions kWh [DBSV90]. During the last decade computational fluid dynamics (CFD) has been used extensively in the analysis and design of hydraulic turbines. Today CFD as a design and analysis tool is applied routinely to all the components of the machine (see for instance [VS88], [KDS96], [LC98], [BFM⁺99]). Due to the lack of detailed measurements of the draft tube flow, the precision and validity range of numerical simulations is not well defined.

2

Hydraulic turbomachinery

[Kov65][Raa85]

Fig. 2.1 shows a simplified view of a low-head hydro-plant employing a Francis turbine. A dam insures the storage reservoir. The water reaches the spiral casing through a conduit. Here the fluid direction is forced from axial to radial. Before reaching the runner the flow direction is regulated with the distributor. The distributor is a mechanism consisting of a large number of hydrodynamically shaped guide vanes disposed around the circumference, which are simultaneously angularly adjustable. From the distributor, the water passes through the runner. The Francis type is a radial turbine: the water flows radial from the exterior to the interior and the direction of the flow changes gradually from radial to axial. The blades are fixed and have a curved shape that induces the necessary pressure difference on the two sides of the blades that causes the rotational motion. The axis of the runner is coupled to the generator, which converts the rotational motion into electric power. The water reaches then the tail water through the draft tube. The diverging draft tube reduces the velocity at the turbine exit and is intended primarily for the regain of head. For constructional reasons most plants have elbow-type draft tubes. The costs of excavation in the deep are very expensive. Often one or two piers are necessary for structural reasons. Head, flow rate and angular velocity give the flow conditions of a Francis turbine. The characteristics of the machine are represented on a $\varphi - \psi$ hill-chart for a given angular velocity. The nondimensional coefficients of the head ψ and of the flow rate φ , allow the comparison with other machines of different dimensions and rotational speeds. The specific speed ν is a nondimensional parameter based on the best efficiency point of the machine and defines the main characteristics of the runner design. Depending on the specific speed, the turbines are divided into low- ($\nu < 0.35$), medium-, and high-speed ($\nu > 0.6$) types. A graph illustrating the hydraulic losses in a Francis machine in function of the specific speed is shown in fig. 2.2. For high specific speed machines the draft tube is the most critical component with respect to the losses because of the increasing available energy at the runner outlet.

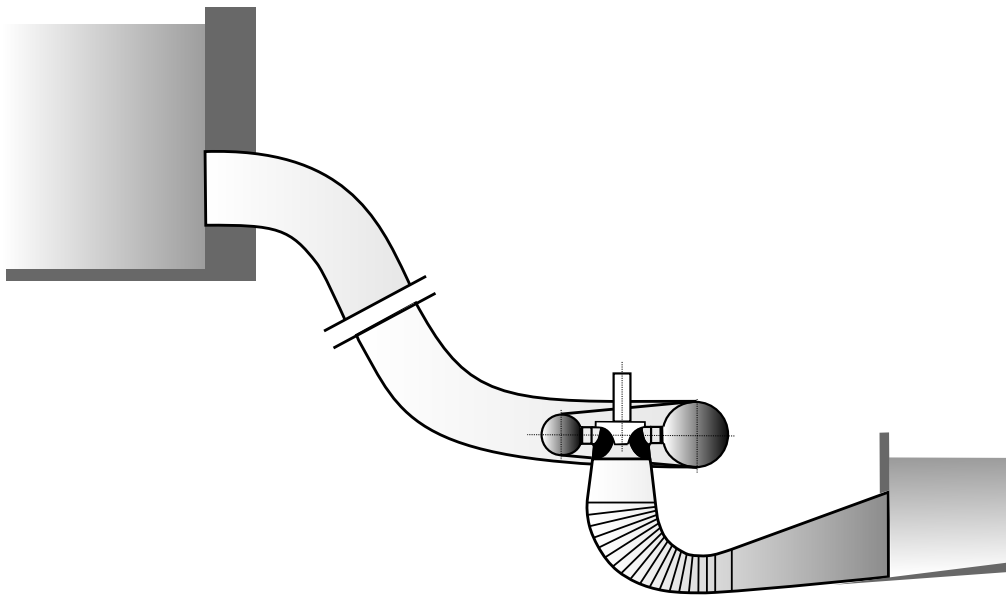


Figure 2.1: Schematic of a power plant.

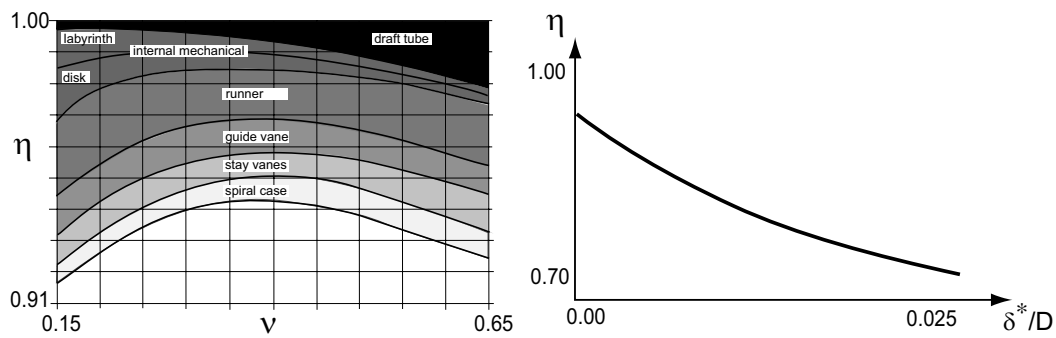


Figure 2.2: a) Losses in a Francis machine depending on the specific speed [OH84], b) influence of the momentum thickness δ^* on the diffuser efficiency [Ack58].

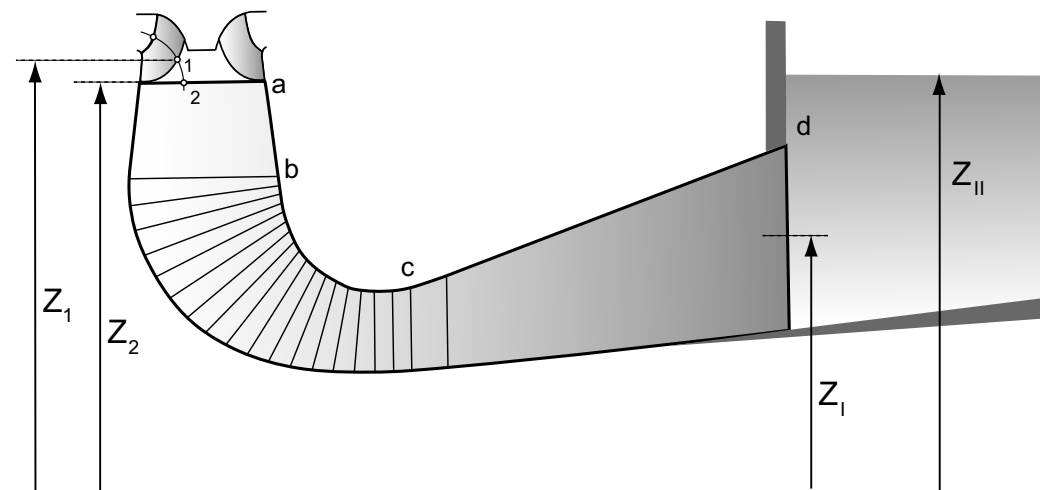


Figure 2.3: Schematic of a draft tube.

2.1 The draft tube

Diffusers are components which act to convert a maximum of dynamic pressure into static pressure. A measure of the efficiency of the diffuser is the static pressure recovery obtained. For conical diffusers with non-swirling inlet flow conditions, best performances are obtained for total internal angles of around 8° and area ratio of 4. Because of design constraints it is desired to use wider-angle diffusers to reduce the total length. The role of the draft tube can be pointed out by considering the energetic balance between sections 1 and II (fig. 2.3) with and without the draft tube (following [Ave01]):

$$\Delta E = g\Delta z + \frac{1}{\rho}\Delta p + \frac{1}{2}\Delta c^2 = g(z_1 - z_{II}) + \frac{1}{\rho}(p_1 - p_a) + \frac{c_1^2}{2} \quad (2.1)$$

where g is the gravitational acceleration, z the geostatic height, p the pressure, c the mean velocity and p_a the atmospheric pressure. c_{II} is considered negligible (large surface). The energetic balance between sections 1-I and I-II can be written as follows:

$$gz_1 + \frac{p_1}{\rho} + \frac{c_1^2}{2} = gz_I + \frac{p_I}{\rho} + \frac{c_I^2}{2} + \Delta E_{\text{loss}_{1-I}} \quad (2.2)$$

$$gz_I + \frac{p_I}{\rho} + \frac{c_I^2}{2} = gz_{II} + \frac{p_a}{\rho} + \Delta E_{\text{loss}_{I-II}} \quad (2.3)$$

where the losses due to the sudden change in the section between I and II can be estimated as $\Delta E_{\text{loss}_{I-II}} = (c_I - c_{II})^2/2 = c_I^2/2$. Without the draft tube $p_1 = p_a$ so that (2.1) becomes:

$$\Delta E_{\text{without}} = g(z_1 - z_{II}) + \frac{1}{2}c_1^2 \quad (2.4)$$

With the draft tube :

$$\Delta E_{\text{with}} = \frac{c_I^2}{2} + \Delta E_{\text{loss}_{1-I}} \quad (2.5)$$

The energetic gain due to the diffuser is therefore:

$$\Delta E_{\text{without}} - \Delta E_{\text{with}} = g(z_1 - z_{II}) + \frac{c_1^2 - c_I^2}{2} - \Delta E_{\text{loss}_{1-I}} \quad (2.6)$$

The draft tube allows the recovery of a part of the kinetic energy between runner outlet and free surface and the level difference.

For an estimation of the static pressure recovery in the draft tube can be decomposed into three elementary components: the inlet cone (a-b, fig. 2.3), a curved diverging diffuser (b-c) and the last straight divergent diffuser (c-d). The application of the energy balance equation from the inlet to the outlet shows the fundamental role played by the cone, where a big part of the static pressure conversion occurs. For each component delimited by the sections i and j we assume: $\Delta p_{ij} = \eta_{ij} \frac{\rho}{2} c_i^2 [1 - (\frac{A_i}{A_j})^2]$, where p is the static pressure, η the

component efficiency, ρ the water density, c the mean normal velocity and A the section surface. Since we are interested in the pressure recovery due to the section expansion, the geostatic height is not considered. Applying Bernoulli and the continuity equation and introducing the data of the studied geometry:

$$\begin{aligned} \frac{p_4 - p_1}{\frac{\rho}{2}c_1^2} &= \eta_{12}\left[1 - \left(\frac{A_1}{A_2}\right)^2\right] + \eta_{23}\left(\frac{A_1}{A_2}\right)^2\left[1 - \left(\frac{A_2}{A_3}\right)^2\right] + \\ &\quad + \eta_{34}\left(\frac{A_1}{A_3}\right)^2\left[1 - \left(\frac{A_3}{A_4}\right)^2\right] = \\ &= 0.48\eta_{12} + 0.32\eta_{23} + 0.15\eta_{34} \end{aligned} \tag{2.7}$$

The ideal recovery factor is 0.95. The maximal recovery occurs in the cone (51%).

In a real flow a crucial role on the pressure recovery in a diffuser is played by the momentum thickness δ^* (loss momentum in the boundary layer as compared with a uniform flow) where an increase of δ^*/D from 0.5% to 3% leads to a drop of the efficiency of 20%, as shown in fig. 2.2 [Ack58].

3

Numerical flow simulation in a draft tube, state-of-the-art

Due to the complexity of the flow in the hydraulic turbine draft tube the first publications on three-dimensional RANS-based numerical studies began only in the second half of the eighties. From the initial 10^4 grid points, we reach today 10^6 points. In [SB86] and [ARC88] the importance of the inlet swirl on the overall pressure recovery and on the stalling characteristics in the downstream region is already recognized. The recovery factor increases up to a given swirl and then drops off. A good agreement in the comparison with three measurement section results and the static pressure evolution is found in [VS88]. The mesh dependence study shows that a $5 \cdot 10^4$ grid points mesh provides a precision comparable with the measurement uncertainty of pitot tube tests. In the Gamm workshop [SR89] seven contributions deal with the flow in the draft tube. Euler and RANS solver are employed. Comparisons with measurements show a fair degree of agreement for the static pressure evolution and important differences in the secondary flow. Experimentally the flow is found to be unsteady in the outlet region. The importance of inlet and outlet boundary conditions is recognized. In [Rup89] and [Rup90] the agreement with measurements is quite satisfactory and the results are more accurate for the case with non-swirling inlet boundary conditions. Numerical results are compared with experimental flow patterns from the oil film method in [TITS90]. The main flow behaviours are in part adequately predicted but not the total loss. Detailed measurements of the flow and pressure field are compared with computations in [CVD⁺90]. Good agreement is found for the overall static pressure evolution and for the velocity field up to the pier. An overall view of knowledge of draft tubes was published in 1990 [DBSV90]. This reference contains a complete data bank about power plant specifications and geometric draft tube dimensions, including plans of all Swiss low head schemes. The pier is found to strongly affect the entire flow field in [DGS92]. The velocity distributions for four operating points are sufficiently close to the measurements even in the case of swirling inlet flow. Discrepancies increase for the velocity profile near the walls. The flow is found to be very sensitive to velocity and turbulence inlet conditions. A numerical optimization of the geometry is successfully achieved in [Chi93]. Other comparisons with measurements can be found in

[PDH⁺94], [RCG94], [SC94], [VSP96], [KHA96], [LC98]. In 1999 a workshop on the flow in a draft tube was held in Sweden [GGK99]. The 26 simulations show a wide range of scatter. Several groups are however able to predict the pressure recovery factor with reasonable accuracy. Second moment closure models do not show any advantages compared with the simple two-equation models. A strong sensitivity to inlet condition is recognized. A contributor estimates that it would require at least $2 \cdot 10^6$ grid points for a pressure recovery error below 1%. In [BFM⁺99] the k - ϵ model is believed to be inaccurate for the description of the flow in the draft tube. Numerical results are compared with measurements on an air test rig of a Kaplan turbine. The same case of the workshop is studied in [KM00]. A Reynolds Stress Transport model is found to perform better than a two-equation model. A full stage simulation of a high specific speed Francis turbine is described in [KDS96]. The application of a LES method to a full machine, however with a coarse mesh, is carried out in [Che95], where the largest peak of the power spectra of the draft tube is found at a Strouhal number of 0.19 and has the greatest effect on the power output oscillation. Computation of the draft tube flow with the LES method on a coarse mesh is also performed in [WJX⁺00], where a rotating inlet eddy is imposed at the inlet. The influence of the eddy is limited up to the elbow. Recently in [RHAS01] and [RS01] the frequency of the typical helical rotating vortex visible at part load is obtained by means of RANS computation with steady inlet boundary conditions.

4

Thesis focus and document organization

Summarizing the bibliographic study the computation of the mean flow field in a draft tube is still a challenging task. Hereto the results of the recent Swedish workshop are a good example. A clear comparison with detailed measurements over a wide range of operating conditions, allowing an estimation of the influence of modeling parameters, is still missing. In spite of the relatively large number of studies, little is known about the flow features in the draft tube. The first unsteady computations reported in the literature indicate that the RANS approach brings, at least for operating conditions showing a strong instability, valuable information. Investigations on other types of unsteadiness are necessary.

The main objectives of the work are therefore the definition of the capacity of the numerical simulation to reproduce the flow in the draft tube and the comprehension of the associated mean and time-dependent flow phenomena. In particular, a typical sudden drop of the pressure recovery near the best efficiency operating condition should be explained and the influence of forced fluctuations introduced by the runner, as well as possible self-sustained oscillations, should be investigated. Due to the spreading use and to the limited computational resources, the Reynolds averaged equations are adopted. Hence the work falls into three main themes:

- verification and validation of computed results,
- analysis of the mean steady flow field,
- analysis of the time-dependent flow phenomena.

The governing equations of internal incompressible flows and the relative discretization applied by the code are first presented. Four reference cases check the numerical approach for different aspects of the draft tube flow (part III). The test cases are:

flow in a slot with an oscillating pressure gradient,

vortex shedding past a square cylinder,
swirling flow in a pipe,
swirling flow in a conical diffuser.

For the first case the analytical solution is derived. In the other cases experimental data are found in the ERCOFTAC database¹. The investigated geometry and operating conditions are described in part IV. The main work begins with the verification of the computations with respect to modeling and discretization choices, which are treated in part V. Part VI is devoted to the flow analysis of the steady computations and to the comparison with measurements. The flow is first analyzed globally with an energetic approach in VI.3, then locally by means of a topological investigation in VI.4. Flow patterns and energy evolution along the draft tube are revealed. The unsteady phenomena are first considered in part VII, where steady boundary conditions are applied. Some operating conditions indeed show periodic self-sustained fluctuations. Unsteady inlet velocity profiles are imposed for the computations presented in part VIII. Firstly, the influence of the forced unsteadiness due to the runner is introduced via the inlet boundary conditions and the evolution of the blades wake is analyzed. An operating point at part load with the rotating vortex is then studied in VIII.2. Finally the linear stability of the inlet profiles is investigated in VIII.4. A short summary and some perspectives are discussed in IX.

¹<http://ercoftac.mech.surrey.ac.uk>

II

Modeling and numerical approach

1

Governing equations

1.1 The Navier-Stokes equations

Most of the flows in nature and in industry are turbulent. In this case the inertia force dominates over the viscous force (large Reynolds number). The governing equations of hydrodynamic turbulent flows are the conservation laws of mass, momentum and energy. In engineering applications many hydraulic flows can be considered incompressible. The disadvantage of this assumption is that hydro acoustic waves are not modeled. In a hydraulic machine these phenomena play an important role on the dynamic of the installation. This is observed in particular during the transient phases such as the start up or at those part load operation conditions where the eigenfrequency of the installation is excited by the typical helical rotating vortex. The flow in our application can be considered isothermal. The fluid is assumed to be a Newtonian continuum. An incompressible and isothermal flow has a constant viscosity and can be described by the velocity field and the pressure. The conservation laws system is known as the Navier-Stokes equations. Experience shows that this system of equations accurately describes the flow of Newtonian fluids. Mathematically the incompressible Navier-Stokes are of mixed elliptic-parabolic and the compressible hyperbolic-parabolic type. The continuity equation can be expressed in a Cartesian coordinate system $(x, y, z)'$ and in tensor notation as follows:

$$\frac{\partial u_j}{\partial x_j} = 0 \quad (1.1)$$

and the momentum conservation:

$$\frac{\partial u_i}{\partial t} + \frac{\partial (u_j u_i)}{\partial x_j} = \frac{1}{\rho} \left(-\frac{\partial p}{\partial x_i} + \frac{\partial \tau_{ij}}{\partial x_j} \right) \quad (1.2)$$

where u_i represents the velocities in the x_i coordinate directions, p is the static pressure, ρ the constant density, and τ_{ij} the viscous stress tensor.

For a Newtonian fluid:

$$\tau_{ij} = \mu \left(\frac{\partial u_i}{\partial x_j} + \frac{\partial u_j}{\partial x_i} \right) \quad (1.3)$$

where μ is the dynamic viscosity.

The equation can be made nondimensional by means of a characteristic length L_o , time scale t_o and velocity v_o .

$$St \frac{\partial u_i^*}{\partial t^*} + \frac{\partial (u_j^* u_i^*)}{\partial x_j^*} = -\frac{\partial p^*}{\partial x_i^*} + \frac{1}{Re} \left(\frac{\partial^2 u_i^*}{\partial x_j^{*2}} \right) \quad (1.4)$$

where $x_i^* = \frac{x_i}{L_o}$, $t^* = \frac{t}{t_o}$, $u_i^* = \frac{u_i}{v_o}$, $p^* = \frac{p}{\rho v_o^2}$, the Strouhal number $St = \frac{L_o}{v_o t_o}$ and Reynolds number $Re = \frac{\rho v_o L_o}{\mu_o}$.

The equations system can be written in conservative form as follows:

$$\frac{\partial G}{\partial t} + \nabla \cdot F = 0 \quad (1.5)$$

where $G = [\rho \quad \rho u \quad \rho v \quad \rho w]'$.

1.2 The Reynolds averaged Navier-Stokes equations [Rod84]

Turbulent fluid motion is highly random, unsteady, three-dimensional: it consists of many eddies with different lengths and time scales. Due to these complexities, the turbulent motions are extremely difficult to describe and thus to predict theoretically. Often the fluctuating turbulent motions contribute significantly to the transport of momentum, heat and mass and hence have a determining influence on the velocity field. The exact equations describing the turbulent motion are believed to be the Navier-Stokes equations, and numerical procedures are available to solve these equations, but the storage capacity and speed of present-day computers is still not sufficient to allow a solution for a practically relevant turbulent flow. This approach is known as direct numerical simulation (DNS). The reason is that the turbulent motion contains elements which are much smaller than the extent of the flow domain and small time scales. Specifying boundary conditions at open boundaries is also a difficult issue. If complex flows have to be computed, turbulent inflow and outflow boundary conditions are also required.

As the turbulent transport process can not be calculated with an exact method, it must be approximated by a turbulence model which, with the aid of empirical information, allows the turbulent transport quantities to be related to the mean flow field. In the Reynolds-averaged procedure, the Navier-Stokes equations are averaged over a time period larger than the largest characteristic period of the flow motion. The physical variables are decomposed into mean and fluctuating components. Only the mean values are solved and therefore it is necessary to express the fluctuating values in function of these ones. The resulting equations describe the mean flow field and introduce an additional unknown: the Reynolds stress. This term describes the influence of the turbulent field on the mean flow. Due to nature of turbulence it is impossible to model this term in a general way. Today the best compromise between range of

applicability and computational economy is still offered by the so-called two-equation models employing differential transport equations for the velocity and length scales of the fluctuating motion. No single turbulence model captures all features of a moderately complex flow. However, many flow features do not depend on a precise evaluation of the Reynolds stresses, being dominated by other phenomena such as inviscid effects.

The instantaneous depending variables r^* are decomposed as follows:

$$r^*(x_i, t) = r(x_i) + r'(x_i, t) \quad (1.6)$$

where r are the time-averaged variables and r' the superimposed fluctuations. The time-averaging operator is defined as:

$$\overline{r^*} = \lim_{\Delta t \rightarrow \infty} \frac{1}{\Delta t} \int_{t_0}^{t_0 + \Delta t} r^* dt = r(x_i) \quad (1.7)$$

where the time interval Δt is long compared with time scale of the turbulent fluctuations.

Inserting the decomposed variables into (1.1) and (1.2) and applying the property $\overline{r'} = 0$ one obtains the Reynolds-averaged Navier-Stokes equations (RANS):

$$\begin{cases} \frac{\partial u_j}{\partial x_j} = 0 \\ \frac{\partial u_i}{\partial t} + \frac{\partial u_j u_i}{\partial x_j} = -\frac{\partial p}{\partial x_i} - \frac{\partial}{\partial x_j} (\tau_{ij} - \overline{\rho u'_i u'_j}) \end{cases} \quad (1.8)$$

where all variables are now time averaged, although the same notation as equations (1.1)-(1.5) is used. The Reynolds stress $\overline{\rho u'_i u'_j}$ can not be expressed exactly as function of the mean flow variables and must be related to known quantities using a turbulence model.

1.3 Turbulence model

The simplest approach to turbulence closure is based on the scalar eddy-viscosity concept, relating the Reynolds stress to the associated primary strain components. Implicit in the concept is a number of assumptions about turbulence which are incompatible with experimental observations, such as: insensitivity to turbulence structure, isotropy of normal stresses, near-isotropy of turbulent transport, local equilibrium of stresses and insensitivity of any stress to strains other than that involved in the eddy-viscosity relation. Typical consequences are: excessive production of shear stress, suppression of separation along curved walls, excessive level of turbulence in regions of strong normal stress and wrong response to swirl.

The Reynolds stress is assumed to be proportional to the local mean velocity gradients, in analogy to the viscous stress in laminar flows (Boussinesq's eddy-viscosity concept (1877)):

$$\overline{\rho u'_i u'_j} = -\mu_t \left(\frac{\partial u_i}{\partial x_j} + \frac{\partial u_j}{\partial x_i} \right) + \frac{2}{3} \rho \delta_{ij} k \quad (1.9)$$

where μ_t is the turbulent (eddy) viscosity, k the turbulent (fluctuating motion) kinetic energy and δ_{ij} is the Kronecker delta¹. The eddy viscosity is not a fluid property as the molecular viscosity, but a flow property that depends strongly on the state of turbulence.

Additionally to the eddy-viscosity concept it is necessary to make the expression applicable also to the normal stresses, which sum is twice the kinetic energy $k = \frac{1}{2}\sqrt{u'_i u'_i}$. The inclusion of the second term in (1.9) assures this property. In analogy to the molecular viscosity that is proportional to the average velocity and the mean free path of molecules, the eddy viscosity is considered proportional to a velocity characterizing the fluctuating motion ($\sim \sqrt{k}$) and to a characteristic length ($\sim \frac{k^{3/2}}{\epsilon}$):

$$\mu_t = \rho c_\mu \frac{k^2}{\epsilon} \quad (1.10)$$

The analogy to the Stokes' viscosity law presumes that the turbulent eddies behave like molecules that collide and exchange momentum. This assumption is conceptually weak, but the eddy-viscosity concept is found to work well in many flow situations. c_μ is an empirical constant. The turbulence model is used to provide the eddy viscosity and the turbulent kinetic energy.

Two equation turbulence models

$k - \epsilon$ model The model solves the transport equations for the turbulent kinetic energy k and for ϵ , the dissipation rate of k , i.e. the rate at which turbulent kinetic energy is converted into internal energy by viscous action. The semi-empirical transport equations are:

$$\frac{\partial(\rho k)}{\partial t} + \frac{\partial(\rho u_j k)}{\partial x_j} = \frac{\partial}{\partial x_j} \left(\frac{\mu_t \partial k}{\sigma_k \partial x_j} \right) + P_k - \rho \epsilon \quad (1.11)$$

$$\frac{\partial(\rho \epsilon)}{\partial t} + \frac{\partial(\rho u_j \epsilon)}{\partial x_j} = \frac{\partial}{\partial x_j} \left(\frac{\mu_t \partial \epsilon}{\sigma_\epsilon \partial x_j} \right) + \frac{\epsilon}{k} (c_{\epsilon 1} P_k - \rho c_{\epsilon 2} \epsilon) \quad (1.12)$$

in which the production rate of turbulent kinetic energy, P_k , is given by:

$$P_k = \mu_t \left(\frac{\partial u_i}{\partial x_j} + \frac{\partial u_j}{\partial x_i} \right) \frac{\partial u_i}{\partial x_j} \quad (1.13)$$

The empirical constants in the model equations take usually the standard values given by Launder and Spalding [LS74].

$k - \omega$ model Standard turbulence models based on the ϵ -equation often predict the onset of separation too late and underpredict the amount of separation later on. This model has been developed to solve these problems. Analogously to the $k - \epsilon$ model two transport equations for the turbulent kinetic energy k and the ‘‘turbulent frequency’’ (inverse time scale) ω are solved. The turbulent viscosity is computed from these scalars:

$$\mu_t = \rho c_\mu \frac{k}{\omega} \quad (1.14)$$

¹ $\delta_{ij} = 1$ for $i = j$ and $\delta_{ij} = 0$ for $i \neq j$.

Reynolds-stress-equation model (RSM, second-order closure scheme)

As the complexity of the flow increases, the limits of the turbulence models become evident (see for instance [Nal87]) and improved models are necessary. Second-order closure schemes do not employ the eddy viscosity concept but solve the transport equations for the individual Reynolds stresses and are therefore better suited for complex strain fields as well as for simulating transport and history effects and anisotropy of turbulence. They automatically account of the effects due to streamline curvature and rotation. While there is no doubt that Reynolds stress models have greater potential to represent turbulent flow phenomena more correctly than the two-equation models, their success so far has been moderate [FP99].

1.3.1 Near-wall treatment

The viscous sublayers are not resolved in most practical calculations with the k - ϵ and RSM model due to the steep gradients present in these regions. Additionally the high Reynolds number turbulence models are not applicable where viscous effects dominate. The turbulent core and the viscous sublayer have independent behaviours. The connecting zone is described in the “wall function” approach by a logarithmic relation between the near wall tangential velocity and the wall shear stress. It is assumed that in this region the velocity profile is entirely determined by the fluid characteristics and is independent from the flow. This relation has been found to have an unexpected large universality, however its application in particular flow situations, e.g. where separation occurs, is questionable. The logarithmic relation can be expressed as:

$$u^+ = \frac{1}{\kappa} \ln(y^+) + C \quad (1.15)$$

with $u^+ = \frac{u}{u_\tau}$, $y^+ = \frac{yu_\tau}{\nu}$, $u_\tau = \sqrt{\frac{\tau_w}{\rho}}$, u_τ is the wall tangential velocity, τ_w the wall shear stress, κ and C are well defined empirical constants. The logarithmic zone corresponds to $30 < y^+ < 400$. The near wall region is divided in two additional zones: the “laminar” sublayer for $0 < y^+ < 3$ with $u^+ = y^+$ and the buffer zone $3 < y^+ < 30$.

2

Flow solver

Due to the spreading use in the industry the numerical computation are carried out with the commercial code TASCflow.

2.1 Numerical method [RGH89][TAS99]

A fully implicit, collocated, finite volume method has been implemented. The conservation equations are integrated over finite control volumes from hexahedral flux elements with a strongly conservative approach. Shape functions are used to evaluate the derivatives for all the diffusion terms.

The finite volume method The governing equations and the Cartesian components of momentum are used in strong conservation form. By integrating over each finite volume and using Gauss's theorem, equation (1.5) becomes:

$$\frac{\partial}{\partial t} \int_V G + \int_S F_i dn_i = 0 \quad (2.1)$$

where V and S denote the volume and surface integrals respectively, and dn_i are the differential Cartesian components of the outward normal surface vector. The surface integrals are integrations of the fluxes of the conserved quantities. The control volume (cv) surfaces are defined by the element mid-planes. Applying the first order implicit Euler temporal scheme the discrete form of (2.1) can be written as:

$$V \left(\frac{G - G^o}{\Delta t} \right) + \sum_{ip} (F_i \Delta n_i)_{ip} = 0 \quad (2.2)$$

where the superscript $()^o$ indicates the old time level, and ip denotes an integration point.

Collocation The modeling of incompressible flows on a collocated grid¹ leads to the problem of pressure field decoupling. To avoid this a method

¹all the variables are stored at the same set of points; the location of the momentum control volumes and the continuity control volumes are not shifted to one another as in the case of a staggered grid.

similar to that of Rhie and Chow has been implemented. The basic principle is to incorporate pressure-velocity coupling into the continuity equation so that pressure appears in a manner that precludes the decoupling. This is done by introducing a pressure redistribution term.

Advection modeling The approach taken is to use an upwind skew scheme that is physically corrected to be second-order-accurate. From a Taylor series expansion a variable in an integration point ϕ_{ip} can be written as $\phi_{ip} = \phi_u + \Delta s \frac{d\phi}{ds} + O(\Delta s^2)$, where s is the streamwise direction. The term ϕ_u is estimated by a skew scheme, and $\Delta\phi = \Delta s \frac{d\phi}{ds}$ is modeled by the advection correction term. The skew scheme primarily addresses the directionality of the flow, while the physical advection correction (PAC) term addresses the streamwise variation of the transported variable and is needed to achieve the second order accuracy in the streamwise direction. The upwind skew scheme is a refinement of the skew upwind difference scheme of Raithby [VTR87].

- Linear profile skew (LPS) scheme :

The value of ϕ_u is determined from a tri-linear interpolation of the ϕ lying on the flux surface that is intersected by the straight line from the integration point upstream in the local flow direction. LPS with PAC is second order accurate. Also available :

- Modified linear profile skew (MLPS) scheme:

The interpolation coefficients obtained with LPS are modified to replace any node which is on the downstream side of the integration point surface, with an equal dependence on the nearest node within the element that is situated in the upstream side of the integration point surface. This modification effectively limits the most damaging negative coefficient influence, but the formal accuracy is no longer of second order.

Diffusion terms Following the standard finite element approach, shape functions are used to evaluate the derivatives for all the diffusion terms. The resultant gradient estimates are first order accurate.

Pressure gradient term The value of the pressure at the integration points is evaluated by linear interpolation using the shape functions.

Algebraic solver The implemented algebraic solver is fully coupled. The base solver used is the coupled Gauss-Siedel. This solver preferentially reduces the high frequency errors and leaves the long wavelength errors relatively unchanged. In order to reduce the long wavelength errors a multigrid linear accelerator is used.

Transient term For steady problems a marching method is used to integrate the unsteady terms until the solution is sufficiently close to the steady solution. In this case the goal is simply to remove the transient portion of the solution as quickly as possible and therefore time accuracy is not required. The strongly nonlinear RANS equations are temporarily linearized to enable an implicit solution approach. No effort is done to recover the nonlinearity of the equations. The transient term is approximated by an implicit first order accurate Euler scheme, which is robust and creates no time step limitations. For unsteady problems an internal loop tries to recover the nonlinearity of the equations. The approach is similar to the Newton-Raphson iterative method but with frozen coefficients. An implicit second order scheme is employed.

Turbulence models In addition to the classical k - ϵ model, the Kato-Launder k - ϵ model [KL93], the classical k - ω Wilcox model [Wil86] and the baseline (BSL) model [TAS99] are implemented. The BSL model blends between the k - ω , applied near the surface, and the k - ϵ applied outside the boundary layer. The classical LRR model proposed by Launder et al. [LS75], which uses a linear relation for the pressure-strain correlation, and the SSG model of Speziale et al. [SSG91], characterized instead by a quadratic relation, are implemented as second-order closure schemes.

Near wall treatment The near wall region is described with the help of a wall function as explained in section 1.3.1. In the buffer zone $3 < y^+ < 30$ it is assumed that: $u^+ = d_1 y^{+3} + d_2 y^{+2} + d_3 y^+ + d_4$ with $d_1 = 6.4264e^{-4}$, $d_2 = -5.2113e^{-2}$, $d_3 = 1.4729$, $d_4 = -1.1422$ and $\kappa = 0.41$, $C = 5.2$ (see (1.15)).

2.1.1 Boundary conditions

No-slip wall The fluid velocity normal to the wall is zero; each boundary integration point mass flow is set to zero. The boundary wall momentum flow includes pressure and viscous forces. The pressure force is computed by interpolation of the control volume pressures. The normal viscous force is set to zero such that the viscous force is equal to the tangential component. Based on a logarithmic velocity profile, the wall shear stress is computed and hence the wall tangential viscous force. The gradients normal to the wall are zero. The flux of k and ϵ through the wall is assumed to be zero. The production of k is estimated in the near wall region, based on an assumption of local equilibrium between the production and dissipation of turbulent kinetic energy.

Inlet The velocity and turbulent kinetic energy profiles are imposed. The turbulent dissipation rate is computed from $\epsilon = k^{3/2}/L_\epsilon$, where L_ϵ is the eddy length scale. The inlet flows of k and ϵ involve advection and diffusion. Diffusion is assumed negligible compared with advection. Pressure is an implicit result of the simulation. The inlet momentum flow involves advection, pressure and viscous force components. The pressure force is computed by interpolation of

the cv pressures. The viscous force is expressed in terms of the cv velocities and the specified velocity.

Outlet The outlet boundary velocity for the purposes of advection is assumed to be an implicit result of the computation. Consistent with a fully developed flow, the normal viscous force component is assumed to be zero. For incompressible flow with one outlet it is possible to leave the pressure unspecified. The outlet momentum flow is composed by the advection, pressure and viscous force components. The normal viscous force is set to zero and the tangential component is computed based on the cv velocities. The boundary pressure is equal to the interpolated nodal pressure. For the transport equations the gradients normal to the outlet face are assumed to be zero. PAC terms at boundary cv are computed by a first order extrapolation of the PAC terms at nearby interior volume.

III

Reference cases

1

Piston reciprocating in simple harmonic motion

1.1 Description

An incompressible viscous fluid in a rectangular duct is forced to move under an oscillating pressure gradient. This type of flow occurs for instance under the influence of a reciprocating piston. This is an extension of the problem of the boundary layer of a viscous fluid bounded by an infinite plane surface which executes a simple harmonic oscillation with a frequency ω , in its own plane, which was first studied by Stokes (from [Sch64]). For this type of flow, transverse waves occur in the fluid, with the velocity perpendicular to the direction of propagation. Stokes introduced the length scale $l_s = \sqrt{(2\nu)/\omega}$ (Stokes length), representing the depth of penetration of the viscous wave. The amplitude of the transverse waves is exponentially damped by e^{-y/l_s} as one moves away from the solid surface (y-direction). The motion of an oscillating flow in a duct is also characterized by the depth of penetration of the viscous wave. In the case of high-frequency oscillations the viscous term can be neglected everywhere except in the very narrow layers near the walls. The width of these layers is in the order of magnitude of the penetration depth of the viscous wave $d \sim \sqrt{\nu/\omega}$. At a large distance from the wall the fluid moves as if it was frictionless and, moreover, its phase is shifted by half a period with respect to the exciting force. A pure pulsating flow in a circular pipe driven by a periodic pressure difference was investigated experimentally by Richardson and Tyler (1929), and its exact analytic solution was obtained by Sexl (1970) and Uchida (1956) (from [Sch64]). The interesting feature of this flow is that the amplitude of the oscillations divided by the amplitude at the axis, has a maximum, which occurs near the wall as shown in figure 1.2. Introducing the nondimensional distance from the wall $y_s = y/l_s = y/\sqrt{(2\nu)/\omega}$, it was found both experimentally and analytically, that the maximum occurs at $y_s = 2.28$. This effect is known as ‘‘Richardson’s annular effect’’ [Sch64]. The solution depends only from the nondimensional frequency $f^* = L/l_s = \sqrt{\omega/(2\nu)}L$, where ω is the imposed frequency and L the half of the duct height. f^* is the ratio of the characteristic length of the geometry to the characteristic length of the

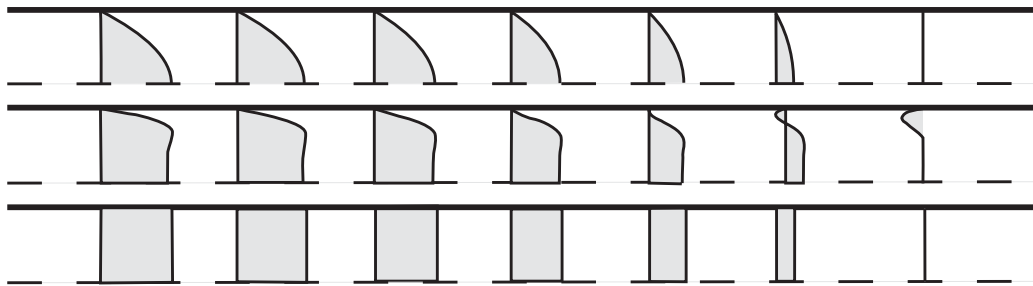


Figure 1.1: Instantaneous velocity profiles on a quarter of a cycle for different f^* (from the top: $f^* = .1, 10, 1000$).

viscous terms. Figure 1.1 shows some examples of velocity profiles. For small f^* the profiles are the same as the quasi-steady solution. For high values the fluid moves like a solid body. The measurements of Binder [BK81] in turbulent channel flow with forced velocity oscillations of small amplitude show that the mean flow and the mean turbulent intensity are not affected by the forced oscillations. The amplitude and the phase shift of the periodic velocity fluctuations follow the laminar Stokes solution at high frequency. At low frequencies near the wall the gradient of the amplitude becomes steeper than in the Stokes flow and the phase shift decreases to slight negative values. The Stokes thickness $l_s = \sqrt{(2\nu)/\omega}$ and the viscous length $l_\nu = \nu/u_\tau$ of the steady wall flow are the relevant length scales. The relevant parameter governing the evolution of the velocity oscillations is $l_s^+ = l_s/l_\nu$. This parameter shows how far the laminar Stokes layer would reach into the inner layer of the steady turbulent flow if there was no interaction between the two flows.

1.2 Analytical solution

An incompressible liquid forced to move in a duct under an oscillating pressure gradient is considered. The velocity vector is supposed to be one-dimensional, so that the velocity vector is $v = (u(x, y, t), 0, 0)$. The Navier-Stokes equations assume the following form:

$$\begin{cases} \frac{\partial u}{\partial t} = \frac{1}{\rho} \left(-\frac{dp}{dx} + \mu \frac{\partial^2 u}{\partial y^2} \right) & \text{in } \Omega \\ u = 0 & \text{on } \partial\Omega \end{cases} \quad (1.1)$$

where Ω is the domain and $\partial\Omega$ the bounding walls. For a sinusoidal pressure gradient:

$$\delta = -\frac{1}{\rho} \frac{\partial p}{\partial x} = A \sin(\omega t) = \text{Im}[Ae^{i\omega t}] \quad (1.2)$$

and by assuming that the velocity function has the following form:

$$u = \text{Im}[f(y)e^{i\omega t}] \quad (1.3)$$

one finds:

$$u = \text{Im} \left[\frac{A}{i\omega} \left(1 - \frac{\cosh(\sqrt{\frac{i\omega}{\nu}} y)}{\cosh(\sqrt{\frac{i\omega}{\nu}} L)} \right) e^{i\omega t} \right] \quad (-L \leq y \leq L) \quad (1.4)$$

where $\nu = \frac{\mu}{\rho}$ and $2L$ is the duct height.

For $\lim_{\sqrt{\frac{\omega}{\nu}} \rightarrow 0} u = \frac{A}{2\nu}(L^2 - y^2) \sin(\omega t)$, the profiles have the classical parabolic shape, with the amplitude according to the instantaneous pressure gradient. Viscous diffusion is rapid enough to keep the profile in a quasi steady state. When the viscous diffusion depth is small compared with the slot width the fluid moves like a solid body: $\lim_{\sqrt{\frac{\omega}{\nu}} \rightarrow \infty} u = -A \cos(\omega t)$.

For a general harmonic oscillation:

$$\delta = -\frac{1}{\rho} \frac{\partial p}{\partial x} = D + A \sin(\omega t - \varphi) \quad (1.5)$$

the velocity profile and the pressure gradient can be developed with the eigenvectors ζ of the Laplace operator in (1.1):

$$\begin{cases} \Delta \zeta = -\lambda \zeta \\ \zeta(0) = \zeta(2L) = 0 \end{cases} \quad (1.6)$$

$$\zeta_k = \sin\left(\frac{k\pi}{2L} y\right), \lambda_k = \left(\frac{k\pi}{2L}\right)^2, k = 1, 3, 5, \dots (0 \leq y \leq 2L) \quad (1.7)$$

$$u = \sum_k u_k \sin\left(\frac{k\pi}{2L} y\right), \delta = \sum_k \delta_k \sin\left(\frac{k\pi}{2L} y\right) \quad (1.8)$$

in this way the partial differential equation is reduced to :

$$\begin{cases} \frac{du_k}{dt} = -\nu \lambda_k u_k + \delta_k \\ u_k(0) = 0 \end{cases} \quad (1.9)$$

$$u_k = \int_0^t e^{-\nu \lambda_k (t-\tau)} \delta_k(\tau) d\tau \quad (1.10)$$

finally the coefficients are:

$$\begin{aligned} u_k = & \frac{4}{k\pi} \left[\frac{D}{\nu \left(\frac{k\pi}{2L}\right)^2} + \right. \\ & \frac{A}{\nu^2 \left(\frac{k\pi}{2L}\right)^4 + \omega^2} \left(\sin(\omega t) \left[\nu \left(\frac{k\pi}{2L}\right)^2 \cos(\varphi) + \omega \sin(\varphi) \right] + \right. \\ & \left. \left. \cos(\omega t) \left[\nu \left(\frac{k\pi}{2L}\right)^2 \sin(\varphi) - \omega \cos(\varphi) \right] \right) \right] + e^{-\nu \left(\frac{k\pi}{2L}\right)^2 t} [\dots] \end{aligned} \quad (1.11)$$

This solution corresponds to the steady parabolic profile due to the constant term D in the pressure gradient in (1.5) superposed to the solution (1.4). The system (1.1) is linear in u .

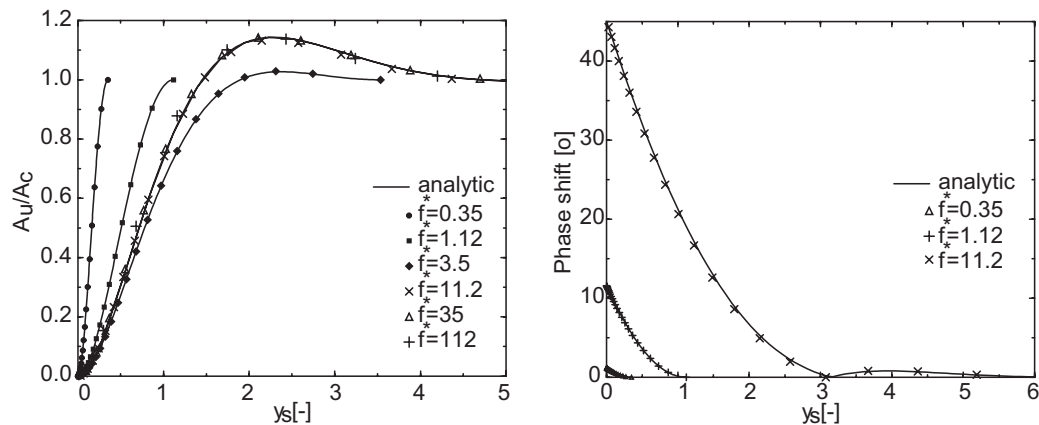


Figure 1.2: a) Relative amplitude of the periodic velocity oscillations versus nondimensional distance $y_s = y/l_s$ where the Stokes length is $l_s = \sqrt{2\nu/\omega}$, b) phase shift of the oscillations from the wall to the axis.

1.3 Simulation

The channel ratio length/height is set to 20. Because of the symmetry of the flow the computational domain covers only the half of the rectangular channel. A 150×50 nodes mesh is used. The ratio of the first interval at the wall to the last at the axis is 0.002. A uniform profile at the inlet and a zero gradient outlet condition are imposed. After a length of four diameters the velocity assumes the form of the developed profile. In order to compare the results with the analytical solution, the pressure gradient that causes the same mass flow evolution as imposed in the computations must be found out. The phase shift between the flow rate and the pressure gradient oscillation tends to π for low frequencies f^* and to $\pi/2$ for high f^* . A laminar flow is considered, the Reynolds number based on the mean velocity and the half channel height is 5. The time step corresponds to $1/30$ of the period. A target of $1.e^{-3}$ for the maximal residuum of the internal loop leads to the same velocity profiles as when the convergence is set to $1.e^{-4}$. However in this case, in some range of the period, wiggles in the pressure gradient are observed. The first order integration scheme needs four times more time steps per period in order to reach the same precision as with the use of the second order scheme. Six frequency ranging from $f^* = 0.35 - 112$ ($l_s = 0.14 - 4.5e^{-4}$) are computed. Results are compared with the analytical solution in figure 1.2. The agreement is excellent. Some cases with $D \neq 0$ (1.5) have been also successfully tested.

2

Vortex shedding past a square obstacle

2.1 Introduction

The separated flow around two-dimensional bluff bodies exhibits, for a sufficiently high Reynolds number, self-induced periodical fluctuations due to vortices being shed alternately from either sides of the body with a dominant frequency $f \approx \frac{0.2U_o}{D}$, as a result of the interaction between the two shear layers. The problem of vortex shedding from bluff bodies has been extensively studied since the pioneering work of Strouhal (1878) and von Karman (1912). The near-field wake flow behind the bluff body is temporally and spatially complex, with direct interaction between the two separated shear layers and regions of irrotational flow entrained into the wake. The separation is characterized by two reversal points in the velocity profile (see fig. 2.1) and a positive pressure gradient in the flow direction in the separated zone. Velocity profiles with reversal points, in particular when coupled with separated regions, often show instability phenomena.

Bluff body wake flows have direct engineering significance. The alternate shedding of vortices in the wake leads to large fluctuating pressure forces in a direction transverse to the flow and may cause structural vibrations and acoustic

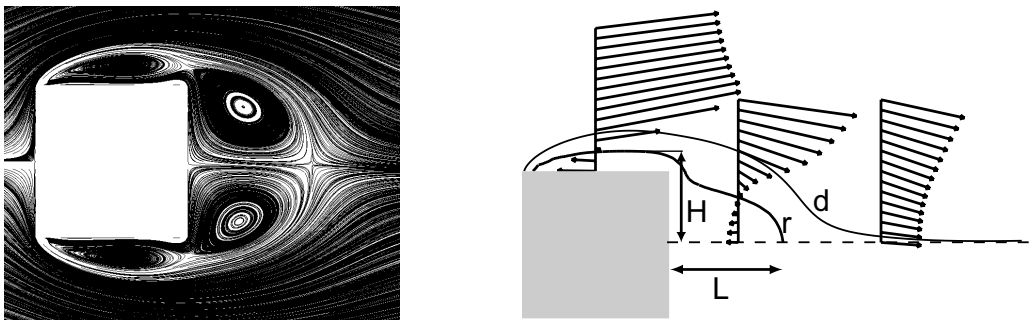


Figure 2.1: Mean flow $Re = 22000$: a) computed streamlines, b) corresponding recirculation (r) and detachment (d) lines and recirculation length (L) and height (H) .

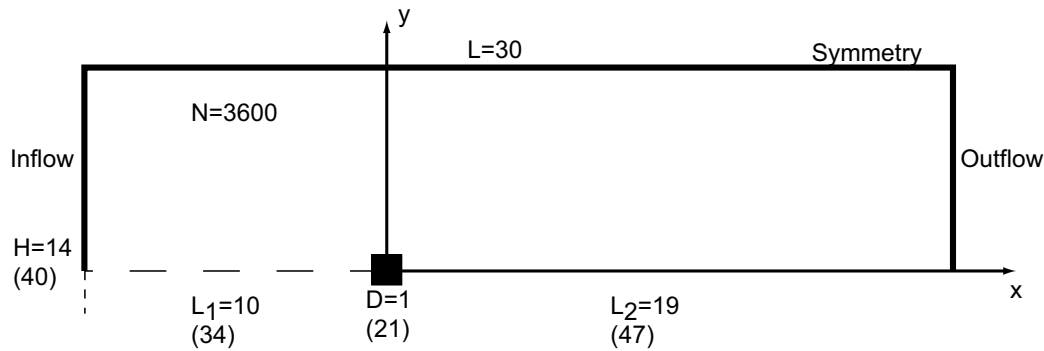


Figure 2.2: Investigated geometry with node distribution.

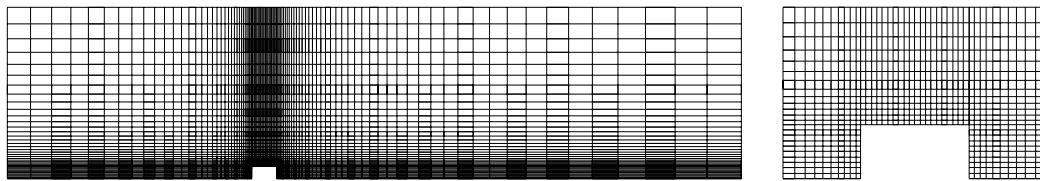


Figure 2.3: Mesh: half domain and particular around the body.

noise.

2.2 Description

The periodic vortex shedding past a square cylinder, which is a simple bluff body with fixed separation points at the sharp edges, is investigated.

The vortex shedding can be characterized by the Reynolds $Re = \frac{U_o D}{\nu}$ and the Strouhal number $St = \frac{f D}{U_o}$. In the literature the stability limit for this bluff body is given by a Reynolds number of about 70. Six laminar ($Re = 70, 100, 150, 200, 250, 300$), and one turbulent ($Re = 22000$) case are computed.

2.3 Computational setup

The dimension of the computational domain and the distribution of grid nodes are given in figure 2.2. The same cartesian mesh (3'600 grid points) as in [Bos95] is used (fig. 2.3). The first grid row near the wall is placed at $d/D=.042$. A uniform velocity $U_o = 1$ and turbulence distribution (2%) are set at the inlet. The viscosity is adjusted to match the Reynolds number. The turbulent dissipation rate ϵ is calculated from the turbulent kinetic energy k as: $\epsilon = k^{3/2}/L_\epsilon$; where $L_\epsilon = 0.081D$ is the eddy length scale, which represents the flow largest eddies dimension. At the outlet and at the lateral boundaries a constant pressure and symmetry conditions are respectively imposed. A computation at $Re = 100$ with a shorter domain has proved that the constant pressure condition does not significantly affect the pressure and velocity distribution of the time averaged solution. The shedding period is discretized with resp. 200

time steps in the laminar cases and 400 in the turbulent case. The time scheme is second order accurate. The convergence criterion for the maximal residuum of the internal loop that recovers the nonlinearity of the equations (II.2.1) is set to $1e^{-3}$ because of the limited computational resources. No appreciable differences are however found when a target of $1.e^{-4}$ is imposed. The pure linear profile advection skew scheme (II.2.1) gives slight better results than the modified scheme. In the turbulent simulation the standard or the Kato-Launder k - ϵ models with wall functions are employed. The Kato-Launder k - ϵ model [KL93] avoids the spurious build up of turbulence energy as a stagnation point is approached. Major improvements should result in the predicted drag and lift coefficients and also in the mean and turbulent flow pattern in the near wake.

2.4 Strouhal versus Reynolds number

Figure 2.10a shows the nondimensional frequencies of the vortex shedding on a wide range of Reynolds numbers (experiments [Oka82], [LR94], [DHP88]). Measurements are compared with the computational results. Six laminar cases and the turbulent case at $Re = 22000$ are represented. The frequencies in the laminar region are underestimated, however the overall behaviour is fairly well captured. In the turbulent case the Strouhal number seems to be quite insensitive to the computational parameters and the predicted values are pretty close to the experimental ones. This indicates that the shedding frequency is not an ideal indicator for the accuracy of the computation.

2.5 Laminar cases: $Re = 70 \dots 300$

The Reynolds number influence on the velocity and pressure distribution are given in fig. 2.4(a-e). As the Reynolds number increases the length of the recirculating region becomes shorter, while the backflow velocity on the axis increases until about a value of 150 and then decreases anticipating the tendency of the shedding frequency (fig. 2.4f).

2.6 Turbulent case: $Re = 22000$

The turbulent periodic flow past a cylinder is a difficult task for turbulence models. For this case measurements were reported by Lyn in [LR94] and [LERP95]. The experimental data are available on the ERCOFTAC database¹. This case was also selected for a workshop held in 1995 designed to assess the state-of-the-art in LES of complex flow [RFBP97].

The experiment reports that the separation and the wake are periodic, although with some modulation. It shows that the inflow to the computational domain is laminar, and that the transition takes place in the separated shear

¹<http://ercoftac.mech.surrey.ac.uk>

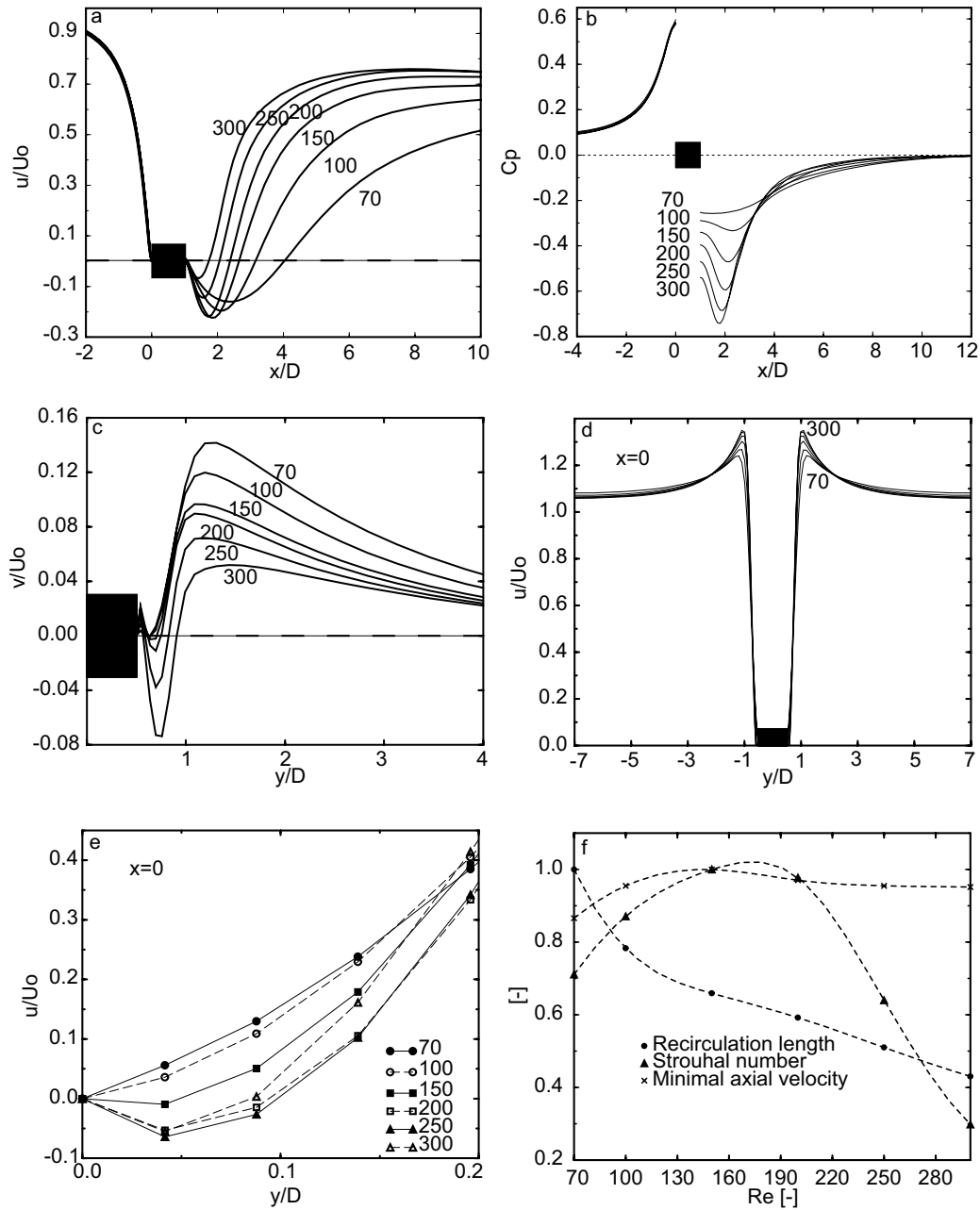


Figure 2.4: Laminar cases $Re = 70 - 300$. a) c) d) e) Velocity profiles (u : streamwise, v : crossflow) and b) pressure distribution (C_p) along the symmetry line. f) Nondimensional frequency versus recirculation length and minimal axial velocity.

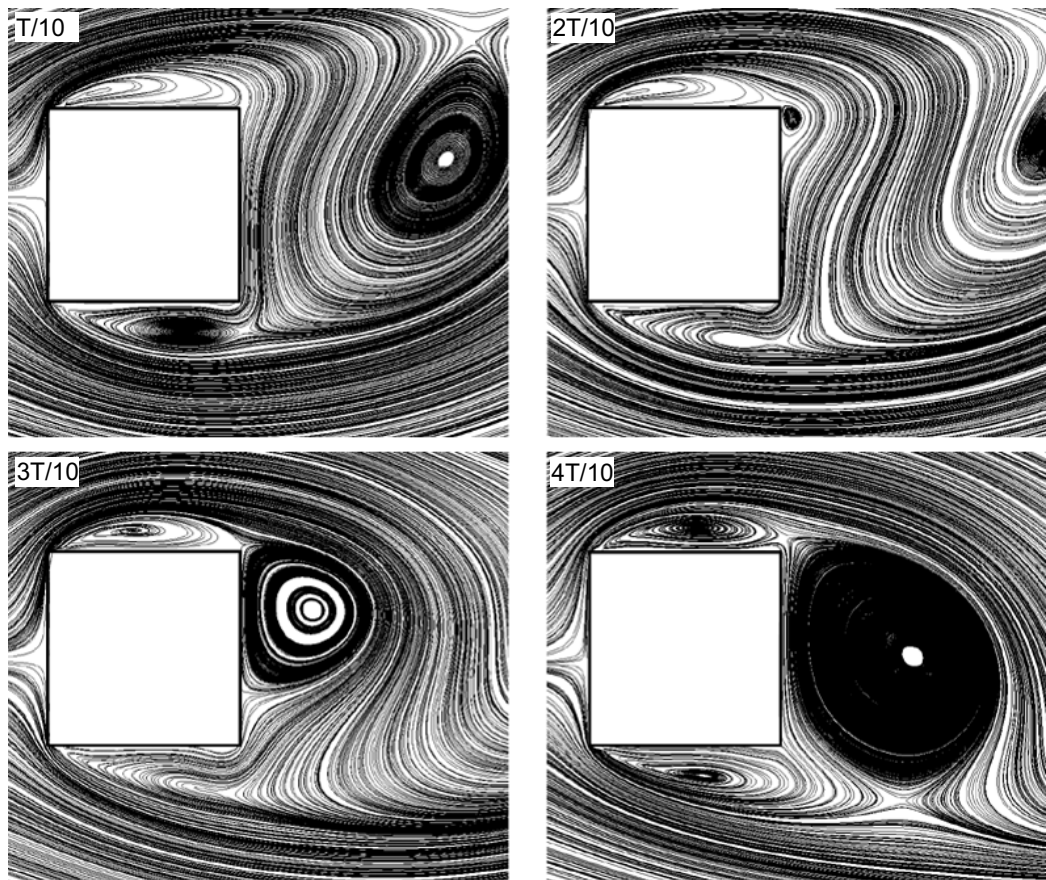


Figure 2.5: Instantaneous streamlines for $t=T/10, 2T/10, 3T/10, 4T/10$, where T is the shedding period. $Re = 22000$.

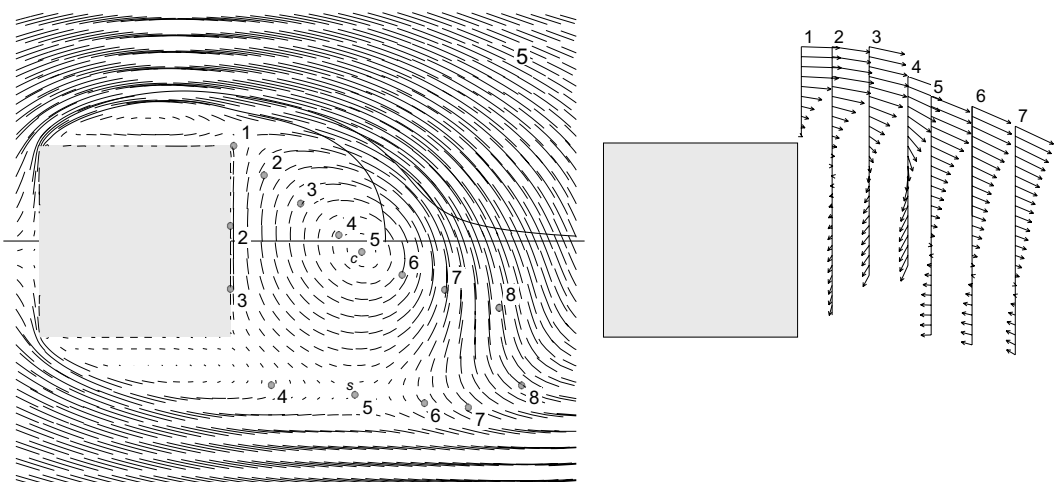


Figure 2.6: Position of the center and the inferior saddle (s) of the instantaneous vortex at eight time steps covering a half period and corresponding velocity profiles on the vertical axis passing by the center (c).

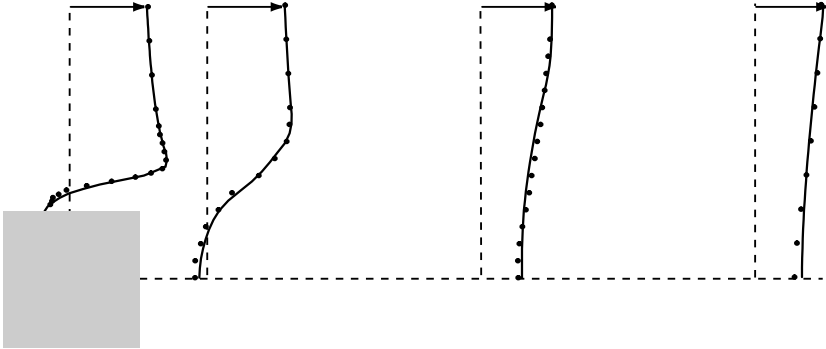


Figure 2.7: Axial velocity of the mean flow field at $Re = 22000$, comparison with measurements of Lyn (points).

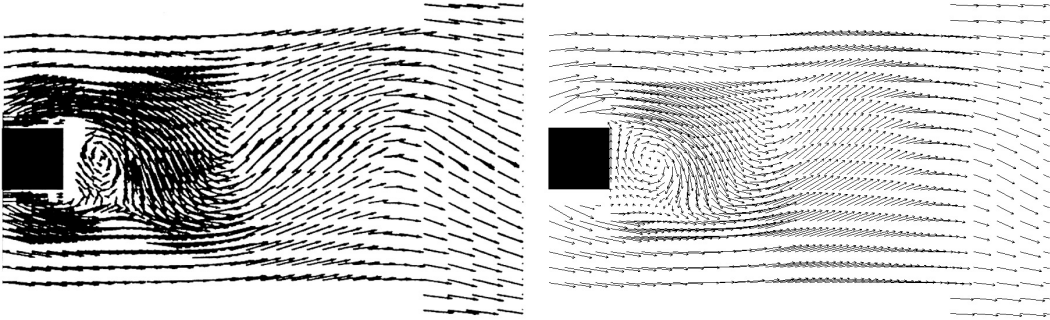


Figure 2.8: Instantaneous vector field $Re = 22000$: a) Lyn's measurements, b) $k-\epsilon$ model.

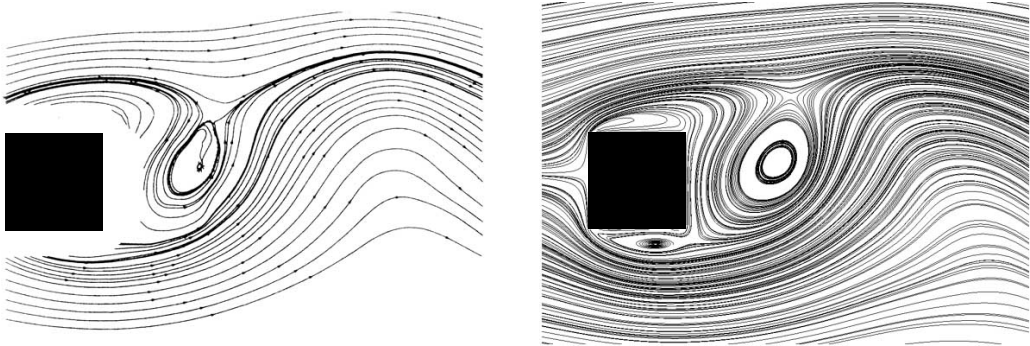


Figure 2.9: Instantaneous streamlines $Re = 22000$: a) Lyn's measurements, b) $k-\epsilon$ model.

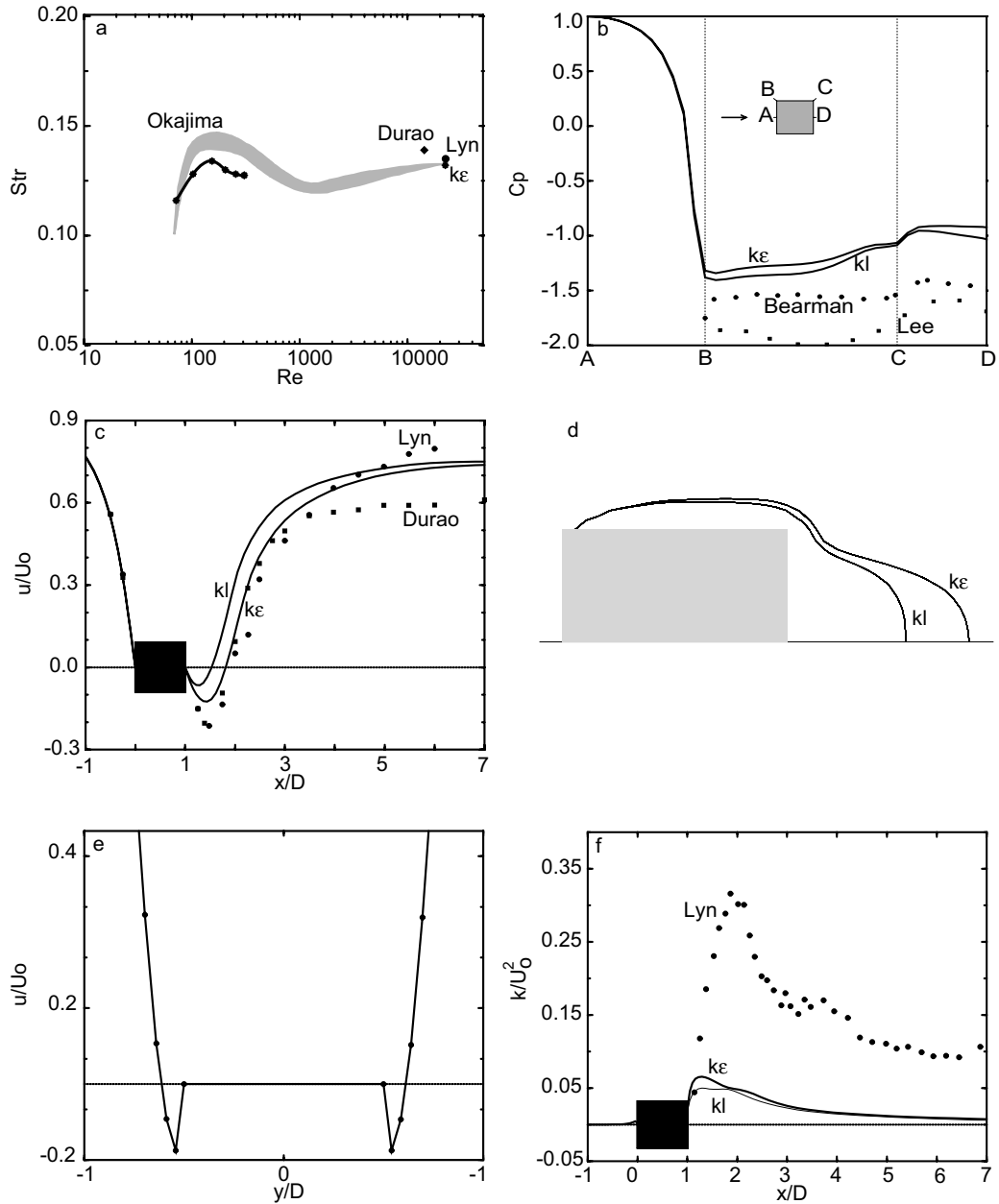


Figure 2.10: Turbulent case $Re = 22000$. a) Nondimensional shedding frequency (Str) versus Reynolds number (Re). b) Mean pressure distribution (cp) at the wall. c) Mean streamwise velocity profiles. d) Recirculation length obtained with the standard $k - \epsilon$ model and the Kato-Launder model (kl). e) Near-wall axial velocity profile, the resolution is insufficient. f) Mean kinetic energy distribution on the symmetry axis.

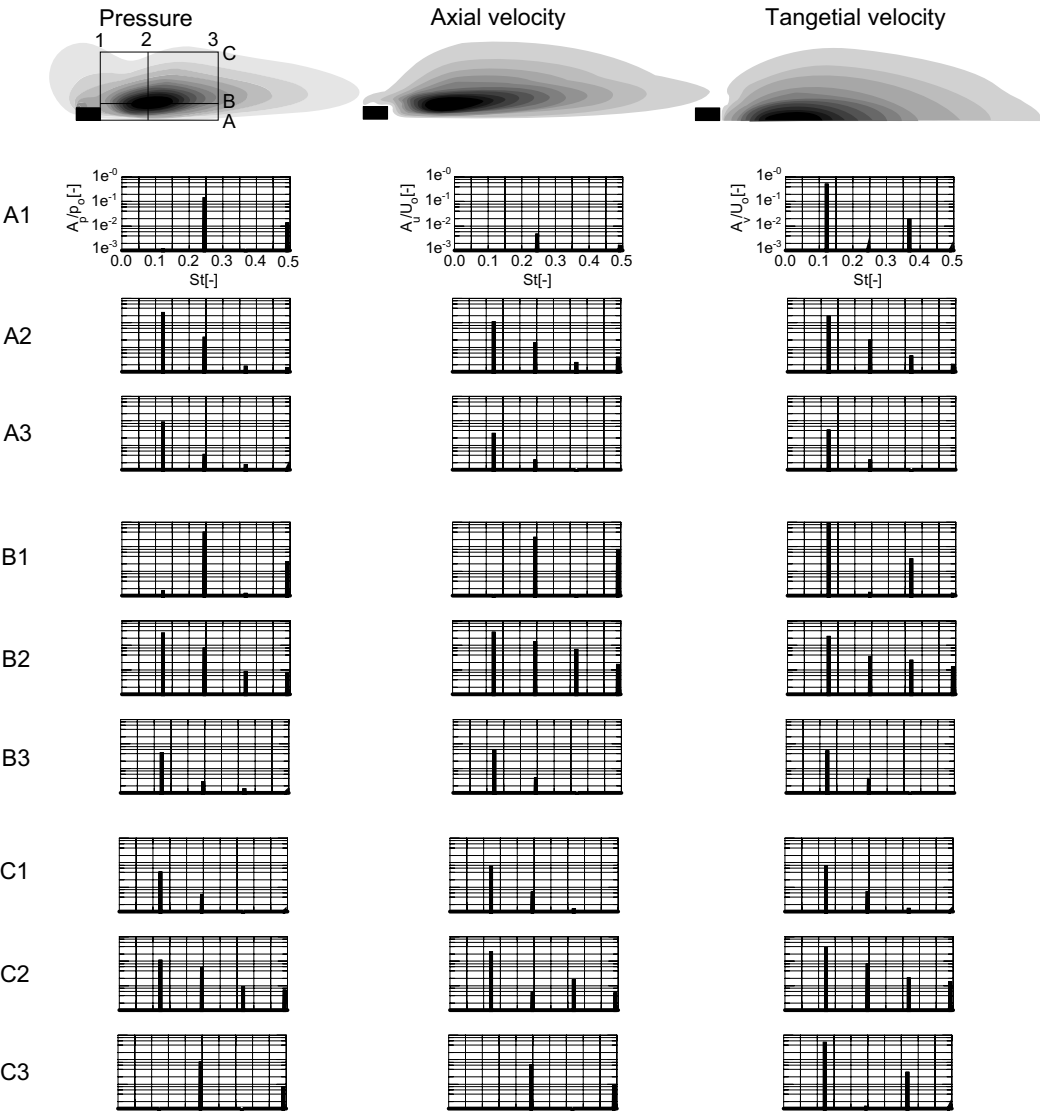


Figure 2.11: Discrete Fourier transform of the velocity and pressure signals at different places in the domain. The distribution of the amplitude corresponding to the shedding frequency is illustrated on the top.

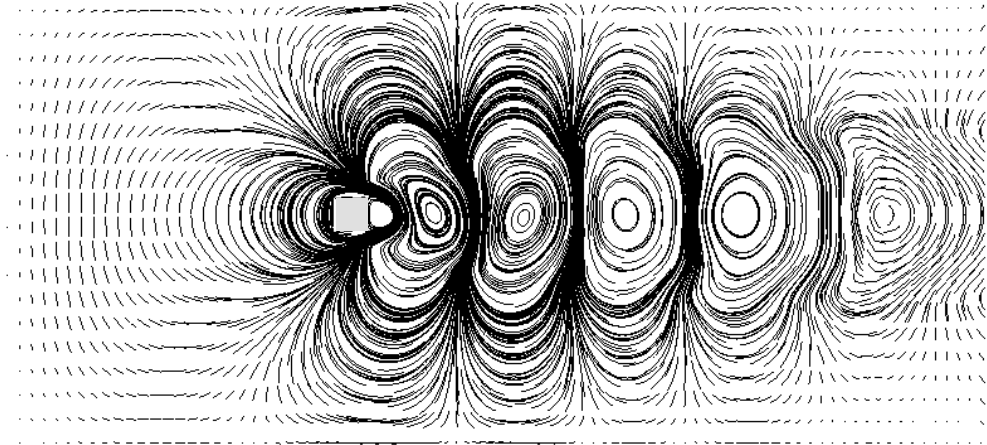


Figure 2.12: Instantaneous streamlines of the fluctuating field at a given phase.

layers on the sides of the cylinder just downstream of the front corners. This is a reason why the square cylinder flow is difficult to simulate. The resolution in this region must be high enough to resolve accurately the developments and transition of the separated shear layer. Given the short length of travel of the reversed flow from the cylinder sides, the boundary layers along the sidewalls are not fully developed turbulent. The validity of the wall function is questionable in this zone. An impression of the nature of the flow can be taken from the sequence of instantaneous streamlines (IS) patterns (fig. 2.5). IS do not contain transient information but describe well the entrainment process. IS can be obtained photographically from short-time exposures of small particles which have been introduced into the flow. Singular points in the instantaneous field are visible only near the body because of the low convection velocity. Outside this zone the observer must travel with the convection velocity in order to see these points. The evolution of the vortex center and saddle positions are illustrated in fig. 2.6 for several phases. The instantaneous fluctuating field shows clearly all the structures (fig. 2.12). The genesis of a new structure is illustrated in fig. 2.13 and interpreted in fig. 2.14. The birth of the structure corresponds to the onset of a saddle point (third sketch in fig. 2.14) and the shedding process by the release of this point (last sketch).

2.7 Comparison with the experimental data

The mean axial flow field is compared with measurements in fig. 2.7. A comparison of the measured velocity vectors and instantaneous streamlines for a given phase with the predicted flow is shown in fig. 2.8 and fig. 2.9. The $k-\epsilon$ model with wall functions is applied. A good general agreement is found. The shedding motion is qualitatively well resolved, but there are significant quantitative differences among the results corresponding to the two tested turbulence models. All computed flows are periodic and symmetric. The Strouhal number falls in a narrow range close to the experimental value. The results for the

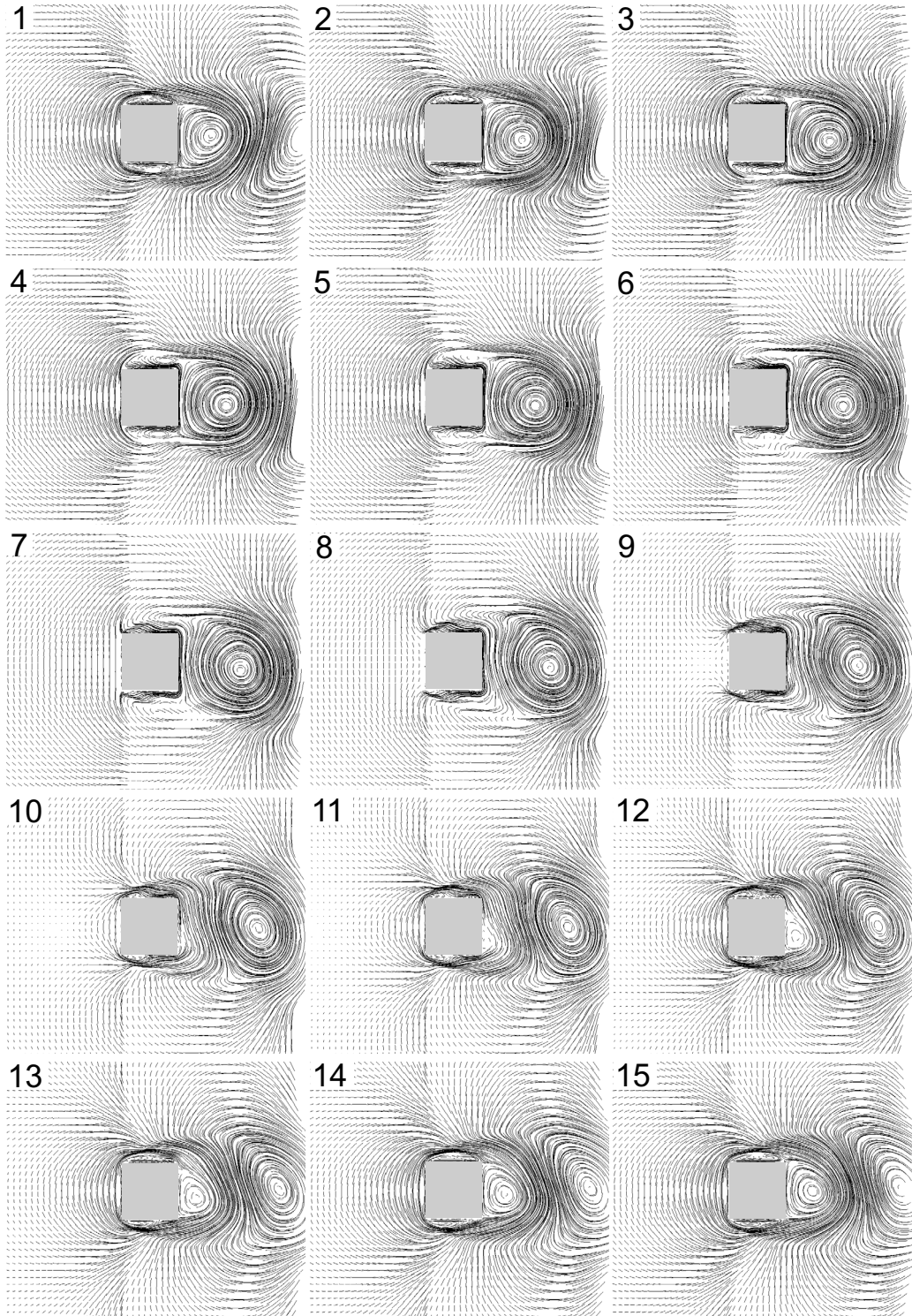


Figure 2.13: Instantaneous streamlines of the fluctuating field, half period, constant step between the images.

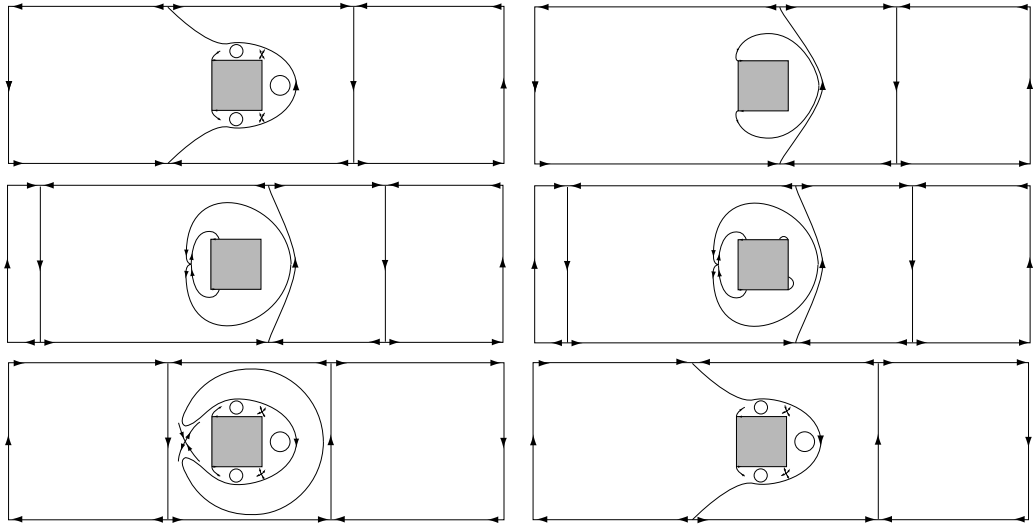


Figure 2.14: Schematic interpretation of fig. 2.13.

length of the time-mean recirculation zone behind the cylinder show important variations. The recirculation zone predicted by the two turbulence models are shown in fig. 2.10d. The following table shows the comparison with the experimental results of the length (L) and height (H) of the mean backflow zone (see fig. 2.1), normalized with the size of the square (D).

	L/D	H/D	St
Measurement Lyn	0.88	0.74	0.132 ± 0.004
$k - \epsilon$	0.81	0.64	0.133
Kato-Launder	0.53	0.63	0.133

It is usually reported in the literature that purely two-dimensional simulations give recirculation zones which are much too long and drag coefficients which are much too small. Results for the mean averaged velocity and pressure distributions are illustrated in fig. 2.10. The pressure on the upstream face is fairly well predicted but the values on the other faces show significant disagreement both with each other and with the experiments, as might be expected from the different results regarding the recirculation zone. One should also note the important difference in the two sets of experimental results ([BT71] and [Lee75] that were however acquired at different Reynolds numbers). The turbulent kinetic energy is shown in fig. 2.10f. Bosch [Bos95] argued that the difference between computations and experiments could be explained by the presence of forces acting parallel to the cylinder axis (irregularity in the flow are observed), which are not taken into account in a 2D computation. In the experiment these irregularities are taken into account by the phase average and increase the turbulent components. Fig. 2.10e shows that the grid distribution near the body is insufficient to resolve the region of reversed flow.

3

Steady swirling flow in a pipe

3.1 Introduction

The flow in the draft tube of a hydro power plant is often swirling when the turbine is operating outside its best efficiency point. Even for optimal conditions the runner is usually designed to supply a certain amount of swirl in the cone. This allows the use of wider cone opening angles without the manifestation of detachments and therefore attaining a higher static pressure recovery in this component. Flows with swirl are known to be a great challenge for turbulence models. The complexity of the mean flow field invalidates the assumption on which simple turbulence models are based, in particular that there is only a single dominant rate of strain. It is believed that the presence of mean rotation may modify the dynamics of the fluctuating velocity field considerably.

The swirling flow in a long pipe is investigated. Due to the simplicity of the geometry, the flow should be largely influenced by the turbulent stresses. The swirl is recognized to decay slowly in pipes. The objective of this study is to evaluate the capability of two turbulence models to simulate this type of flow. However it should be noted that the swirl decay at large distances from the inlet is relatively unimportant for this work. The mean-line length of the draft tube is about only five inlet diameters. The measured profiles in the pipe have similar characteristics to those measured at the inlet of the investigated draft tube.

3.2 Description of the case

Steenbergen has performed measurements in a hydraulically smooth pipe with diameter $D = 70[mm]$, the fluid being water (see ERCOFTAC database¹ and [Ste95]). The Reynolds number, based on the diameter and on the bulk velocity ($4.3[m/s]$), is $300'000$. The data has been obtained with a 2-component laser-Doppler system and contains the distribution of mean velocities and Reynolds stresses. Eight axes of measurements are available: the first is used to define the inlet boundary conditions for the computation. The location of the seven

¹<http://ercoftac.mech.surrey.ac.uk>

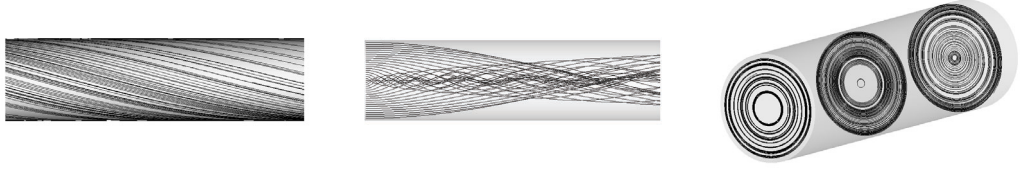


Figure 3.1: Streamlines: a) skin friction lines, b) started from the vertical inlet axis line, c) on three sections using the tangential velocity field.

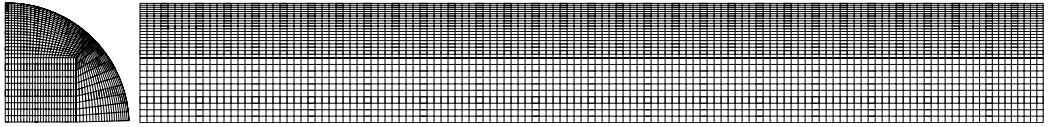


Figure 3.2: Fine mesh, 770k mesh points: a) quarter of the inlet, b) half longitudinal section.

axes is as follows: 3.4, 7.2, 17, 23.8, 30.6, 44.2 and 71.3 (diameters downstream the inlet). An impression of the nature of the flow can be taken from fig.3.1, where streamlines are shown in the region of the pipe inlet (computation with the k - ϵ model).

3.3 Computational setup

The classical k - ϵ and the LRR-RSM models, coupled with wall functions, are employed. The fluid properties are set to values corresponding to water at atmospheric conditions. The inlet velocity profiles and the turbulent kinetic energy are interpolated with cubic splines from the measurement points (fig. 3.5). The values at the wall are set as nine tenths of the nearby interior measurement point values. The turbulent dissipation rate ϵ is calculated from the turbulent kinetic energy k as: $\epsilon = k^{3/2}/L_\epsilon$; where L_ϵ is the eddy length scale, which represents the flow largest eddies dimension. It is usual to assume an eddy length scale of one order of magnitude smaller than the diameter. In this case better results are achieved with $L_\epsilon = 0.014D$. For the RSM model the Reynolds' stresses are computed from the turbulent kinetic energy. The code does not allow imposing the measured profiles. The outlet of the computational model is set at $74D$. The computation is considered converged to the steady solution when the value of the maximal normalized equation residual is less than 10^{-4} . Two meshes of respectively 510k, covering the whole domain (cylinder of length $74D$), and 770k (fig. 3.2) nodes, covering only a length of $3.7D$, are compared. In spite of the strong mesh density difference (the finer mesh domain is much smaller) the velocity profiles are similar (fig. 3.3). The solution on the coarser mesh is considered sufficiently close to the exact solution. The nondimensional distance from the wall of the first grid point is within the range $25 < y^+ < 35$.

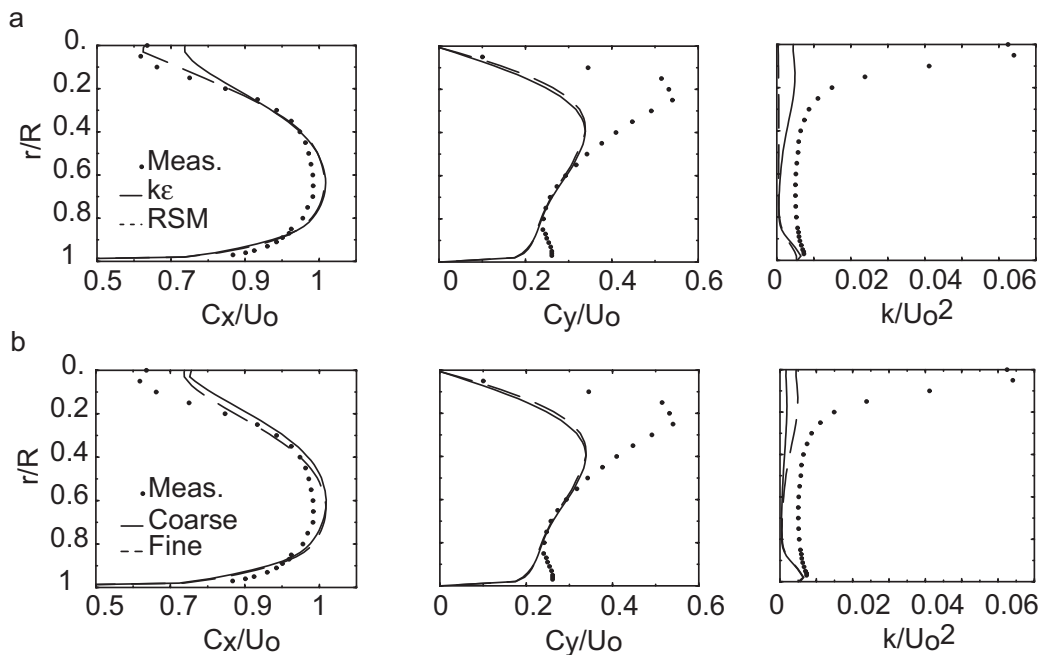


Figure 3.3: First measurement axis: a) turbulence model influence, fine mesh, b) mesh influence, $k-\epsilon$ model.

3.4 Comparison with the experimental data

The eddy-viscosity based models are expected to be inadequate for swirling flows. The evolution of the local specific energies (see Nomenclature, IX) in fig. 3.4 and the profiles at the first measurement axis (fig. 3.3) differ only slightly for the two turbulence models. The RSM model better resolves the axial velocity depression in the central zone in the first half of the domain. However, this velocity component differs considerably from the measurements in the second half. Indeed the flow is accelerated in the central zone, leading to a central peak, while in the measurements the profile develops toward a parabolic profile. The swirling component does not differ considerably from that obtained by the $k-\epsilon$ model. It is believed that only second-order closure schemes are capable of capturing the physics of swirling flows, in this computation however the applied RSM models does not effectively improve the solution. Unfortunately it was not possible to impose the measured Reynolds' stresses. The velocity and turbulent kinetic energy profiles resulting from the computation with the 510k nodes mesh using the $k-\epsilon$ model are compared with the measurements in fig. 3.5. As expected, important differences are observed. In particular the strong gradient in the central zone for the swirling component, and therefore also the axial velocity depression, are smeared out too fast in the computation. The flow develops too rapidly toward a solid-body rotation velocity distribution. Similar results are also observed in [Ste95]. The gradient is however represented with a sufficient number of mesh points. As noted above, the used eddy length scale is small compared with the values used for non-swirling flows. With larger values the damping tendency is accentuated. A

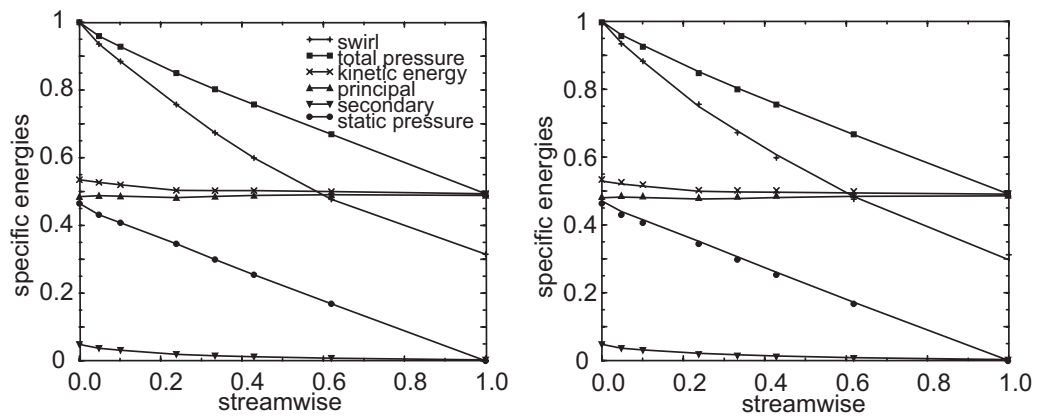


Figure 3.4: Specific energies evolution from the inlet to the outlet, coarse mesh. The evaluation are done at the measurement axes positions: a) k - ϵ model, b) curves: RSM model, symbols: k - ϵ model.

reduction of the length scale reduces the radial mixing of momentum resulting in a stronger dependence of the initial velocity distribution. The computational results show that the imposed turbulent kinetic energy profile with the important peak in the central zone is damped in a very short distance. Indeed if a constant k is imposed, only negligible differences are observed. This could be explained by the fact that the Prandtl-Kolmogorov hypothesis relates directly the turbulent kinetic energy with the turbulent viscosity and thus the model adopts large eddy viscosity in the central zone, leading to the rapid turbulent momentum transfer. However the same behaviour occurs using the RSM model.

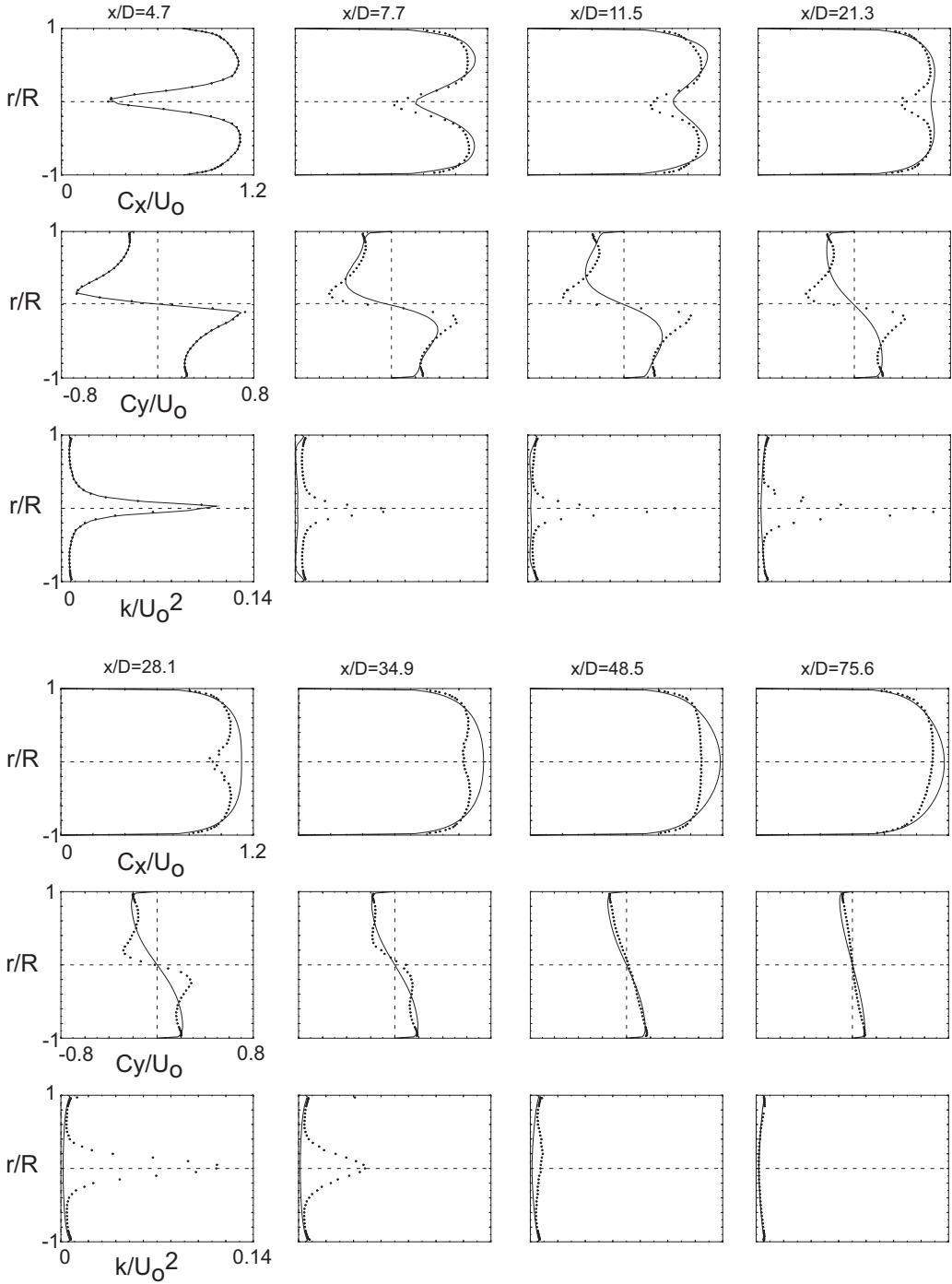


Figure 3.5: Comparison with the experimental data, coarse mesh, $k-\epsilon$ model.

4

Steady swirling flow in a diffuser

4.1 Introduction

The swirling flow in a straight diffuser is investigated. This case is considered as an extension of the previously described swirling flow in a pipe (III.3). However the inlet flow condition differs considerably from the previous case.

The art of draft tube design is to decelerate the flow avoiding flow separation. The opening angle of the cone results from this compromise. The divergent geometry introduces an adverse pressure gradient that raises the risk of flow separation. The swirl has the opposite effect and prevents boundary layer separation. The adverse pressure gradient due to the diffuser as seen from a particle near the wall in a swirling flow is smaller compared with a non-swirling one because of its trajectory angle. The centrifugal effect resulting from the tangential velocity brings energy at the boundary layer and raises the axial velocity component on the axis eventually leading to the formation of backflow zones as observed in the predicted flow field of this configuration in a small region near the outlet (see streamlines in fig. 4.1b). The decay of swirl in the diffuser leads to the decay in the radial pressure gradient. This produces a larger positive axial pressure gradient at the axis than it would be the case for a non-swirling flow.

4.2 Description of the case

The steady turbulent swirling flow in a diffuser has been experimentally investigated by Clausen et al. [CKW93]. The experimental data is available on the ERCOFTAC database¹. A rotating swirl generator of diameter $D = 0.26 [m]$ supplies a conical diffuser with an included angle of 20° and area ratio 2.84, placed $0.38D$ downstream the swirl generator. The cone is $1.96D$ long (fig. 4.1). A rotating cylinder including a honeycomb screen at its inlet creates the swirling flow. The fluid is air with a kinematic viscosity of $1.5e^{-5} [m^2/s]$,

¹<http://ercoftac.mech.surrey.ac.uk>

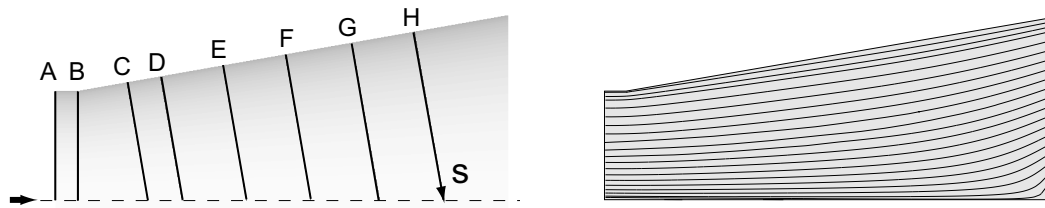


Figure 4.1: Investigated geometry: a) measurement axes, b) tangential streamlines on the longitudinal plane, k - ϵ model.

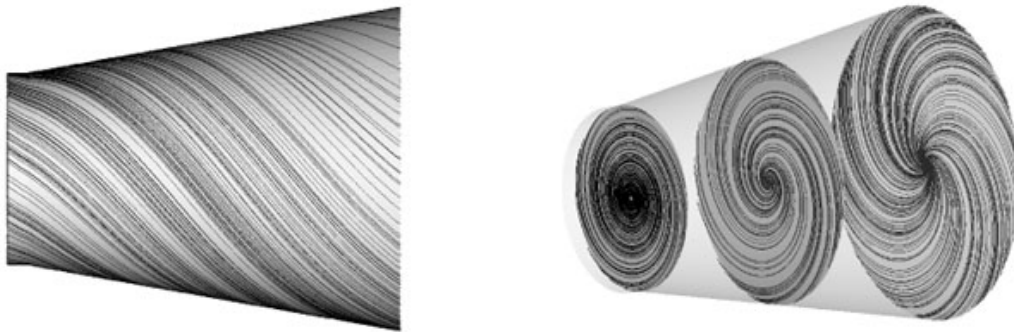


Figure 4.2: Streamlines, k - ϵ model: a) skin friction lines, b) tangential streamlines on three normal sections.

the average axial velocity at the inlet is $U_o = 11.6 [m/s]$ and the diffuser discharges to the atmosphere. The corresponding diameter based Reynolds number is 202'000. The inlet velocity profile is measured at $0.01D$ upstream the cone. Measurements are available at seven stations along the diffuser on axes perpendicular to the wall (fig. 4.1). An impression of the nature of the flow can be taken from fig. 4.1 and 4.2, where streamlines tangential to several surfaces are shown (computation with the k - ϵ model). The main aim of the experiment was to measure the mean velocities and the Reynolds stresses in a swirling diffuser flow that is close to separation and recirculation. The imposed swirl is of sufficient magnitude to prevent boundary layer separation but just insufficient to cause backflow in the core flow. This test case was computed assuming circumferential symmetry by Armfield and Fletcher [AF89] and by Page et al. [PGM96]. Armfield and Fletcher compare two k - ϵ models and two algebraic Reynolds stress models. All the models lead to qualitatively satisfactory agreement, with the algebraic Reynolds stress models giving better results on the fine detail. The k - ϵ models underpredict the magnitude of the near wall axial and swirling velocity peak. The algebraic Reynolds stress models describe the peaks accurately, but place the axial velocity peak too close to the wall and therefore underestimate the axial velocity. The authors argue that the reason why the k - ϵ model gives less satisfactory results is that the eddy viscosity is much larger than the experimental value. Two commercial codes using the classical k - ϵ model are compared in [PGM96]. Computed values are judged in good agreement with measured flow parameters along the diffuser. The performances of the two codes are similar.

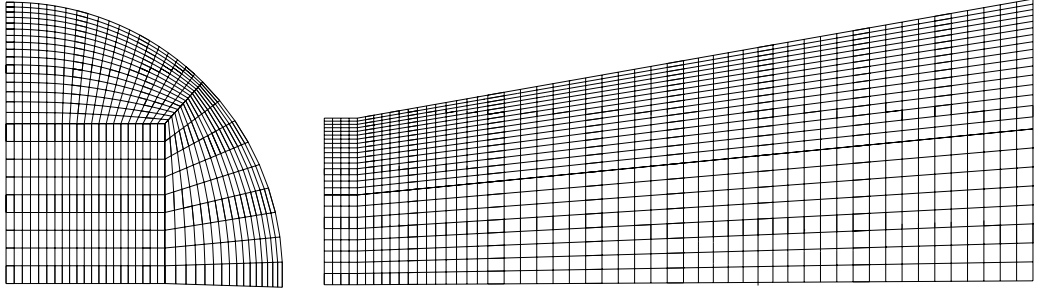


Figure 4.3: Coarse mesh, 140k nodes: a) quarter of the inlet, b) half longitudinal section.

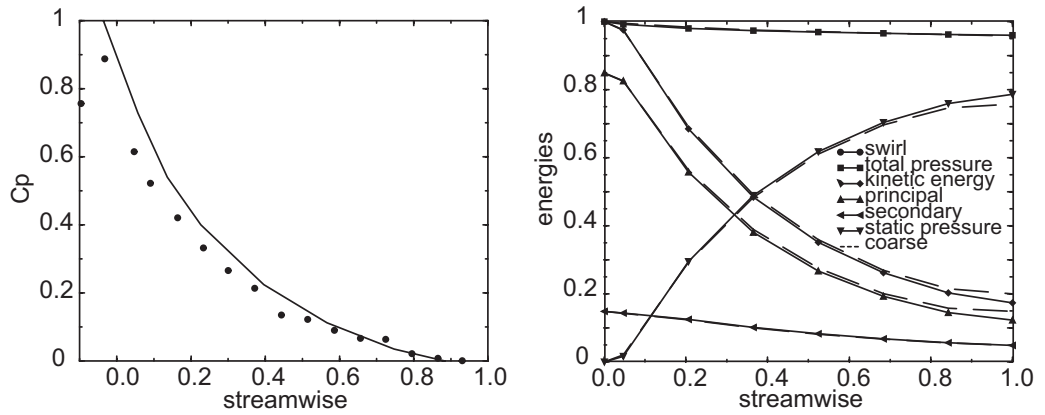


Figure 4.4: From the inlet to the outlet: a) normalized pressure at the wall, fine mesh, $k-\epsilon$ model, b) specific energies evolution. Coarse mesh versus fine mesh, $k-\epsilon$ model.

4.3 Computational setup

The classical $k-\epsilon$ and the LRR-RSM models, coupled with wall functions, are employed. The fluid properties are set to values corresponding to the experiment. The inlet velocity profiles are interpolated with cubic splines from the measurement points (fig. 4.5A). The values at the wall are set as the half of the interior nearby point values. The turbulent kinetic energy is assumed to be 5% of the total energy. The turbulent dissipation rate ϵ is calculated from the turbulent kinetic energy k as: $\epsilon = k^{3/2}/L_\epsilon$; where $L_\epsilon = 0.04D$ is the eddy length scale, which represents the flow largest eddies dimension. The computation is considered converged to the steady solution when the value of the maximal normalized equation residual is less than 10^{-4} . Two meshes of respectively 140k (fig. 4.3) and 770k nodes are compared. The evolution of the local specific energies (see Nomenclature, IX) is illustrated in fig. 4.4. The difference in the static pressure recovery for the two meshes is 3.6%. The nondimensional distance from the wall of the first grid point is within the range $100 < y^+ < 300$.

4.4 Comparison with the experimental data

The velocity and the kinetic energy profiles are compared with the measurements in fig. 4.5 and the normalized pressure at the wall in fig. 4.4a. The results are fairly satisfactory. The near wall axial velocity peak is however underpredicted while the centerline axial velocity is accentuated. The maximal difference reaches the 50% on the centerline. The swirling component compares better with the experiment, while the kinetic energy values differ considerably from the measurements. The strong peak and gradient near the wall are clearly underpredicted. The second order closure scheme does not improve the solution.

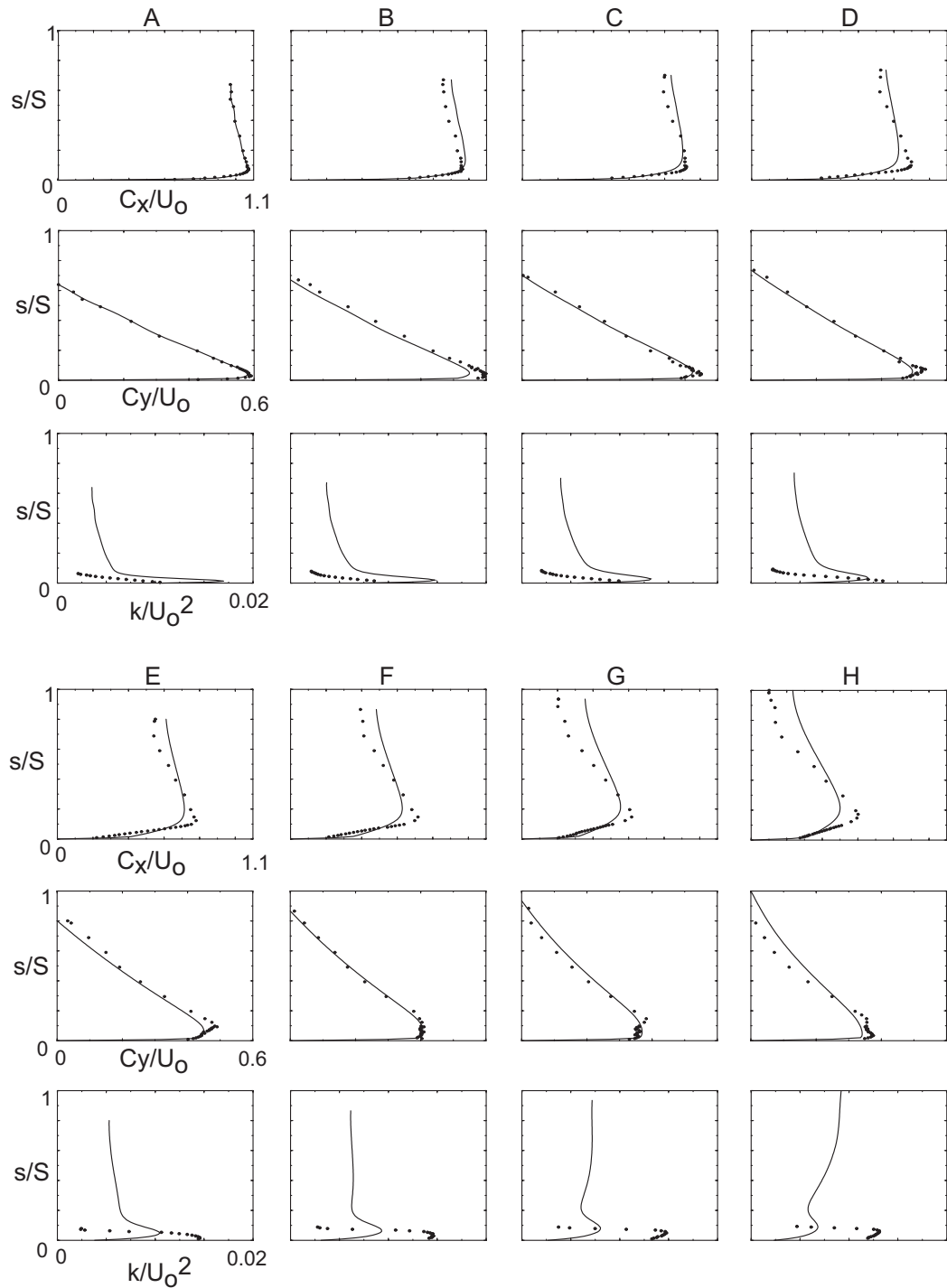


Figure 4.5: Comparison with the experimental data, fine mesh, $k-\epsilon$ model.

5

Summary

The capability of the code to describe a laminar unsteady flow is tested simulating the flow in a slot with an oscillating pressure gradient. The code describes accurately this type of flow on a wide range of frequency. The simulation of the flow past a bluff body shows that low frequency self-sustained instabilities can be described with enough precision by the model, in spite of the quasi steady approach of the turbulence models. The influence of the turbulence modeling is however important on the fine details. The swirling flow in a simple geometry is computed with the k - ϵ and a RSM model. As expected the eddy viscosity based model is not able to capture accurately this type of flow especially at large distances from the inlet. More surprisingly the second order closure scheme does not improve the prediction. Similar results are obtained also for a swirling flow in a straight diffuser. These tests confirm the doubt upon the adequacy of the model to describe accurately the flow in the draft tube.

IV

Case study

1

Investigated geometry

1.1 Reduced scale model machine

Investigations are carried out on a vertical axis reduced scale model (1:10) of an existing water turbine at the test rig facilities of the EPFL - Laboratory for Hydraulic Machines. A high specific speed ($\nu = 0.56$, $n_q = 92$) Francis runner supplies the symmetrical draft tube with a single pier, designed to reproduce the typical drop in the pressure recovery occurring near the best efficiency region. The geometry and the cross area evolution are shown in fig. 1.3. The runner diameter measures 0.4 [m].

Following IEC recommendations [IEC99] the draft tube is connected to an outlet tank as shown in fig. 1.1 and 1.2. 17 runner blades, 20 guide vanes and 10 stay vanes characterize the machine.

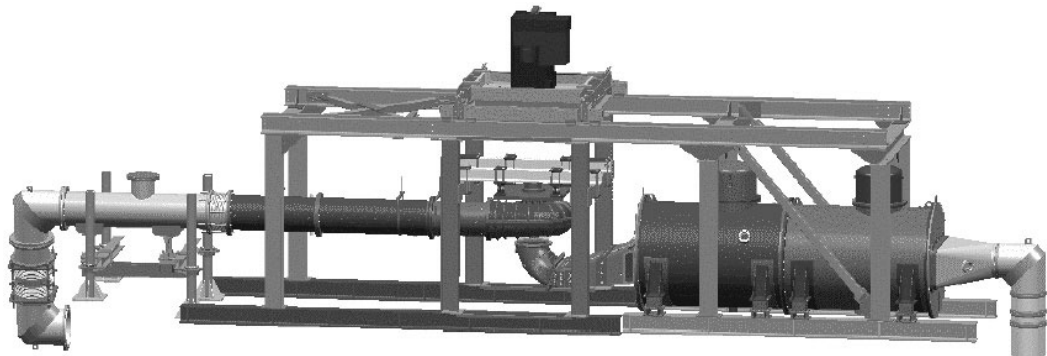


Figure 1.1: Test rig, upper part.

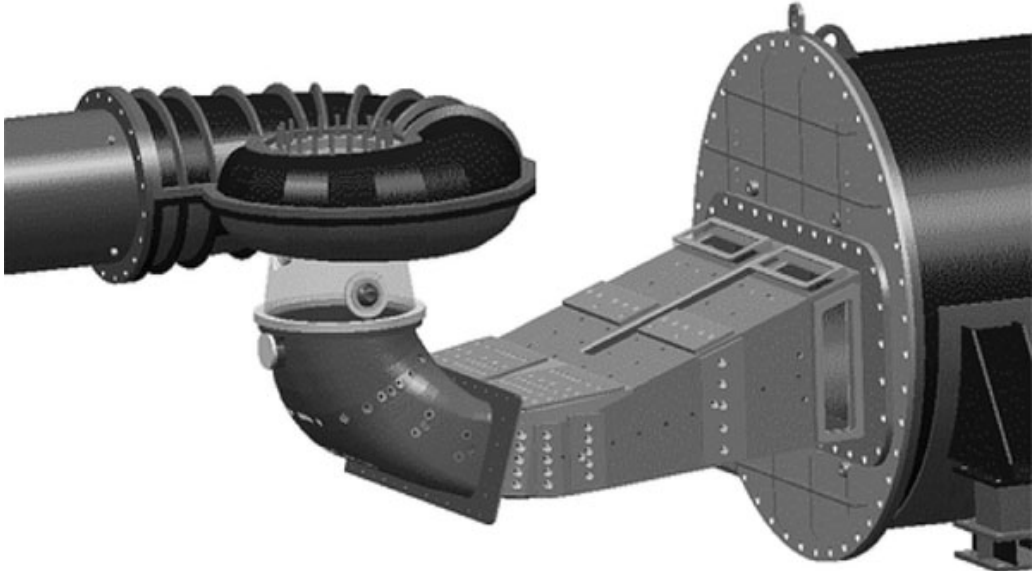


Figure 1.2: Machine reduced scale model.

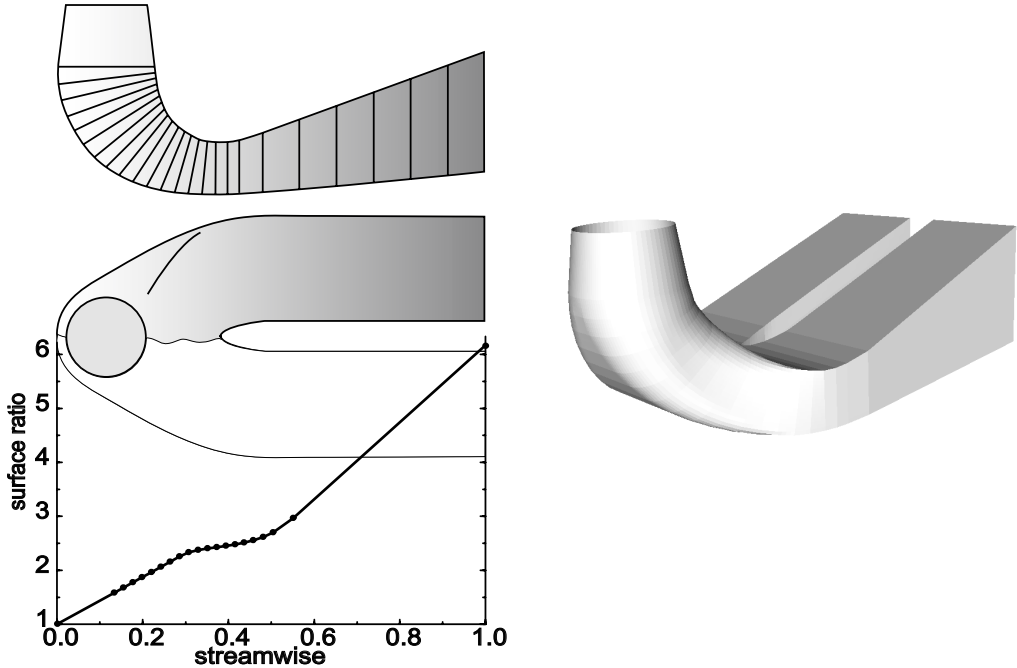


Figure 1.3: Draft tube, cross-area evolution graph.

2

Measurements

Jorge Arpe and Gabriel Ciocan have carried out the experimental investigations presented in this work.

2.1 The test rig

The test rig is equipped with accurate measuring instrumentation and is suitable for development and acceptance tests according to the IEC standard [IEC99]. The test rig has a maximum head of 100 [m] and a maximum discharge of 1.5 [m³/s]. The maximum rotational speed is 2500 [rpm] and the pump power is 2 x 300 [kW]. The flow rate is measured by an electromagnetic flow meter adapted for discharges in the range 0.05-1.5 [m³/s]. The specific hydraulic energy is measured with a differential pressure transducer that allows three sensibility ranges: 0-2, 0-5, 0-10 [bar]. The transducer is calibrated by the use of a digital balance.

2.2 Measuring techniques

The draft tube equipment consists in 300 taps for unsteady wall pressure transducers and 10 windows for the flow surveys with five sensors pressure probes and Laser Doppler Anemometer (LDA) (fig. 1.2). Additional details are given in [CMAK01] and [CKA00].

The wall pressure is acquired simultaneously at up to 96 positions at the frequency of up to 51.2 [kHz]. The 2 [bar] piezoresistive transducers have sensibility of 40 [mV/bar]. The measurement uncertainty is estimated to be less than 3%.

The steady pressure probe consists in five differential 1 [bar] transducers with a sensibility of 330 [mV/bar]. The probe is suited for velocities of more than 3 [m/s] and probe orientation angles of $\pm 25^\circ$ with respect to the flow direction. In these conditions the measurement uncertainty is estimated to be less than 5%.

The unsteady pressure probe has five absolute 1 [bar] transducers with a sensitivity of 500 [mV/bar]. The probe is suited for velocities of more than 3 [m/s] and probe orientation angles of $\pm 25^\circ$ with respect to the flow direction. The measurement uncertainty is estimated to be less than 3%.

The LDA device is a two component system. It uses back scattered light and the signals are transmitted by optical fiber. The source is an argon-ion laser of 5 [W]. A spectrum analyzer performs the signal processing. Spherical silver coated glass particles of 10 [μm] having water density introduced in the circuit, reduce the acquisition time. The three components of the velocity vector are obtained with a non-orthogonal optical arrangement. Two additional surveys are necessary for the determination of the Reynolds' stress tensor. An encoder fixed on the shaft of the runner delivering a reference impulse per each rotation through a photosensitive cell, is used to evaluate the phase average synchronised with the angular position of the runner. The encoder provides the time basis for the velocity acquisition. The acquisition of 15'000 instantaneous velocities are necessary to obtain a 2% uncertainty on the phase averaged flow; 60'000 for a 3% uncertainty on the Reynolds' stress tensor.

Wall friction measurements are performed with a hot-film probe. Temperature influence, sensor contamination and offset drift are quantified and included in the treatment procedure.

3

Machine characteristics

3.1 Machine performance

The machine and draft tube performances measured at the rotational speed of 1000 [rpm] are shown in fig. 3.1 over a wide range of heads and flow rates. The draft tube efficiency is estimated by the recovery factor defined as $\chi = (p_2 - p_1)/(\rho c_1^2)$, where the reference section 1 is set at $0.6D$ from the runner outlet and section 2 is placed near the outlet as shown in fig. 3.3. The static pressure p is estimated with two pressure ring manifolds connecting respectively four and eight locations at the sections 1 and 2 (fig. 3.3).

3.2 Investigated operating conditions

The experimental results presented in this chapter are obtained by Gabriel Ciocan. The investigation is carried out at the constant head $\psi^* = 1.06$. For the six flow rates corresponding to $\varphi^* = 0.919$, $\varphi^* = 0.973$, $\varphi^* = 0.994$, $\varphi^* = 1.027$, $\varphi^* = 1.054$ and $\varphi^* = 1.108$, detailed experimental data are available. The velocity profiles are obtained on the diameter along the draft tube's longitudinal axis by means of the LDA technique and are shown in the figures 3.4, 3.5, 3.6. This axis is positioned $0.2D$ below the runner outlet (fig. 3.3).

3.2.1 Time averaged velocity profiles

An impression of the nature of the flow can be taken from figures 3.5 and 3.6. The evolution of the axial velocity component at the inlet (fig. 3.4) is characterized by the decreasing importance of the low velocity zone at the center, caused by the higher swirl characterizing the lower flow rates. The circumferential velocity component inverts its rotational direction for the operating points at the higher flow rates (fig. 3.4 and 3.5). An intuitive explanation of the sign change is given by considering the velocity triangles at the runner blades as shown in fig. 3.2. At the design point the circumferential component C_{u_T} is usually minimized. By the fact that the relative velocity angle β_T is fixed by the blade geometry, a change in the flow rate will play on α leading to the inversion of the rotation direction when the flow rate is increased.

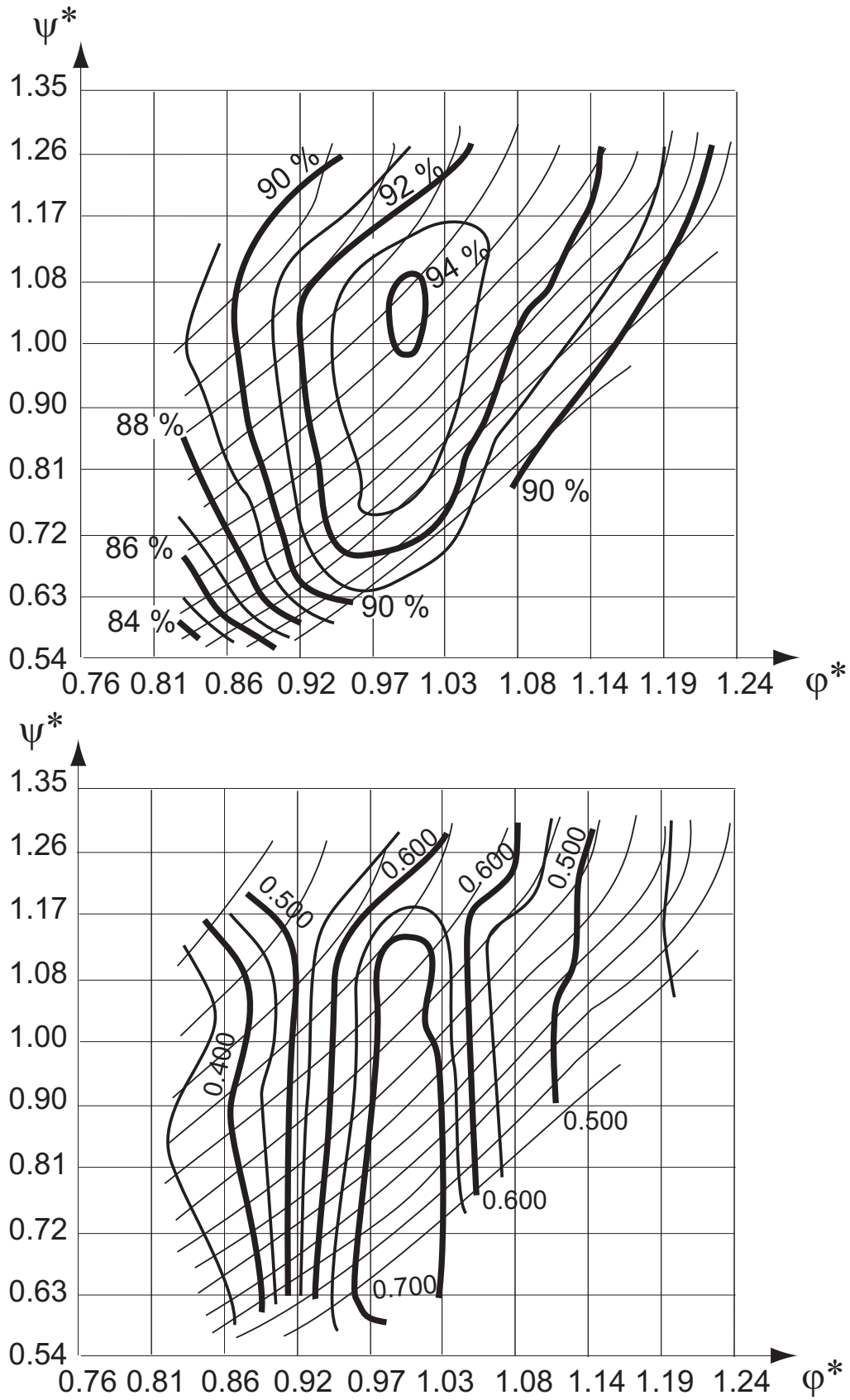


Figure 3.1: Hill-charts: a) machine efficiency, b) draft tube recovery factor.

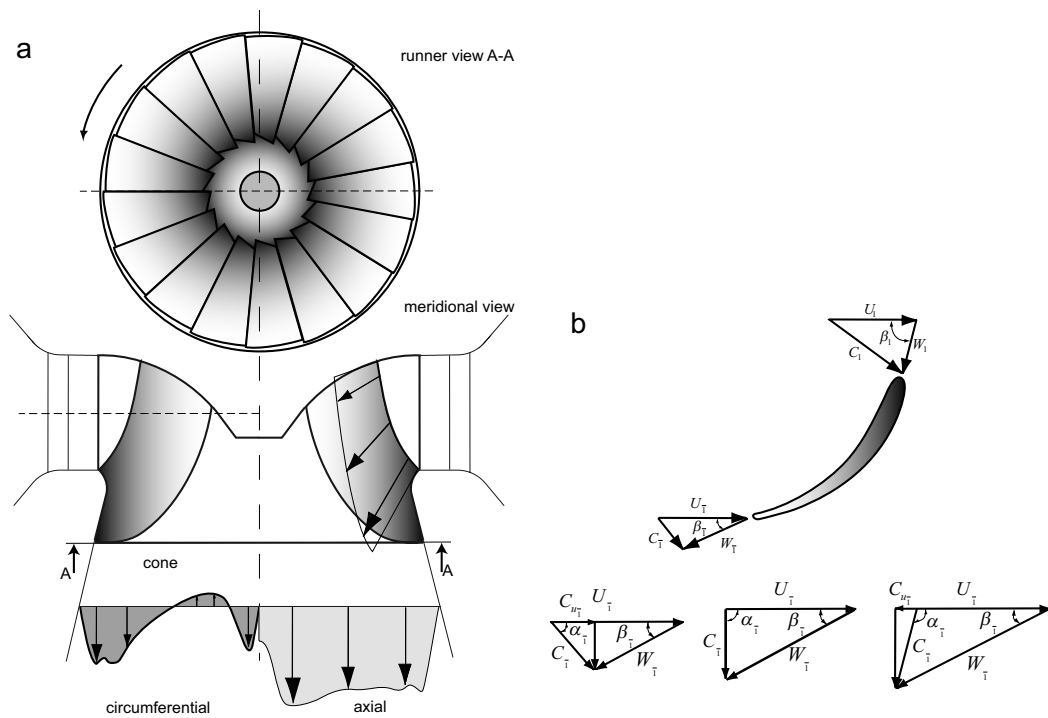


Figure 3.2: a) Schematic of the runner with the velocity profiles in the cone, b) schematic of the flow angles at the inlet and outlet of the blades. The absolute velocity component C , the relative velocity component W and the circumferential component U are shown.

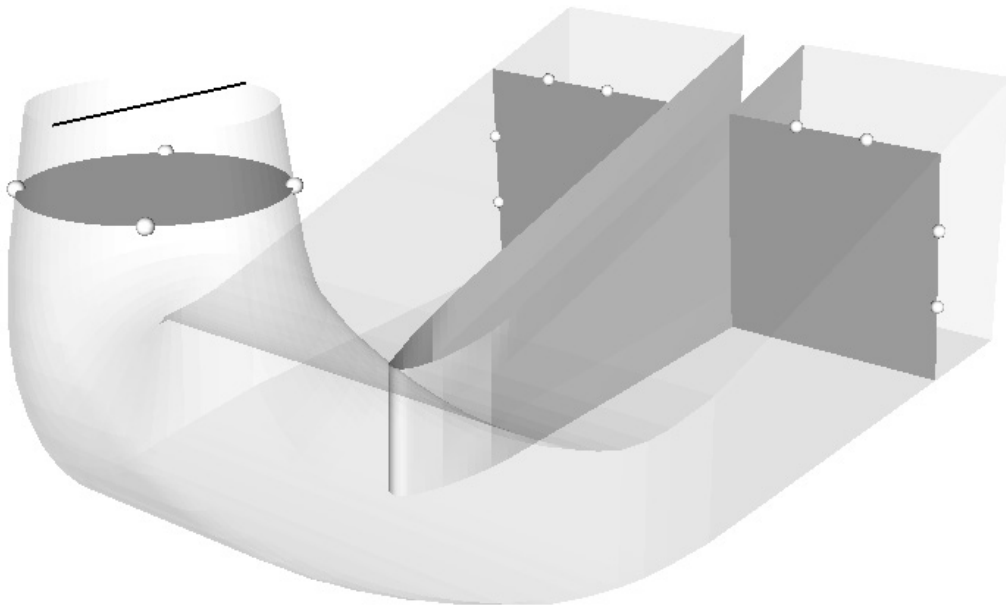


Figure 3.3: Pressure ring manifolds and measurement axis.

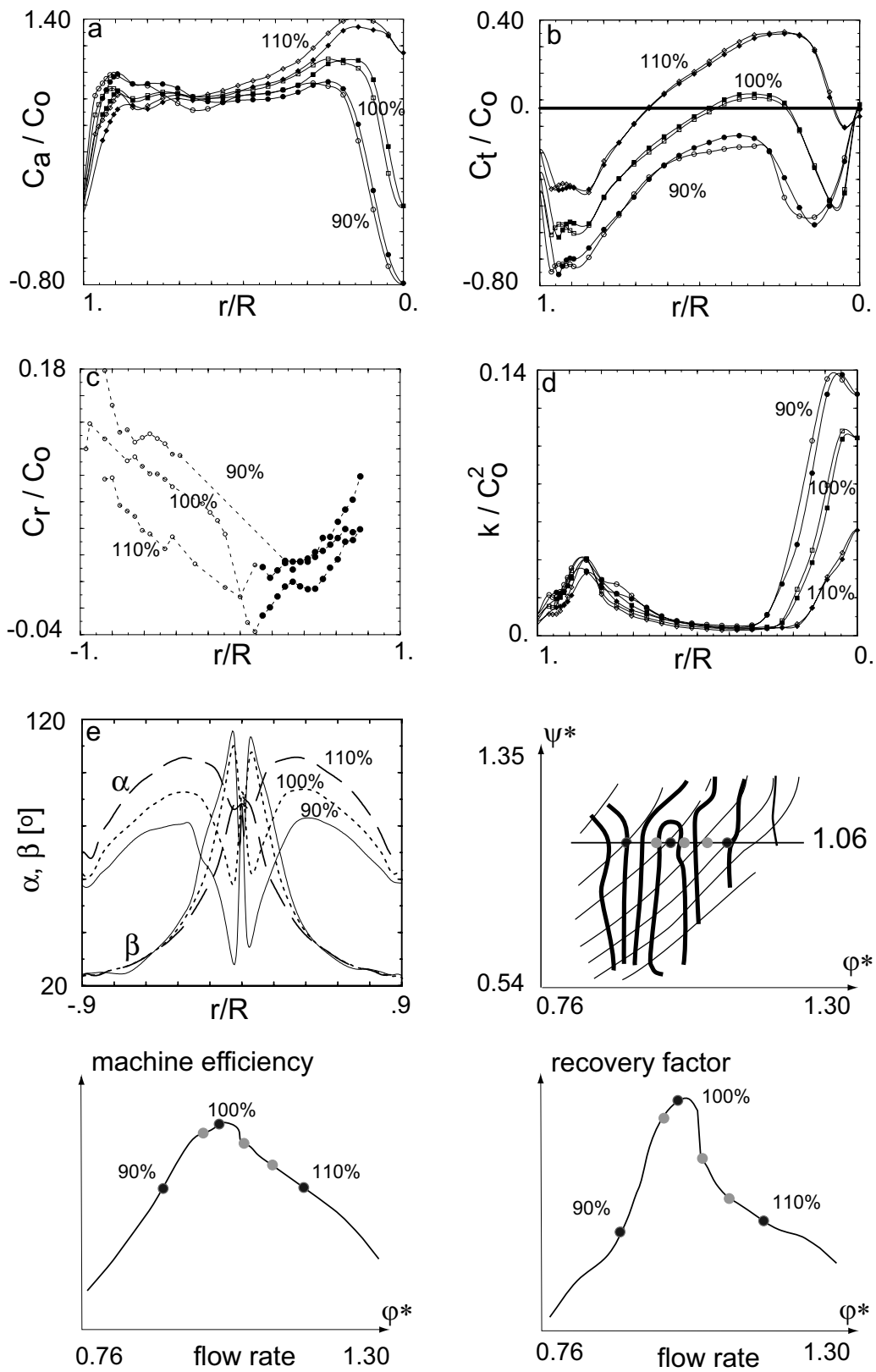


Figure 3.4: a), b), c), d) Velocity and kinetic energy inlet profiles for three operating points corresponding to $\varphi^* = 0.919$, $\varphi^* = 0.994$ and $\varphi^* = 1.108$. Filled points correspond to the external radius. e) Flow angles. C_a : axial velocity component, C_t : circumferential velocity component, C_r : radial velocity component, k : turbulent kinetic energy, C_o : mean sectional velocity magnitude.

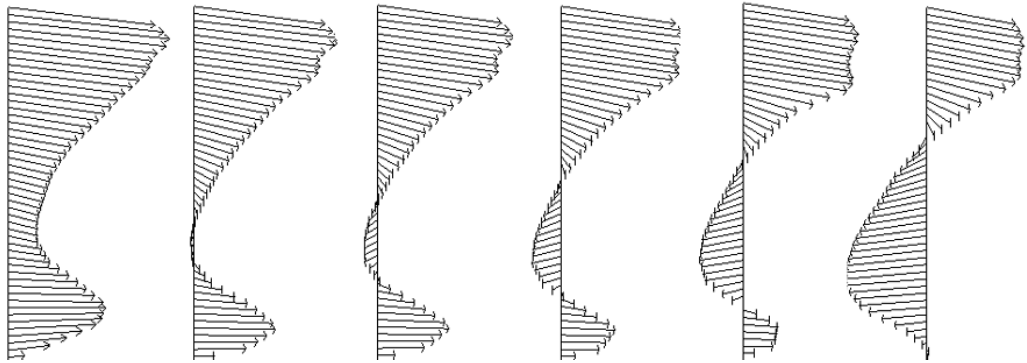


Figure 3.5: Velocity vector on the inlet radius for $\varphi^* = 0.919$, $\varphi^* = 0.973$, $\varphi^* = 0.994$, $\varphi^* = 1.027$, $\varphi^* = 1.054$ and $\varphi^* = 1.108$ (bottom: center, top: wall).

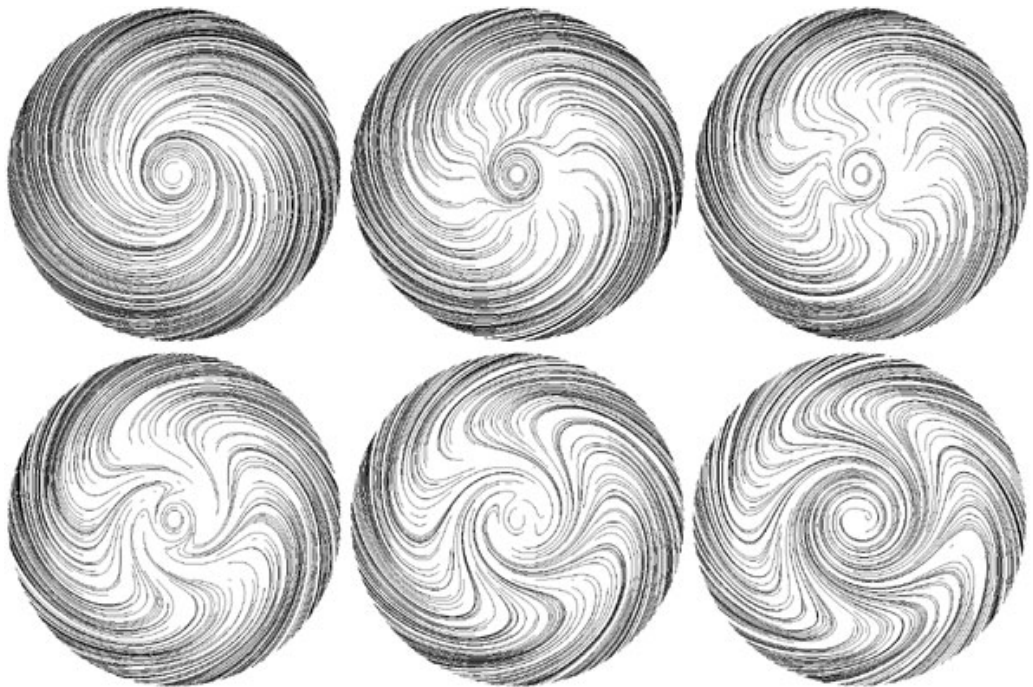


Figure 3.6: Tangential streamlines at the inlet section for $\varphi^* = 0.919$, $\varphi^* = 0.973$, $\varphi^* = 0.994$, $\varphi^* = 1.027$, $\varphi^* = 1.054$ and $\varphi^* = 1.108$.

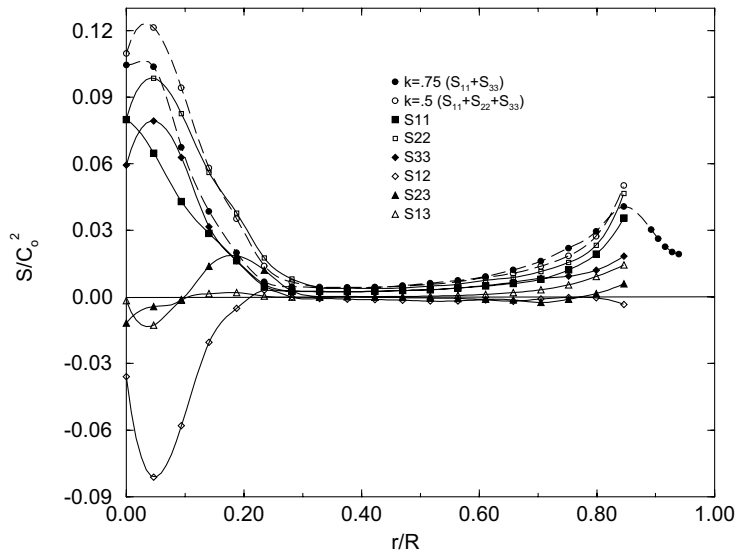


Figure 3.7: Reynolds' stresses, $\varphi^* = 0.994$.

The distribution of α and β (defined in fig. 3.2) is given in fig. 3.4. β still follows the blade angle in the external region. The radial velocity component is nearly linear, showing the influence of the bend. The turbulent kinetic energy (fig. 3.7) differentiates mainly in the core, showing higher values for low flow rates where the swirl is higher. The turbulent kinetic energy is considered for the mean flow field as the sum of all fluctuations including the deterministic ones introduced by the blade passage. By assuming turbulence isotropy for the normal stress components:

$$\bar{k} = 3/4\{(\tilde{c} + c')_x^2 + (\tilde{c} + c')_z^2\} \quad (3.1)$$

where the signal is decomposed into mean- (time independent), fluctuating- (phase averaged) and turbulent- components:

$$c = \bar{c} + \tilde{c} + c' \quad (3.2)$$

The isotropy assumption is a fairly good approximation as shown in fig. 3.7. The maximal difference in the turbulent kinetic energy, estimated with the isotropy assumption or computed with the three normal stresses, is 20% in the central zone.

Note on the best efficiency profile

The best efficiency profile is characterized by the steeper slope of the circumferential velocity component in the center.

3.2.2 Phase averaged velocity profiles

The rotational periodicity allows the evaluation at the runner outlet of the phase average with respect to the angular position of the runner. 11 diameters distributed on a sector of $2\pi/17$ [rad] (the runner has 17 blades) are measured.

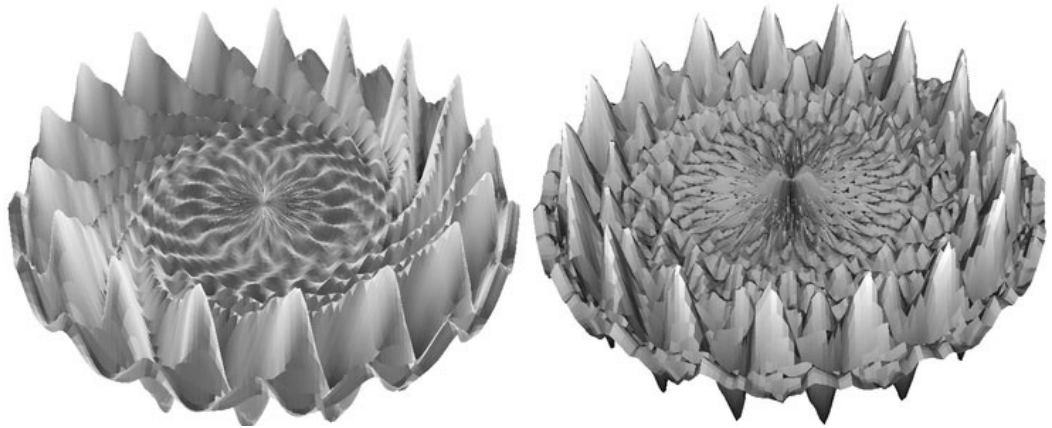


Figure 3.8: Phase averaged fluctuating circumferential (left) and axial (right) velocity components $\varphi^* = 0.994$.

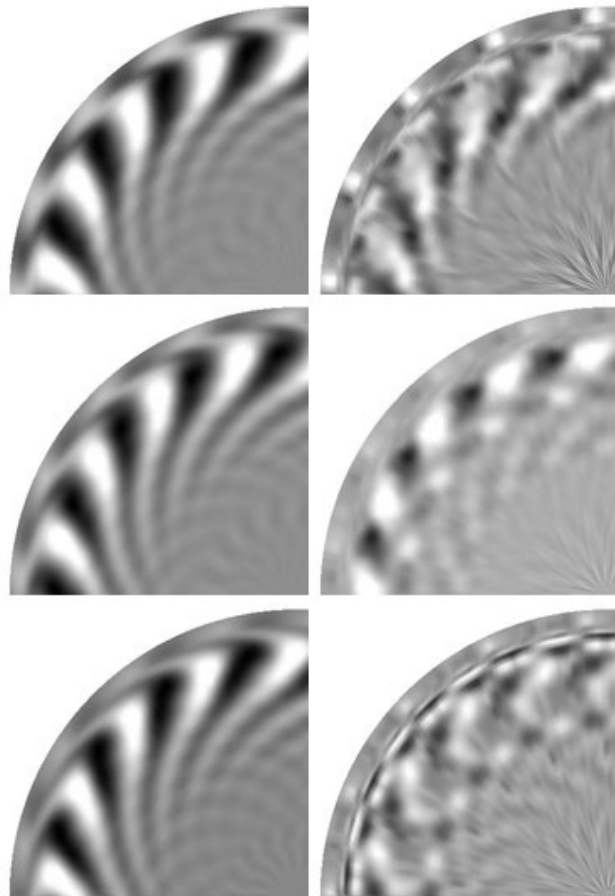


Figure 3.9: Phase averaged fluctuating tangential (left) and axial (right) velocity components, $\varphi^* = 0.919$, $\varphi^* = 0.994$, $\varphi^* = 1.108$ (from the top). The tangential maximal fluctuations correspond respectively to 15%, 17% and 14%, and the axial fluctuations to 1.1%, 2% and 0.9% of the mean axial velocity.

The measured fluctuating velocity field does not differ significantly between the two radii. The amplitude of the oscillation at the runner passage frequency represents a few percent of the mean velocity and is therefore not negligible. The fluctuating field for three operating points is shown in fig. 3.8 and 3.9. The blades influence is clearly recognizable. The amplitude of the fluctuations can reach 17% of the mean axial velocity for the tangential, and 2% for the axial velocity components.

V

Modeling and discretization

1

Introduction

In this chapter modeling and discretization choices are discussed. Modeling includes also data input to the code as the geometrical data, the boundary and initial conditions. A reasonable agreement with experimental results is not a sufficient proof of accuracy, especially if adjustable parameters are involved. Modeling errors (difference between the real flow and the exact solution of the mathematical model) and discretization errors (difference between the exact solution of the conservation equations and the exact solution of the algebraic system obtained by the discretization) should be estimated. For this purpose computational results and comparisons with experimental data are shown. The recovery factor is used as quantitative comparison value and skin-friction lines give a qualitative idea of the flow differences between the results. The detailed flow discussion is however presented only in part VI. While the results depend on the interaction between the different parameters, they are here discussed as independent variables for simplicity. Investigated parameters are: mesh density, outlet region modeling, inlet radial velocity component, near wall velocity profile, inlet turbulent dissipation, inlet turbulent kinetic energy, advection modeling and turbulence modeling. Investigations are carried out by varying a parameter one at a time. The other parameters correspond to the best choices resulting from each investigation.

1.1 Steadiness

In this part the flow is assumed to be steady even if this is not always justified and the steadiness is always a scale dependent characteristic in real flows. It is assumed that in the operating range considered in this study (IV.3.2) the main flow characteristics can be described assuming flow steadiness. It should be mentioned that measurements show regions with strong fluctuations in particular for the operating at higher flow rate. Time-dependent computations are discussed later.

1.2 Convergence

The computation is considered converged to the steady solution, when the value of the maximal normalized equation residual is less than 10^{-4} . No appreciable difference is observed in the recovery factor, in the specific energies evolution along the draft tube, on the experimentally investigated velocity and pressure profiles when the criterion is set to 10^{-5} . Some points in the domain are also monitored during the iterative process and show the achievement of the steady state.

1.3 Independent of the initial solution

All operating points have been computed by increasing or decreasing the flow rate using the solution of the previous point as initial state. No difference has been observed.

2

Mesh

2.1 Domain

Three different domains are compared (fig. 2.1): 1) the draft tube on its own, 2) with the addition of a downstream channel, and 3) with the addition of the first part of the test rig downstream tank (see (IV.1), fig. 1.2). The influence of this choice is discussed in (V.4).

2.2 Topology

The geometry of the simple draft tube model is discretized with a structured multiblock mesh. The blocks are shown in fig. 2.2. A butterfly topology with a C-shaped grid around the pier is used.

2.3 Quality

Different grid distributions are tested. The minimal skew angle in the cells is 42° and the maximum aspect ratio of the cells is 14. The y^+ values of the first grid points off the wall remain within the range of 20 and 400 for all operating points and meshes, where the majority of the points lies between $30 < y^+ < 100$

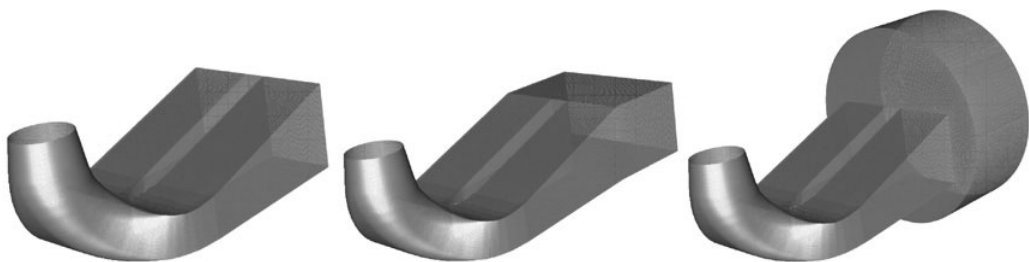


Figure 2.1: Treatment of the outlet region.

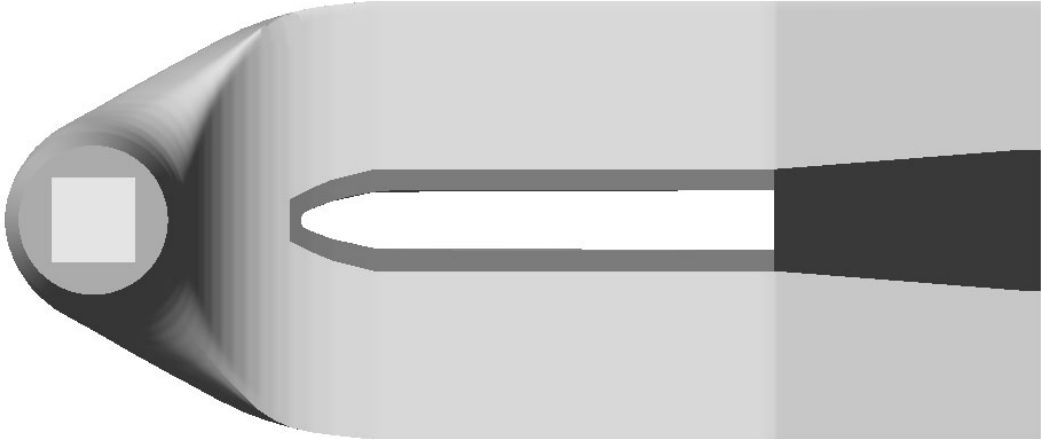


Figure 2.2: Mesh blocks.

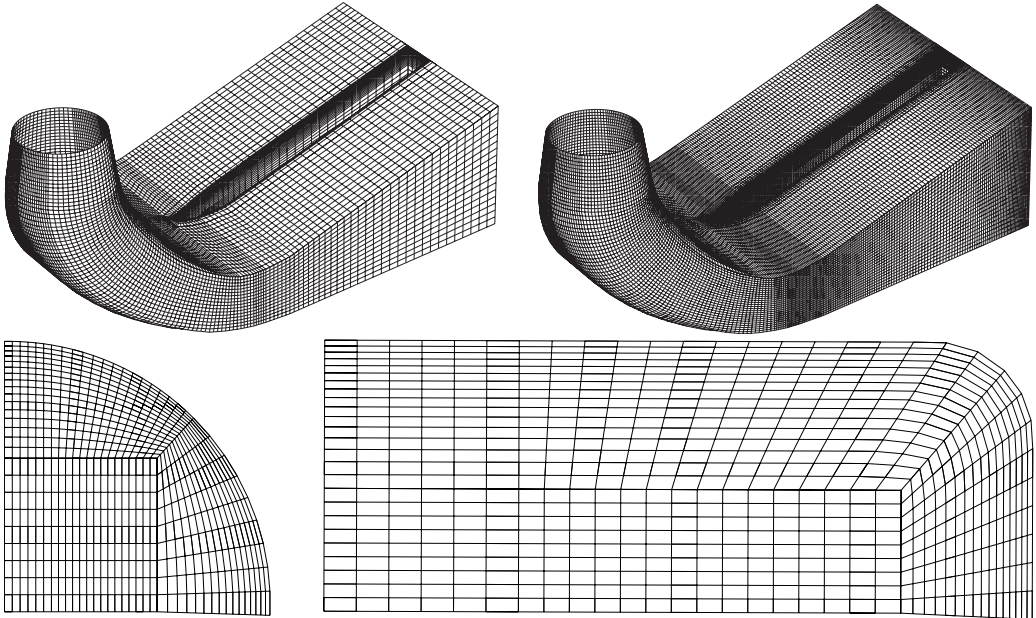


Figure 2.3: Mesh examples: a) 330'000 and 1'100'000 grid points , b) Quarter of two section, 330'000 nodes mesh.

3

Grid convergence

3.1 Introduction and definitions

An a posteriori numerical error estimation based on the generalized Richardson extrapolation, not requiring any restriction to integer refinement and applicable to solution functionals, is carried out. This extrapolation does not however assure the maintenance of conservation properties. Following Roache [Roa93] [Roa97] [Roa98] the more conservative Grid Convergence Index is also reported. It is required that the observed rate equals the formal convergence rate. The actual asymptotic rate of convergence may differ from the formal rate due to the competition of truncation error terms, or because the refinement is not achieved where necessary or a finer scale is missed. Error estimation using unrelated grids (not obtained simply one from the other) poses a challenge. However, it is mostly the case when working with complex three-dimensional meshes.

The Richardson extrapolation assumes that the discrete solutions f have a series representation:

$$f = f_{\text{exact}} + \sum_{i=1}^b g_i h^{i-1} \quad (3.1)$$

the functions g_i are defined in the continuum, b is the order of the discretization and h is the grid spacing. By combining two separate discrete solutions f_1, f_2 on two different grids, so as to eliminate the leading order error terms in the assumed error expansion, a more accurate estimate of f_{exact} is found

$$f_{\text{exact}} \simeq f_1 + (f_1 - f_2)/(r^p - 1) \quad (3.2)$$

where r is the refinement ratio and p the order of the discretization. The extrapolation is $(p+1)$ accurate for upstream-weighted methods for advection. The estimated fractional error for the fine grid solution f_1 is

$$E_1 = \epsilon/(r^p - 1), \quad \epsilon = (f_2 - f_1)/f_1 \quad (3.3)$$

and for the coarse solution:

$$E_2 = r^p E_1 \quad (3.4)$$

The actual fractional error for the fine grid solution A_1 is

$$A_1 = (f_1 - f_{\text{exact}})/f_{\text{exact}} \quad (3.5)$$

The estimated fractional error is a good approximation of the actual fractional error, when the solution is of reasonable accuracy.

The idea behind the Grid Convergence Index (GCI) is to approximately relate the obtained ϵ to the ϵ that would be expected from a grid refinement study of the same problem, with the same fine grid, and using a grid doubling with a second-order method. This allows a uniform reporting of grid convergence tests and a more conservative error band as the estimated fractional error.

$$GCI_1 = 3\epsilon/(r^p - 1), \quad GCI_2 = r^p GCI_1 \quad (3.6)$$

The asymptotic range is achieved when

$$GCI_{23} \simeq r^p GCI_{12} \quad (3.7)$$

where 1, 2 and 3 refer to respectively the fine, intermediate and coarse grid.

3.2 Error estimation

The recovery factor obtained with four meshes are compared at $\varphi^* = 0.994$. The number of nodes corresponds to the effective number of points in the draft tube geometry (overlapping nodes at the block interfaces are counted only once and the downstream channel is not considered). The grid refinement is reported simply in terms of the total number of grid points used in the two meshes as $r_{ij} = (N_i/N_j)^{\frac{1}{3}}$. The meshes have the same topology but the grid refinement is not uniform in the space. This may give an inaccurate estimation of the accuracy depending on whatever the grid refinement occurs in the critical areas or not. Depending on the mesh resolution at the inlet the resulting flow rate will change and must be corrected to retrieve the measured value by multiplying the velocity field by a factor. Slight differences in the inlet boundary conditions introduce an additional uncertainty. The first three meshes seem to be in the asymptotic range; (3.7) is reasonably well satisfied (actual asymptotic rate of convergence $p=2.2$ to be compared with the theoretical order $p=2$). This

$N_1=1'855'152$	$N_2=1'107'237$	$N_3=633'720$	$N_4=328'360$
$r_{12}=1.187717$	$r_{23}=1.204429$	$r_{13}=1.430520$	$r_{14}=1.781051$
$\chi_1=0.7739$	$\chi_2=0.7737$	$\chi_3=0.7733$	$\chi_4=0.7826$
$E_1=0.17-0.08$	$E_2=0.20-0.11$	$E_3=0.28-0.16$	
$GCI_1=0.51-0.23$	$GCI_2=0.61-0.33$	$GCI_3=0.83-0.49$	

Table 3.1: $\varphi^* = 0.994$. N : number of nodes, r : grid refinement ratio, χ : recovery factor, E : estimated fractional error, GCI : grid convergence index. Values for E , GCI are reported in [%] using $p = 1 - 2$.

results are expected to be only partially representative for other operating

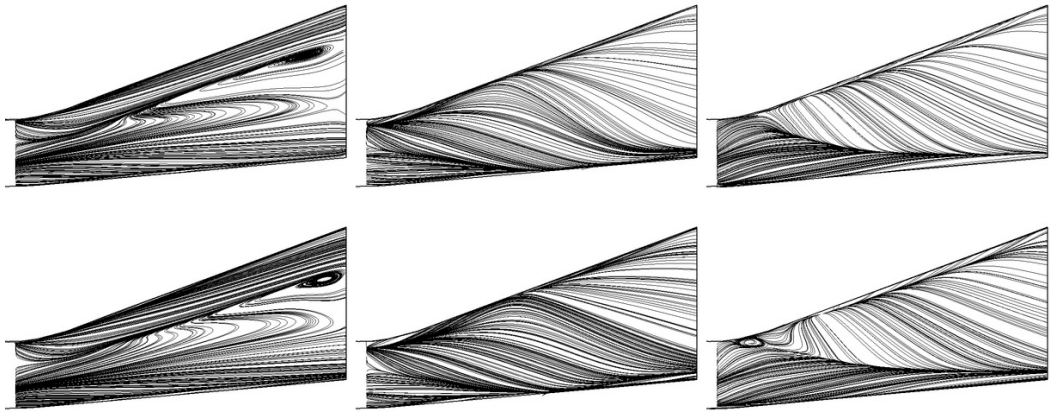


Figure 3.1: Skin friction lines at the pier, left side, a) $\varphi^* = 0.919$, b) $\varphi^* = 0.994$, c) $\varphi^* = 1.108$ (from the left to the right). $N_4=328'360$ (top), $N_2=1'107'237$ (bottom). Note: the lines are not started from the same positions for the two meshes.

conditions due to the important flow differences. The results for the meshes N_2 and N_4 are compared also at the points $\varphi^* = 0.919 - 1.108$ in table 3.2. As observed for $\varphi^* = 0.994$ we can expect that the solution obtained with N_4 is not in the asymptotic range and consequently the estimated fractional error is only indicative. As expected the mesh influence for the operating points

$N_2=1'107'237$	$N_4=328'360$	$N_2=1'107'237$	$N_4=328'360$
$r_{24}=1.499559$		$r_{24}=1.499559$	
$\chi_2=0.5783$	$\chi_4=0.5584$	$\chi_2=0.5305$	$\chi_4=0.5385$
$E_2=6.89-2.75$	$E_4=10.33-6.20$	$E_2=3.02-1.21$	$E_4=4.53-2.72$

Table 3.2: a) $\varphi^* = 0.919$ b) $\varphi^* = 1.108$. See caption in table 3.1.

lying outside the optimal range increases. The skin friction lines show however only slight differences, visible in particular in the backflow zone for $\varphi^* = 0.919$ (fig. 3.1).

4

Outlet boundary condition

While the position of the inlet section is fixed by the location of the measurements, the treatment of the outlet region must be investigated. The RANS equations can have an elliptic character and possibly the flow of a channel has an influence on the other side in the outlet region. In high Reynolds number flows, upstream propagation of error should be weak. Backflow zones can occur however for most of the operating conditions.

Three different domains are compared (fig. 2.1): 1) the draft tube on its own (hereafter referred as case “simple”), 2) with the addition of a downstream channel (“box”; following the philosophy that boundaries should be as far downstream of the region of interest as possible), and 3) with the addition of the first part of the test rig downstream tank (“tank”). On the test rig this part ends with flow tranquilizing screens. These screens are modeled considering this region as a porous object with a factor describing the fraction open to fluid ($\beta = 0.433$). Moreover a simple momentum loss model applying to the fluid flow within the porous region is provided. A source term is added to the momentum equations. This term consists of a pressure gradient scaled with the local dynamic head: $\nabla P = k \frac{\rho C^2}{2}$. The factor $k = 30$ is set following the experimental values contained in [Ide69]. For all cases the pressure is set constant at the outlet. The same results are obtained when the pressure is left unspecified. The influence of the outlet is investigated for $\varphi^* = 0.919$, $\varphi^* = 0.994$, $\varphi^* = 1.108$. The recovery factor is only slightly affected by this choice as illustrated in table 4.1. For the point at the lowest flow rate the only

	$\varphi^* = 0.919$	$\varphi^* = 0.994$	$\varphi^* = 1.108$
“simple”	$\chi=0.5602$	$\chi=0.7802$	$\chi=0.5053$
“box”	$\chi=0.5584$	$\chi=0.7826$	$\chi=0.5385$
“tank”	$\chi=0.5597$	$\chi=0.7742$	$\chi=0.5405$
meas.	$\chi=0.4937$	$\chi=0.7584$	$\chi=0.5192$

Table 4.1: Influence of the outlet boundary conditions on the recovery factor.

differences are visible in the small backflow region situated on the left channel as shown in fig. 4.1. The obtained recovery factor differs by only tenths of a percent point. At $\varphi^* = 0.994$ some differences are visible for the case “tank” at the outlet corners of the pier due to the abrupt section expansion (fig. 4.2).

The recovery factor is for this case closer to the experimental value, with a difference of one percent from the other cases. At the highest flow rate the backflow region occurring on the right channel, is similarly predicted in the cases “box” and “tank” (fig. 4.3). The recovery factor for the “simple” case is six percent lower than for the other cases.

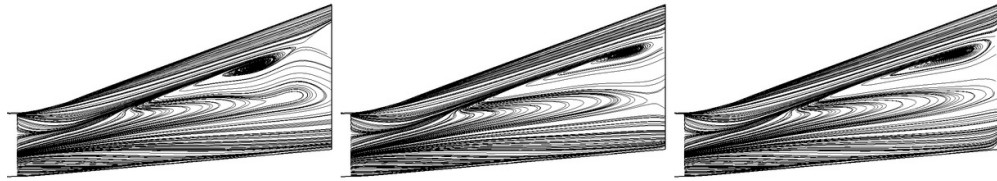


Figure 4.1: Skin friction lines at the pier, left side, $\varphi^* = 0.919$. a) Case “simple”, b) “box”, c) “tank”.

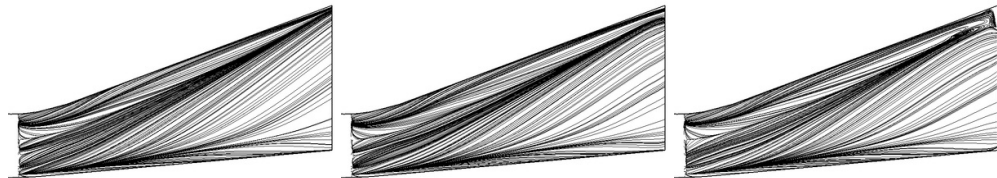


Figure 4.2: Skin friction lines at the pier, right side, $\varphi^* = 0.994$. a) Case “simple”, b) “box”, c) “tank”.

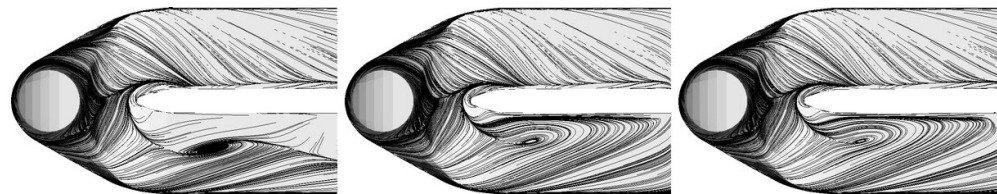


Figure 4.3: Skin friction lines, view from above, $\varphi^* = 1.108$. a) Case “simple”, b) “box”, c) “tank”.

5

Inlet radial velocity component

Some discrepancies on the radial component of the velocity are observed between the LDA and steady probe measurements. The probe indicates a velocity vector that is parallel to the surface near the walls, with a nearly linear evolution in the interior. LDA results show a slope indicating a more pronounced effect due to the bend. For this reason two different distributions are investigated. While the axial and tangential velocity components are interpolated by cubic splines, this type of interpolation leads to oscillation for the radial component. This is due to the inferior number of measurement points and the poor smoothness of the profile. The profile is therefore interpolated by the best linear fit. The profiles for $\varphi^* = 0.919$, $\varphi^* = 0.994$ and $\varphi^* = 1.108$ are illustrated in fig. 5.1. The dotted line describes the evolution of the radial component with the equation $C_r = C_n \tan(\theta r/R)$ (hereafter “geometrical” distribution), θ being the cone half opening angle. The inclination of the velocity vector in the radial direction is therefore determined by the geometry of the cone (similarly to the steady probe measurements). The influence of the inlet radial velocity component is investigated for a) $\varphi^* = 0.919$, b) $\varphi^* = 0.994$, c) $\varphi^* = 1.108$. The recovery factor is affected by this choice as illustrated in table 5.1. Skin friction lines are shown in fig. 5.2, 5.3, 5.4.

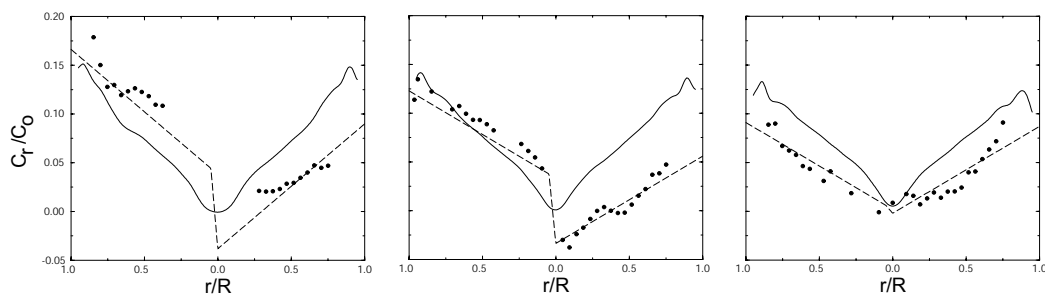


Figure 5.1: Inlet radial velocity distribution. a) $\varphi^* = 0.919$, b) $\varphi^* = 0.994$, c) $\varphi^* = 1.108$. Points: LDA measurements, dotted line: best linear fit to the measurements, solid line: “geometrical” distribution.

	$\varphi^* = 0.919$	$\varphi^* = 0.994$	$\varphi^* = 1.108$
best linear fit	$\chi=0.5642$	$\chi=0.7955$	$\chi=0.6224$
“geometrical” distribution	$\chi=0.5584$	$\chi=0.7826$	$\chi=0.5385$
measured	$\chi=0.4937$	$\chi=0.7584$	$\chi=0.5192$

Table 5.1: Influence of the inlet radial velocity component on the recovery factor.

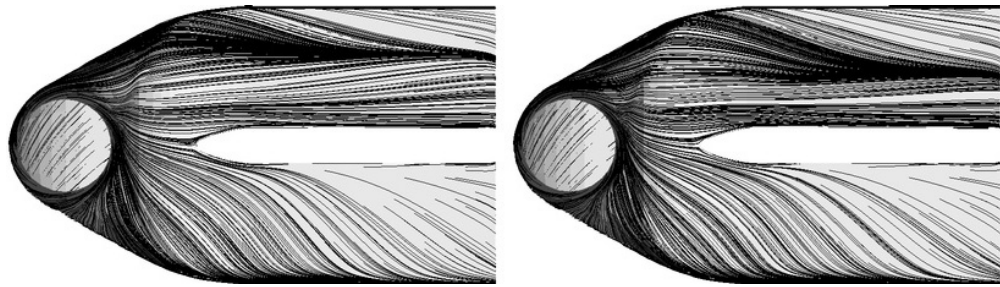


Figure 5.2: Skin friction lines, view from above, $\varphi^* = 0.919$: a) “geometrical” distribution, b) best linear fit distribution.

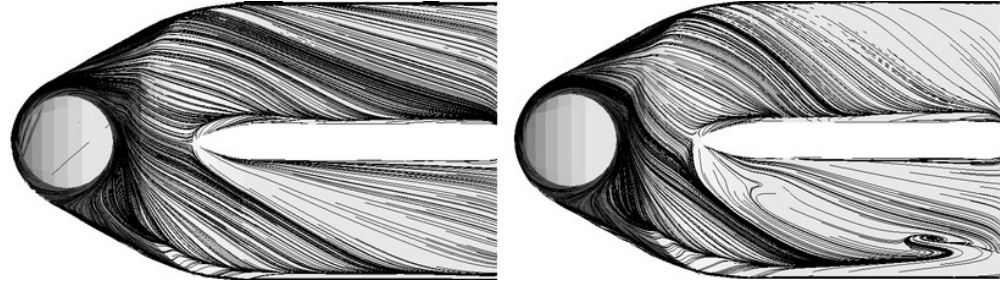


Figure 5.3: Skin friction lines, view from above, $\varphi^* = 0.994$: a) “geometrical” distribution, b) best linear fit distribution.

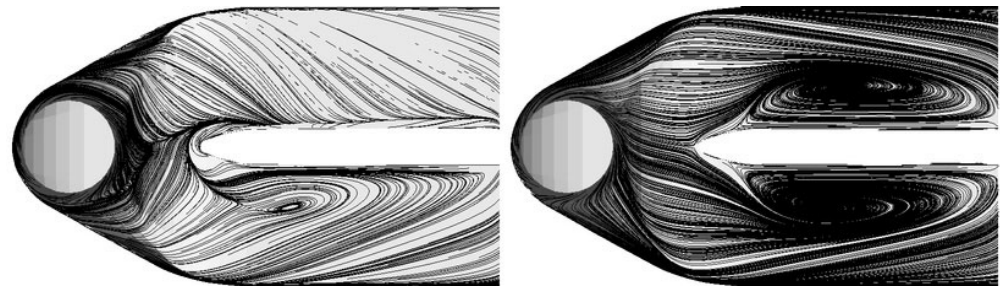


Figure 5.4: Skin friction lines, view from above, $\varphi^* = 1.108$: a) “geometrical” distribution, b) best linear fit distribution.

6

Near wall velocity profile

The measured velocity profiles are interpolated by cubic splines. The nearest measurement point is at .076 inlet diameters from the wall. In order to control the extrapolation at the wall, the velocity is here imposed to be a factor f of the nearby interior measurement point value. This factor plays a role on the wall velocity gradient and consequently on the wall friction. The swirl is proportional to the squared radius and therefore the velocity near the wall can have an important weight. The influence of this parameter is investigated for the extreme points at $\varphi^* = 0.919$ and $\varphi^* = 1.108$. The recovery factor is clearly affected by this choice, varying almost linearly with f as illustrated in table 6.1. The importance of the momentum thickness on the pressure recovery was already recognized by Ackeret, as described in the introduction (I.2), fig. 2.2. Indeed, most of the recovery does take place in the cone. The stronger influence occurs for the point with the highest swirl, where the boundary flow energy is higher. The influence on the skin friction lines is illustrated in fig. 6.1 and 6.2. The flow angles in the cone are strongly affected especially at the highest flow rate. Comparisons with measurements are shown in fig. 6.3. The near-wall steep gradients are reproduced in the computations only in the case $f = 0.900$.

	$\varphi^* = 0.919$	$\varphi^* = 1.108$
$f = 0.005$	$\chi=0.6099$	$\chi=0.5860$
$f = 0.215$	$\chi=0.6121$	$\chi=0.5772$
$f = 0.900$	$\chi=0.5584$	$\chi=0.5385$
meas.	$\chi=0.4937$	$\chi=0.5192$

Table 6.1: Influence of the near wall velocity profile on the recovery factor.

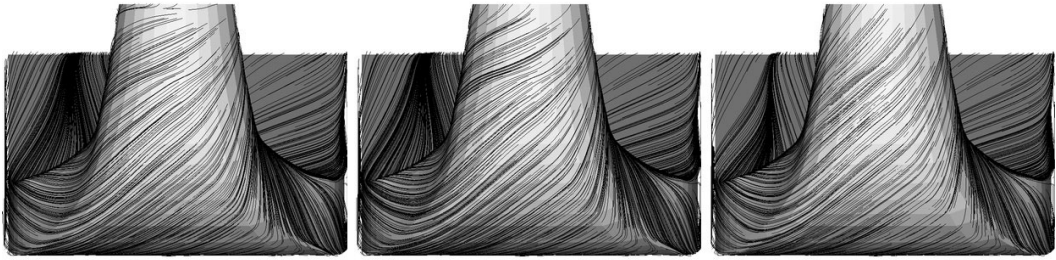


Figure 6.1: Skin friction lines, view from behind, $\varphi^* = 0.919$. a) $f = 0.005$, b) $f = 0.215$ and c) $f = 0.900$.

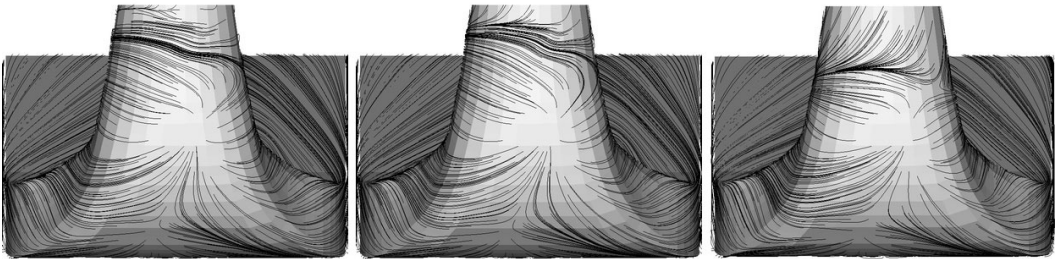


Figure 6.2: Skin friction lines, view from behind, $\varphi^* = 1.108$. a) $f = 0.005$, b) $f = 0.215$ and c) $f = 0.900$.

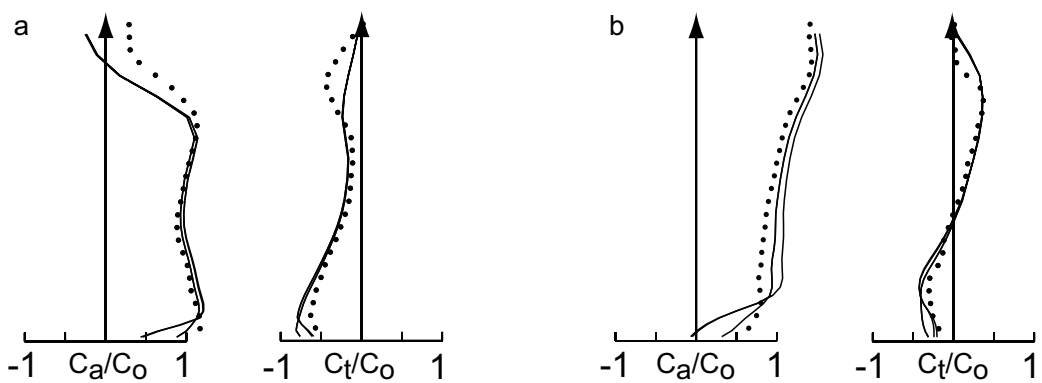


Figure 6.3: Axial (C_a) and tangential (C_t) velocity profile at the section 1.75, from the wall to the cone center. Points: measurements, solid lines: $f = 0.005$, $f = 0.215$ and $f = 0.900$: a) $\varphi^* = 0.919$, b) $\varphi^* = 1.108$. The near-wall steep gradients are partially reproduced in the computations only in the case $f = 0.900$.

7

Inlet turbulent dissipation

LDA measurements indicate a locally isotropic turbulence (IV.3.2), which is an assumption of the $k - \epsilon$ model. This could be explained by the fact that the inlet swirl is still moderate. Blade passage introduces periodic velocity fluctuations that do not correspond to statistic turbulence. These fluctuations are here recognizable only in a limited region outside the central core and at some distance from the wall. The turbulent kinetic energy imposed in the computations includes all types of fluctuations. In the standard $k - \epsilon$ model it is assumed that $\epsilon = k^{3/2}/L_\epsilon$. For the computation of ϵ from the measured turbulent kinetic energy, the length scale L_ϵ defining the size of the largest eddies must be determined. L_ϵ can be assumed to be of the same order as the smallest distance between the runner blades, which is $0.03 D$. From the Boussinesq hypothesis and the measurements results it is possible to estimate the turbulent viscosity μ_t . With the tangential components of the velocity: $-\rho \overline{c'_1 c'_2} = \mu_t (\frac{\partial c_1}{\partial x_2} + \frac{\partial c_2}{\partial x_1})$, where c_1, c_2 are the tangential components of the velocity and x_1, x_2 the corresponding orthogonal basis. From the Prandtl-Kolmogorov modeling of the turbulent viscosity $\mu_t = \rho c_\mu L_\epsilon \sqrt{k}$, the eddy length can be calculated, c_μ being a constant. The estimation shows that the length is nearly constant, except in the central zone and near the wall. The corresponding value is about $0.02 D$ and thus in the same order of the smallest distance between the runner blades. The influence of this parameter is investigated for the operating points at $\varphi^* = 0.919$, $\varphi^* = 0.994$ and $\varphi^* = 1.108$. The recovery factor is clearly affected by this choice as illustrated in table 7.1. Better numerical results with

	$\varphi^* = 0.919$	$\varphi^* = 0.994$	$\varphi^* = 1.108$
$L_\epsilon = 0.0001$	$\chi=0.5524$	$\chi=0.7688$	$\chi=0.5304$
$L_\epsilon = 0.001$	$\chi=0.5584$	$\chi=0.7826$	$\chi=0.5385$
$L_\epsilon = 0.01$	$\chi=0.5475$	$\chi=0.8018$	$\chi=0.6339$
meas.	$\chi=0.4937$	$\chi=0.7584$	$\chi=0.5192$

Table 7.1: Influence of the inlet turbulent dissipation length on the recovery factor.

respect to the measurements (recovery factor, surveys at the sections 1.75, 15.5, 20.75) are obtained with $L_\epsilon = 0.001$, i.e. with one order of magnitude smaller values than the previous estimates. The flow angles in the cone and

the backflow regions are affected by this parameter especially at higher flow rates as shown in fig. 7.1, 7.2, 7.3 and 7.4. In particular at $\varphi^* = 1.108$ the experimentally observed backflow region in the right channel is not predicted with $L_\epsilon = 0.01$ (fig. 7.3).

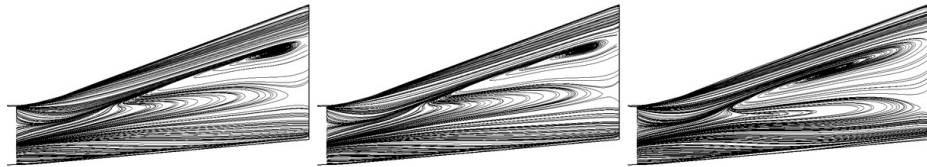


Figure 7.1: Skin friction lines at the pier, left side, $\varphi^* = 0.919$: a) $L_\epsilon = 0.0001$, b) $L_\epsilon = 0.001$, c) $L_\epsilon = 0.01$.

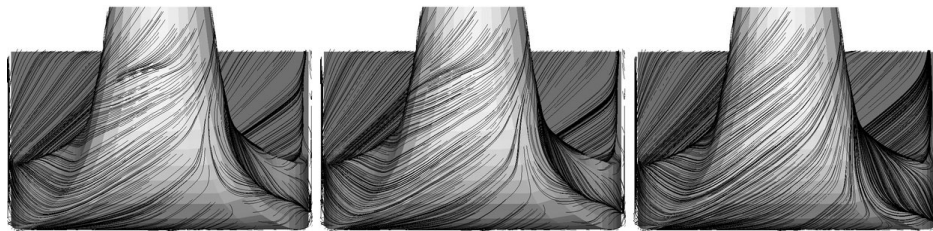


Figure 7.2: Skin friction lines, view from behind, $\varphi^* = 0.994$: a) $L_\epsilon = 0.0001$, b) $L_\epsilon = 0.001$, c) $L_\epsilon = 0.01$.

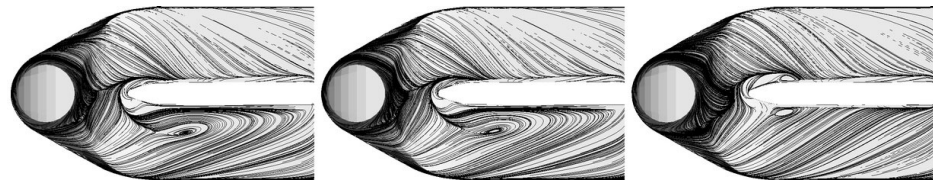


Figure 7.3: Skin friction lines, view from above, $\varphi^* = 1.108$: a) $L_\epsilon = 0.0001$, b) $L_\epsilon = 0.001$, c) $L_\epsilon = 0.01$.

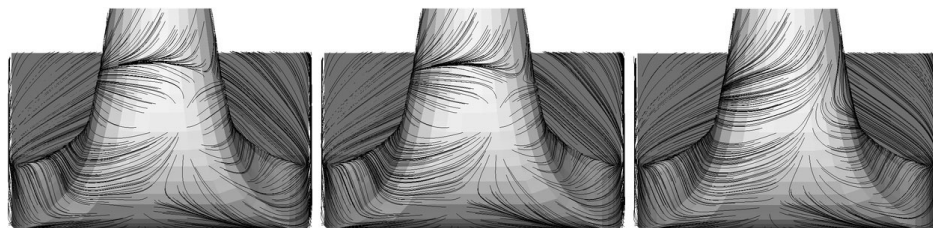


Figure 7.4: Skin friction lines, view from behind, $\varphi^* = 1.108$: a) $L_\epsilon = 0.0001$, b) $L_\epsilon = 0.001$, c) $L_\epsilon = 0.01$.

8

Inlet turbulent kinetic energy

The computational results show that the imposed turbulent kinetic energy profile with the important peak in the central zone (IV.3.2) is smeared out in a very short distance. This could maybe be explained by the fact that the Prandtl-Kolmogorov hypothesis directly relates the turbulent kinetic energy with the turbulent viscosity and thus the model adopts large eddy viscosity in the central zone, leading to the rapid turbulent momentum transfer. This is however observed also in the test cases even when the RSM model is used. The influence of the inlet turbulent kinetic energy is investigated for the operating point at $\varphi^* = 0.919$. The turbulent kinetic energy is either assumed to be resp. 1% of the total energy ($Tu = 0.01$), 0.1% ($Tu = 0.001$) or the experimental profile is imposed. The influence on the recovery factor is illustrated in table 8.1. The recovery factor as well as the skin friction lines (fig. 8.1) and the velocity and pressure profiles at the experimentally investigated sections are quite unaffected by the imposed inlet turbulent kinetic energy.

	$\varphi^* = 0.919$
$Tu = 0.001$	$\chi = 0.5472$
$Tu = 0.01$	$\chi = 0.5529$
experimental profile	$\chi = 0.5584$
measured	$\chi = 0.4937$

Table 8.1: Influence of the inlet turbulent dissipation length on the recovery factor.

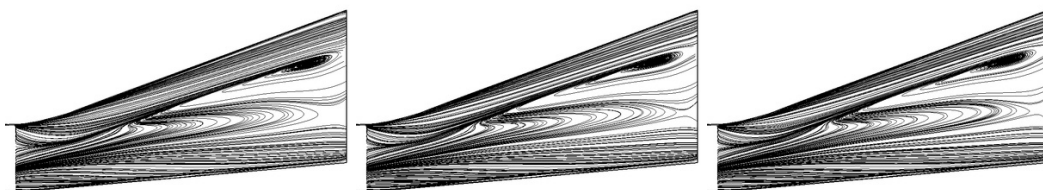


Figure 8.1: Skin friction lines at the pier, left side, $\varphi^* = 0.919$, $L_\epsilon = 0.001$. a) $Tu = 0.01$, b) $Tu = 0.001$, c) experimental profile.

9

Advection scheme

The linear profile skew scheme (LPS) is compared with the modified linear profile skew scheme (MLPS) (II.2.1). While the MLPS is a hybrid scheme and the formal accuracy is no more of second order, the comparisons with the experimental data show better performances as the LPS scheme. The main flow evolution (VI.4) is the same for the two schemes, however with a shift with respect to the flow rate. The LPS scheme anticipates the flow evolution obtained with the MLPS scheme when the flow rate is increased. This can be seen in the recovery factor prediction shown in fig. 9.1 and in the skin friction lines (fig. 9.2, 9.3). In particular the phenomenon responsible for the pressure recovery drop (described later) is already visible at $\varphi^* = 0.994$ (fig. 9.3) when the LPS scheme is adopted. The MLPS scheme correctly describes the begin of the drop after the flow rate corresponding to $\varphi^* = 0.994$. While at a first glance the recovery factor seems to be better predicted with the LPS scheme, the analysis of the flow evolution and the comparisons with the velocity and pressure profiles at the sections 1.75, 15.5 and 20.75, clearly indicate that better results are obtained using the MLPS scheme.

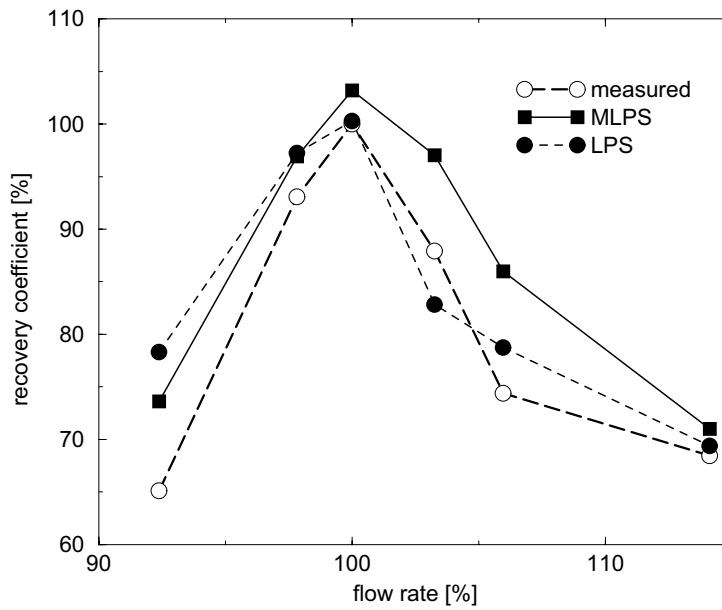


Figure 9.1: Recovery factor obtained with two advection schemes.

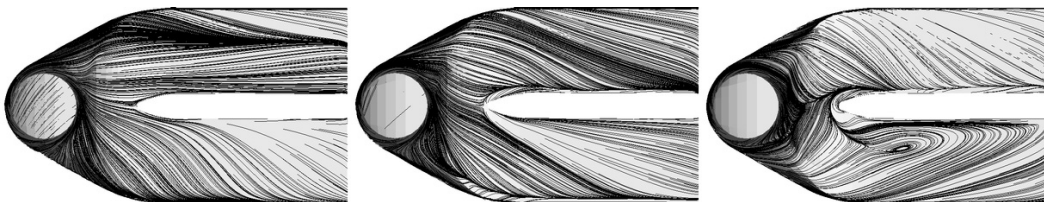


Figure 9.2: Skin friction lines, view from above, a) $\varphi^* = 0.919$, b) $\varphi^* = 0.994$, c) $\varphi^* = 1.108$. MLPS scheme.

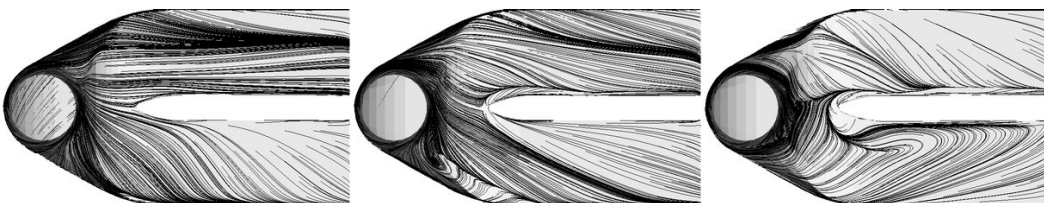


Figure 9.3: Skin friction lines, view from above, a) $\varphi^* = 0.919$, b) $\varphi^* = 0.994$, c) $\varphi^* = 1.108$. LPS scheme.

10

Turbulence modeling

10.1 $k - \omega$ model

The use of the $k - \omega$ and BSL models (II.2.1) does not improve the agreement with the experimental data in comparison with the standard $k - \epsilon$, even for the operating point at $\varphi^* = 1.108$ where a large separated region is found to play an important role on the recovery factor (V.7), as shown in table 10.1.

	$\varphi^* = 0.994$	$\varphi^* = 1.108$
$k - \omega$	$\chi=0.8012$	$\chi=0.6318$
BSL	$\chi=0.8021$	-
$k - \epsilon$	$\chi=0.7826$	$\chi=0.5385$
meas.	$\chi=0.7584$	$\chi=0.5192$

Table 10.1: Influence of the turbulence model on the recovery factor.

10.2 Reynolds-stress-equation model (RSM)

Reynolds stress models are characterized by a higher degree of universality and should better describe in particular the effects of streamline curvature and secondary flows as well as the characteristics of swirling flows. The recovery factors obtained using the RSM-LLR model are reproduced in table 10.2. It

	$\varphi^* = 0.919$	$\varphi^* = 0.994$
<i>RSM - LLR</i>	$\chi=0.5675$	$\chi=0.7652$
$k - \epsilon$	$\chi=0.5584$	$\chi=0.7826$
meas.	$\chi=0.4937$	$\chi=0.7584$

Table 10.2: Influence of the turbulence model on the recovery factor.

should be mentioned however that the code does not allow specifying the measured stress profiles at the inlet. These are computed from the turbulent kinetic energy. Even if the recovery factor matches better with the use of the RSM model for the operating point at $\varphi^* = 0.994$, the comparisons with the

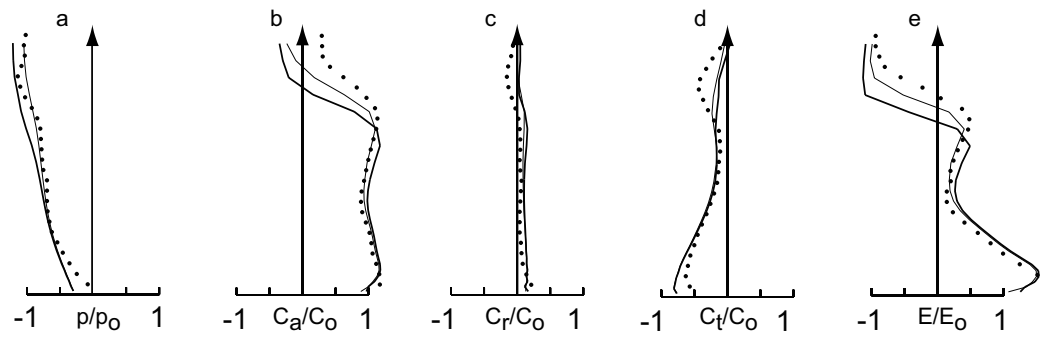


Figure 10.1: a) Pressure, b) axial velocity, c) radial velocity, d) tangential velocity and e) energy profile at the section 1.75, from the wall to the cone center. Points: measurements, fine solid line: $k - \epsilon$, large solid line: RSM. $\varphi^* = 0.919$.

measured velocity and pressure profiles at the sections 1.75 and 15.5 and 20.75 indicate better performances for the standard $k - \epsilon$ for both operating points. The profiles on one axis at the section 1.75 for the point at higher swirl, corresponding to the flow rate $\varphi^* = 0.919$, are shown in fig. 10.1.

11

Summary and conclusions

For operating points lying in the optimal range the mesh with $N_3=633'720$ effective nodes insures a GCI smaller than 1% for the recovery factor. The mesh influence increases for the extreme points. While the mesh with $N_4=328'360$ does not lie in the asymptotic range in the prediction of the recovery factor, the results obtained with this mesh show the same flow topology as the finer meshes and compare even slightly better with the measured velocity and pressure profiles (sections 1.75, 15.5). For these reasons and the limited computational resources the investigations are carried out with the mesh consisting of $N_4=328'360$ nodes.

Globally the outlet boundary condition has little influence on the recovery factor and on the overall flow. Experimentally the level of the water in the tank of the test rig does not affect the performances of the draft tube. These facts indicate a parabolic behaviour of the flow at the outlet. This is explained by the uniformity of the pressure in the two channels in the outlet region. However, when an important recirculation occurs in the outlet region, the case “simple” leads to relatively important differences compared with the other cases. Due to the computational economy the outlet region will be treated as in the case “box” with the simple addition of a downstream channel. The simulation of the first part of the test rig downstream tank (case “tank”) does not considerably improve the solution.

The radial velocity component can affect considerably the flow in the draft tube in spite of the small magnitude of this component. While for the operating points at $\varphi^* = 0.919$ and $\varphi^* = 0.994$ the differences using the two distributions are relatively small, at $\varphi^* = 1.108$ the flow differs considerably. The “geometrical” distribution leads to better results in comparison with the measurements (recovery factor, surveys at the sections 1.75, 15.5, 20.75) for all operating points.

Steep gradients for the inlet velocity at the wall better reproduce the experimental data. The velocity value at the wall is set to be nine tenths of the value at the first measurement point.

For the point at higher flow rate ($\varphi^* = 1.108$) the inlet eddy length scale plays an important role on the recovery factor. A too lower inlet turbulent dissipation rate causes a failed prediction of the experimentally observed backflow zone and leads to a clearly overestimated recovery factor. For the other operating points the influence is clearly less important. The inlet eddy length scale is set to $L_\epsilon = 0.001$ ($0.002D$) for all operating points.

The inlet turbulent kinetic energy has a small influence on the results. The experimental profile is imposed.

While both advection schemes predict the same flow evolution when the flow rate is increased, the LPS scheme anticipates this evolution in comparison with the MLPS scheme and to the measurements. A better match with experiments is obtained using the MLPS scheme.

In spite of the potential of advanced turbulence models the standard $k - \epsilon$ model leads to the best agreement with the experiments. It should be mentioned however that the code does not allow specification of the measured stress profiles at the inlet.

It is clear from this study that in spite of the detailed measurements, these are still insufficient. The simulation of the flow in the draft tube requires the calibration of several parameters.

Garbage in, garbage out (saying in the CFD community).

VI

Steady flow computation

1

Introduction

In this part the flow field obtained with the modeling choices discussed in part V and summarized in table 1.1, are first compared with the experimental data (VI.2) and then analyzed in (VI.3) and (VI.4). Measurements are available on the sections illustrated in fig. 1.1.

In addition to the experimentally investigated operating conditions, four additional flow rates between respectively $\varphi^* = 0.994-1.027$ and $\varphi^* = 1.027-1.054$ are computed. The inlet conditions are linearly interpolated from the measured profiles.

domain	“box”
mesh, number of nodes	328'360
radial velocity distribution	“geometrical”
near wall velocity extrapolation	$f = 0.900$
inlet turbulent dissipation	$L_\epsilon = 0.001$
inlet turbulent kinetic energy	experimental profile
advection scheme	MLPS
turbulence model	$k - \epsilon$

Table 1.1: Computational parameters. See part V.

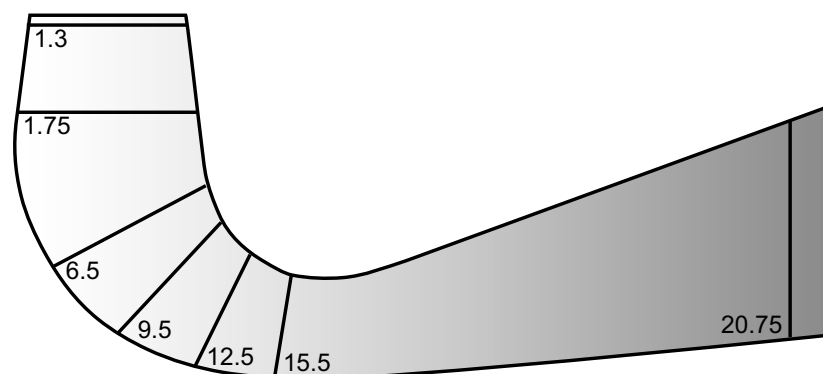


Figure 1.1: Measurement sections.

2

Comparison with experimental data

No one believes the CFD results except the one who performed the calculation, and everyone believes the experimental results except the one who performed the experiment.

(saying in the aerodynamics community, quoted in [Roa98]).

The velocity and pressure profiles in sections 1.75 and 15.5 and the wall pressure measurements were carried out by Jorge Arpe. Gabriel Ciocan obtained the two-dimensional velocity field in sections 20.75 and the wall friction at three positions in the cone.

2.1 Recovery factor

The recovery factor is compared with the measurements in fig. 2.1. The overall agreement is fairly good. The pressure recovery drop takes place at the same flow rate which is observed experimentally. However, the computations overestimate the recovery factor over the whole range, with a maximal difference of 14% of the measured value. Near the best efficiency conditions the maximal difference is 6%.

2.2 Velocity and pressure profiles, sections 1.75 and 15.5

The velocity and pressure profiles acquired with the five-sensor steady probe on 16 measurement axes on sections 1.75 and 15.5 are compared with the computations for three operating conditions in fig. 2.2, 2.3 and 2.4. On the whole the flow is fairly well predicted. Locally important differences occur for all velocity components. Despite the short distance from the inlet, at the section 1.75 for the operating point at higher swirl corresponding to $\varphi^* = 0.919$, the maximum velocity difference reaches $.5C_o$. The averaged difference value is $.1C_o$. This is explained by the known difficulties of the $k - \epsilon$ model to correctly simulate swirling flows as already observed in (III.3). Just upstream the pier

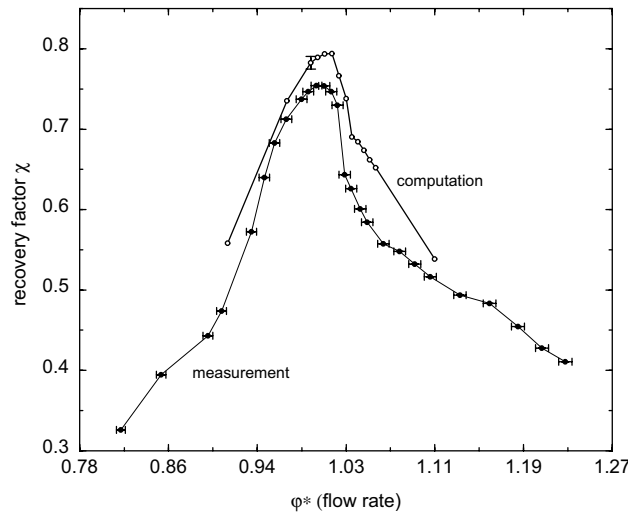


Figure 2.1: Static pressure recovery. Comparison measurement computation. The GCI (V.3) is reported for $\varphi^* = 0.994$.

on section 15.5, the averaged difference values range from $.1$ to $.3C_o$ and the maximum difference is $.5C_o$. The reference pressure corresponds to the value at the outlet ring manifold (IV.3.2).

2.3 Wall pressure, sections 1.3, 1.75, 6.5, 9.5, 12.5

The wall static pressure is compared at six sections in fig. 2.5 for three operating conditions. The global agreement is fairly good. Locally the differences reach 80% of the measured value. The computations clearly overestimate the bend influence at the section 1.75, but the differences decrease in the following sections.

2.4 Velocity field, sections 20.75

Two velocity components acquired with the LDA system at 950 points on sections 20.75 are compared with the computations in fig. 2.6 and 2.7. The estimated flow rate distribution in the two channels is listed in table 2.1. Better agreement is observed for the extreme points. The central points are less satisfactory, probably due to rapid flow changes occurring in this region.

2.5 Wall shear stress in the cone

The obtained values are clearly underestimated as well as the influence of the divergent geometry (position 1 and 2), while the influence of the bend (position 1 and 3) is correctly resolved. As discussed in (VI.6) the near wall velocity

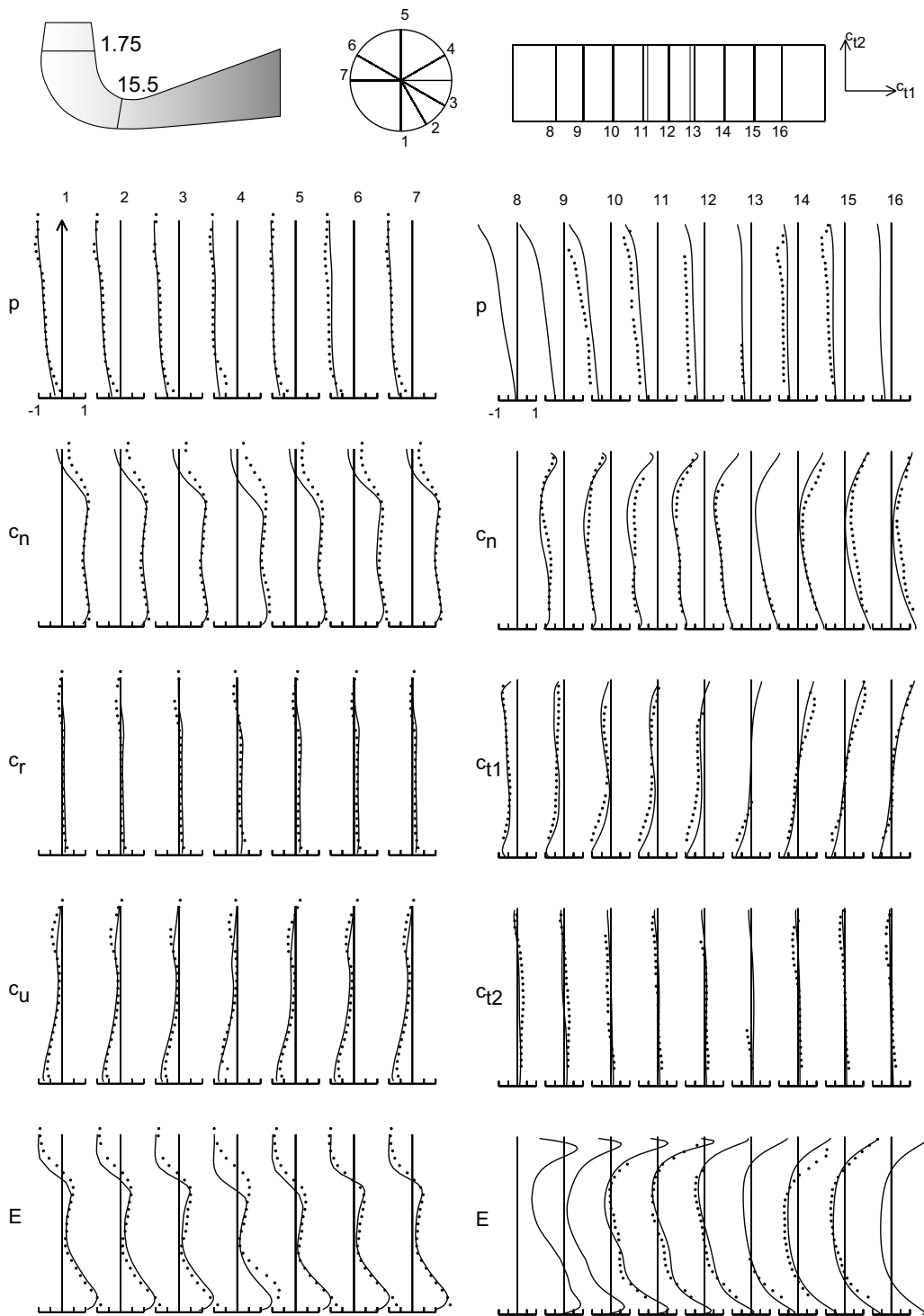


Figure 2.2: Sections 1.75 (left) and 15.5 (right), $\varphi^* = 0.919$: comparisons measurements (points) - computations (line). Section 1.75: from the wall to the center, section 15.5: from the upper wall to the bottom. p : static pressure, c_n : normal velocity component, c_r : radial velocity component, c_u , c_{t1} , c_{t2} : tangential velocity component, $E = p + 1/2\rho c^2$: total pressure. The velocity is divided by the mean normal velocity C_o of the investigated section and the pressure by $1/2\rho C_o^2$. The reference pressure corresponds to the value at the outlet ring manifold (IV.3.2).

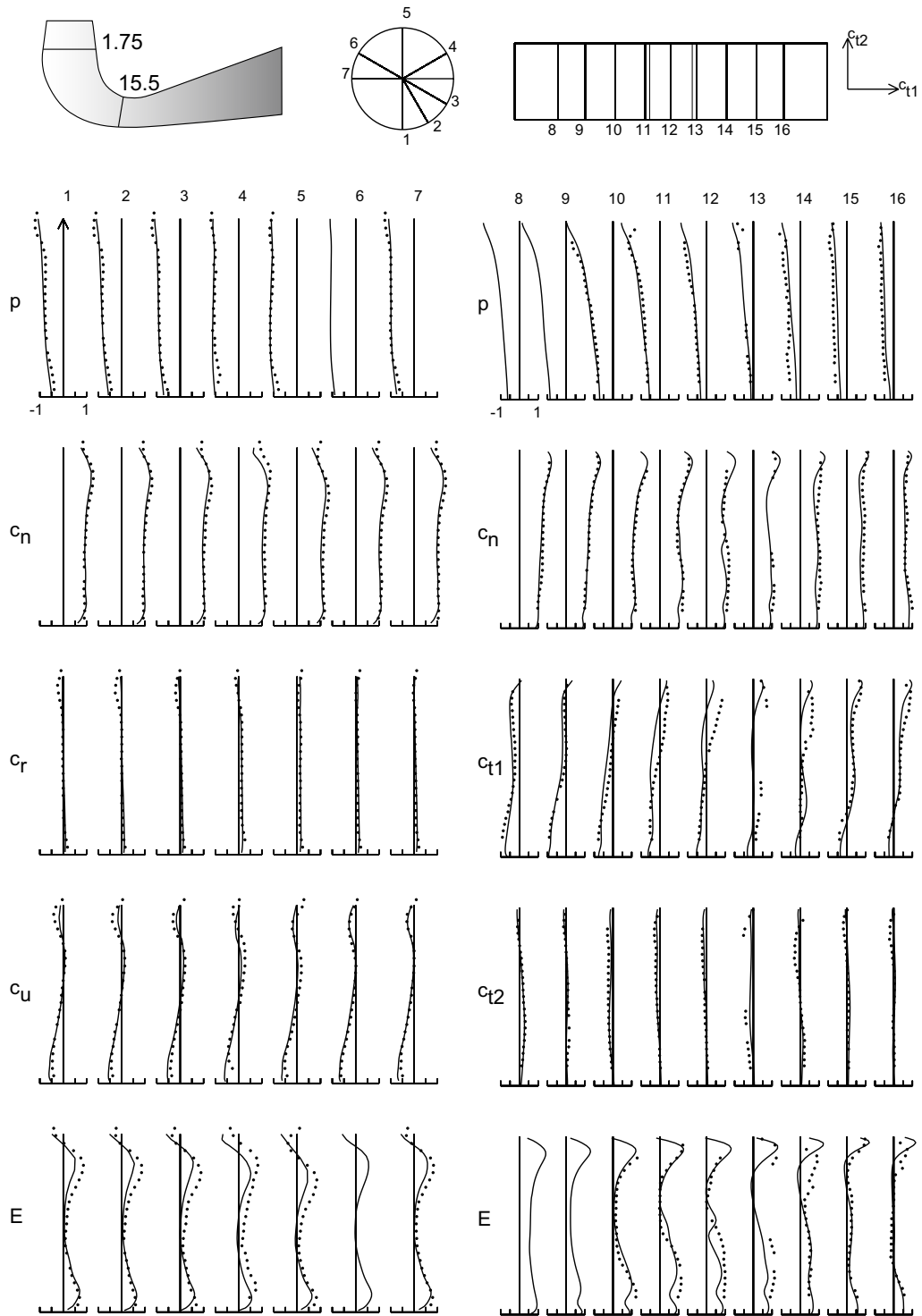


Figure 2.3: Sections 1.75 (left) and 15.5 (right), $\varphi^* = 0.994$: comparisons measurements (points) - computations (line). Section 1.75: from the wall to the center, section 15.5: from the upper wall to the bottom. p : static pressure, c_n : normal velocity component, c_r : radial velocity component, c_u , c_{t1} , c_{t2} : tangential velocity component, $E = p + 1/2\rho c^2$: total pressure. The velocity is divided by the mean normal velocity C_o of the investigated section and the pressure by $1/2\rho C_o^2$. The reference pressure corresponds to the value at the outlet ring manifold (IV.3.2).

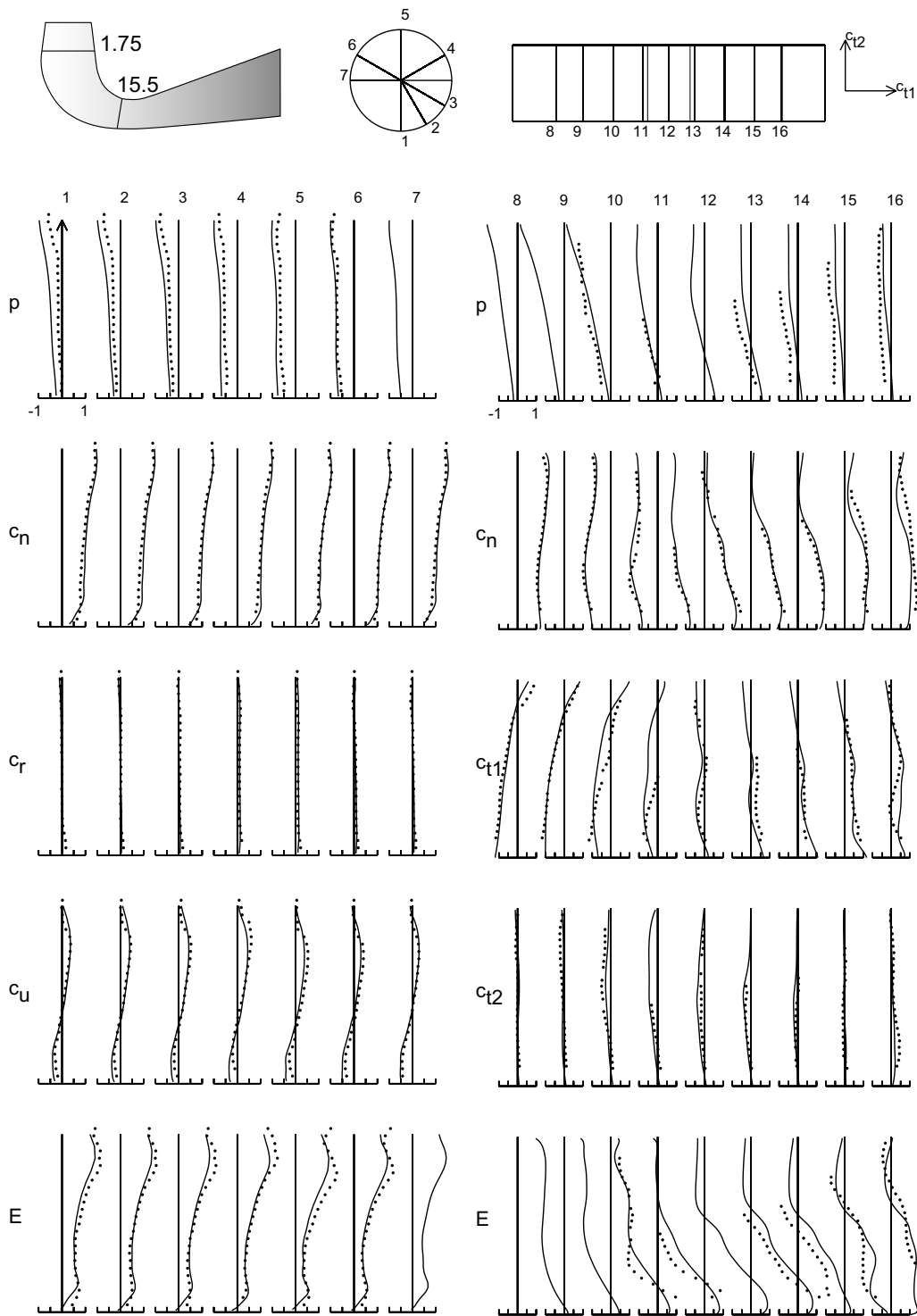


Figure 2.4: Sections 1.75 (left) and 15.5 (right), $\varphi^* = 1.108$: comparisons measurements (points) - computations (line). Section 1.75: from the wall to the center, section 15.5: from the upper wall to the bottom. p : static pressure, c_n : normal velocity component, c_r : radial velocity component, c_u , c_{t1} , c_{t2} : tangential velocity component, $E = p + 1/2\rho c^2$: total pressure. The velocity is divided by the mean normal velocity C_o of the investigated section and the pressure by $1/2\rho C_o^2$. The reference pressure corresponds to the value at the outlet ring manifold (IV.3.2).

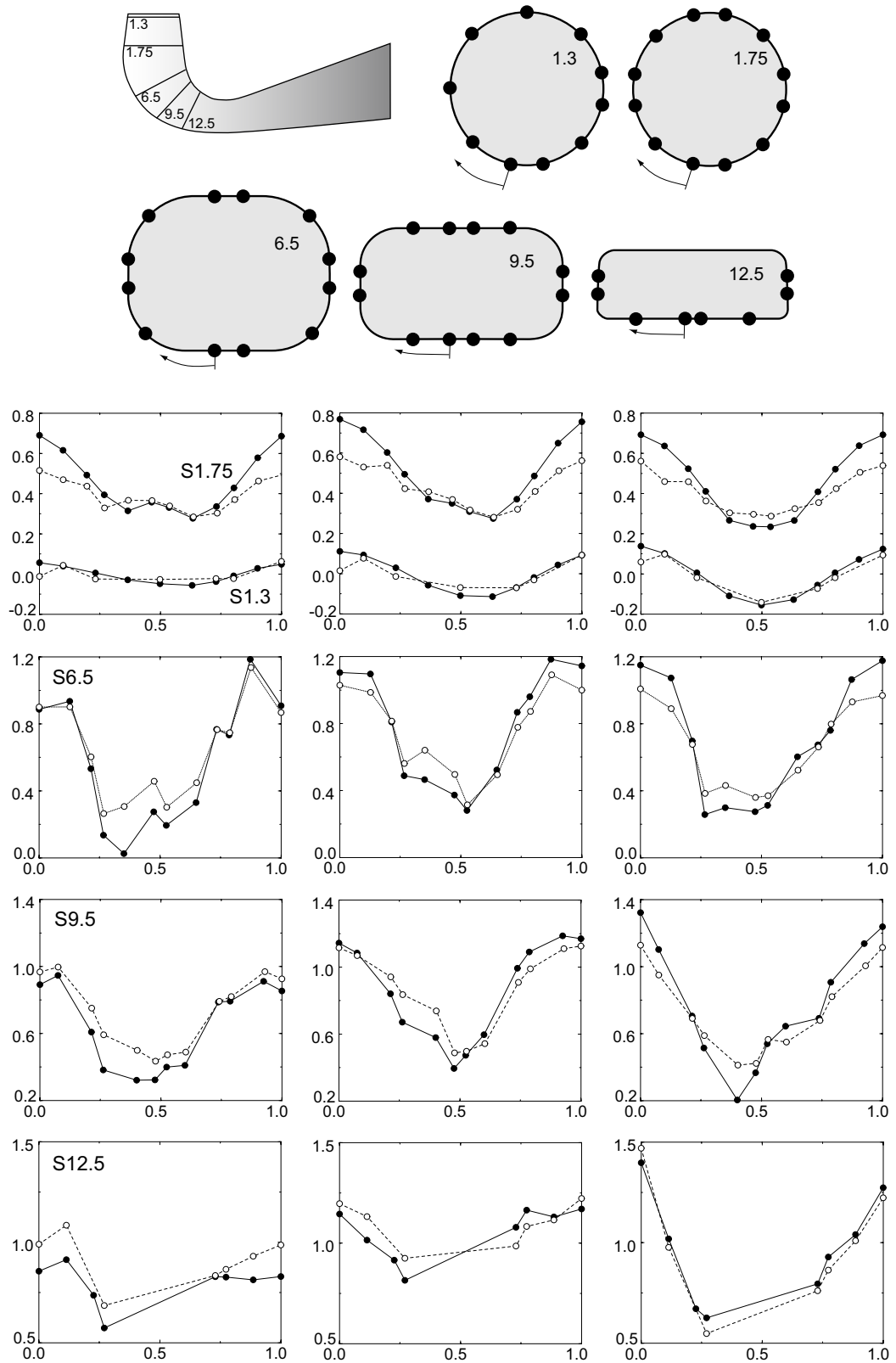


Figure 2.5: Wall static pressure, sections 1.3, 1.75, 6.5, 9.5, 12.5. $\varphi^* = 0.919$, $\varphi^* = 0.994$, $\varphi^* = 1.108$ (from the left to the right). The pressure values are divided by the mean value on section 1.3 and the reference is set at the same section. Solid line: computation, dotted lines: experiments.

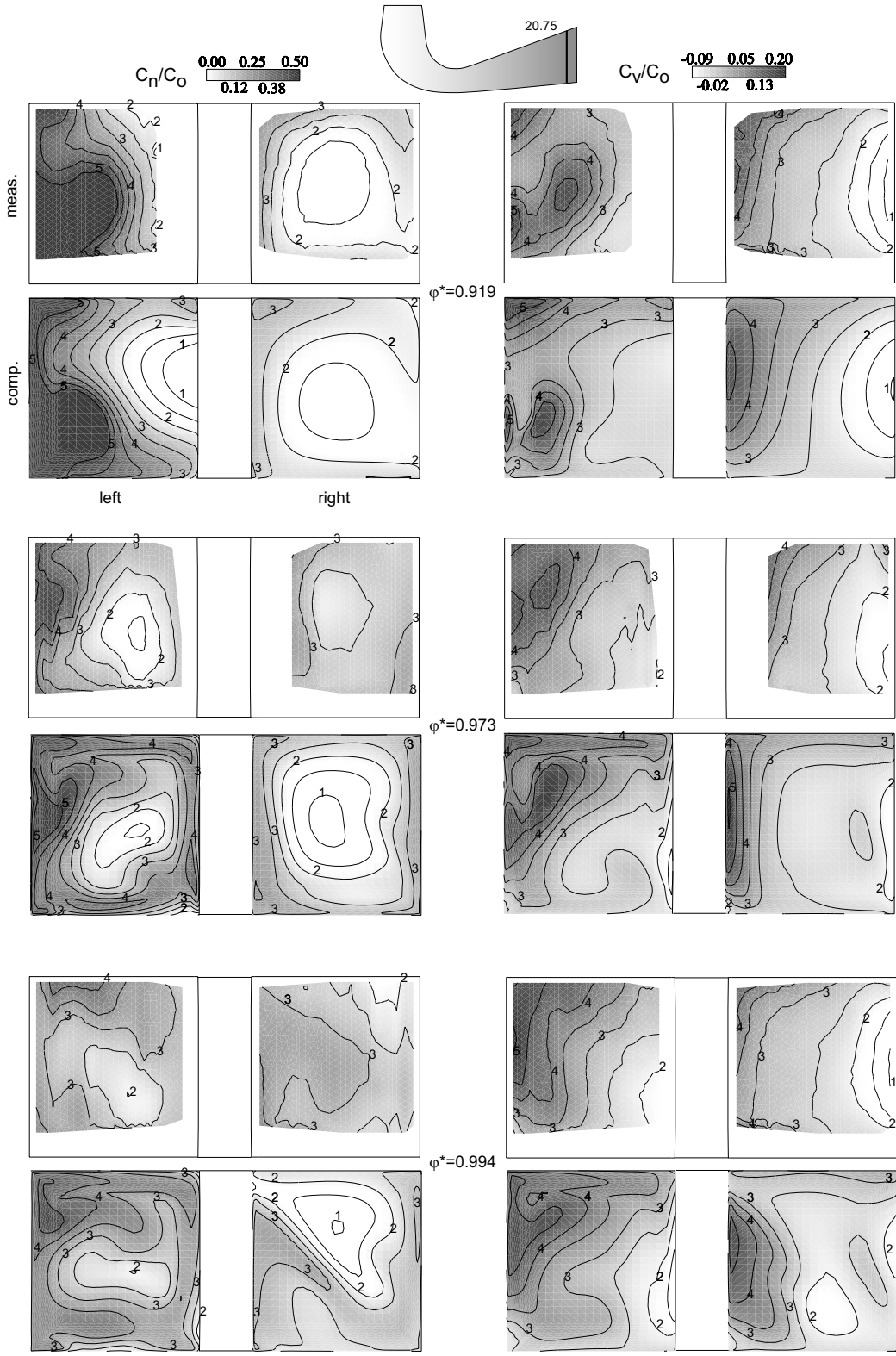


Figure 2.6: Outlet velocity field, comparisons with measurement. $\varphi^* = 0.919$, $\varphi^* = 0.973$, $\varphi^* = 0.994$.

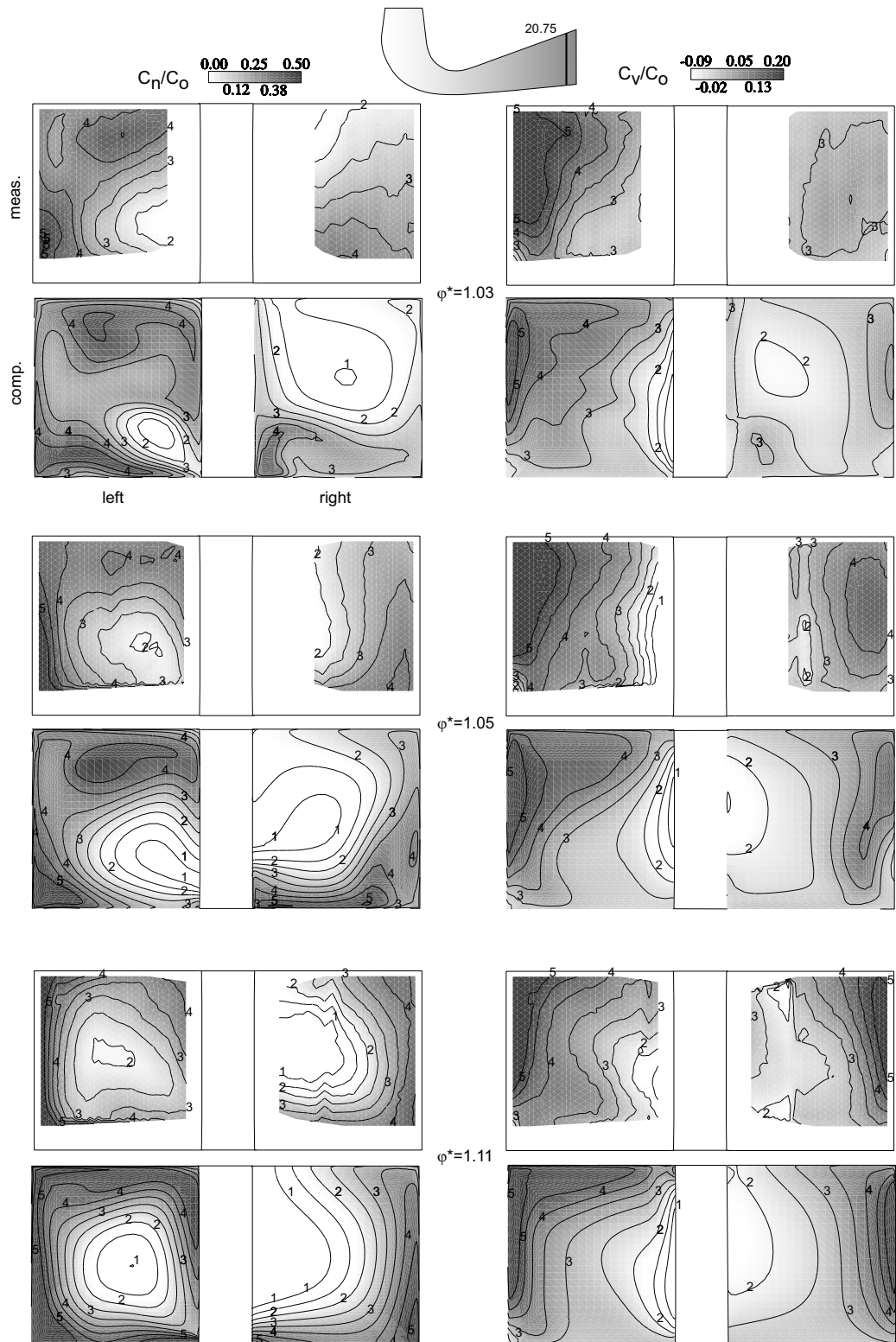


Figure 2.7: Outlet velocity field, comparisons with measurement. $\varphi^* = 1.027$, $\varphi^* = 1.054$, $\varphi^* = 1.108$.

operating point	measurement	computation
$\varphi^* = 0.919$	73%	72%
$\varphi^* = 0.973$	57%	66%
$\varphi^* = 0.994$	51%	63%
$\varphi^* = 1.027$	64%	68%
$\varphi^* = 1.054$	63%	62%
$\varphi^* = 1.108$	62%	66%

Table 2.1: Flow rate on the left channel. Note that only less than three quarters of the total rate flows through the measured sections. The experimental value is therefore only indicative.

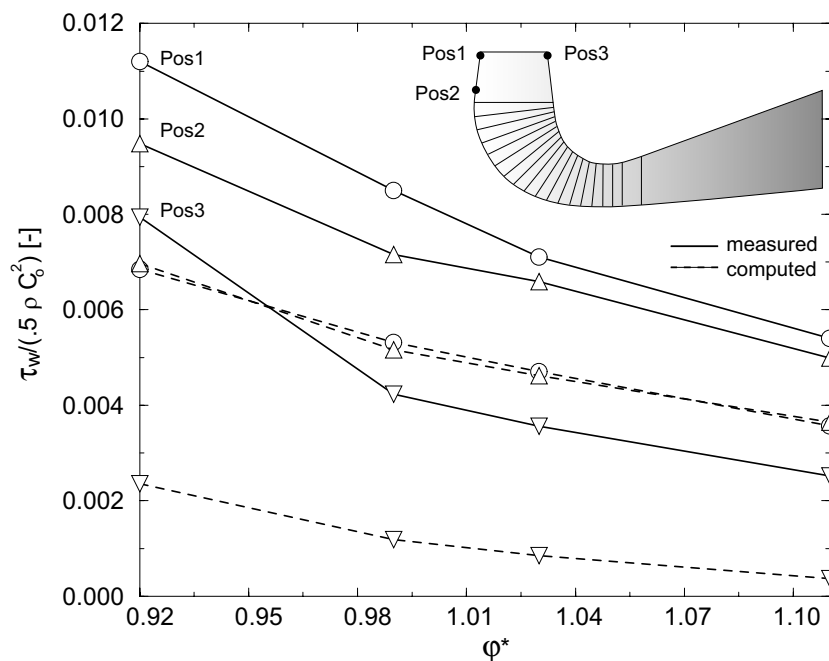


Figure 2.8: Wall friction. Comparison with measurements.

gradient in the cone plays an important role on the overall draft tube efficiency. Best results are obtained with the steepest profiles of the tested set. The measured wall shear stresses indicate that the gradient is even higher. However, the experimental data should be viewed with some degree of reservation due to its preliminary nature.

2.6 Summary

While the main flow features are well captured for all the investigated operating conditions, locally important differences between the numerical and measured flow field are observed. The model is not able to describe the fine details.

3

Flow analysis: flow rate and specific energy balance

The flow rate and the specific energy evolution (see Nomenclature, IX) at three operating points are compared in fig. 3.1. The domain is split into two symmetrical parts allowing a comparison between the left and the right channel, even upstream at the pier's leading edge. The main static pressure recovery difference does take place in the bend. The flow rate distribution in the channels is shown in fig. 3.2. The specific static pressure energy recovery is summarized in fig. 3.3 over the whole computed operating range. As expected (I.2) most of the recovery occurs in the cone. An efficiency drop taking place in the second half of the bend is clearly visible in the range $\varphi^* = 1.021 - 1.049$. This deficiency is partially recovered in the last part. On the left side the pressure recovery drops due to a flow acceleration, while on the right channel the pressure recovery is very small in the straight diffuser, indicating an unfavorable flow situation. The two nearby computed operating points before the drop ($\varphi^* = 1.008 - 1.014$) do not show appreciable differences in the evolution of specific energies as shown in fig. 3.4. The first point in the recovery drop region differs considerably from the nearby points showing an important change in the flow rate distribution. The flow rate in the left side increases from 62% to 66%. An increase of the specific kinetic energy is also observed. The flow rate in the right channel starts again to increase between $\varphi^* = 1.0320 - 1.038$ (fig. 3.4).

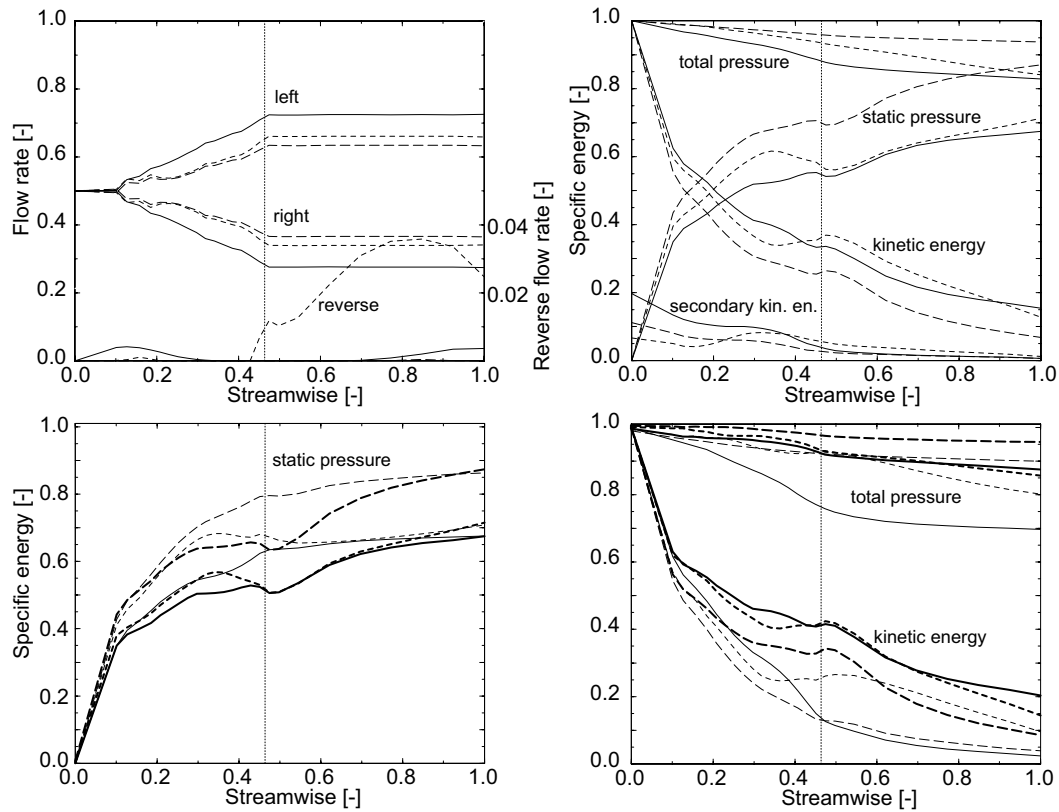


Figure 3.1: Top: flow rate and specific energies evolution. Bottom: left (thick line) - right (thin) side decomposition. Solid line: $\varphi^* = 0.919$, long dashed line: $\varphi^* = 0.994$, dashed line: $\varphi^* = 1.108$.

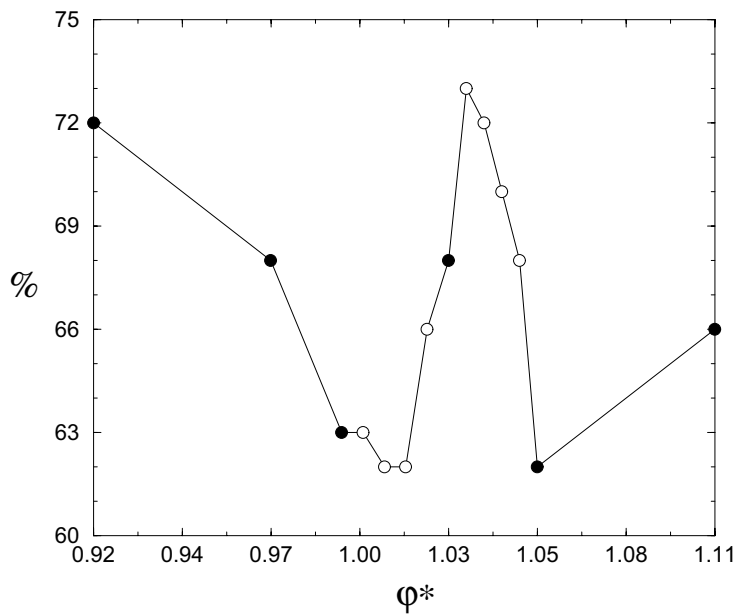


Figure 3.2: Flow rate distribution, left side percentage.

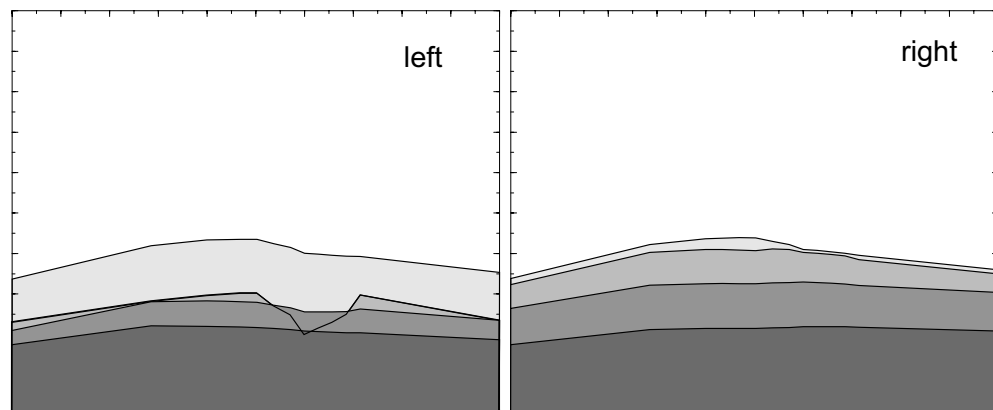
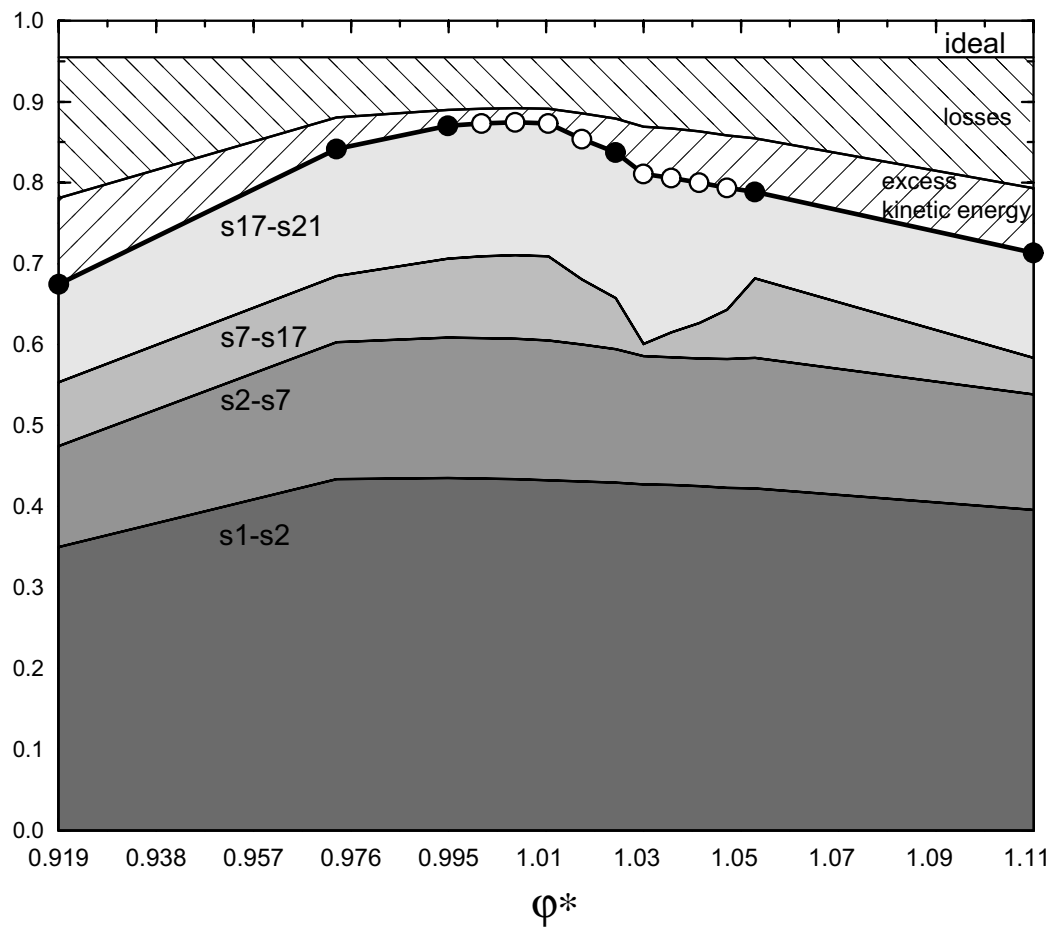


Figure 3.3: Specific static pressure recovery. The recovery occurring in the cone (s1-s2), first half of the bend (s2-s7), second half of the bend (s7-s17) and diffuser (s17-s21) and in the left- and right-side of the draft tube are put in evidence.

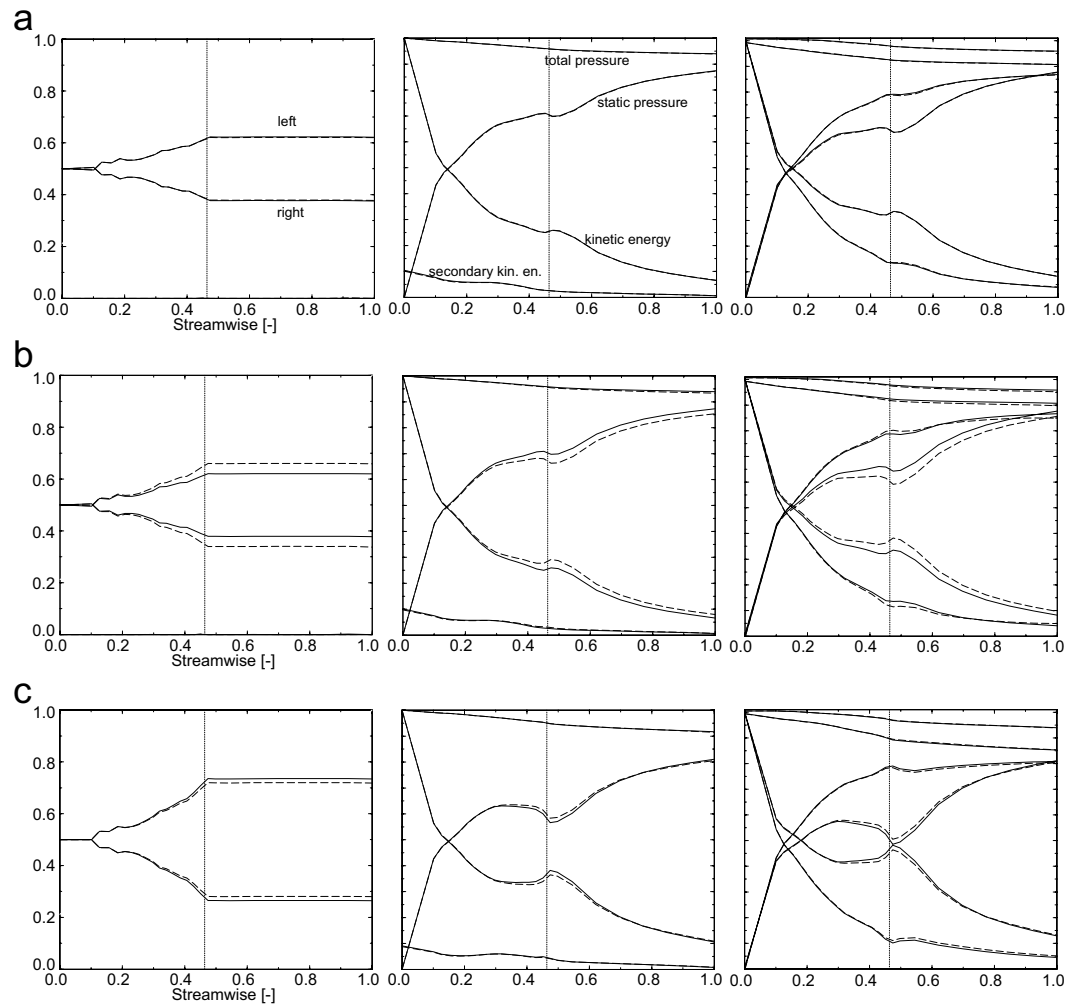


Figure 3.4: Flow rate, specific energies evolution and left (thick line) - right (thin) side decomposition: a) solid line: $\varphi^* = 1.008$, dashed line: $\varphi^* = 1.014$ (before the drop, best efficiency), b) solid line: $\varphi^* = 1.014$, dashed line: $\varphi^* = 1.021$ (begin of the drop), c) solid line: $\varphi^* = 1.0320$, dashed line: $\varphi^* = 1.0380$ (minimum of the drop).

4

Flow analysis: velocity field

For the central and the extreme points ($\varphi^* = 0.994$, $\varphi^* = 0.919$ and $\varphi^* = 1.108$) the skin friction lines and the tangential streamlines on several cross-sections, are shown in fig. 4.1 to 4.6. The pictures reveal a change of the flow direction in the channels due to the increase of the secondary flow introduced by the bend when the flow rate is increased and due to the change of the rotation direction at the inlet (IV.3.2). While at $\varphi^* = 0.919$ the inlet swirl forms a vortex that develops in the right channel and reaches the outlet (fig. 4.7), for the other points the vortex core is only detectable in the inlet region. The vortex core lines are extracted from the flow data using the eigenvector method of Sujudi and Haines [SH95]. The algorithm looks for the points in the velocity field where a single real eigenvector exists and this is parallel to the velocity vector. The technique is based on decomposing finite elements into tetrahedrons and then solving closed-form equations to determine the velocity gradient tensor values at the nodes. Due to the linear implementation, the algorithm has problems finding cores of curved vorticities. A review of vortex visualization methods can be found in [Rot00]. Due to the change of the rotation direction in the central region at the inlet for the higher flow rates, the vortex core moves in the opposite direction as at $\varphi^* = 0.919$. The centrifugal effect introduced by the increase of the flow rate is evident in the mid-plane section shown in fig. 4.8. The consequent separation at the upper wall forms an U-shaped vortex (fig. 4.9).

4.1 Topology evolution

4.1.1 Introduction

The efficiency drop (VI.3) is hereafter explained by putting in evidence the topological changes in the flow with the flow rate as parameter. The framework introduced in Tobak & Peake [TP82] is adopted to describe a three-dimensional separated flow region in the draft tube. Similar terminologies are discussed also in Hornung & Perry [HP84] and other references cited therein. The skin friction lines are considered as trajectories having the properties of a continuous vector field subjected to precise topological rules. Elementary singular (or critical) points of the field can be categorized mathematically. Critical points are

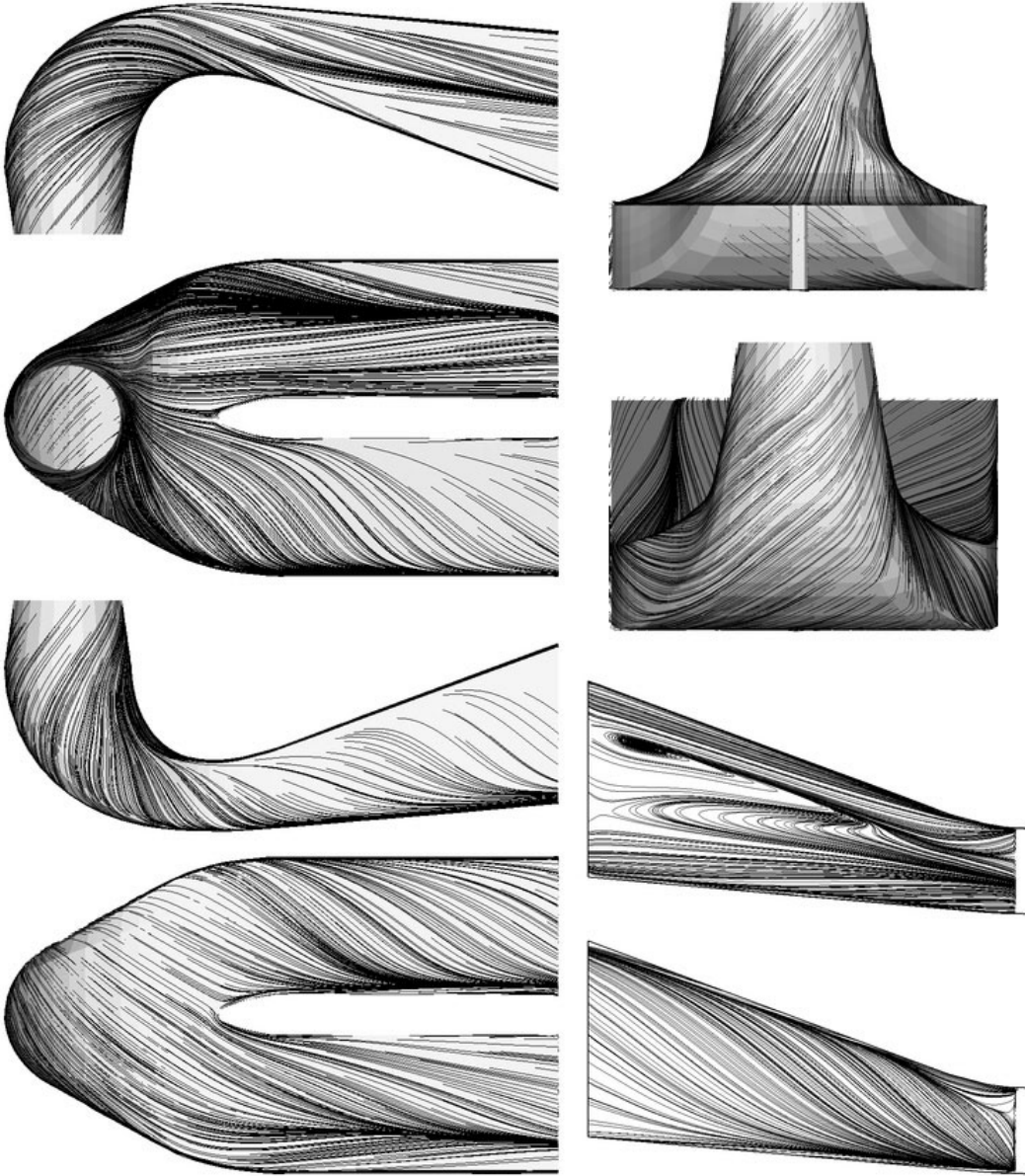


Figure 4.1: Skin friction lines, $\varphi^* = 0.919$.

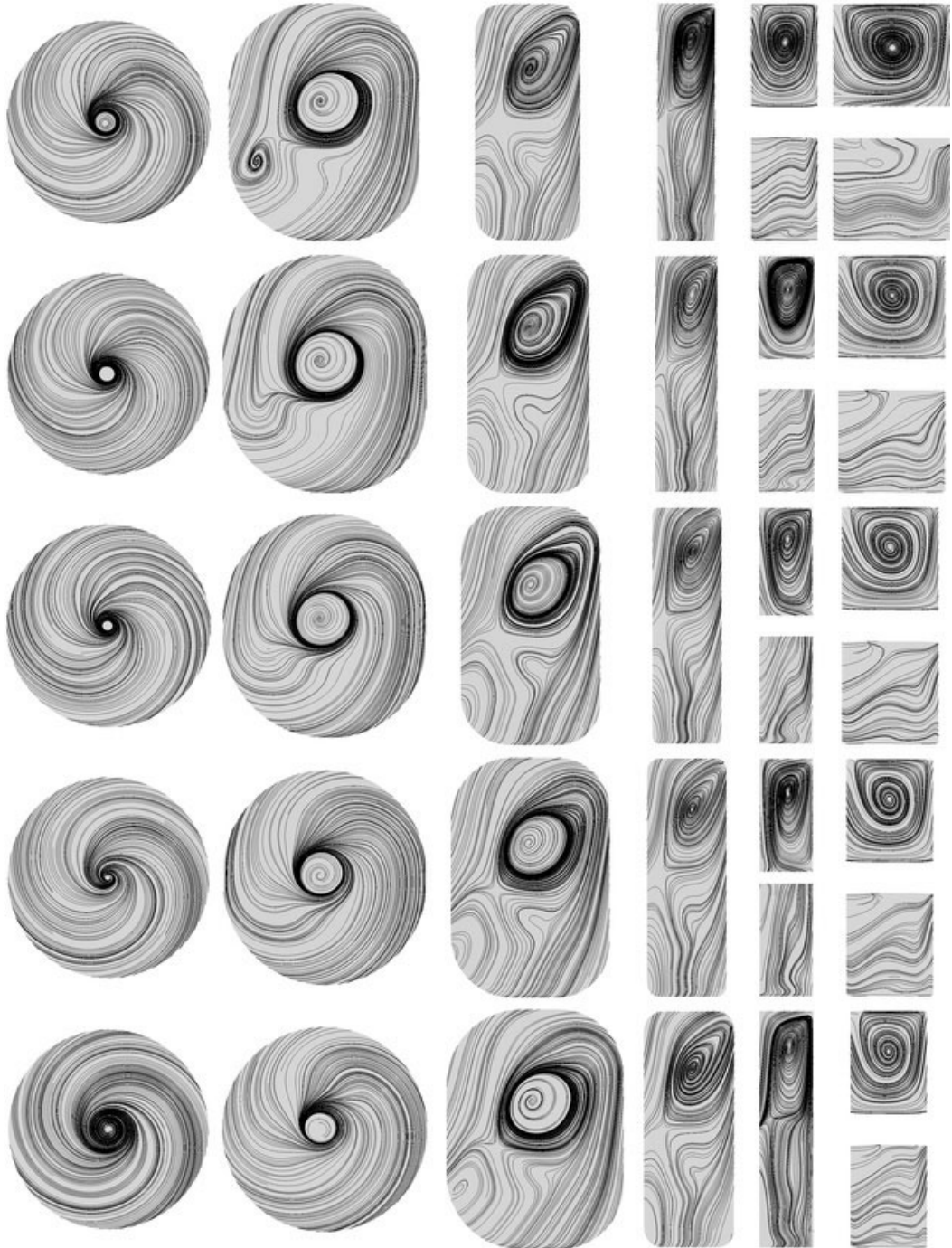


Figure 4.2: Tangential streamlines on cross-sections from the inlet to the outlet, $\varphi^* = 0.919$.

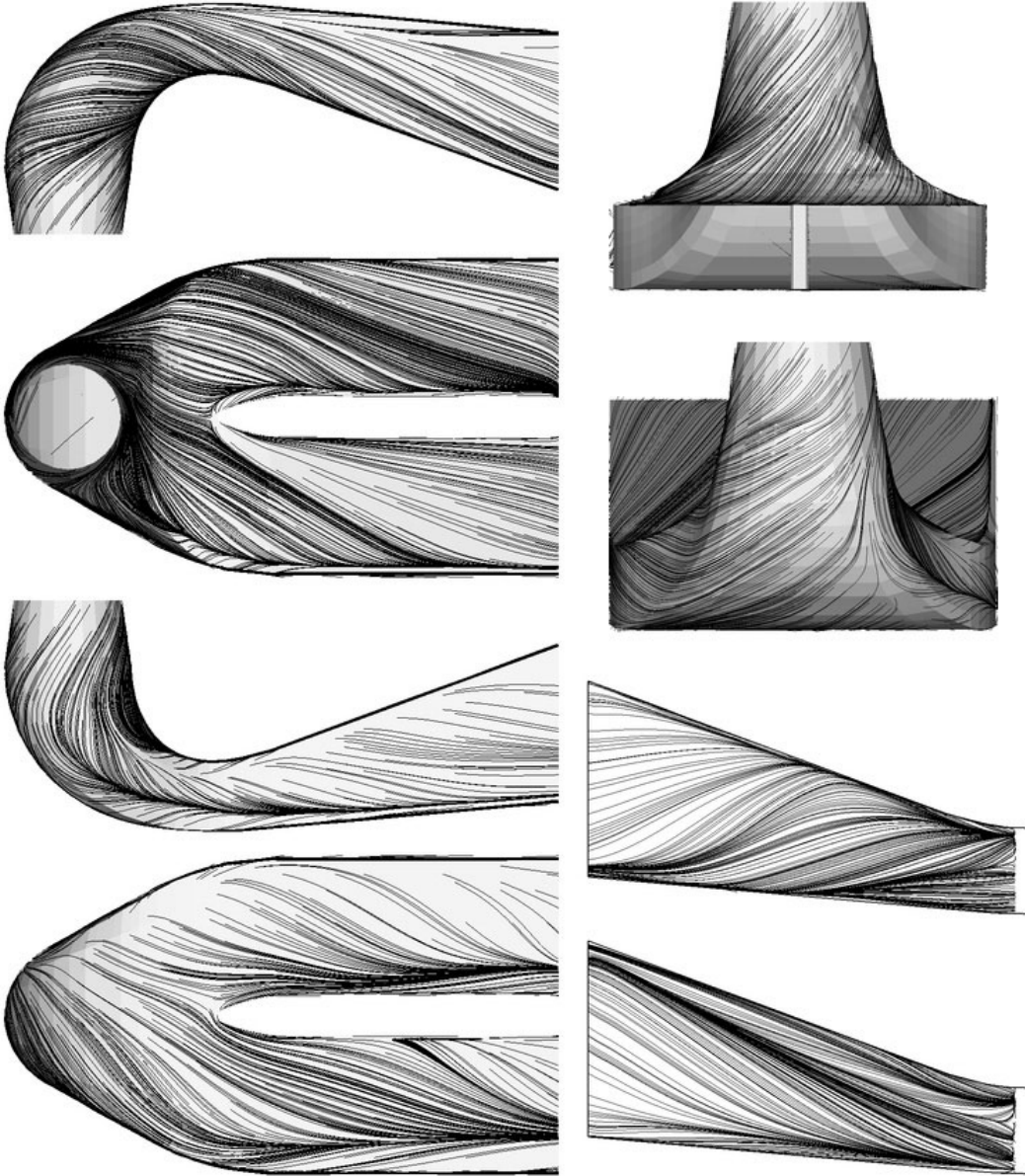


Figure 4.3: Skin friction lines, $\varphi^* = 0.994$.

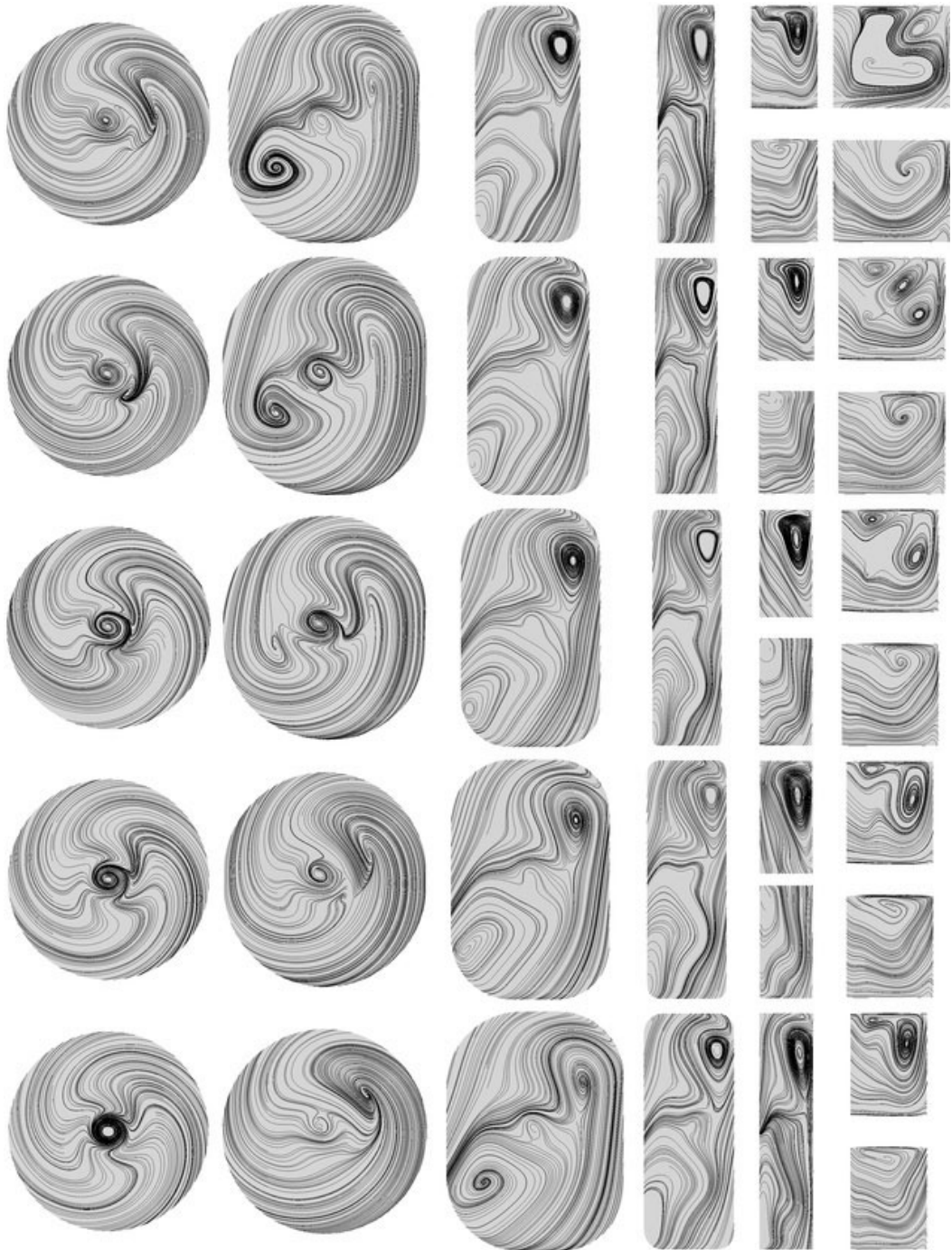


Figure 4.4: Tangential streamlines on cross-sections from the inlet to the outlet, $\varphi^* = 0.994$.

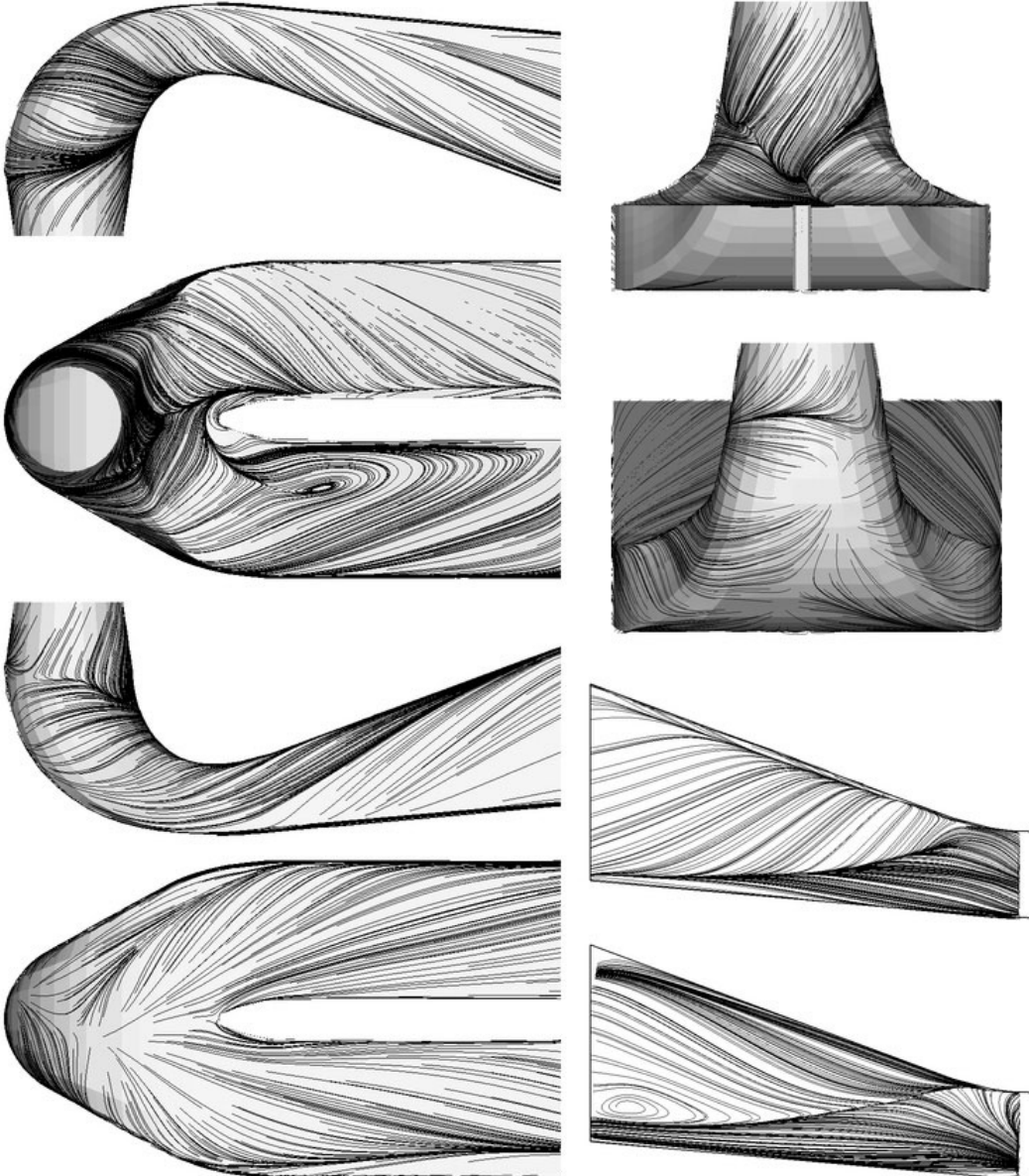


Figure 4.5: Skin friction lines, $\varphi^* = 1.108$.

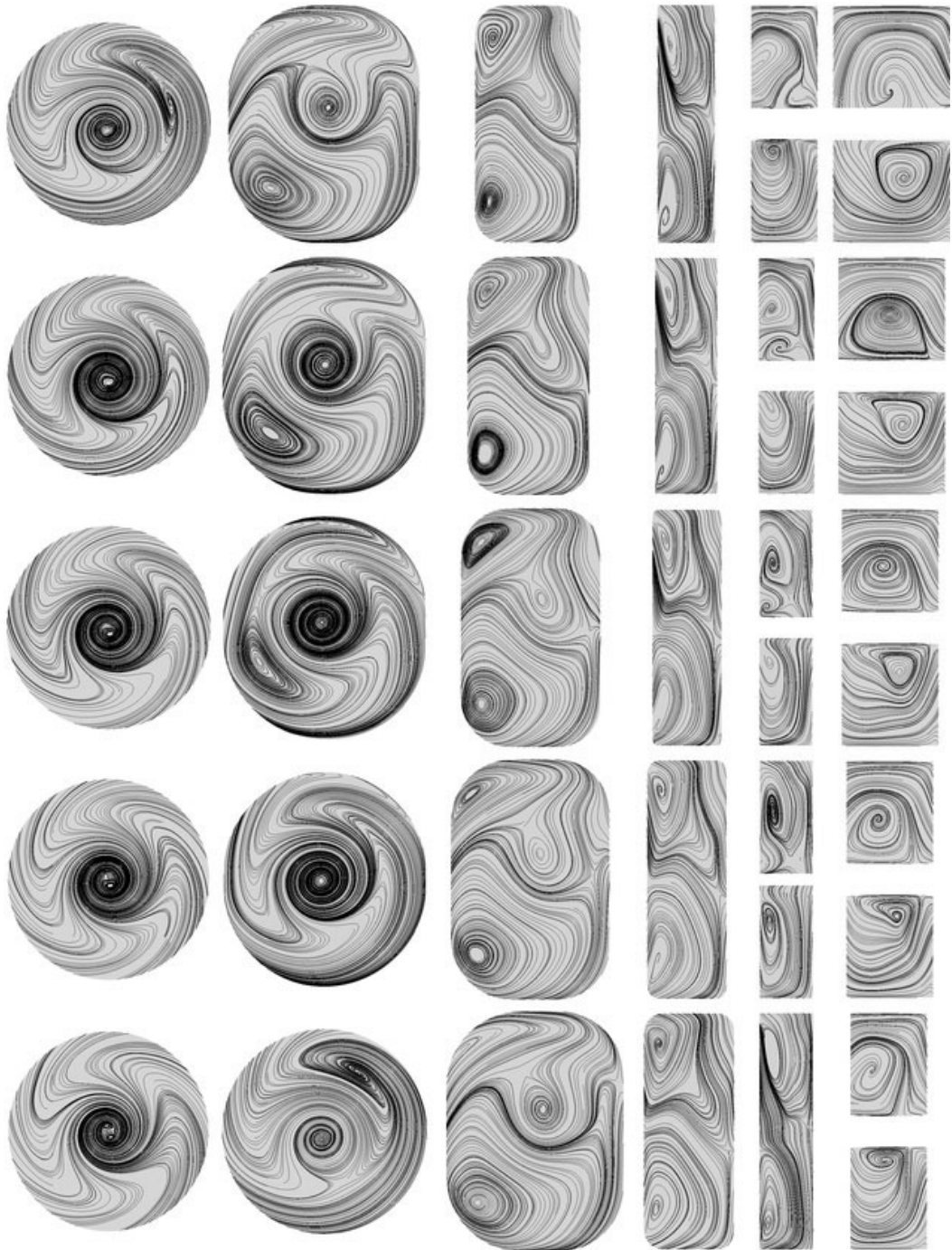


Figure 4.6: Tangential streamlines on cross-sections from the inlet to the outlet, $\varphi^* = 1.108$.

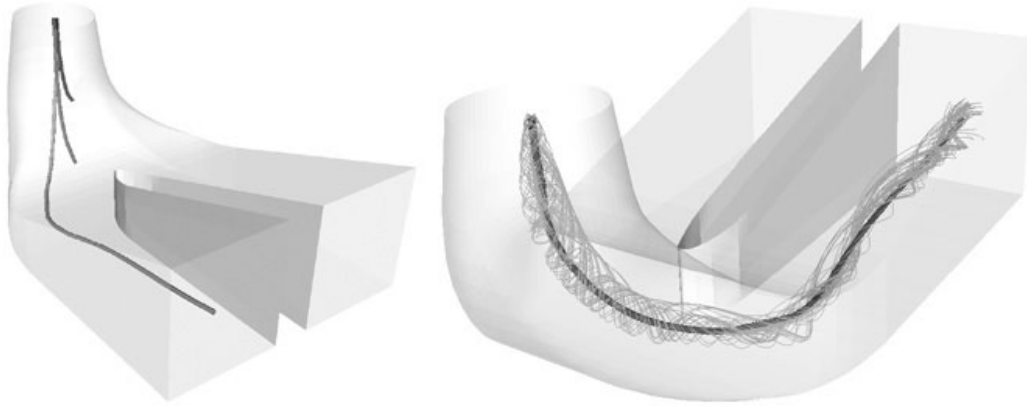


Figure 4.7: Central vortex cores identified with the eigenvector method of Sujudi and Haines [SH95]: a) $\varphi^* = 0.919$ (light), $\varphi^* = 0.994$, $\varphi^* = 1.108$ (dark), b) surrounding streamlines, $\varphi^* = 0.919$.

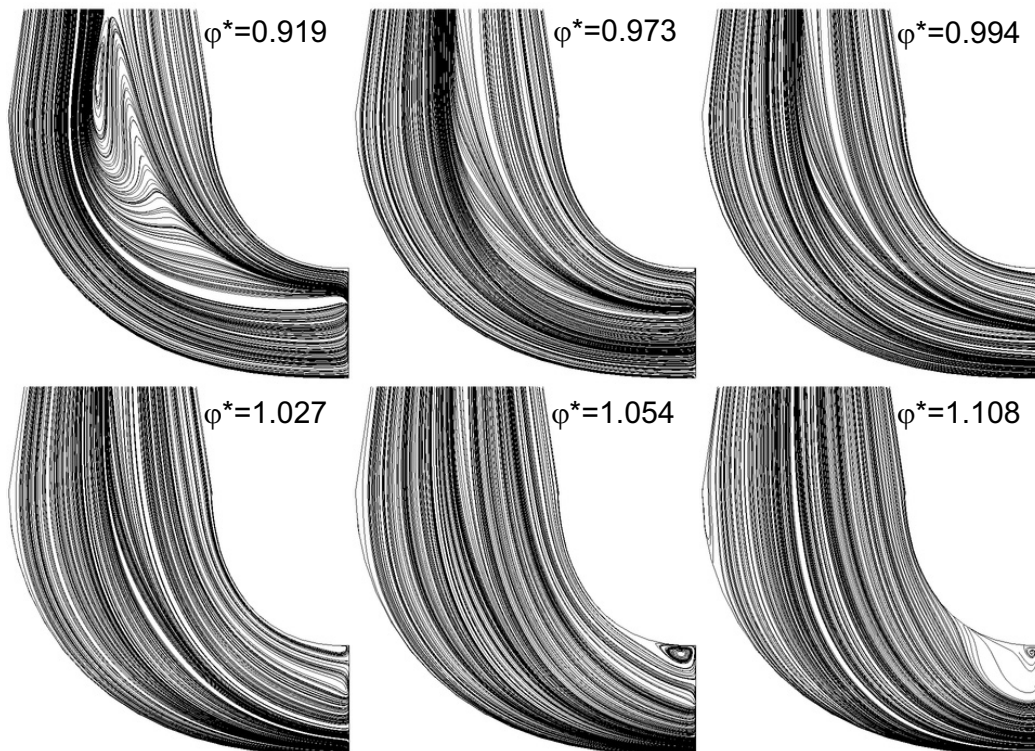


Figure 4.8: Tangential streamlines at the symmetry mid-plane, cone and bend.

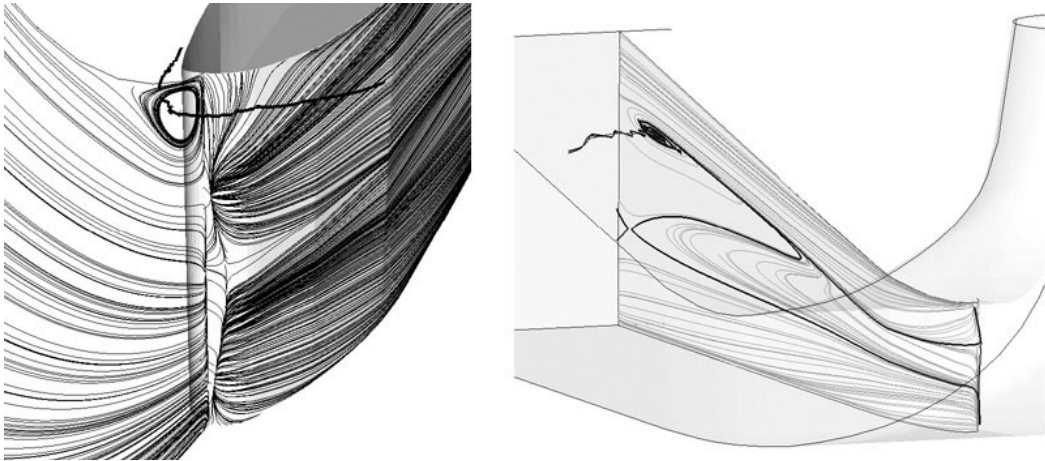


Figure 4.9: Examples of flow separation and vortex generation: a) $\varphi^* = 1.054$. U-shaped vortex at the upper side of the pier, b) $\varphi^* = 0.919$. Left side of the pier.

points in the flow field where the streamline slope is indeterminate and the velocity is zero relative to an appropriate observer. Asymptotically exact solutions of the Navier-Stokes equations can be derived close to the critical points, and these give a number of flow patterns (see Perry & Chong [PC87]). Two patterns are said to be topologically equivalent if a stretching process can distort them into one another. If the topology of a critical point is changed by an infinitesimal change in any of the relevant flow parameters, this point is said to be structurally unstable. The flow is called structurally stable relative to a parameter if a change in the parameter does not alter the topological structure. An instability is called global if it permanently alters the topological structure of the velocity field. A global instability results in the emergence of a saddle point in the surface pattern. The flow patterns at the wall are investigated and particular attention is focused on separation (or bifurcation) lines. These are lines drawn in the flow toward which other trajectories are asymptotic. A universal definition of separation in a three-dimensional flow is still subject of debate. The specification of separation by means of a reverse flow or vanishing wall shear stress is usually inadequate in three-dimensional flows. A necessary condition for the occurrence of flow separation is the convergence of skin friction lines (or wall streamlines, or limiting streamlines) onto a separation line. The regions of flow separation are important because of the reduced kinetic energy and the consequent blockage effect that they can introduce. Following the Tobak & Peake's terminology the separation line emerging from a saddle point is a global line of separation and leads to global flow separation. When the separation line does not originate from a saddle point, the line is called a local line of separation and leads to local flow separation. A global instability leads to flow bifurcation. At supercritical bifurcation, as a relevant parameter is increased just beyond the critical value, the flow adopts a new stable form. The bifurcation flow breaks the symmetry of the precedent flow, adopting a form of lesser symmetry in which dissipative structures arise to absorb just the

amount of excess available energy that the more symmetrical flow no longer was able to absorb. A particular global form of separation is marked by the onset on the surface of a focus in company with a saddle point. One leg of the line of separation emanating from the saddle point winds into the focus to form the curve on the surface from which the dividing surface stems. The focus on the wall extends into the fluid as a concentrated vortex filament, while the surface rolls up around the filament. This flow behaviour was first hypothesized by Legendre in 1965 and confirmed by the experiments of Werlé (1962) and takes the name of Werlé-Legendre separation. The cooperation between these two scientists is described in [Dél01]. Kinematically possible combinations of elementary structures of flow patterns on the surface and in the interior domain (plane of flow symmetry) can be found in Dallmann's article in [JOe85].

4.1.2 Flow stability

The main flow characteristics are summarized in fig. 4.10 where the aforementioned change of the flow direction in the channels due to the increase of the secondary flow introduced by the bend and to the change of the rotation direction at the inlet, is put in evidence by the main separation lines. The three operating points before the efficiency drop show local separation lines without any critical point at the surface. After the drop the flow stemming from the cone region situated exterior side of the bend curvature, is forced by the secondary flow to the inner side, while the flow angle imposed by the blades geometry remains constant for all operating points. The collision of these two flow directions leads to the onset on the surface of a focus and a saddle point leading to a global separation (see also fig. 4.11 and 4.12). The flow pattern in the inner domain can be seen in fig. 4.13, where the vortex core stemming from the focus and the tangential streamlines on two cross-sections are shown, and in fig. 4.14 illustrating section 12 (half bend). There is a practical difficulty to define the separation region delimited by the stream surface (dividing surface), originating from the line of separation. A simple separation region extraction algorithm is used to define a volume. Streamlines are started from the zone at the wall where separation occurs. A streamline is then equidistantly divided and from each point the intersection of the corresponding normal plane with all other streamlines is computed. From each group of points the mean point is calculated and used to define a new line and the procedure is repeated until the desired convergence is achieved. From each cloud of points, corresponding to the intersection of the normal plane of this mean line with all streamlines, the best fitting ellipse to the external points of the cloud is computed. The resulting tube with elliptic sections approximates the separation zone. The procedure is illustrated in fig. 4.15 and the vortex evolution in fig. 4.16. The vortex moves toward the center of the section and increases its size and strength until $\varphi^* = 1.032$, then begins to decay and at $\varphi^* = 1.054$ the focus changes into a node (fig. 4.12). The correlation with the flow rate distribution shown in fig. 3.2 and with the pressure recovery illustrated in fig. 3.3 is evident.

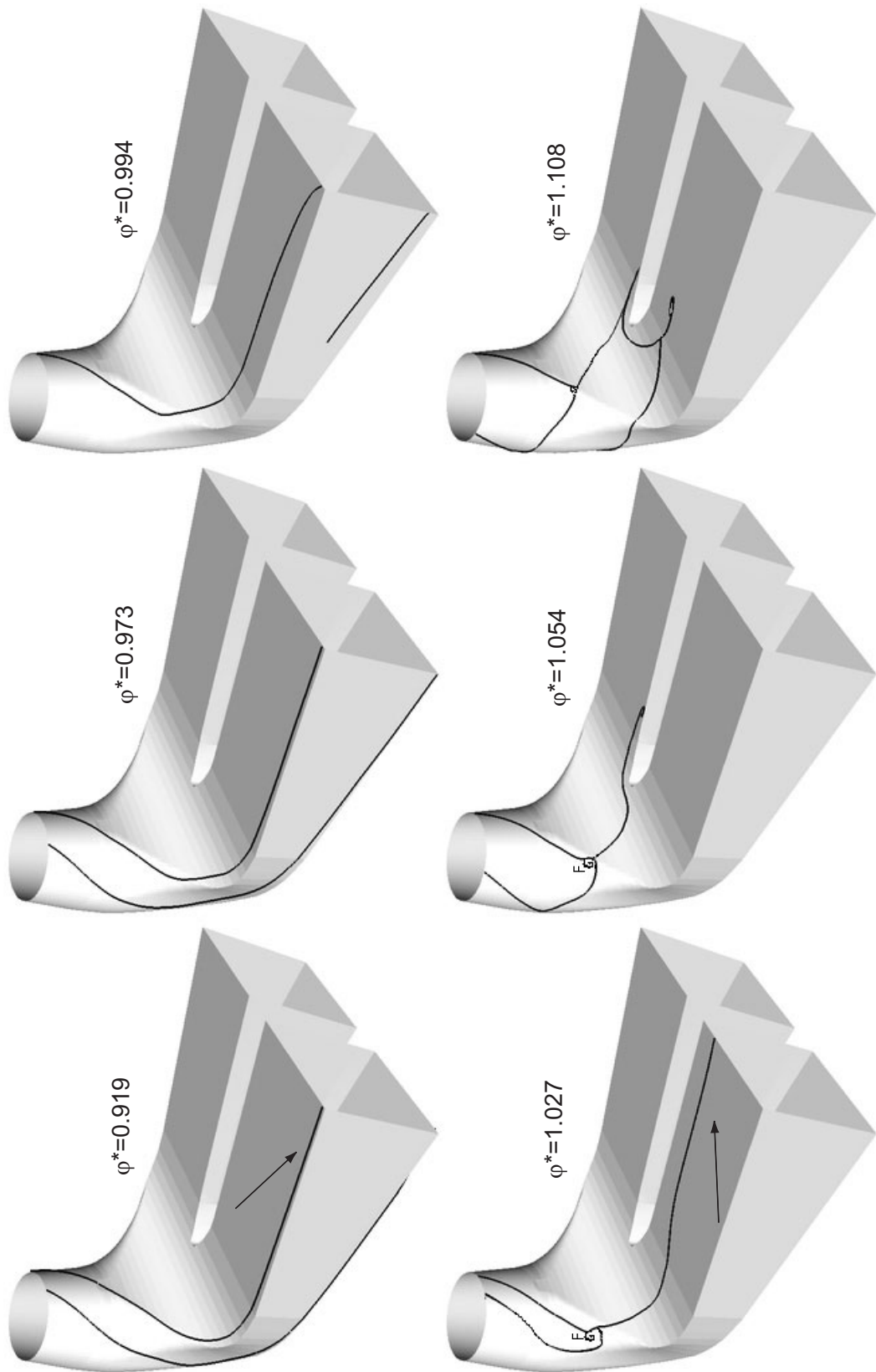


Figure 4.10: Flow topology, main separation lines and critical points. Onset on the surface of a focus in company with a saddle point. Before the efficiency drop: $\varphi^* = 0.919$, $\varphi^* = 0.973$, $\varphi^* = 0.994$, after: $\varphi^* = 1.027$, $\varphi^* = 1.054$, $\varphi^* = 1.108$.

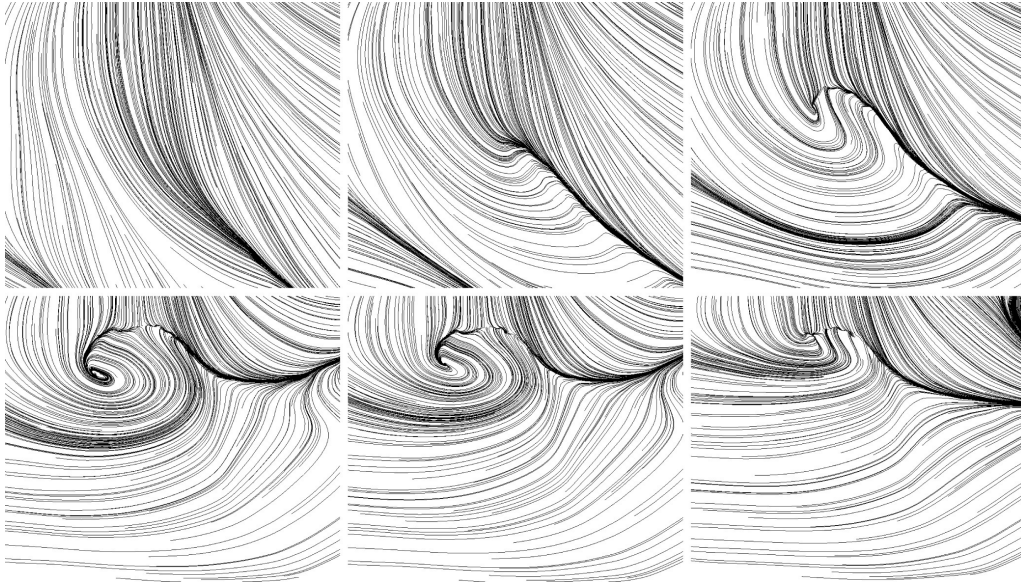


Figure 4.11: Skin friction lines, onset on the surface of a focus in company with a saddle point. Before the efficiency drop: $\varphi^* = 0.994$, $\varphi^* = 1.014$, after: $\varphi^* = 1.021$, $\varphi^* = 1.032$, $\varphi^* = 1.038$, $\varphi^* = 1.054$.

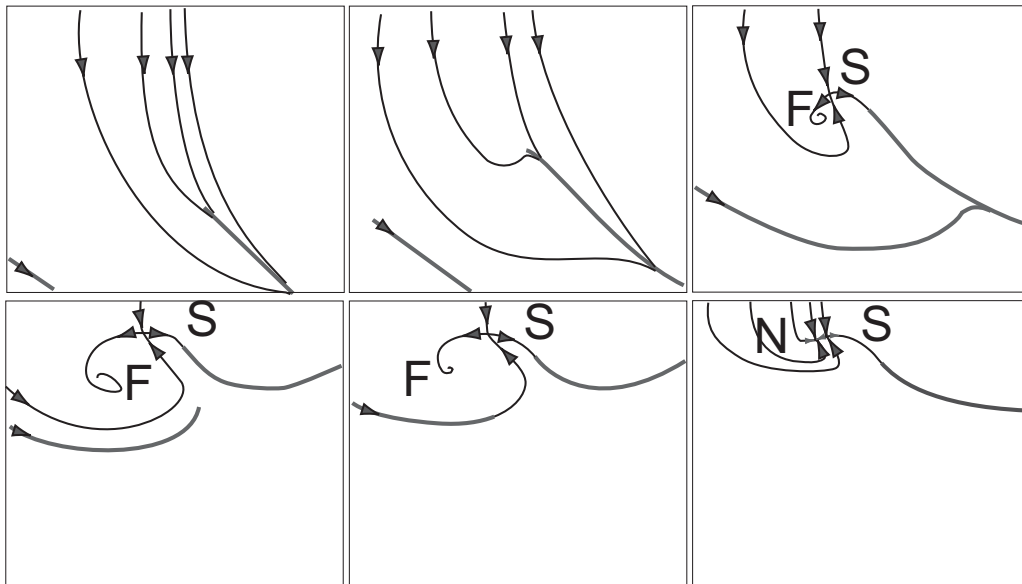


Figure 4.12: Interpretation of fig. 4.11. S: saddle, F: focus, N: Node.

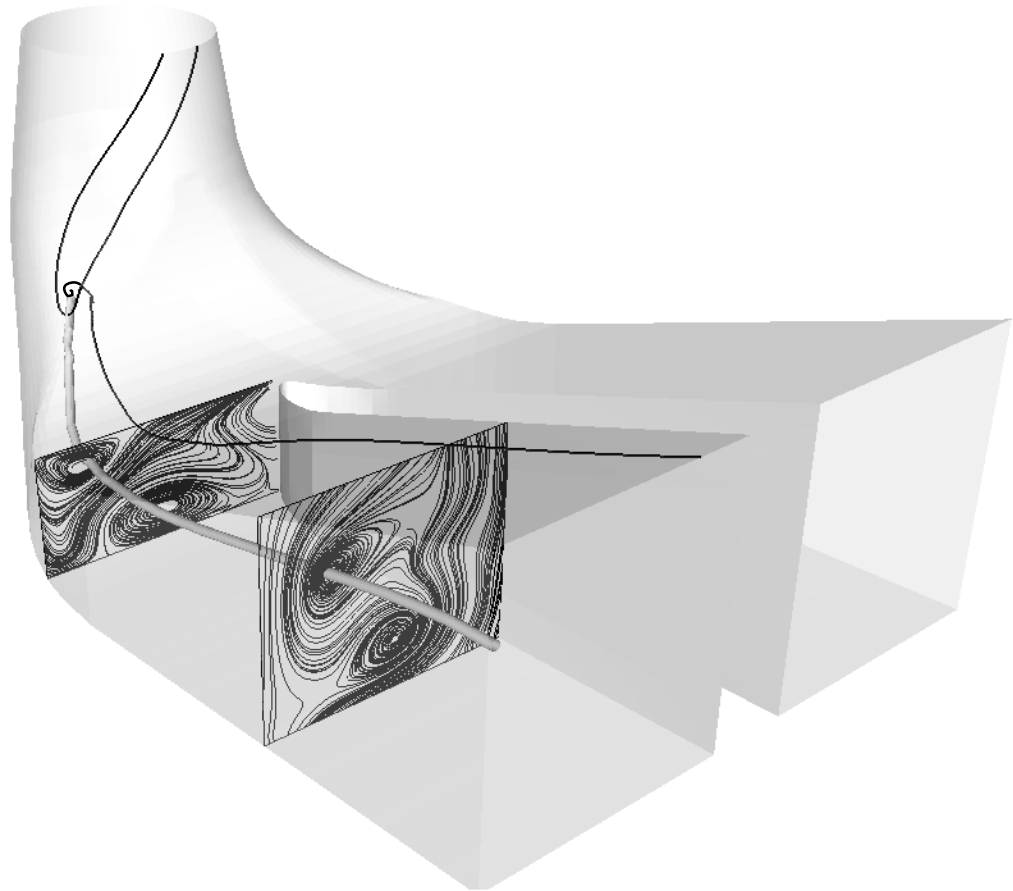


Figure 4.13: Vortex core and separation line, $\varphi^* = 1.021$.

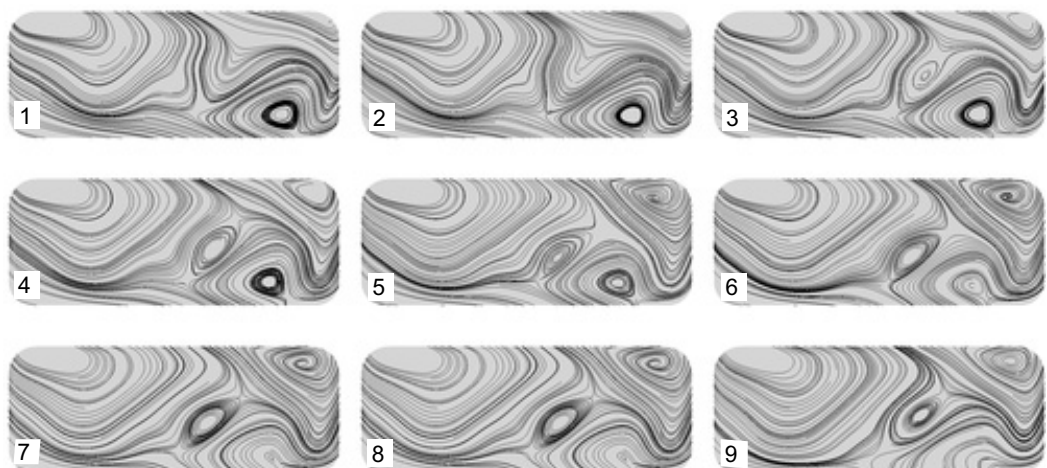


Figure 4.14: Tangential streamlines. Section 12. Before the efficiency drop: $\varphi^* = 1.008$, $\varphi^* = 1.014$, after: $\varphi^* = 1.027$, $\varphi^* = 1.032$, $\varphi^* = 1.038$, $\varphi^* = 1.043$, $\varphi^* = 1.049$, $\varphi^* = 1.054$.

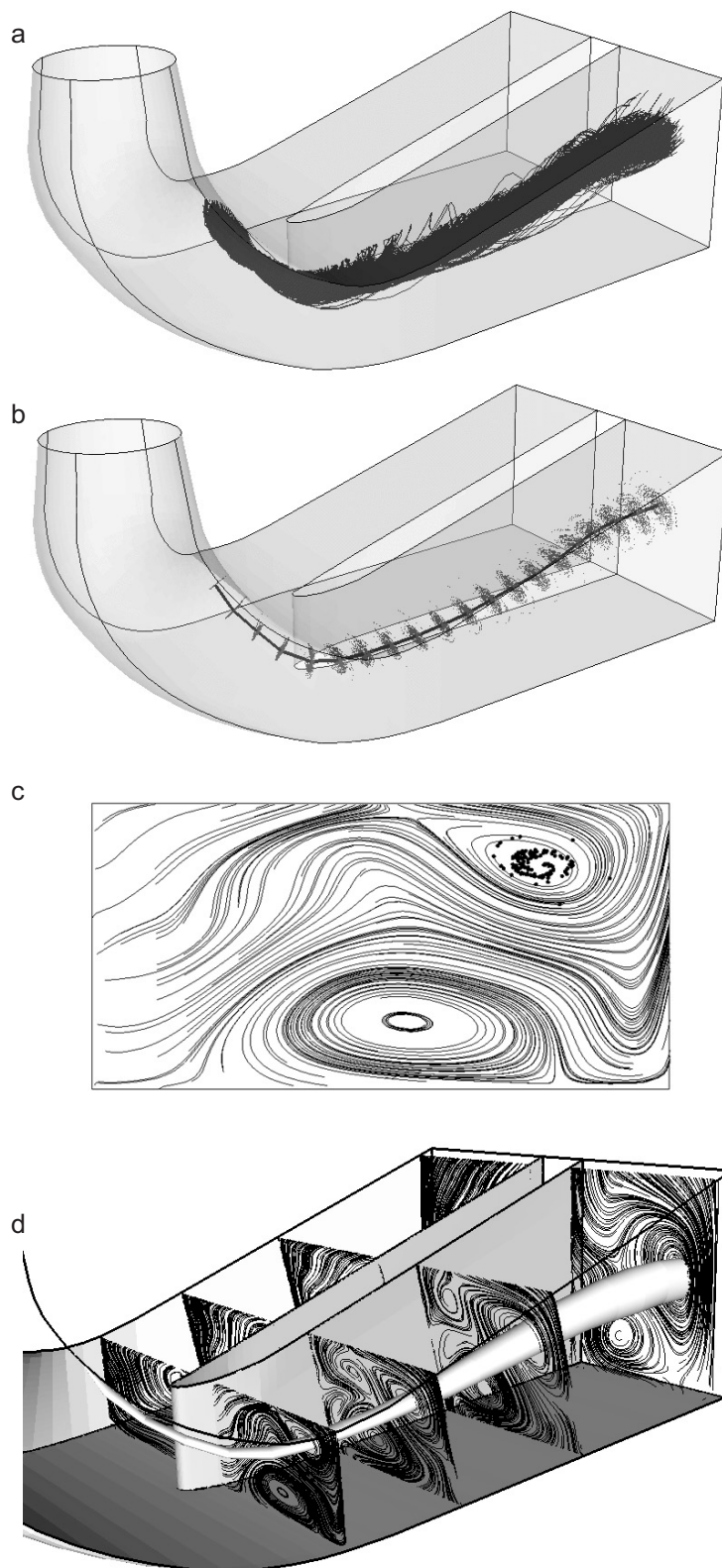


Figure 4.15: Vortex region extraction, $\varphi^* = 1.027$: a) streamlines originating from a zero velocity region, b) mean-line and clouds of points resulting from the intersection with the streamlines and the normal planes to the mean-line, c) right channel, tangential streamlines and cloud of points, d) resulting vortex tube.

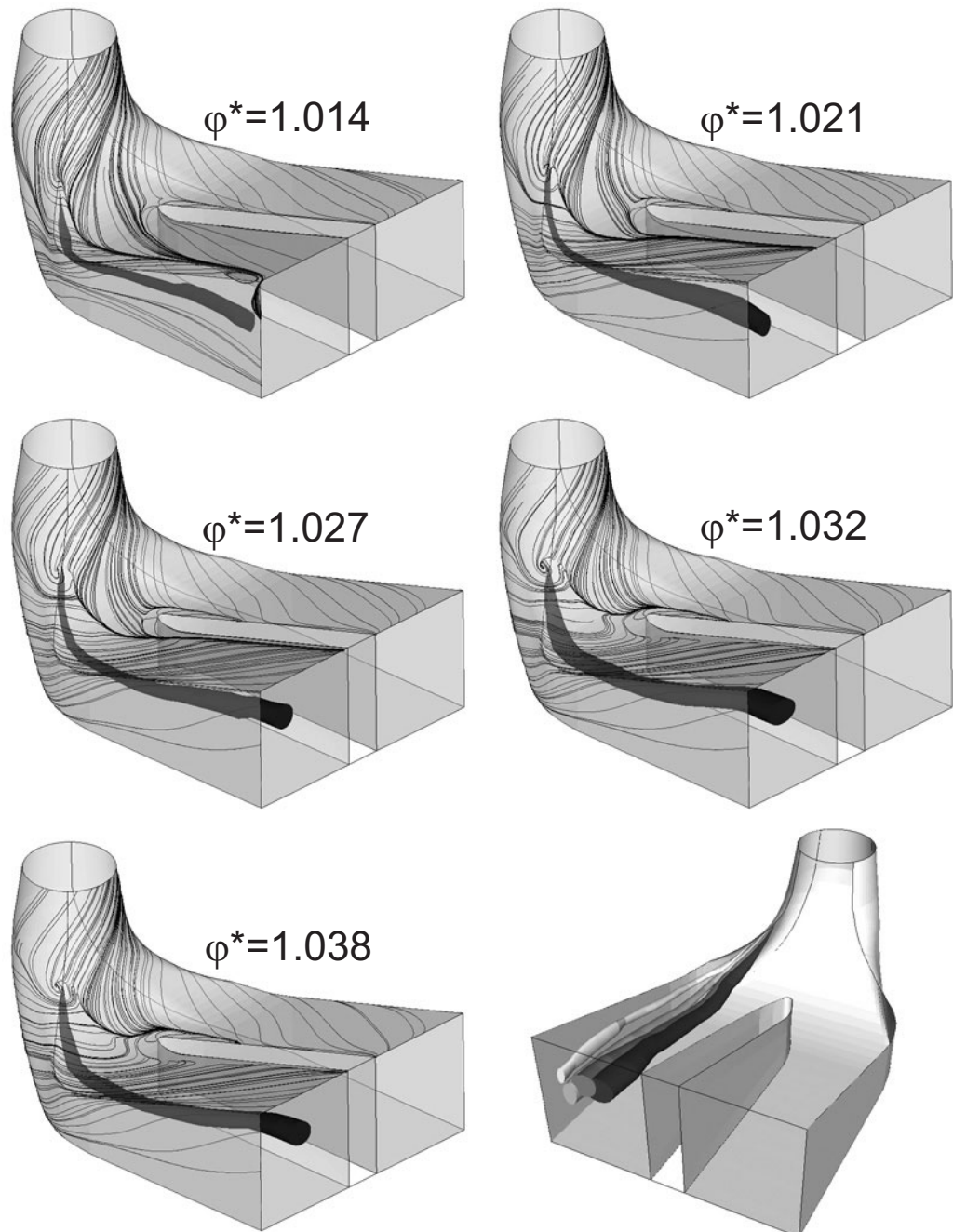


Figure 4.16: Vortex evolution. Before the drop: $\varphi^* = 1.014$, after: $\varphi^* = 1.021$, $\varphi^* = 1.027$, $\varphi^* = 1.032$, $\varphi^* = 1.038$. The last picture summarizes the first four operating conditions.

4.1.3 Conclusion

The efficiency drop (VI.3) is explained by a global instability that has the flow rate as parameter. The topological structure of the velocity field changes with the emergence of a saddle point and a focus in the surface pattern, leading to the global Werlé-Legendre separation that blocks the right channel.

VII

Time-dependent flow computation with steady boundary conditions

1

Introduction

Simple direct observations of the flow in the draft tube model prove the unsteady nature of the flow also at the macroscopic scales and low frequency (in the order of Hertz). The existence of self-sustained unsteadiness is first investigated. The boundary conditions are kept steady. The application of the two-equation turbulence models quasi-steady approach for the simulation of unsteady flows is questionable, and the limitations are still not well defined. The test case of the bluff body shows that at least this type of self-sustained vortex shedding can be reproduced with such an approach. The instability is however of low frequency and exists also in the laminar range and therefore the main mechanism is not dictated by the turbulent term. At two operating points, under particular circumstances and in spite of the steady boundary conditions, the numerical investigations show an unsteady periodic flow characterized by self-sustained vortex shedding.

1.1 Kelvin-Helmholtz instability [Bat67][DR81][Ge98]

In the framework of the linear instability theory one may distinguish between amplifiers, the dynamics of which are sensitive to inflow perturbations, and oscillators, which sustain intrinsic global modes tuned at a well defined frequency. For two-dimensional parallel shear flows, the purely mechanical (inviscid) Kelvin-Helmholtz instability is connected with the presence of an inflection point in the velocity profile (in contrast to e.g. viscous instabilities such the Tollmien-Schlichting instability occurring for instance in a pressure driven Poiseuille flow). This classical inflection point criterion (Rayleigh, 1880) provides a necessary (but not sufficient) condition for the inviscid instability of parallel flows. It can be shown that it is a consequence of the conservation of momentum. The unbounded vortex sheet defined by $U(y) = U_1, y > 0$; $U(y) = U_2, y < 0$, where $U_1 > U_2$ (fig. 1.1), is the simplest example of unstable flow leading to the well-known Kelvin-Helmholtz vortices. The shear layer rolls up to spanwise co-rotating vortices convected in the streamwise direction. From the Rayleigh's equation (corresponding to the Orr-Sommerfeld equation in the limit $\lim Re \rightarrow \infty$) it results a real phase speed $c = \omega/k$, where ω is the real frequency and k the real wave number, equal to the average velocity $\bar{U} = .5(U_1 + U_2)$. This flow is always unstable; for all wavelength, there be-

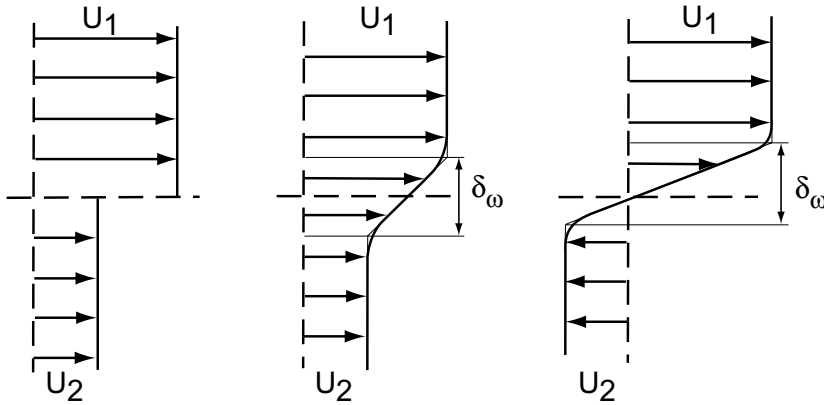


Figure 1.1: Shear flows: a) unbounded vortex sheet, b) mixing layer $R < 1$, c) mixing layer $R > 1$.

ing no length scale of the basic flow. For a real shear layer of finite thickness, it can be shown that short waves are stable. Waves which propagate in the basic flow direction grow most rapidly, so, after some time, these waves will be dominant. The mechanism of instability has been described by Batchelor by considering two irrotational regions corresponding to the uniform flows of respective velocity U and $-U$ separated by a thin longitudinal stripe of rotational fluid. By supposing that this rotational zone is perturbed and undulates in a sine wave about the interface, the two crests of the sine will travel in the opposite directions. This will steepen the vortex sheet transforming it into a spiral. Within the linear instability analysis, the vorticity is indeed transported by the basic flow. The velocity ratio $R = \Delta U / (2\bar{U})$ is an essential parameter in the determination of the absolute/convective nature of the instability. For $R < 1$ (co-flow mixing layer) a *spatially* developing mixing layer extremely sensitive to external noise, is observed. In unforced mixing layers, the various scales of natural white noise are differently amplified: the power spectra in the roll-up region then exhibit a large bandwidth of amplified frequencies with a maximum at a natural frequency f_n . This quantity is observed to scale with the vorticity thickness $\delta_w(0)$ and the average velocity \bar{U} so that the Strouhal number remains constant to approximately $St = f_n \delta_w(0) / \bar{U} = 0.03$. In the roll-up region the vortices are characterized by a predominant shedding rate f_n and associated wavelength $\lambda = \bar{U} / f_n$. In the case of counterflow mixing layers with $R > 1$, *temporally* evolving Kelvin-Helmholtz vortices with a well defined natural wave number k_n are observed. Such a configuration is quite insensitive to external noise and acts as a self-sustained hydrodynamic oscillator. It has been shown that the nature of the instability changes from *convective* (localized disturbances are swept away from the source) to *absolute* (disturbances spread upstream and downstream) for $R > 1.315$ for the hyperbolic-tangent mixing layer. The most amplified wave number (the amplification rate is maximal for this wave number) calculated by Milchalke (1964) for a velocity profile of hyperbolic-tangent form, is given by $k = 0.44 / \delta_0$ corresponding to a spatial wavelength $\lambda = 14\delta_0$.

2

Operating point in the efficiency drop at $\varphi^* = 1.021$

The 1'100'000 grid points mesh leads to the same main flow topologies as the standard mesh with 330'000 points for most of the computed operating points, but not for the first point in the efficiency drop ($\varphi^* = 1.021$). While the coarser mesh predicts the leg of the line of separation emanating from the saddle point to develop in the right channel (fig. 2.2), the other simulation shows a stronger focus and the line of separation can reach the other channel allowing a large backflow region in the right channel (fig. 2.1). This configuration could indicate that the previously described flow bifurcation (VI.4.1) is not the only possible one, showing the sensitivity of the flow in this operating region to small perturbation. The absence of hysteresis phenomena on the measured recovery factor seems however to indicate that experimentally the same bifurcation is always observed. The finer mesh results show a periodical vortex shedding along the separation lines of the backflow region (fig. 2.1) as illustrated in figures 2.4, 2.6 and 2.7. The topological configurations of the process are sketched in fig. 2.5. The vortex motion occurs along the separation lines connecting two saddle points. A saddle point coupled with a focus is periodically shed on either the separation line directed toward the left channel or on the line at the upper wall of the right channel. The vortex movement stops when the other saddle point is reached. A heuristic explanation of the mechanism is that the vortex motion on the right channel directly induces flow acceleration in the backflow region and this also indirectly by restricting the shape of this area. The increased kinetic energy feeds the generation of the focus in the cone, which is successively convected away when the kinetic energy decreases again because the vortex on the channel disappears when the saddle is reached. Near the wall on the right channel between the two saddle points, the periodical variation of the kinetic energy in the backflow region has in fact an amplitude of 25% of the mean value. The shedding frequency is $f = 2.38[Hz]$ corresponding to a Strouhal number of $St = fD/U_o = 0.14$ (D inlet diameter, U_o mean inlet velocity). The period is discretized with 60 time steps. A further increase of the time resolution does not have an influence on the shedding frequency. The convergence criterion for the maximal residuum of the internal loop that recovers the nonlinearity of the equations (II.2.1), is set to $1e^{-3}$ because of

the limited computational resources. This criterion is found accurate enough for the unsteady reference cases. The instantaneous flow rate distribution and specific energies (see Nomenclature, IX) flow evolution along the draft tube do not show important oscillations. The global efficiency variation is 1%. The pressure oscillations and corresponding phase are illustrated resp. in fig. 2.8 and 2.9. The wavelength is clearly recognizable. The backflow regions induce a phase shift.

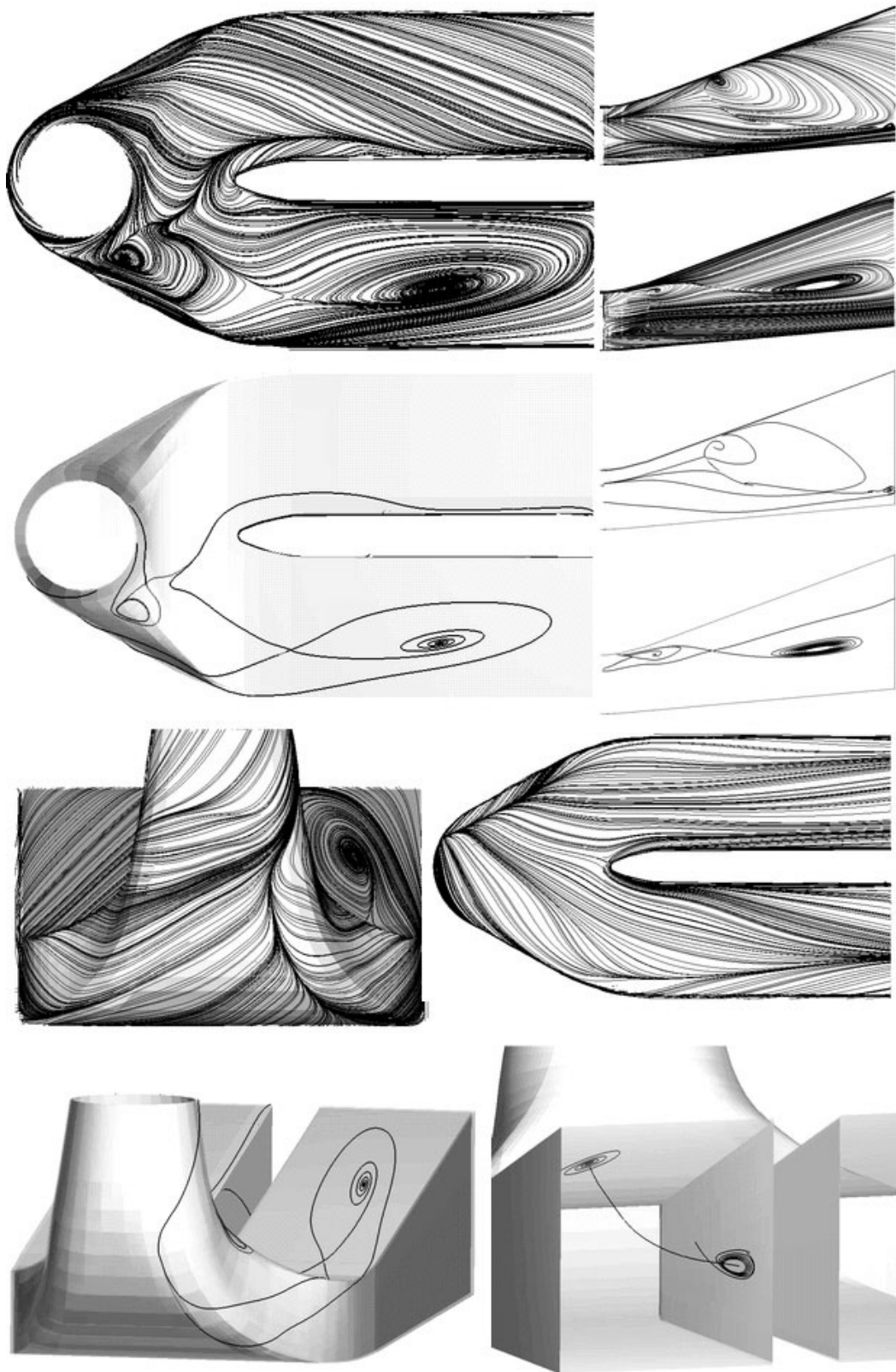


Figure 2.1: Mean flow topology.

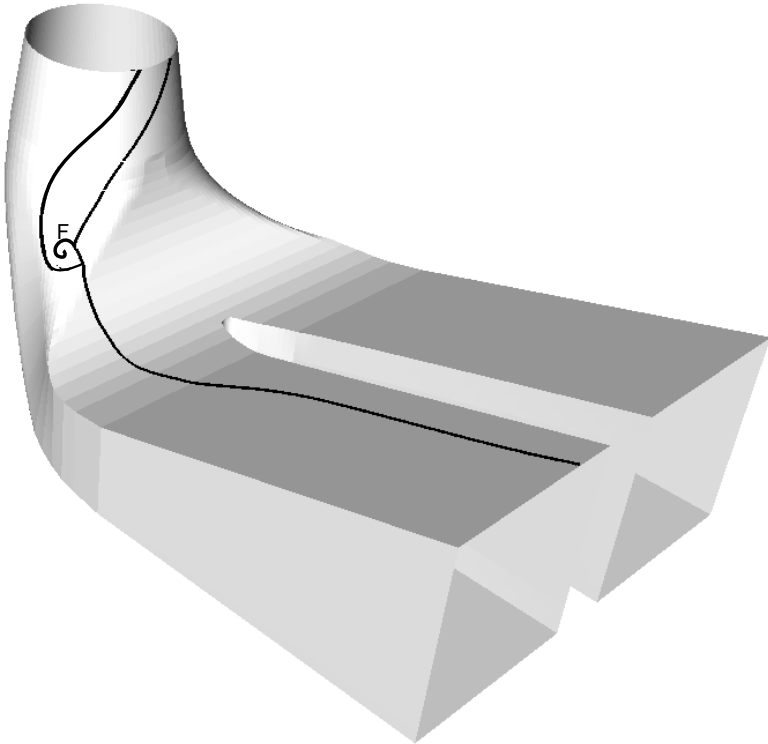


Figure 2.2: Topology of the steady solution obtained with the standard mesh. F: focus.

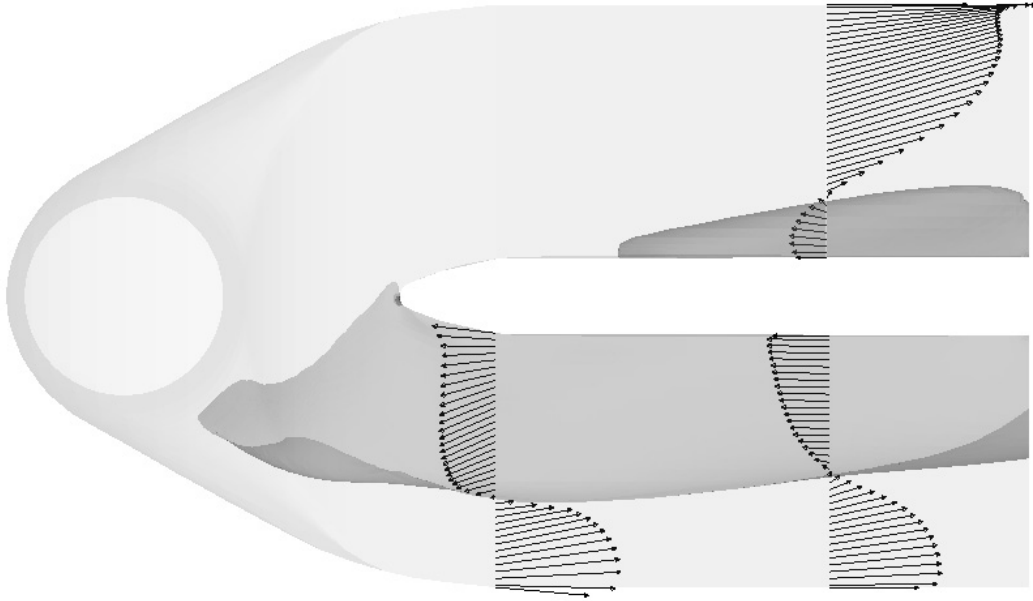


Figure 2.3: Backflow region and velocity profiles.

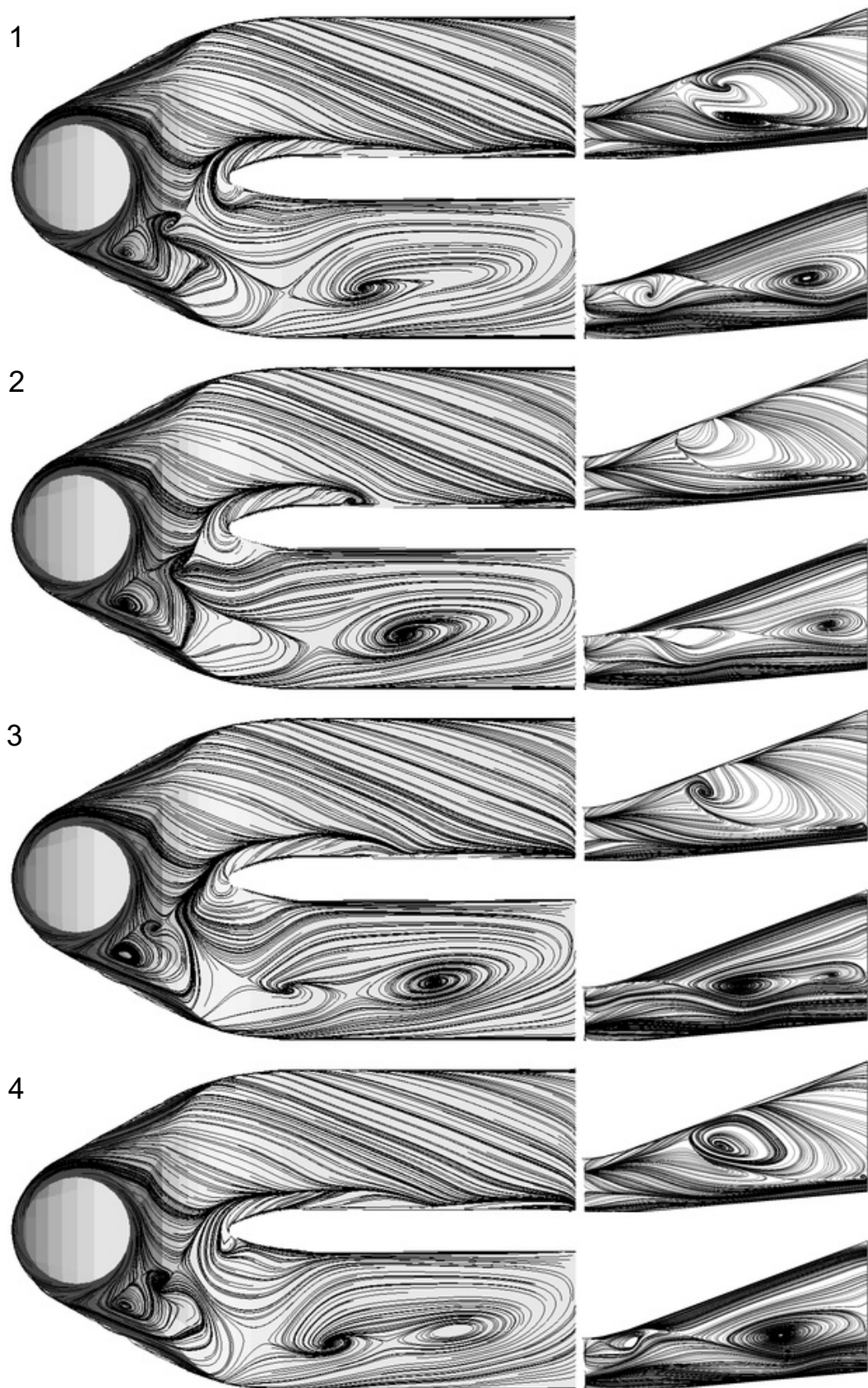


Figure 2.4: Skin friction lines at four phases equally spaced over a period.

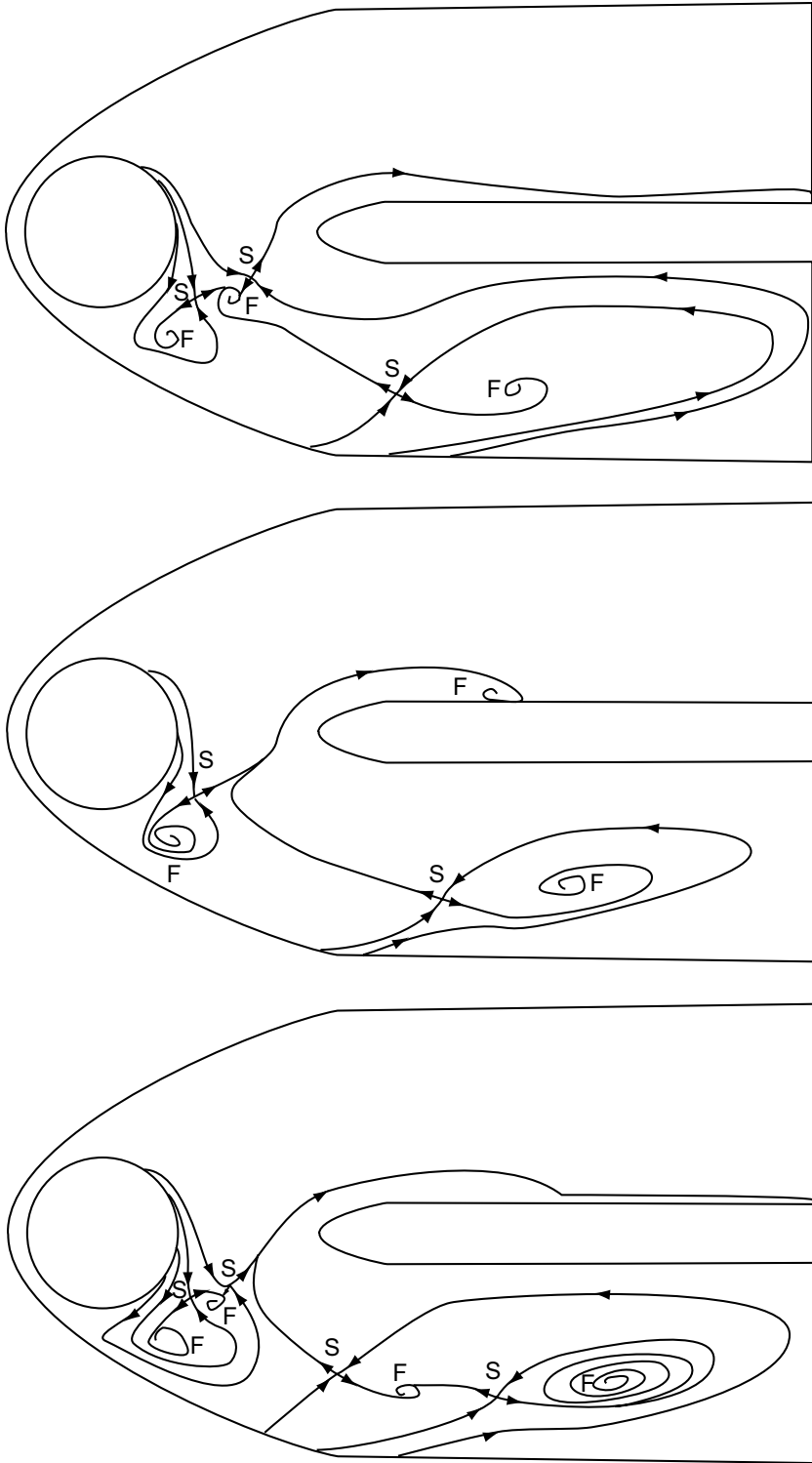


Figure 2.5: Topological phases. S: saddle, F: focus.

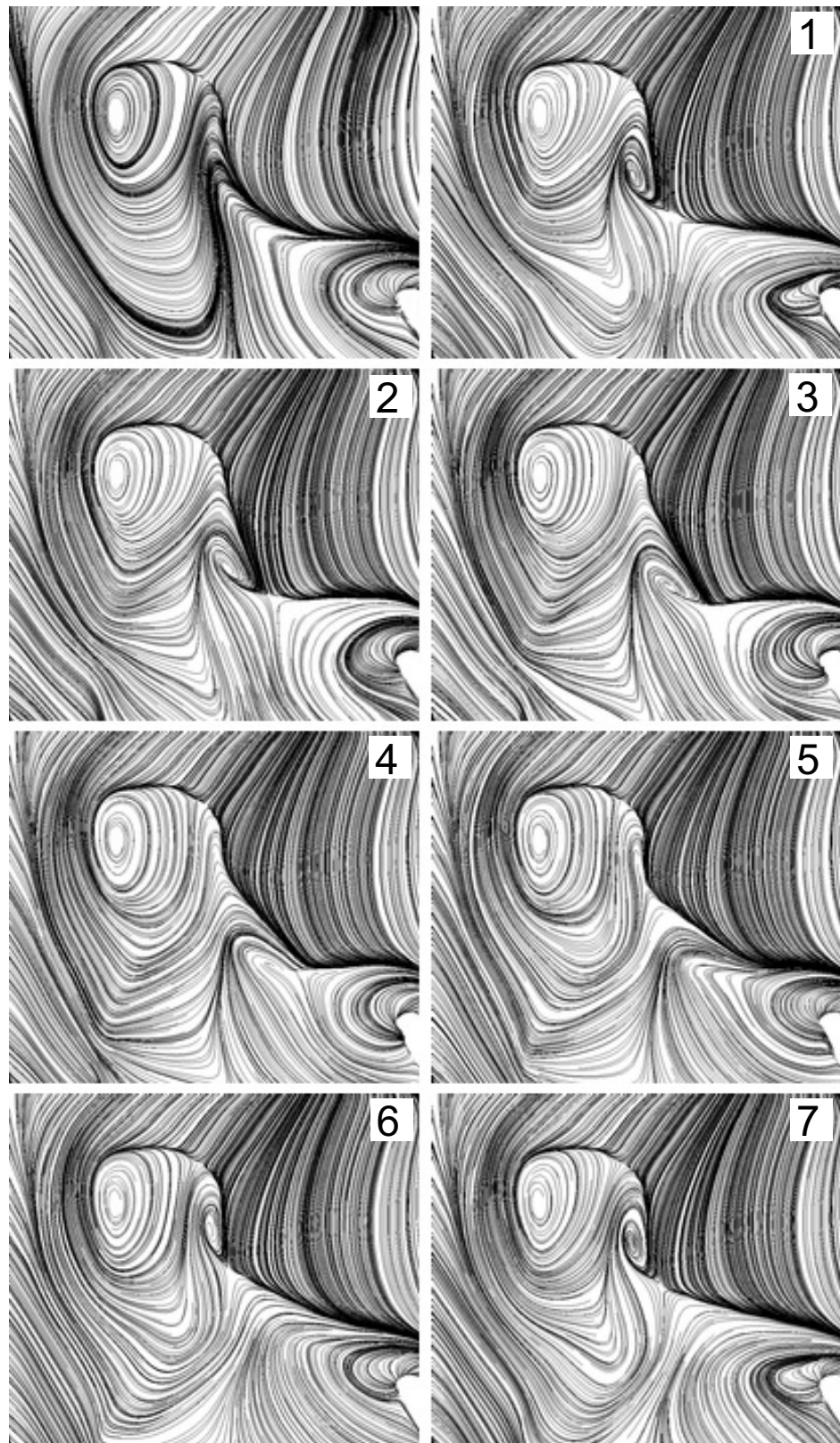


Figure 2.6: Particular of the cone showing the vortex shedding. The leading edge of the pier is visible on the bottom right. Skin friction lines at seven phases equally spaced over a period. The first picture represents the averaged flow.

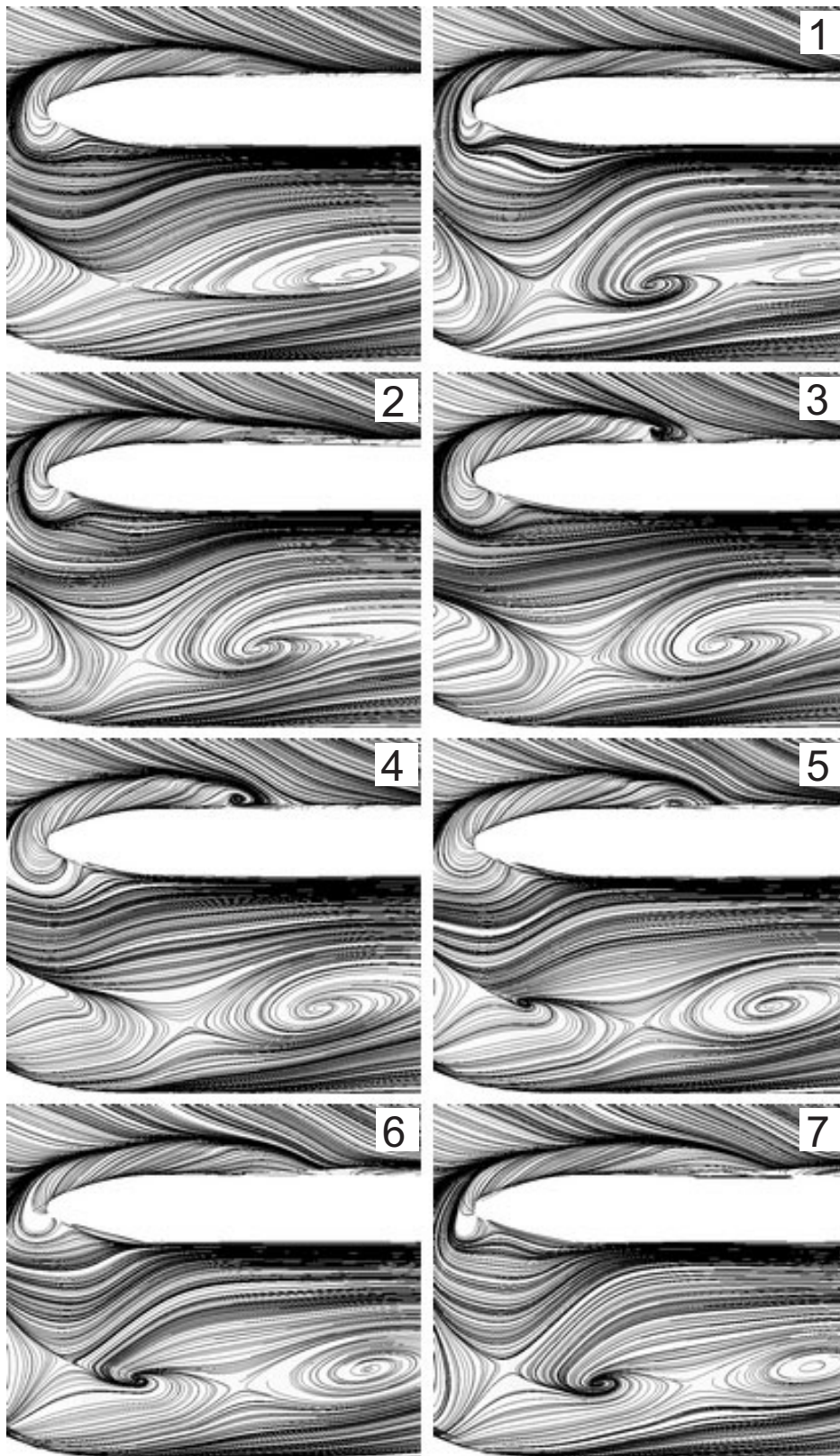


Figure 2.7: Top view of the right channel showing the vortex shedding. The first part of the pier is visible. Skin friction lines at seven phases equally spaced over a period. The first picture represents the averaged flow.

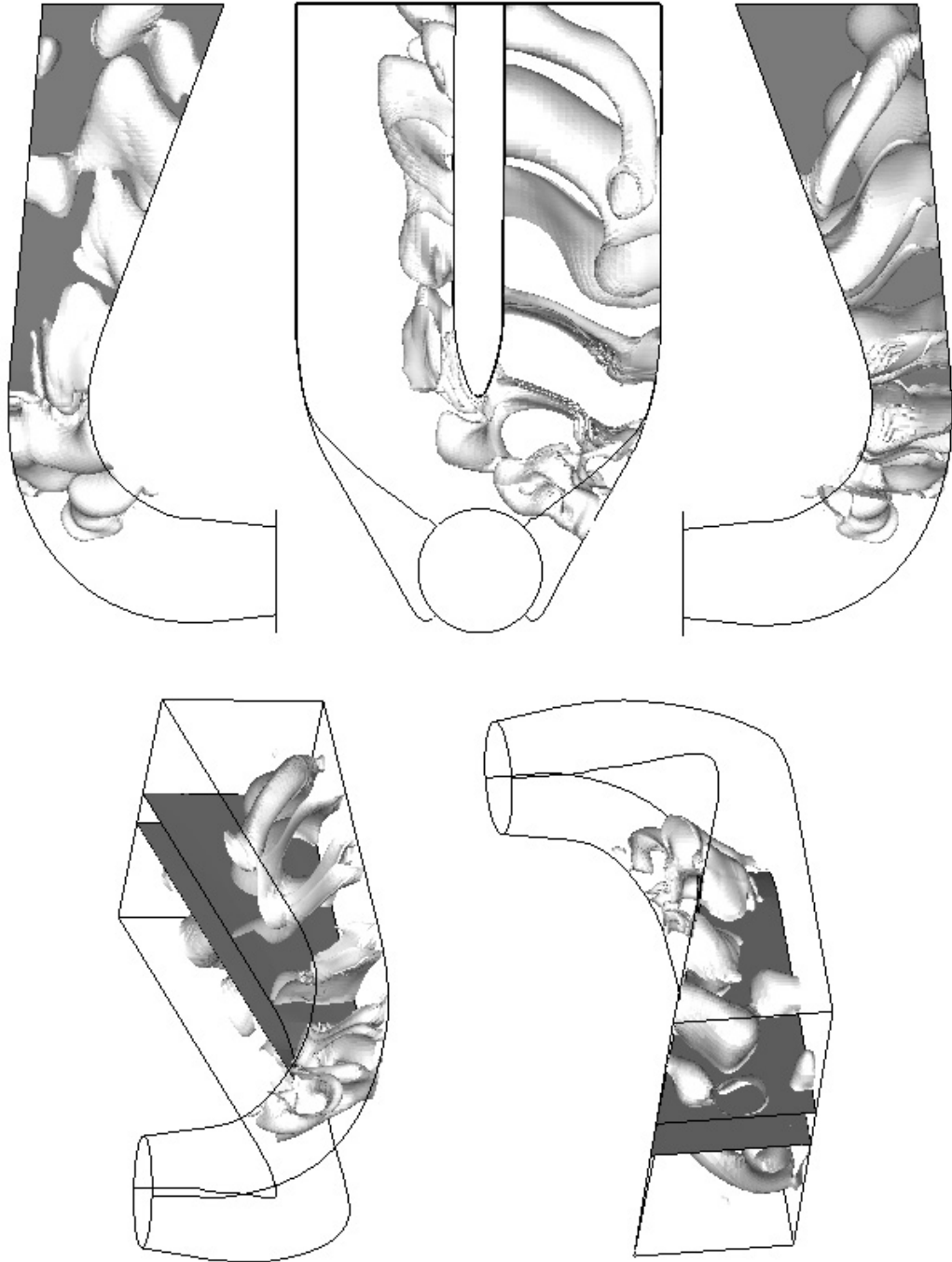


Figure 2.8: Isocontour of the fluctuating pressure field. The wave-train nature of the oscillation is clearly recognizable.

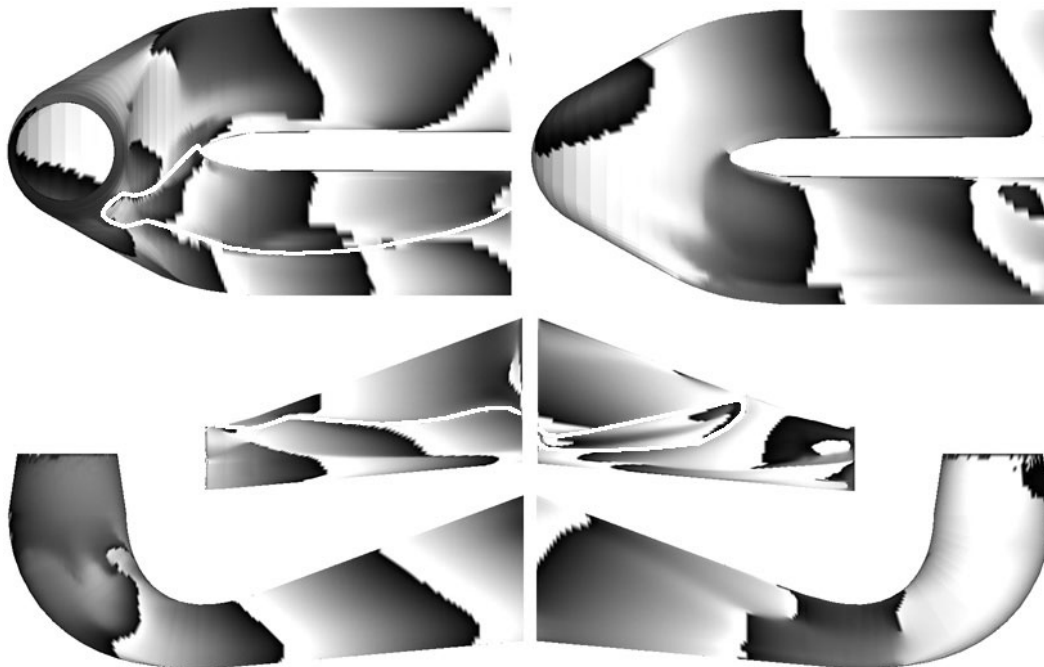


Figure 2.9: Phase of the wall pressure fluctuations at the shedding frequency (from $-\pi$ (white) to π (black)). The white lines limit the backflow regions.

3

Operating point at the highest flow rate $\varphi^* = 1.108$

At this operating point low frequency large-sized vortex shedding is directly observable at the draft tube outlet. A computation with a 900'000 points mesh predicts a self-sustained vortex shedding along the separation line limiting a backflow region at the pier wall (fig. 3.2). The near-wall flow field is compared with the solution obtained with the standard mesh in fig. 3.1. While the incidence of the separation line with respect to the upper wall is small in the simulation with the standard mesh, in the other case the line is almost perpendicular to the wall, giving rise to an additional saddle point and a focus compared with the first solution. The focus moves along the line between two saddle points modifying the surrounding flow field and giving rise to the interaction with the upstream saddle. This interaction leads to the periodical vortex shedding. When the focus reaches a critical distance from the upstream saddle, a line emanating from this point rolls, building a focus and a new downstream saddle (fig. 3.3, 3.4). The streamlines stemming from the focus region are illustrated in fig. 3.6. The fluctuating velocity field is shown in fig. 3.5. The maximal kinetic energy and pressure fluctuations (fig. 3.7) reach 3% of the inlet kinetic energy. Small fluctuations are visible also at the left side. The shedding frequency is $f = 1.11[Hz]$ corresponding to a Strouhal number of $St = fD/U_o = 0.06$ (D inlet diameter, U_o mean inlet velocity). The period is discretized with 30 time steps. A further increase of the time resolution does not have an influence on the shedding frequency.

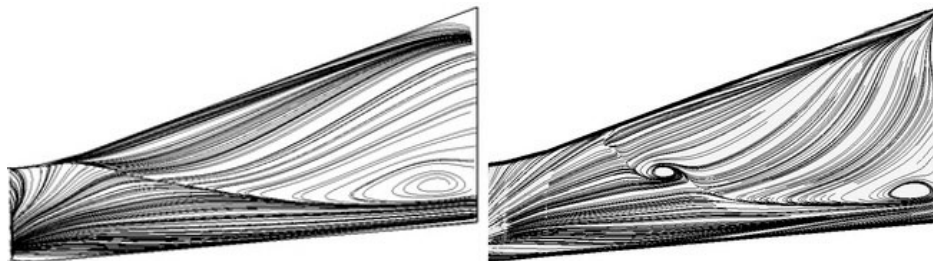


Figure 3.1: Skin friction lines, right side of the pier: a) steady flow solution, standard mesh, b) unsteady flow solution, mean flow field, 900'000 mesh.

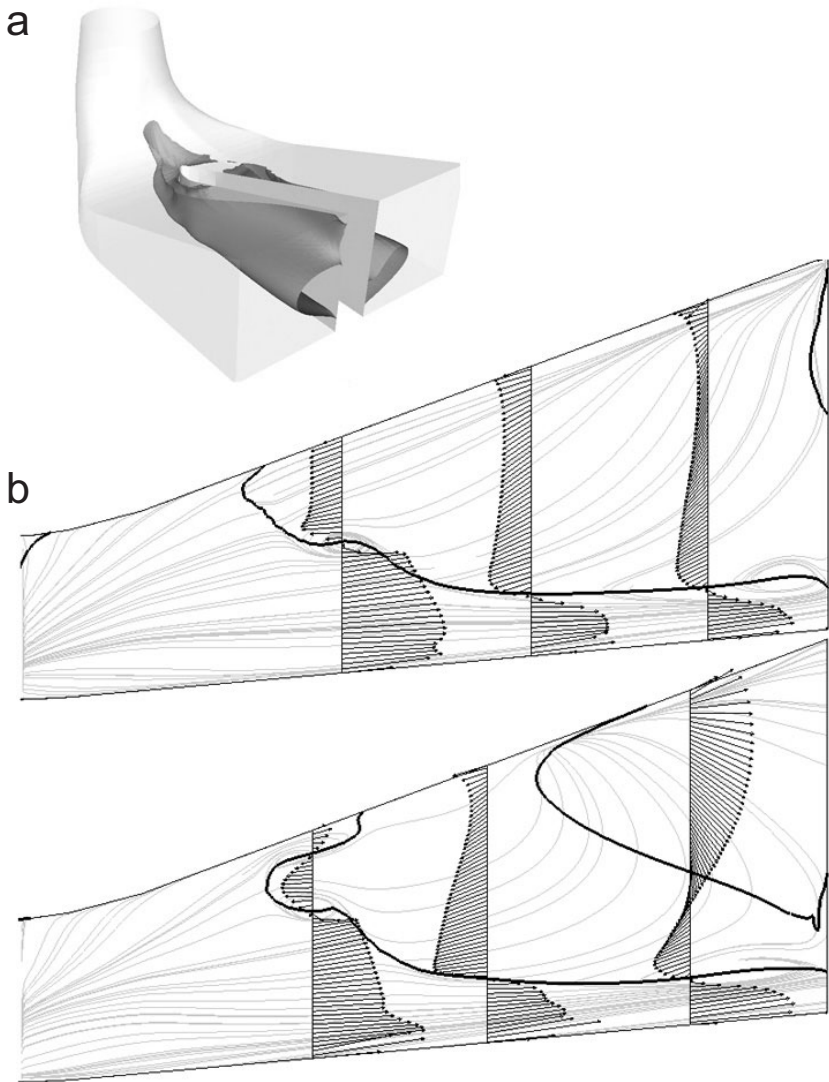


Figure 3.2: Velocity profiles: a) backflow region, b) near-wall velocity profiles at the pier surface.

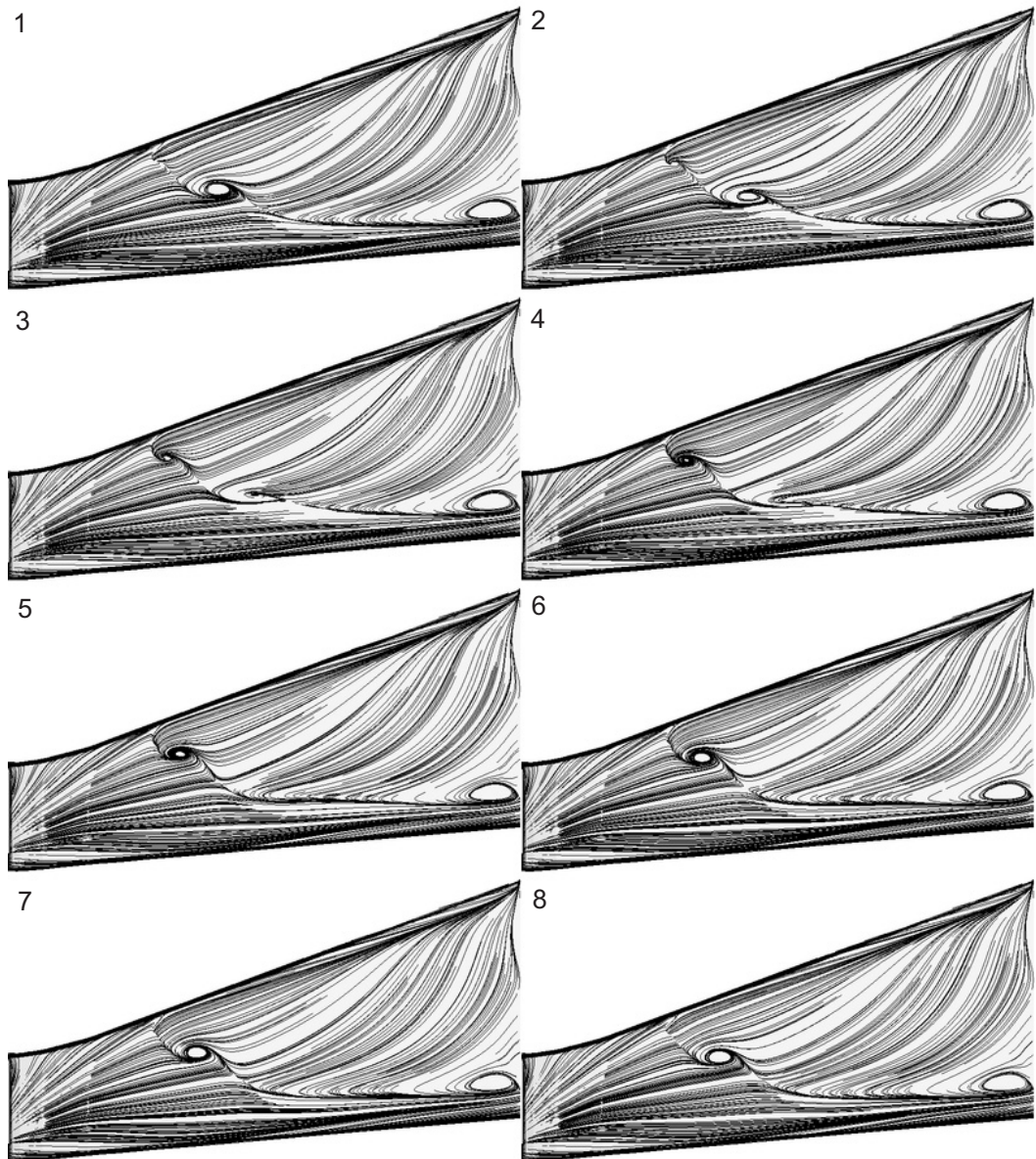


Figure 3.3: Skin friction lines at height phases equally spaced over a period. Right side of the pier.

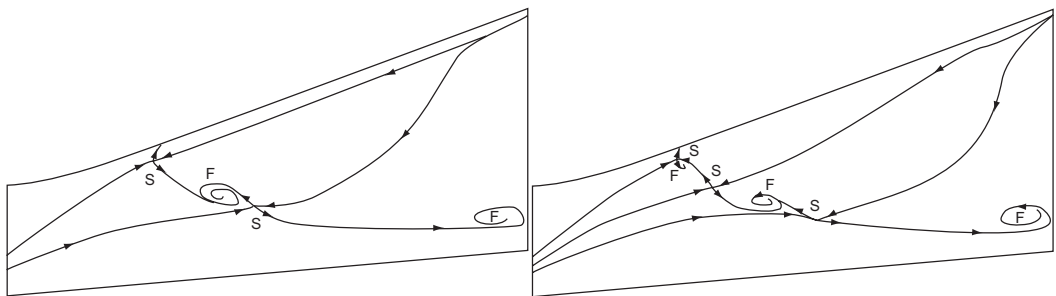


Figure 3.4: Topological bifurcation. S: saddle, F: focus.

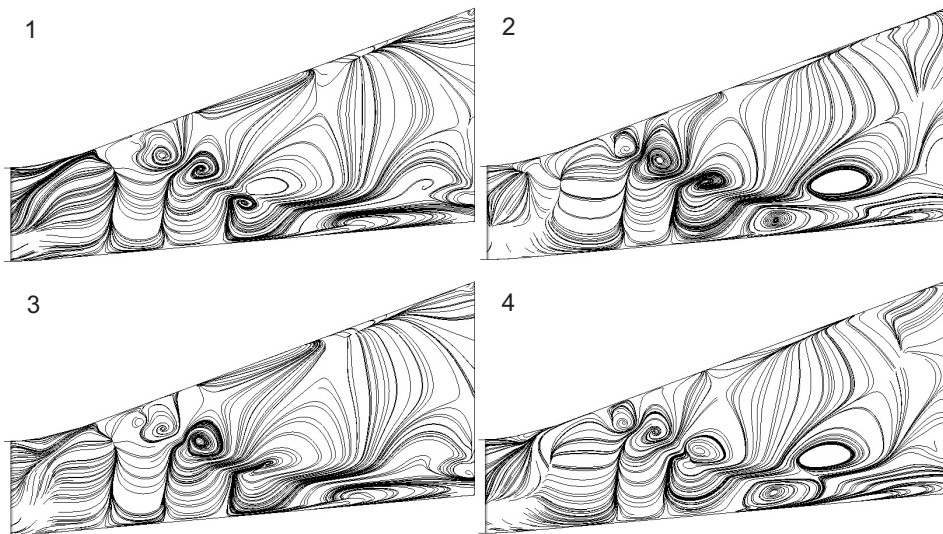


Figure 3.5: Skin friction lines of the fluctuating field at four phases equally spaced over a period. Right side of the pier.

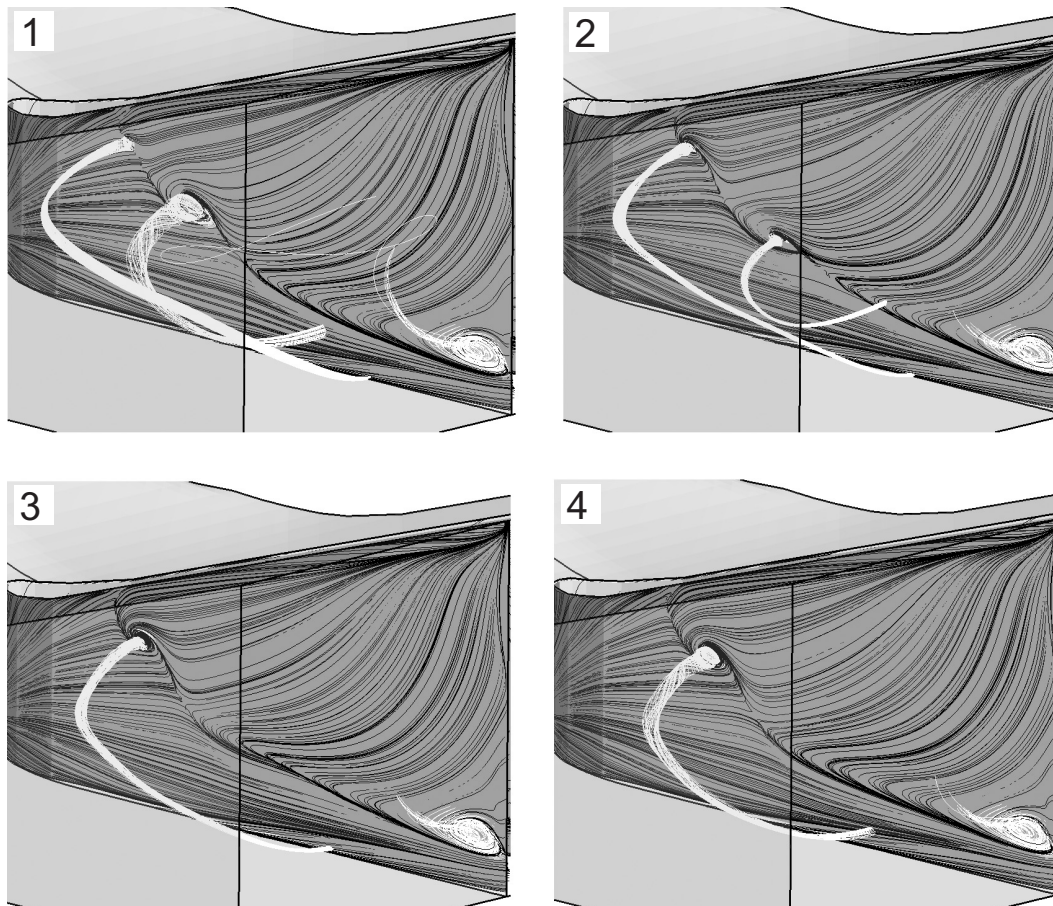


Figure 3.6: Skin friction lines at four phases equally spaced over a period. Right side of the pier. Streamlines have been also started from regions near the foci (in white).

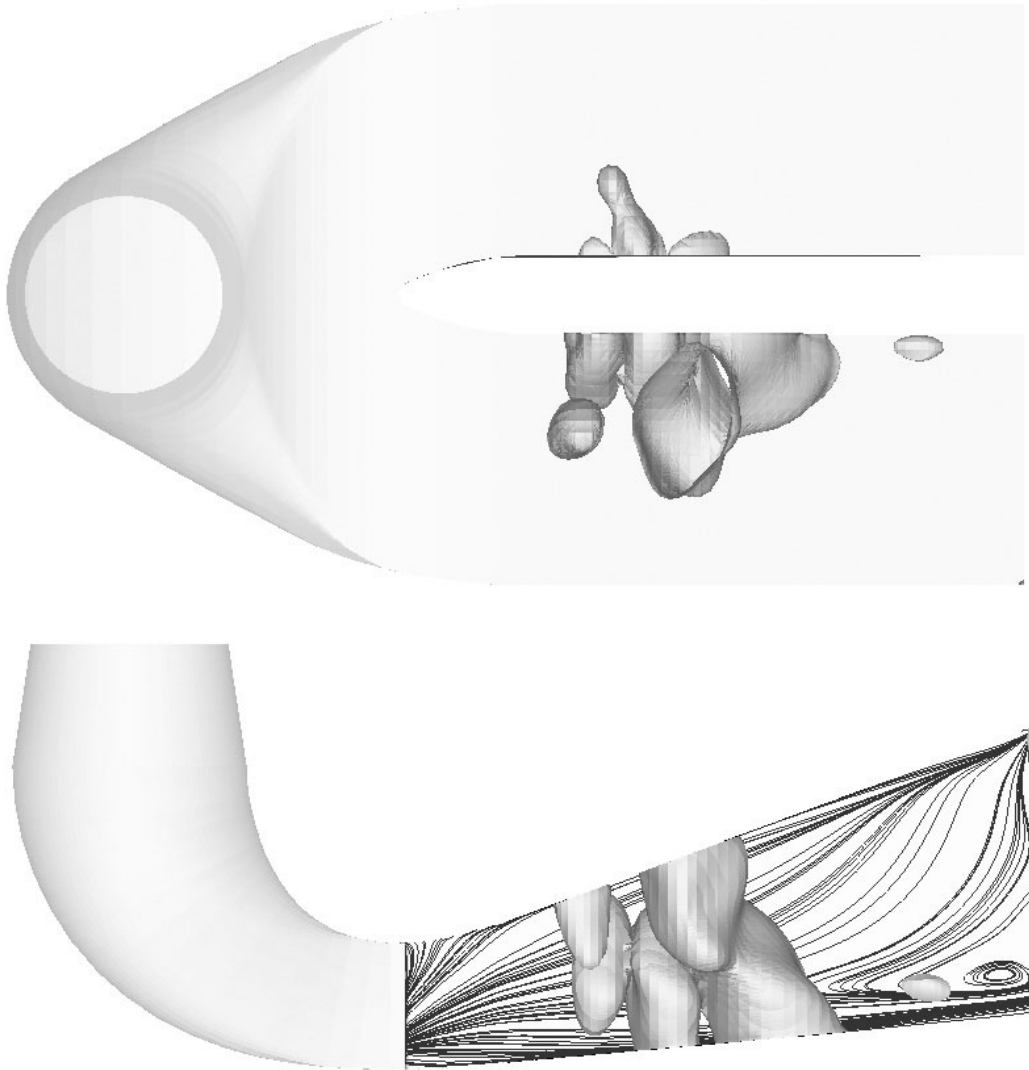


Figure 3.7: Isocontour of the fluctuating pressure field. The wave-train nature of the oscillation is clearly recognizable.

4

Conclusion

Two computations at different operating conditions employing a finer mesh predict self-sustained vortex shedding. Both cases are characterized by the existence of a backflow region and a focus placed between two saddle points along the separatrix defining the border of this region at the wall. The focus moves along the line modifying the surrounding flow field and giving rise to the interaction with the upstream saddle. This interaction leads to periodical vortex shedding. The Strouhal number defined with the inlet diameter and velocity is $St \sim 0.1$. The velocity profiles at the backflow region interface are unstable in the sense of the inflection point criterion, and could present the Kelvin-Helmholtz instability mechanism. Typically the velocity ratio of these profiles is greater than the value necessary for the onset of an absolute instability for the hyperbolic-tangent mixing layer. Of course the studied case is fully three-dimensional and non-linear and therefore the two-dimensional linear theory can only give some indications. From the computations it seems that a necessary condition for the instability of the counterflow mixing layers in such three-dimensional configurations, is the presence of two saddle points along the interface.

These results should be viewed however with some degree of reservation, owing to the sensitivity of the results to numerical parameters.

VIII

**Time-dependent flow
computation with unsteady
inlet boundary conditions**

1

Phase averaged inlet velocity profile

The runner rotation introduces fluctuations at different frequencies. Usually one observes the rotational frequency due to the axis asymmetry, the blade passage frequency caused by the velocity difference between the two blade sides and the product of the guide vanes blades with the runner frequency. The purpose of this chapter is the study of the evolution of the unsteadiness introduced by the blade passage. The measured phase averaged velocity profiles tuned at the runner frequency and averaged on a representative blade-to-blade channel presented in (IV.3.2), are made to turn at the runner frequency in the computation. The amplitude of the oscillation at the runner passage frequency represents a few percent of the mean velocity and cannot be neglected. For simplicity this fluctuation is however not taken into account. A computation with the standard mesh leads to the complete damping of the blade fluctuations already in the first cell rows, even with a high temporal resolution. The study is therefore carried out in the cone only, allowing a better spatial resolution. Due to the fact that the inlet measurement section lies several centimeters below the runner outlet and the profile still shows fluctuations of 10% of the mean velocity value, it seems unlikely that the fast damping is a physical process. However measurements show that the blade passage influence almost disappears at the cone outlet.

1.0.1 Numerical tests

- Several spatial and temporal resolutions have been tested, which always lead to the fast damping of the fluctuations. The tested time steps range from 9 to 300 per blade passage and the finer mesh reaches $1.8M$ nodes (fig. 1.1). The typical resulting evolution of the fluctuation amplitude is shown in fig. 1.2. It should be mentioned that the choice of a CFL number near to the unity (though not required, the employed scheme being unconditionally stable) in the axial and circumferential directions leads to a prohibitive spatial resolution. Even with the scarce temporal resolution of 9 steps per blade passage the mesh covering only half height of the cone requires $1.2M$ nodes.
-

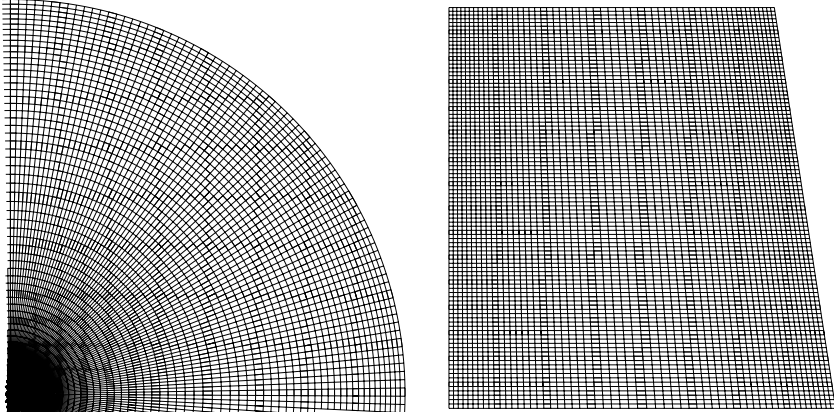


Figure 1.1: Fine mesh, 1800 k nodes.

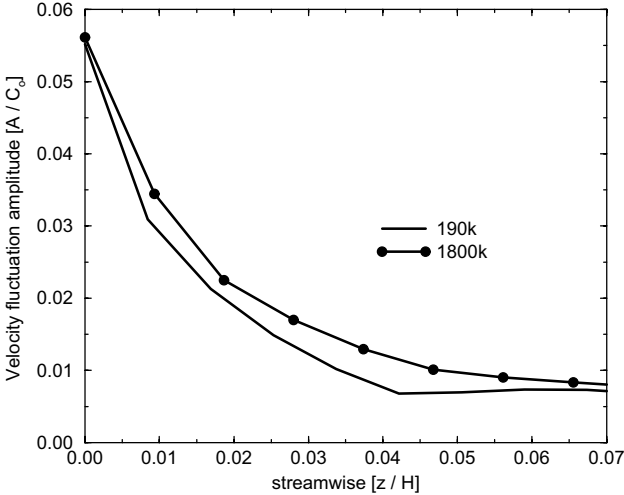


Figure 1.2: Amplitude of the fluctuations introduced by the blades, mesh influence. H: cone height.

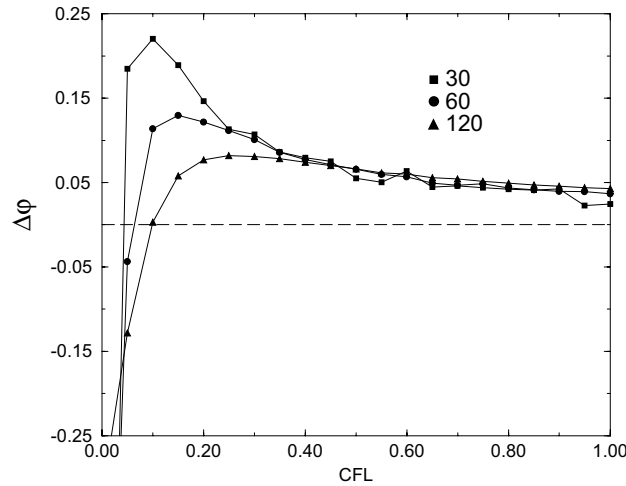


Figure 1.3: Phase shift error in [rad] vs CFL number for a temporal resolution of 30, 60 or 120 time steps per period.

- The same damping is observed when the turbulence model is switched off.
- The steady computation in a rotating frame with counter-rotating walls predicts the same damping.
- If the angular frequency is reduced by a factor of 10, the velocity fluctuations are propagated until the outlet.
- The influence of the CFL number is investigated for the simplest inviscid one-dimensional case. The evolution equation for a velocity field $v = (u(t), 0, 0)$ reduces to:

$$\frac{\partial u}{\partial t} = -\frac{1}{\rho} \frac{\partial p}{\partial x} \quad (1.1)$$

To a velocity oscillation $u(t) = \bar{u} + \tilde{u} \cos(\omega t)$ corresponds a pressure gradient $\frac{\partial p}{\partial x}(t) = \rho \omega \tilde{u} \sin(\omega t)$. The phase shift between velocity and pressure gradient is therefore $\pi/4$. The angular frequency corresponding to the blade passage is imposed. The error in the phase shift prediction versus CFL number is plotted in fig. 1.3 for a temporal resolution of 30, 60 or 120 time steps per period. For CFL numbers below 0.2 the error increases considerably. Similar results are obtained for a ten times slower frequency. The resulting error in the pressure gradient amplitude is however greater for the higher frequency. The high runner rotation frequency typically forces small CFL numbers as illustrated above in the case of the cone.

1.0.2 Theoretical considerations

Temporal and spatial accuracy

As illustrating example the one-dimensional convection equation

$$\frac{\partial u}{\partial t} + u \frac{\partial u}{\partial x} = 0 \quad (1.2)$$

is discretized using the central second order difference scheme. The resulting leading error terms can be expressed in terms of the reference spatial length L , the reference convection velocity U , the relevant angular frequency of the unsteadiness ω , the number of mesh points N_x over L and the number of time steps N_t in one period:

$$\frac{\text{temporal error}}{\text{spatial error}} \sim K \left(\frac{N_x}{N_t} \right)^2 \quad (1.3)$$

where $K = \omega L/U$ is the reduced frequency representing the relevance of the unsteadiness on the convection. As the reduced frequency is increased, the CFL number ($CFL = U \Delta t / \Delta x = 2\pi / K^{3/2}$) quickly decreases if the temporal to spatial error ratio (1.3) is kept close to 1. The blade passage is characterized by $K = 110$, leading to a $CFL = 0.005$. This illustrates that the choice of the spatial and temporal resolution is not trivial.

Dynamical equation for the periodic motion

The dynamical equations governing the mean flow field and the periodic motion can be derived by decomposing the flow into the averaged and fluctuating components. The influence of the random fluctuations is taken into account with the modeling of the Reynolds' stress tensor. The signals are written as $f = \bar{f} + \tilde{f}$, where \bar{f} is the mean (time-averaged) contribution and \tilde{f} the periodic wave. Substituting the decomposed fields into the continuity and momentum equations and time averaging, the dynamical equation for the mean flow field can be expressed as:

$$\begin{cases} \frac{\partial \bar{u}_i}{\partial x_i} = 0 \\ \rho \bar{u}_i \frac{\partial \bar{u}_i}{\partial x_j} = -\frac{\partial \bar{p}}{\partial x_i} + \mu \frac{\partial^2 \bar{u}_i}{\partial x_j^2} - \frac{\partial \bar{S}_{ij}}{\partial x_j} - \frac{\partial \overline{\tilde{u}_i \tilde{u}_j}}{\partial x_j} \end{cases} \quad (1.4)$$

and the fluctuating flow field :

$$\begin{cases} \frac{\partial \tilde{u}_i}{\partial x_i} = 0 \\ \rho \left(\frac{\partial \tilde{u}_i}{\partial t} + \bar{u}_j \frac{\partial \tilde{u}_i}{\partial x_j} + \tilde{u}_j \frac{\partial \bar{u}_i}{\partial x_j} \right) = -\frac{\partial \tilde{p}}{\partial x_i} + \mu \frac{\partial^2 \tilde{u}_i}{\partial x_j^2} - \frac{\partial \tilde{S}_{ij}}{\partial x_j} + \frac{\partial}{\partial x_j} (\overline{\tilde{u}_i \tilde{u}_j} - \tilde{u}_i \tilde{u}_j) \end{cases} \quad (1.5)$$

where S_{ij} represents the Reynolds' stress tensor. The organized motion acts in the same way as the turbulent motion on the mean flow field. An estimation of the terms of the dynamical equation from the computational results for the periodic motion shows that the total derivative is mainly balanced by the pressure term. When the ten times slower angular frequency is imposed (the fluctuations are in this case propagated), the pressure fluctuation has a phase shift close to $\pi/4$ with respect to the velocity fluctuation. The fluctuations are almost in phase opposition when the runner rotational frequency is imposed.

1.0.3 Conclusion

When the measured phase averaged velocity profile is made to turn at the runner frequency, the resulting flow shows an unphysical fast damping of the fluctuations. If the frequency is reduced by a factor ten, the oscillations are propagated until the cone outlet. Surprisingly the steady computation in a rotating frame leads to the same damping. The validity of the quasi-steady turbulence models and wall functions for a moderate to fast unsteadiness is questionable. The subject is discussed in [Les99]. The influence of the turbulence model in this case is unclear because the turbulent terms are here negligible. Also unclear is the influence that possible inaccuracy in the inlet boundary conditions could have on the fluctuations. The disappearance of the fluctuations is probably attributable to an unexplained error in the prediction of the phase shift between velocity and pressure fluctuations. Such an error is also observed in the one-dimensional inviscid pulsating flow, especially for small CFL numbers. It seems that the code is not able to describe correctly high frequency three-dimensional unsteadiness.

2

Rotating helical vortex

2.1 Introduction [Oha91]

Hydroelectric power units equipped with (in particular) Francis turbines occasionally experience severe oscillations of hydraulic, mechanical and electrical quantities when operating at off-design load. At part load (50 – 80% of the best efficiency point flow rate) these oscillations are related to the onset of a periodic rotating roughly helical vortex. The vortex frequency f_n is typically between 0.2 and 0.3 of the runner rotational frequency f_r . The amplitude of pressure fluctuations associated with this phenomenon is greatly influenced by the turbine design and the dynamic response of the whole installation. Such low frequency pressure fluctuations are a special threat to stability of operation because they may propagate the whole piping system and cause hydraulic resonance. This occurs under particular conditions causing synchronous pressure and mass oscillation on the whole installation. It seems that a necessary condition for the synchronous pressure oscillations is the presence of an elbow in the draft tube. It is supposed that the excitation mechanism of the hydraulic oscillations is the interaction of the vortex with the secondary flow introduced by the elbow. The nondimensional vortex frequency $St = f_n D / U_o$ (f_n vortex frequency, D inlet diameter, U_o mean inlet velocity) is fairly well predicted by simple theoretical models having the inlet swirl number as parameter, indicating the direct independence from the runner rotational speed (which is linearly related to the mean velocity U_o). Similar flow behaviours can be indeed also obtained with a set of fixed guide vanes instead of a turbine runner. As example the Nishi's model [NMaYS82] assumes that the vortex rotates around a central reversed flow region and relates the swirl number with the radius of this core. The flow is assumed to consist in a dead irrotational water zone at the center and in a free-vortex flow field outside. The rotational speed of the vortex core is calculated as the half of the swirling velocity component evaluated at the radius of the stalled region and corrected by an empirical factor.

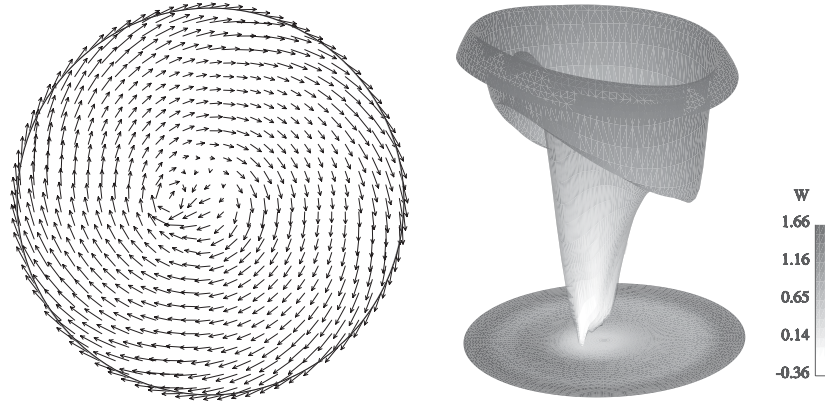


Figure 2.1: Inlet conditions, a) tangential and b) axial velocity field.

2.2 Phase averaged inlet profile

In the case study the helical vortex is visible at $\psi^* = 1.063$ in the range $0.676 < \varphi^* < 0.865$ corresponding to 70 – 85% of the best efficiency point flow rate. The velocity profiles are however not yet experimentally investigated. LDA measurements at the runner outlet obtained by Gino Blommaert are available for a similar machine [Blo95]. The experimental investigations are carried out at 70% of the best efficiency point flow rate ($H = 15[m]$, $Q = 0.37[m^3/s]$), both in the presence or absence of vapour in the vortex (this is obtained by adjusting the pressure level of the installation). The velocity profiles are found to be quite similar. A two phases compressible flow computation is outside the scope of this work but suitable because the volume of vapour is known to influence the vortex frequency and the level of the pressure fluctuations. The inlet velocity condition for the computation is interpolated from the phase averaged profiles obtained on a radius at 21 temporal steps, for the conditions without vapour. The phase average is tuned on the precession frequency $f_n = 0.224f_r = 2.6[Hz]$ (Strouhal number $St = f_n D/U_o = 0.4$, where D is the inlet diameter and U_o the mean inlet velocity). The profile shown in fig. 2.1 is made to turn at the vortex frequency.

2.2.1 Mesh and computational parameters

Because of code's limitations, the inlet region is meshed differently as in the previous investigations. A polar mesh with 40 grid points in the radial direction, 120 in the circumferential and 50 points in the axial direction is used to discretize the cone. The same choices used for the previous computations are applied. The convergence criterion for the maximal residuum of the internal loop that recovers the nonlinearity of the equations (II.2.1), is set to $1e^{-3}$. The time step is 1/60 of the period. The turbulence intensity is set to 5%.

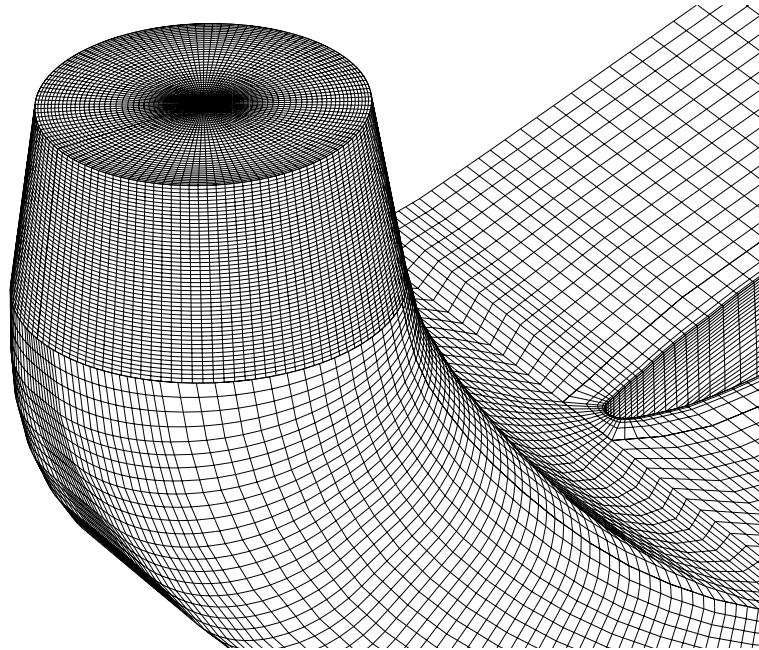


Figure 2.2: Mesh.

2.2.2 Results

The inlet profile and the velocity field in the cone shown in fig. 2.3 illustrate that the vortex core corresponds to the position of the maximal axial reversed flow. The backflow region rotates in the cone with the vortex (fig. 2.4) and does not occupy statically the central region. The longitudinal swirling regions giving rise to the helical motion are shown in fig. 2.5. The skin friction lines and tangential streamlines on several cross-sections for the global and fluctuating velocity field for a given phase, are given in fig. 2.6 to 2.9. The skin friction lines are almost identical for all the phases near the wall showing that this region is almost unaffected by the vortex movement. This is also visible in fig. 2.10 showing four phases. The vortex becomes static already in the bend. Fig. 2.11 displays the vector field, the position of the vortex core obtained by the eigenvector method of Sujudi and Haines [SH95] and the position of the local minimum of pressure. While in the cone the pressure local minimum corresponds quite well with the vortex core, in the bend the pressure gradients introduced by this component become predominant. The vortex core lines are shown in fig. 2.12. For some phases there is a discontinuity in the lines near the half bend (fig. 2.13), the secondary flow introduced by the bend being almost static. As previously discussed this interaction is suspected to be the excitation mechanism of the synchronous pressure and mass oscillation. The pressure and velocity signals in the domain are composed by the modes at the vortex frequency (mainly) and few harmonics only, as shown in fig. 2.14. The maximal pressure fluctuations reach 100% of the inlet kinetic energy at the inlet section and decay quickly, the flow in the channels being almost steady.

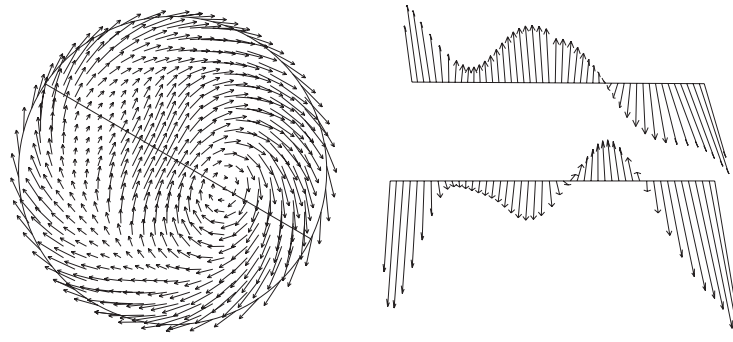


Figure 2.3: Example of velocity profiles in the cone. Tangential and axial vectors along the line passing through the vortex center.

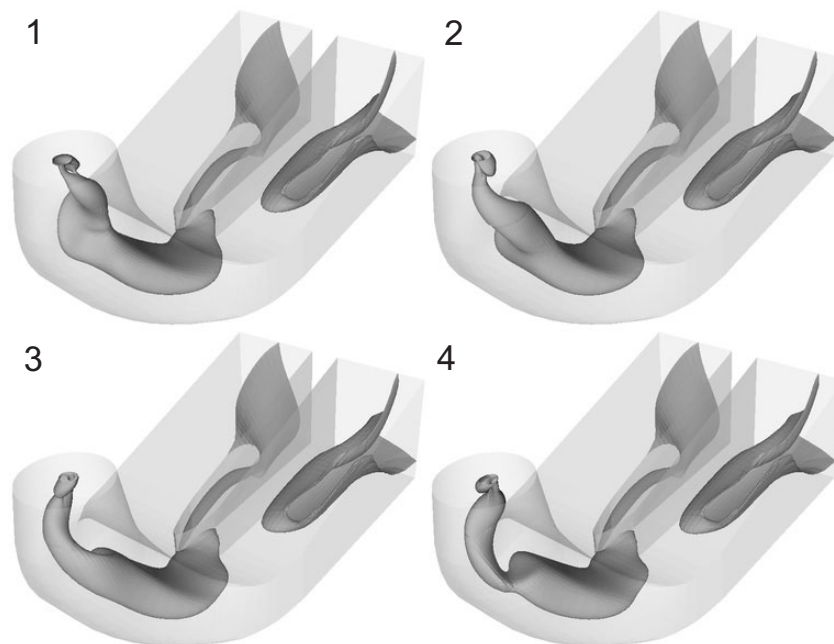


Figure 2.4: Backflow region at four phases equally spaced over a period.

The amplitudes of the pressure fluctuations normalized with the maximal value at each cross-section are shown in fig. 2.14. The fluctuations in the channels are weak. The phase at the vortex rotational frequency shows clearly coherent structures (fig. 2.16). The vortex motion affects only weakly the flow rate distribution in the two channels ($\pm 1\%$), while the static pressure recovery (efficiency) fluctuates between the values of 21% and 26% of the inlet kinetic energy (fig. 2.17).

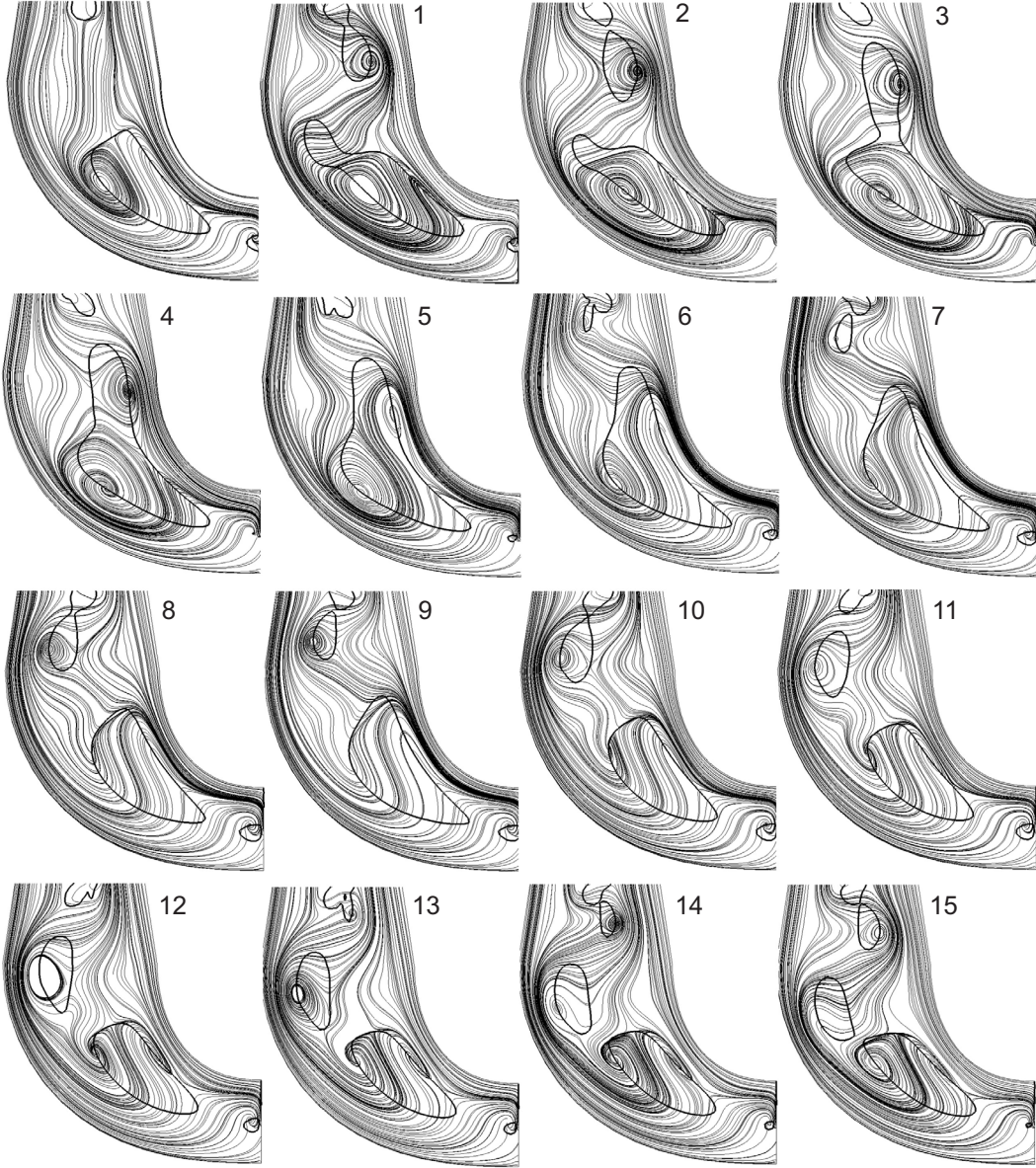


Figure 2.5: Tangential streamlines and backflow region (large lines) at several phases equally spaced over a period. The first picture represents the mean flow.

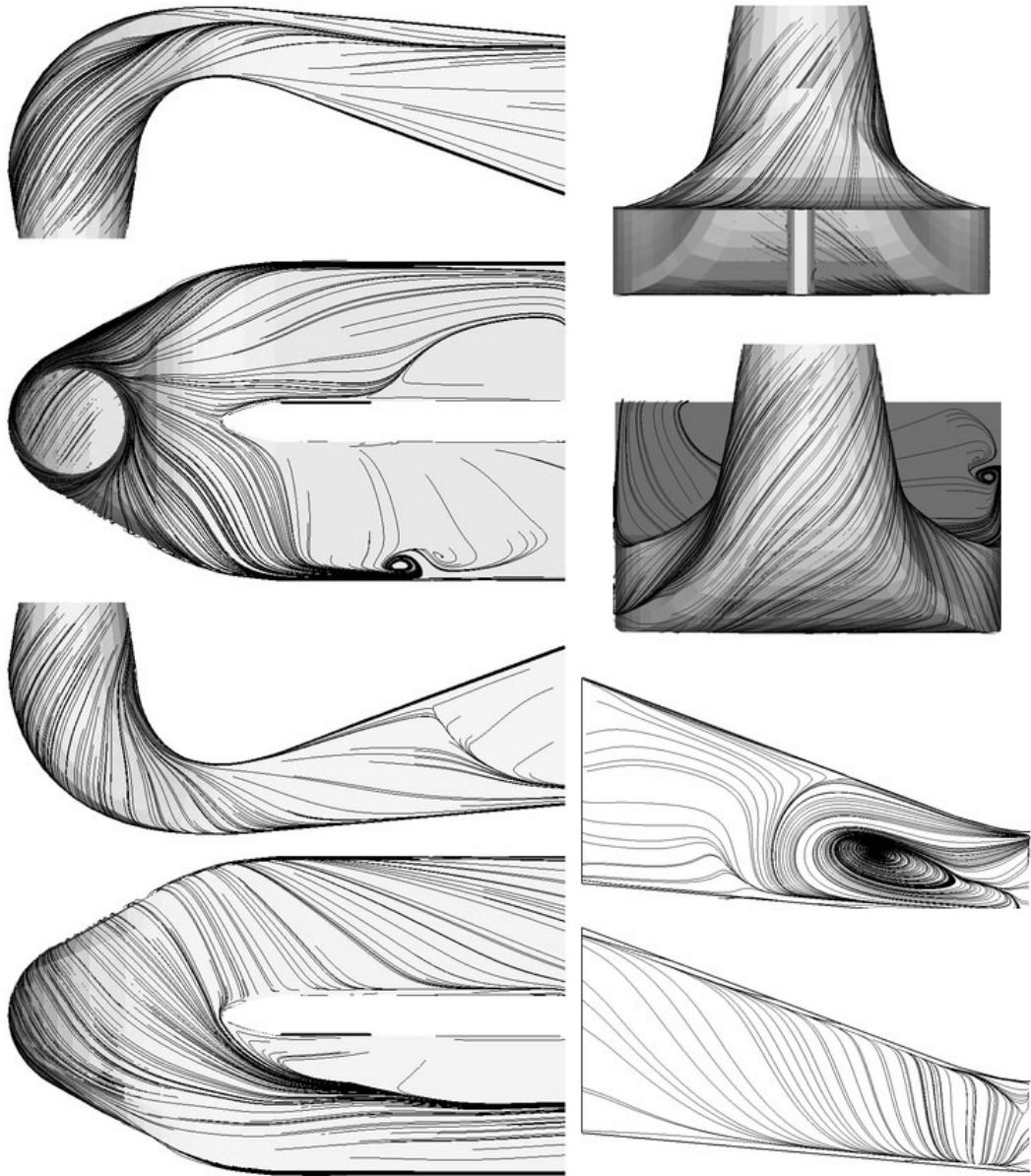


Figure 2.6: Skin friction lines for a given phase.

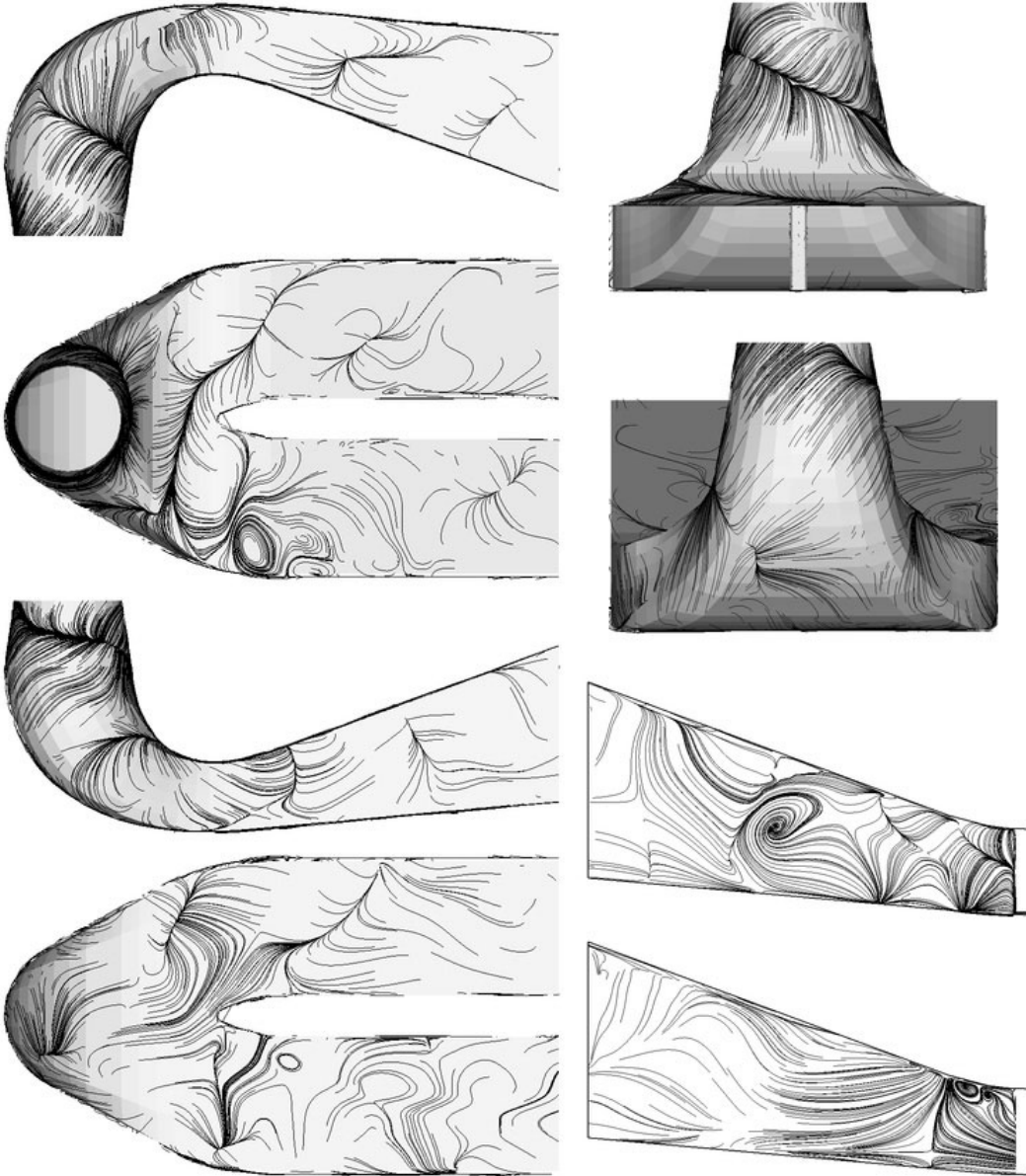


Figure 2.7: Skin friction lines of the fluctuating field at a given phase corresponding to fig. 2.6.

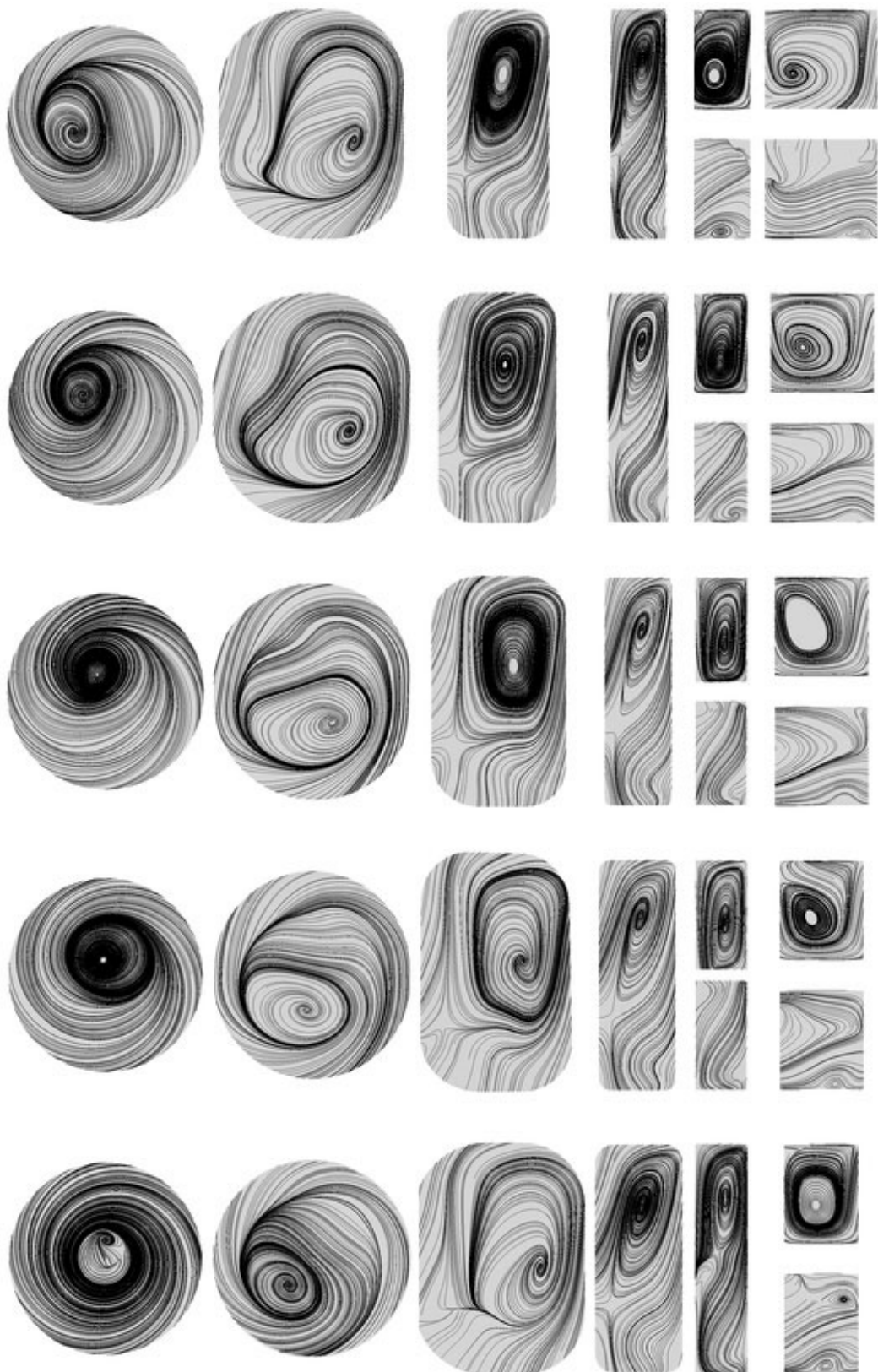


Figure 2.8: Instantaneous tangential streamlines at a given phase corresponding to fig. 2.6. From the inlet to the outlet.

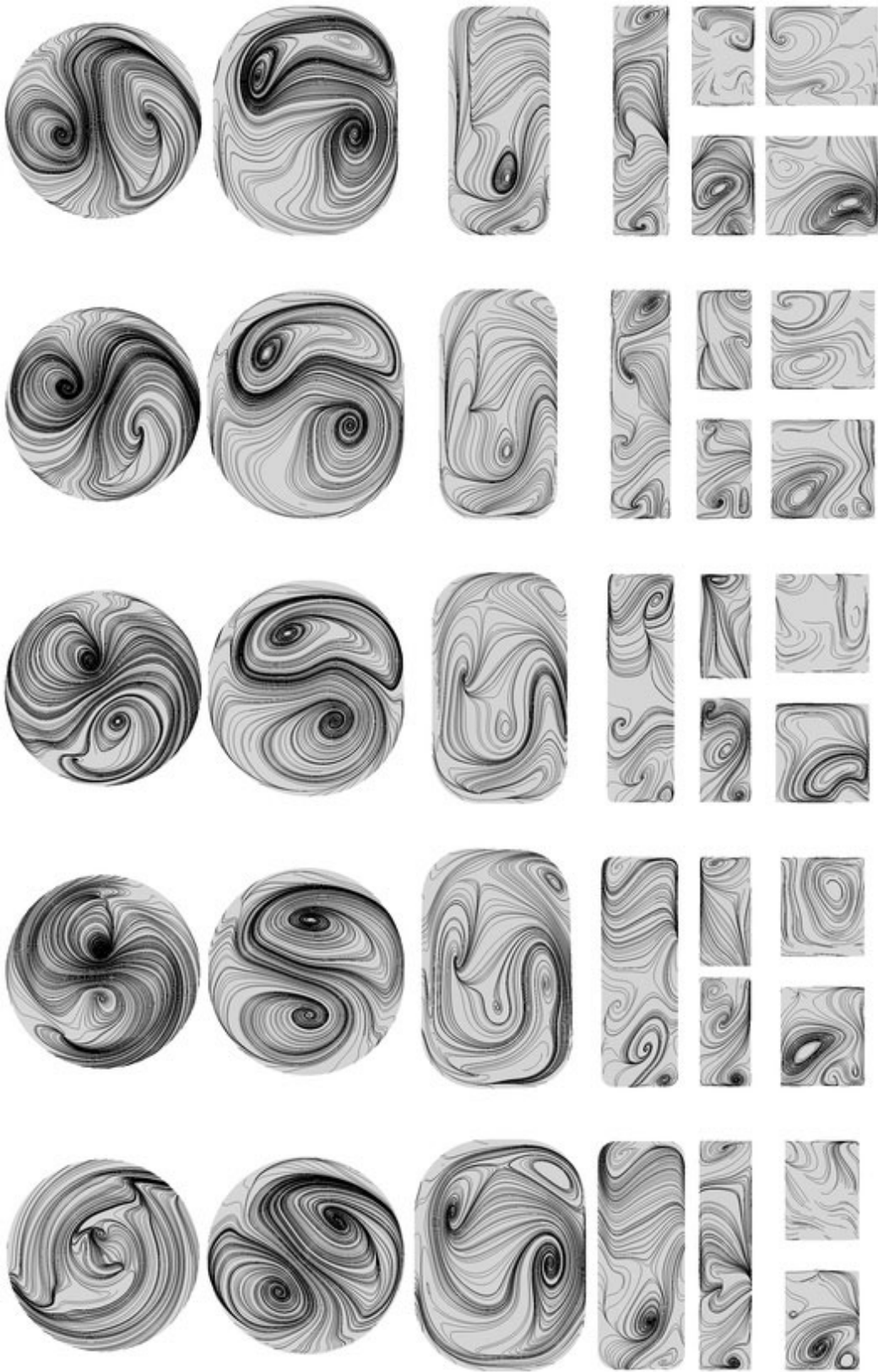


Figure 2.9: Instantaneous tangential streamlines of the fluctuating field at a given phase corresponding to fig. 2.6. From the inlet to the outlet.

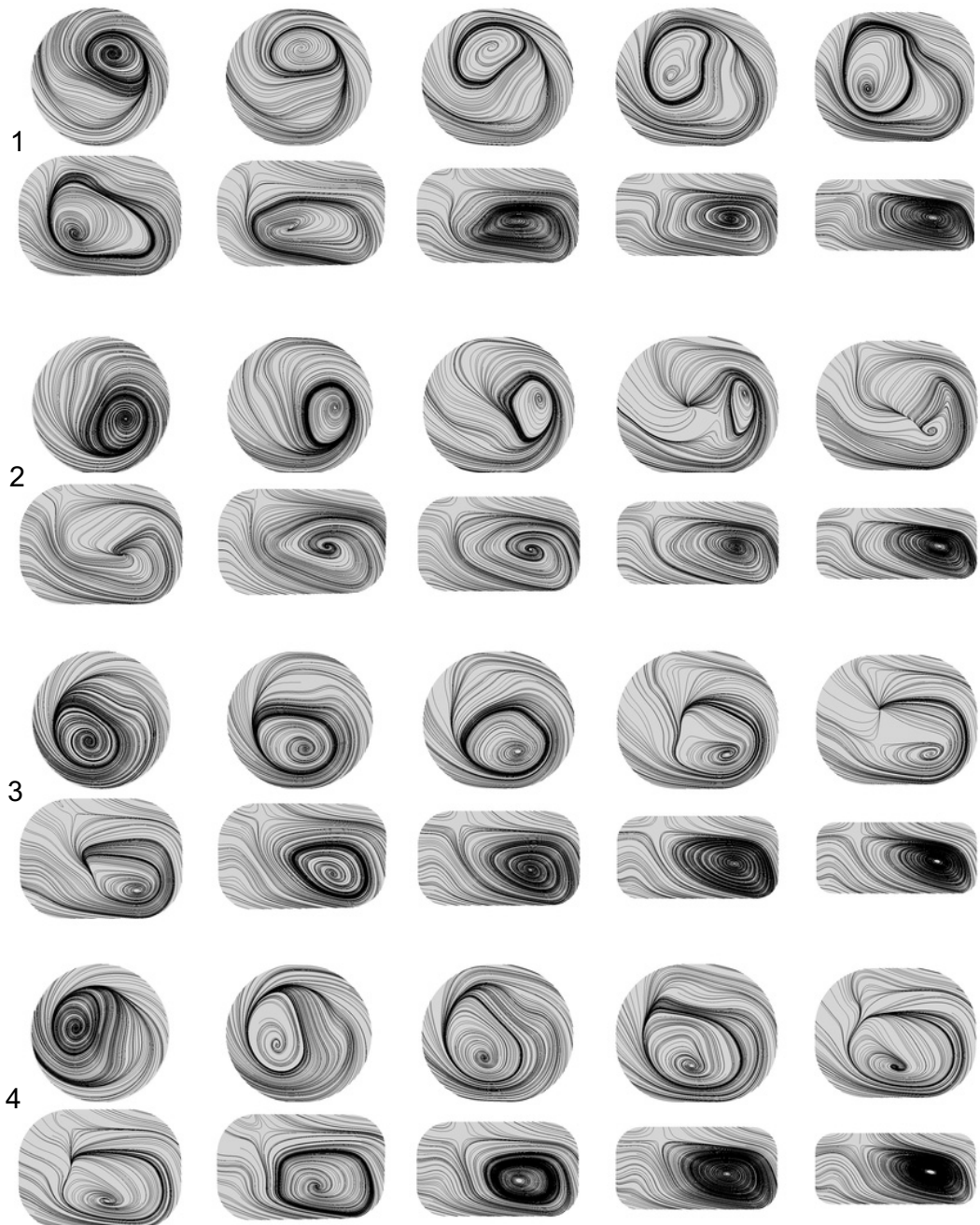


Figure 2.10: Instantaneous tangential streamlines at four phases equally spaced over a period. From the inlet to section 7.

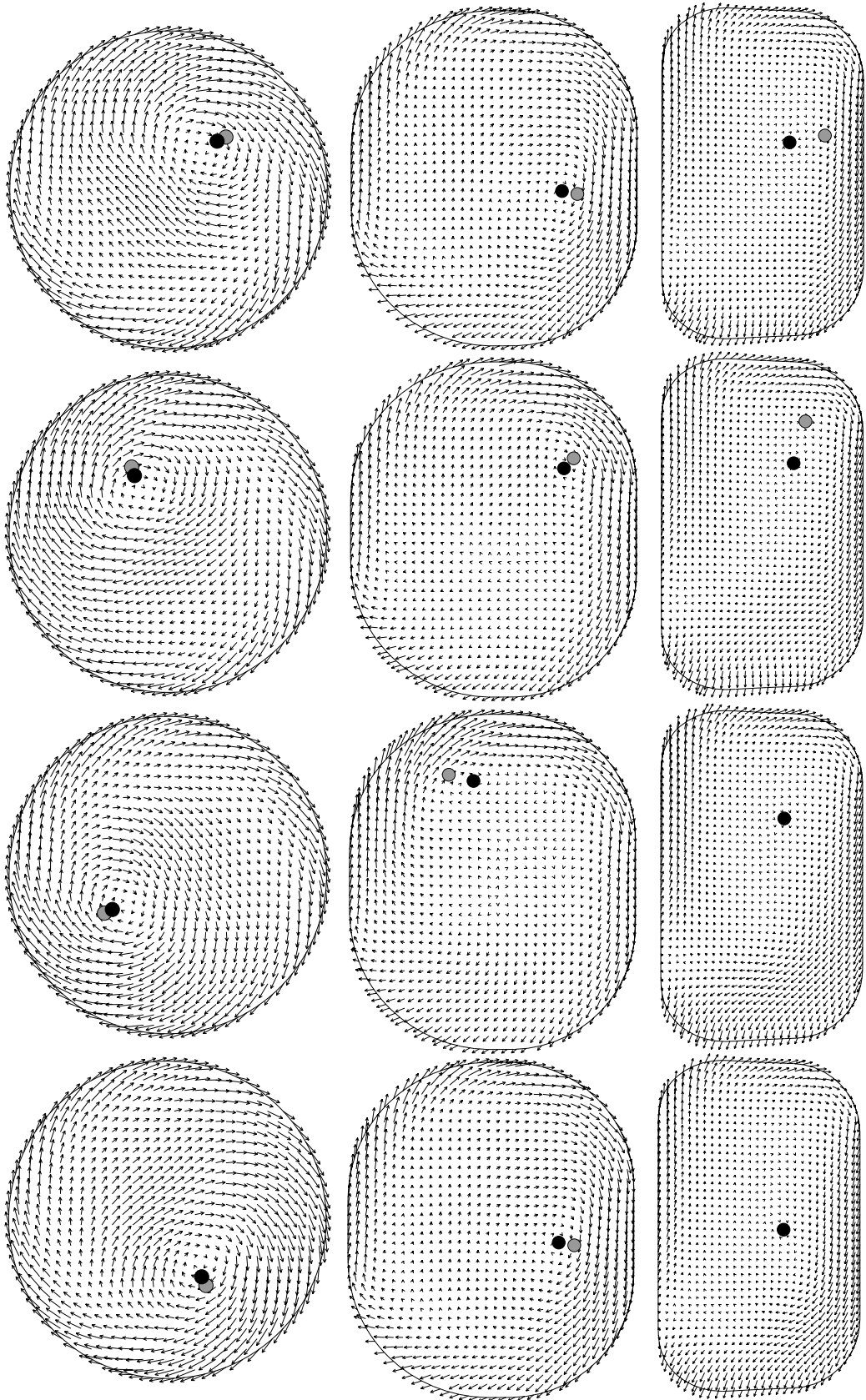


Figure 2.11: Position of the vortex core for a given phase identified with the eigenvector method of Sujudi and Haines [SH95] (black circles) and local minimum of pressure (gray circles), cross sections from the inlet to the bend.

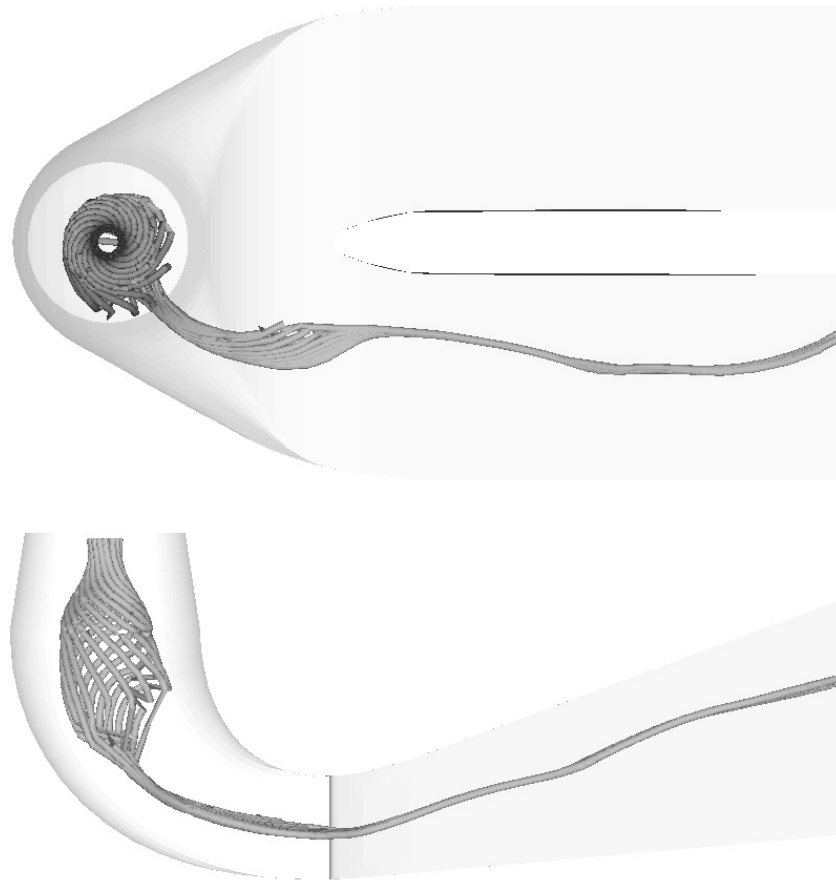


Figure 2.12: Vortex core identified with the eigenvector method of Sujudi and Haines [SH95]. 15 phases equally spaced over a period.

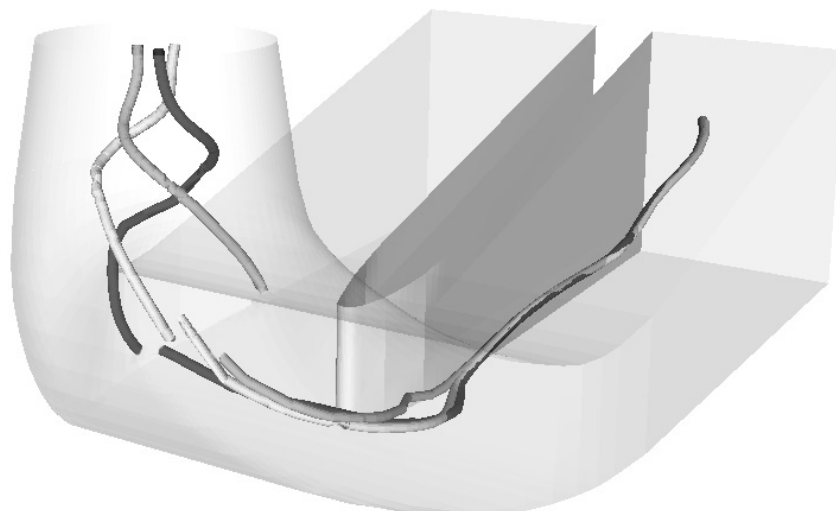


Figure 2.13: Discontinuity in the vortex core at three phases.

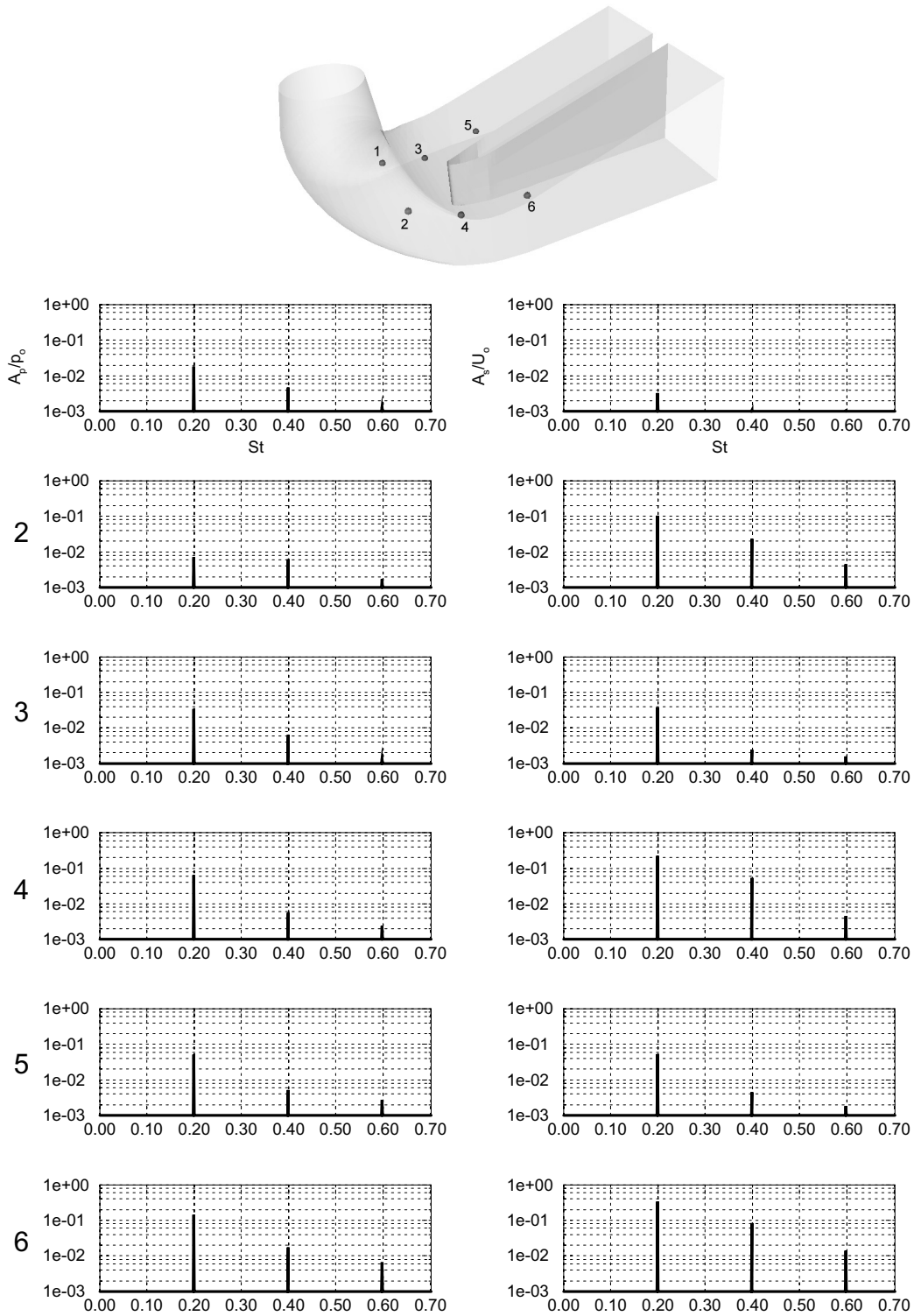


Figure 2.14: Discrete Fourier transform at several locations for the pressure and velocity signals.

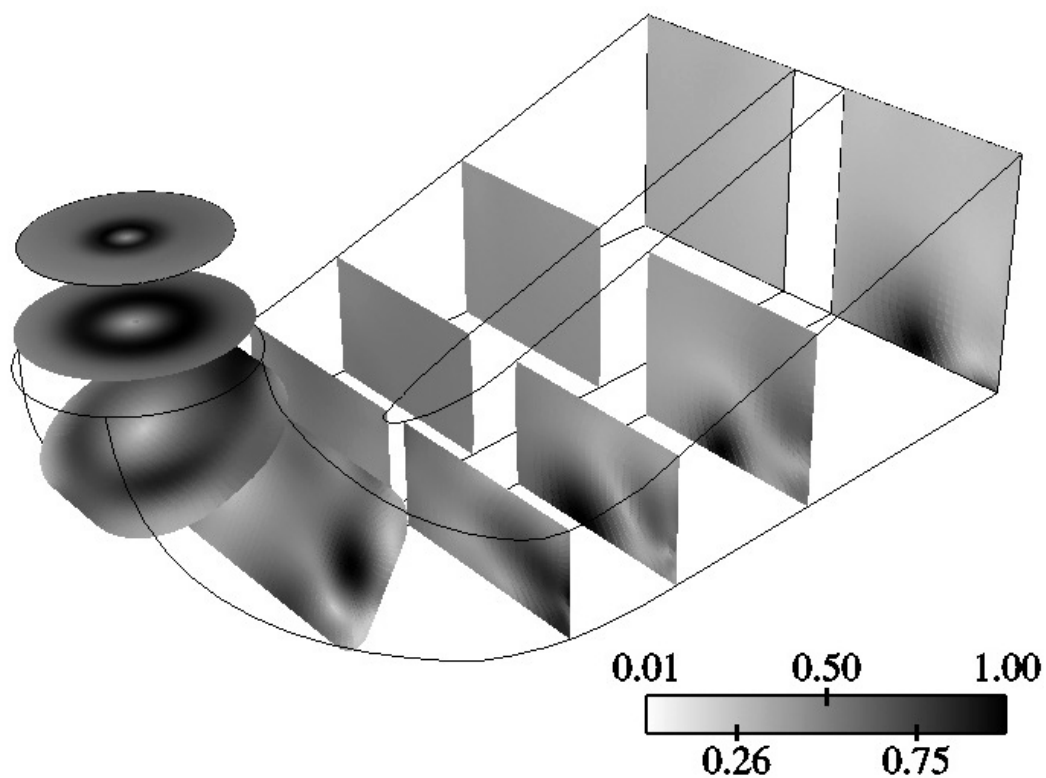


Figure 2.15: Amplitude of the pressure fluctuations at the vortex rotational frequency. The values are divided by the maximal amplitude of the corresponding cross-section.

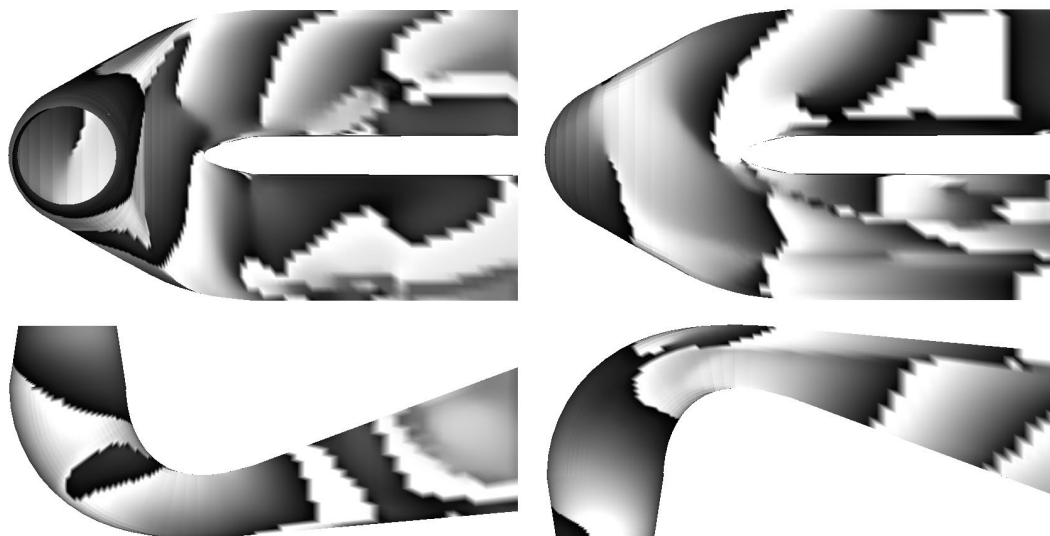


Figure 2.16: Phase of the wall pressure fluctuations, vortex frequency (from $-\pi$ (white) to π (black)) .

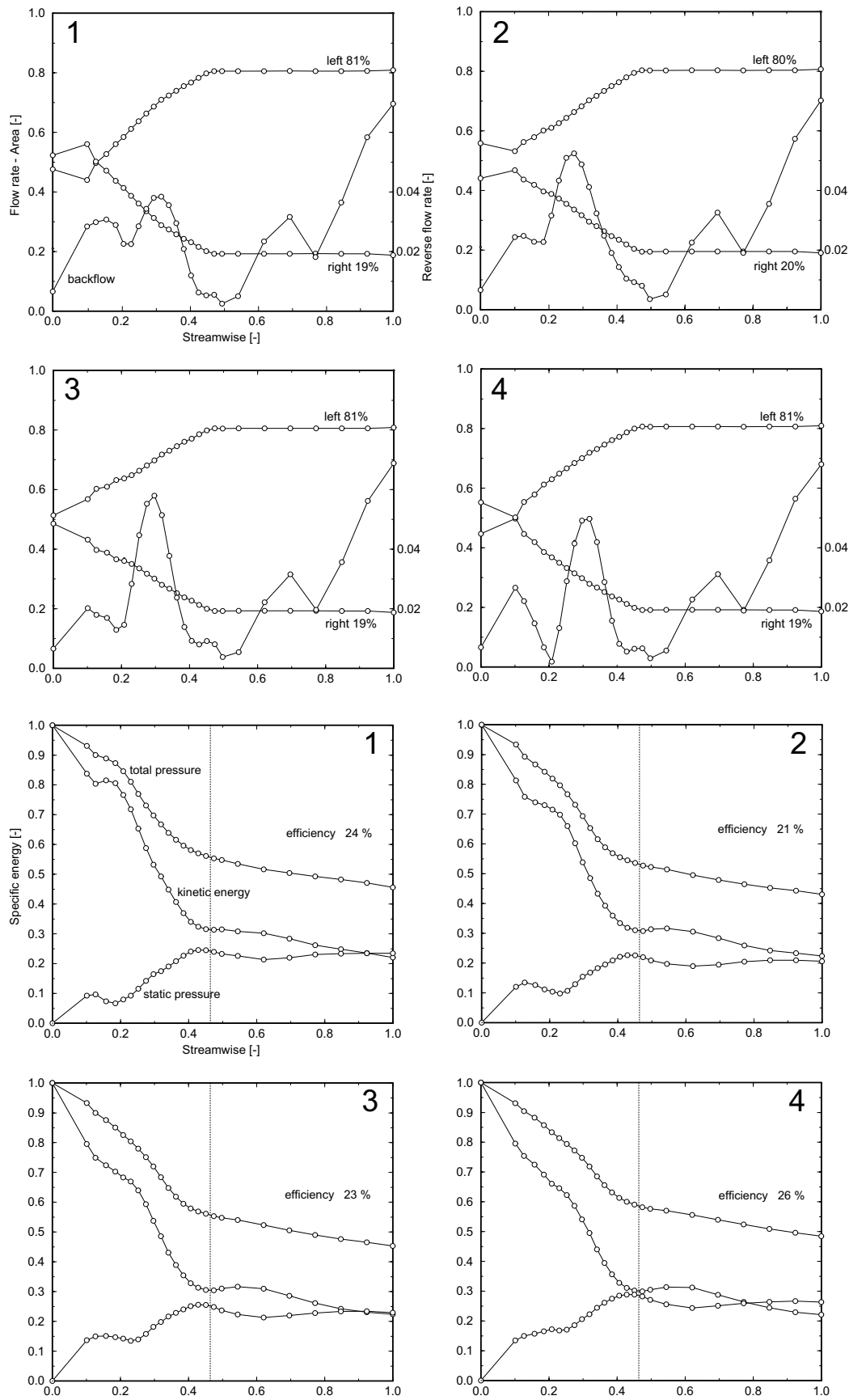


Figure 2.17: Flow rate distribution and specific energies evolution along the draft tube at four phases equally spaced over a period.

2.3 Time averaged inlet profile

In order to investigate the stability of the mean flow field, the axial symmetrical time averaged velocity profile (fig. 2.18) is imposed in the computation. The usual mesh is employed. While the $k - \epsilon$ model leads to a steady solution, the use of the RSM model captures the development of the rotating vortex in spite of the steady boundary conditions. The resulting velocity field is less smooth than that obtained with the $k - \epsilon$ model and the vortex core can be identified only in the cone as shown in fig. 2.19. The reverse flow region in the cone is however more symmetrical as in the previous case. The obtained vortex rotational frequency is inaccurate to within 9%. A difference of 1% is found on the frequency when the period is discretized with 60 or 120 time steps, indicating therefore the necessity of a high temporal accuracy. It should be noted that the symmetrical profile is imposed at some distance from the runner outlet. This and the fact that measurements were carried out on a different geometry and the negligence of compressibility effects are possible explanations for the lack of accuracy in the obtained frequency. The damping effect of the $k - \epsilon$ model could probably explain the steadiness of the flow downstream the bend, as observed when the phase averaged profile is imposed.

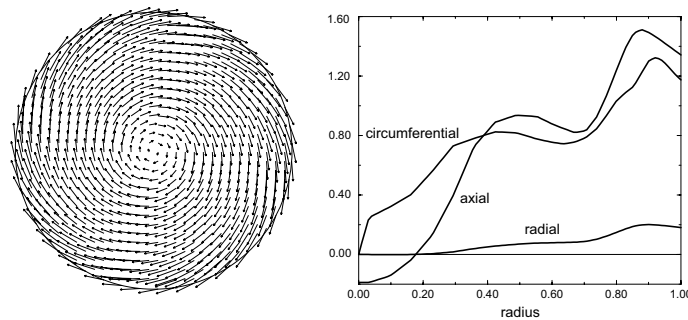


Figure 2.18: Inlet conditions, velocity field.



Figure 2.19: Vortex core identified with the eigenvector method of Sujudi and Haines [SH95]. 15 phases equally spaced over a period.

3

Conclusion

It seems that the code is not able to describe the evolution of the fluctuations introduced by the runner having a nondimensional frequency $St = 18$. For this reason it was not possible to investigate the influence of the forced oscillations on the self-sustained instabilities discussed in the previous part. On the other hand, at least in the first part of the draft tube, the rotating vortex seems to be qualitatively well predicted. This unsteadiness is however characterized by a lower frequency $St = 0.4$. As an additional comparison the self-sustained instabilities show slow oscillation having typically $St = 0.1$. Therefore it seems that problems arise in the computation of time-dependent flows when the unsteadiness largely dominates the convective terms. Even if it is not excluded, there is no direct evidence that this is due to the turbulence modeling.

4

Linear stability of the time averaged inlet profiles

There has been considerable work on the stability of vortex flows since the pioneer works of Howard & Gupta [HG62] and Batchelor & Gill [BG62]. Main objective was to understand the properties of aircraft trailing vortices and the phenomenon known as vortex breakdown ([Hal72] and [Lei78]). Most of these investigations focused on Batchelor's trailing vortex [Bat64]. The inviscid instability properties were first examined by Lessen, Singh & Paillet [LSP74] and more recently by Mayer & Powell [MP92]. Purely viscous modes display growth rates that are orders of magnitude below their inviscid counterparts ([LP74], [Kho91], [MP92]). The influence of swirl on the inviscid helical modes leads first to the attenuation of the co-rotating mode and to the enhancing of the counter-rotating one. The further increase of swirl gradually damp all modes until complete stabilization of the flow. The absolute-convective instability properties of the Batchelor vortex were determined by direct numerical simulation of the linear impulse response in [DCH98]. The application of swirl considerably widens the range of profiles giving rise to absolute instability. Only a slight amount of counterflow is necessary to trigger absolute instability.

The measured time averaged velocity profile at the runner outlet differs however from the flows considered in these studies. As preliminary investigation the temporal linear stability analysis is therefore carried out on the experimental profiles (fig. 2.18). The study should find out if the frequency of the rotating vortex is determined by its initial genesis due to infinitesimal perturbations, or by the following non-linear effects. The fluctuations observed for the points at part load are very strong and the investigation is therefore mainly addressed to a better understanding of the possible basic instability mechanism. The linearized stability equation system in cylindrical coordinates is solved by the Chebyshev spectral collocation method described in [KM89]. The discretization leads to a generalized eigenproblem. The method has been applied to the Poiseuille flow in a fixed or rotating pipe and to the Batchelor's trailing vortex and the results are in good agreement with those reported in the literature. Experimentally the helical vortex has a short wavelength and a very small diameter near the best efficiency region and its length increases up

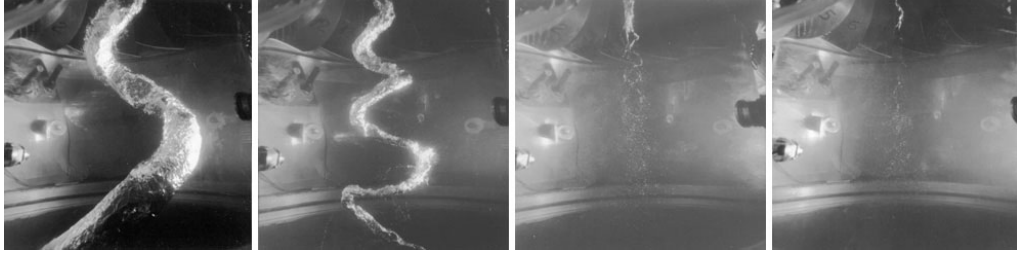


Figure 4.1: Vaporous core of the vortex in a $\nu = 0.5$ Francis turbine [Jac93]. From the left a) 80%, b) 90%, c) 95%, d) 100% of the best efficiency flow rate.

to about one diameter as the flow rate is decreased, as shown in fig. 4.1.

Governing equations

The flow with velocity $\mathbf{U} = (U_r(r), U_\theta(r), U_z(r))^T$ relative to cylindrical coordinates (r, θ, z) , is subjected to small disturbances. The velocity and pressure perturbation are respectively $\mathbf{u}'(r, \theta, z)$ and $p'(r, \theta, z)$. The following normal-mode type of disturbance is assumed

$$\mathbf{u}' = (iF(r), G(r), H(r))^T e^{i(\alpha z + n\theta - \omega t)} \quad (4.1)$$

$$p' = P(r) e^{i(n\theta + \alpha z - \omega t)} \quad (4.2)$$

Here α is the real axial wave number (wavelength $\lambda_z = 2\pi/\alpha$), n the integer azimuthal wave number (wavelength $\lambda_\theta = 2\pi/n$), and the complex temporal frequency ω determines by its imaginary part ω_i the amplification of the disturbance and by its real part the frequency $\omega_r/(2\pi)$. $F(r)$, $G(r)$, $H(r)$ and $P(r)$ are the complex disturbance eigenfunctions. Substituting the assumed flow field in the Navier-Stokes equations and neglecting the nonlinear terms, the linearized form of the governing equations is obtained. They can be written in nondimensional form as follows:

$$F' + \frac{F}{r} + \frac{nG}{r} + \alpha H = 0 \quad (4.3)$$

$$-\frac{iF''}{Re} + i \left[U_r - \frac{1}{Re r} \right] F' + \left[\omega + i \frac{dU_r}{dr} - \frac{nU_\theta}{r} - \alpha U_z + \frac{i}{Re} \left(\frac{n^2 + 1}{r^2} + \alpha^2 \right) \right] F + \left[\frac{i2n}{Re r^2} - \frac{2U_\theta}{r} \right] G + P' = 0 \quad (4.4)$$

$$-\frac{G''}{Re} + \left[U_r - \frac{1}{Re r} \right] G' + \left[-i\omega + \frac{inU_\theta}{r} + i\alpha U_z + \frac{U_r}{r} + \frac{1}{Re} \left(\frac{n^2 + 1}{r^2} + \alpha^2 \right) \right] G + \left[i \frac{dU_\theta}{dr} + \frac{2n}{Re r^2} + \frac{iU_\theta}{r} \right] F + \frac{inP}{r} = 0 \quad (4.5)$$

$$-\frac{H''}{Re} + \left[U_r - \frac{1}{Re r} \right] H' + \left[-i\omega + \frac{inU_\theta}{r} + i\alpha U_z + \frac{1}{Re} \left(\frac{n^2}{r^2} + \alpha^2 \right) \right] H + i \frac{dU_z}{dr} F + i\alpha P = 0 \quad (4.6)$$

where Re is the Reynolds number based on the cone radius, and primes denote differentiation with respect to the radial coordinate. The variation of the mean axial profile in the z -direction appearing in the z -momentum equation (4.6) is neglected. It has been confirmed experimentally that this gradient is small. Helical vortices very similar to those observed in the cone of Francis turbines can be seen also in simple cylinders. This approximation is therefore expected to have only a slight influence on the main results. The radial component is consequently also neglected. The system represents an eigenproblem, with ω as eigenvalue and is solved for a given axial and circumferential wave number. At the outer wall the no-slip conditions are enforced and at the centerline all physical quantities must be smooth and bounded. As discussed in [KM89] the boundary conditions are for $n = 1$: $F = G = H = P = 0$ at the wall and $H = P = 0$, $F + G = 0$, $2F' + G' = 0$ at the centerline.

Numerical method

An interpolant polynomial is constructed in terms of the values of the flow variable at collocation points by employing a truncated Chebyshev series. Chebyshev polynomials are defined on the interval $(-1,1)$ by $T_k(\zeta) = \cos[k \cos^{-1}\zeta]$, where the following transformation relates the variable to the physical radius: $\zeta = 1 - 2r$. The collocation points are the extrema of the last retained Chebyshev polynomial in the truncated series: $\zeta_j = \cos\frac{\pi j}{N}$, $j = 0, 1, \dots, N$. As example the eigenfunction F is approximated with

$$F(\zeta) = \sum_{k=0}^N a_k T_k(\zeta) \quad (4.7)$$

the derivatives of the variables are determined explicitly using the interpolant:

$$\frac{dF}{d\zeta} \Big|_j = \sum_{k=0}^N A_{jk} F_k, \quad \frac{d^2 F}{d\zeta^2} \Big|_j = \sum_{k=0}^N B_{jk} F_k \quad (4.8)$$

$j = 0, 1, \dots, N$, where A_{jk} and B_{jk} are the elements of the derivative matrices and are given as:

$$A_{jk} = \frac{C_j (-1)^{k+j}}{C_k (\zeta_j - \zeta_k)} \quad (j \neq k) \quad (4.9)$$

$$A_{jj} = -\frac{\zeta_j}{2(1 - \zeta_j^2)}$$

$$A_{00} = -A_{NN} = \frac{2N^2 + 1}{6}$$

$$B_{jk} = A_{jm} A_{mk} \quad (4.10)$$

with $C_0 = C_N = 2$, $C_j = 1$ for $1 \leq j \leq N-1$. The extension to the others variables is straightforward. Inserting the polynomials in (4.3)-(4.6) the governing equations can be represented in the generalized eigenvalue format as

$$D\mathbf{X} = \omega E\mathbf{X}, \quad \mathbf{X} = [F \ G \ H \ P]^T \quad (4.11)$$

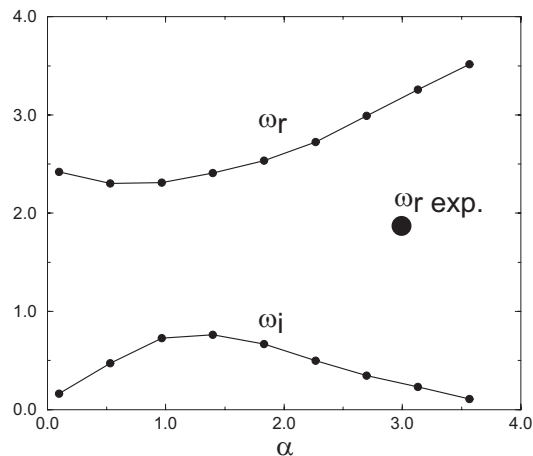


Figure 4.2: Variation of the growth rate ω_i and frequency ω_r versus axial wave number α of the disturbances for the most amplified helical ($n=1$) mode, $\varphi^* = 0.703$, measured profile.

D and E are square matrices with dimension $4(N+1)$. Since E is singular, an artificial compressibility factor $\gamma\omega P$ is introduced in the continuity equation (γ is a very small value). The generalized eigenproblem is solved using the QZ algorithm implemented in the NAG library.

Results

The radius is discretized with 151 points. The time averaged measured profile at $\varphi^* = 0.703$ is first considered. The variation of the nondimensional growth rate and frequency of the disturbances for the most amplified helical ($n=1$) mode plotted against the axial wave number is shown in fig. 4.2. Experimentally the nondimensional frequency and axial wave number of the helical vortex are respectively 1.86 and about 3. As described in the previous chapter the frequency obtained with the RANS computation is 9% lower than the experimental value. The most amplified computed wave number is 1.43 corresponding to a frequency of 2.48 and a growth rate of 0.73 (fig. 4.2). As expected the frequency is not accurately predicted (50% error). However, the fluctuating field shown in fig. 4.4 is similar to that obtained with the RANS computation (fig. 2.9, chapt. 2). In particular the distance of the vortex core to the center is very close in the two cases. In order to identify the main instability mechanism the mean profiles are simplified as shown in fig. 4.3. Two additional operating points at higher flow rate are also investigated. The results are illustrated in fig. 4.3 and 4.4. The simplified profiles show the same characteristics as the experimental profiles. The observations illustrated in fig. 4.1 agree in the main trend with the predicted axial wavelength and fluctuating field. The points at the higher flow rates are even more unstable than the point at part load.

Even when neglecting the swirling component at $\varphi^* = 0.703$ the simplified axial profile shows unstable modes. The perturbation field is similar to that

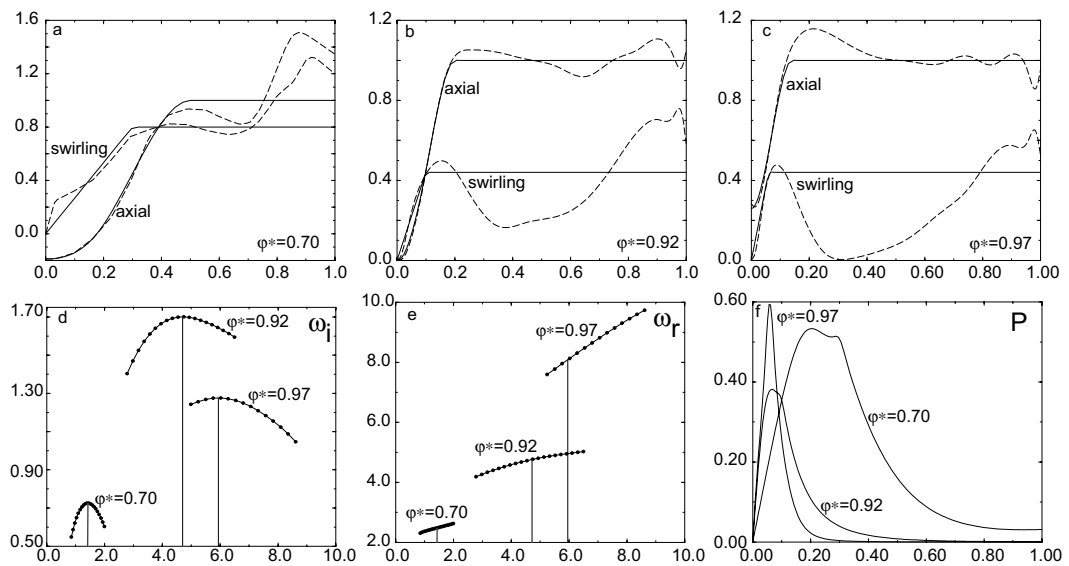


Figure 4.3: a) b) c) Simplified profiles (dotted lines: experimental). d) Variation of the growth rate ω_i and e) frequency ω_r versus axial wave number α of the disturbances for the most amplified helical ($n=1$) mode. f) Spatial distribution of the amplitude of the eigenfunction P .

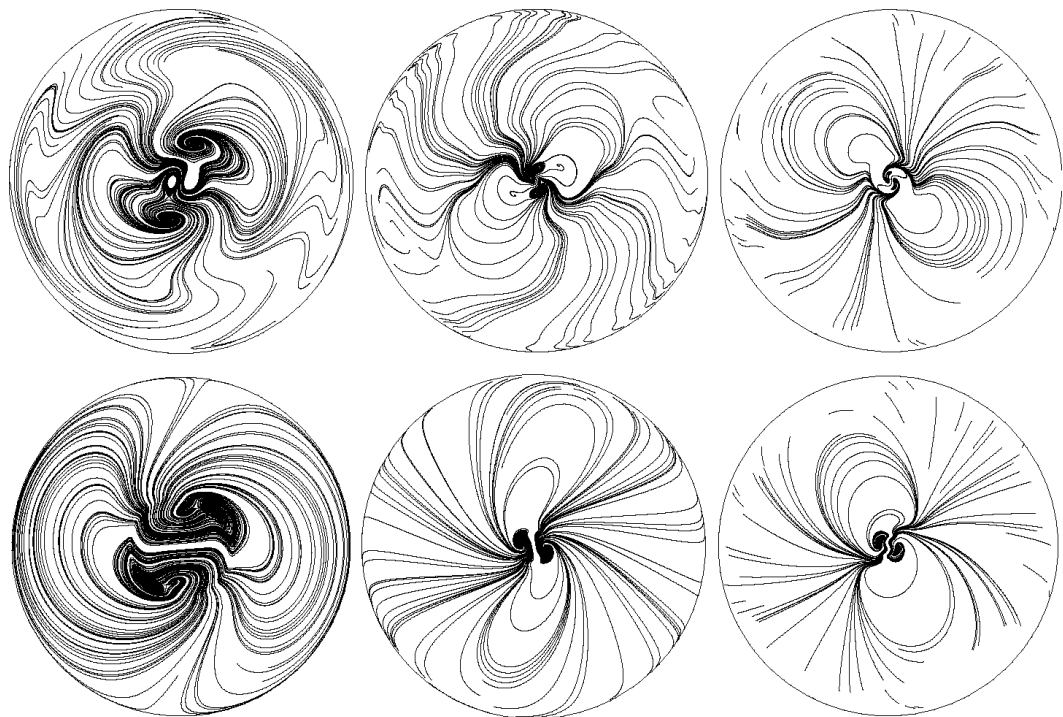


Figure 4.4: Streamlines of the most amplified perturbation velocity field for the three operation conditions. From the left $\varphi^* = 0.703$, $\varphi^* = 0.919$, $\varphi^* = 0.973$. Top: experimental profile, bottom: simplified profile.

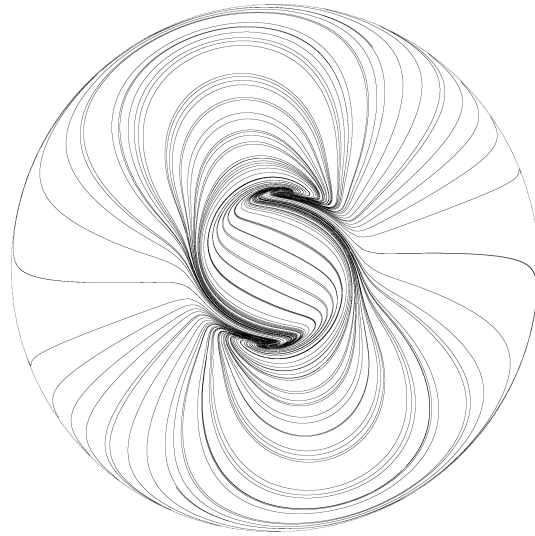


Figure 4.5: Streamlines of the most amplified perturbation velocity field for the simplified axial velocity profile without the swirling component, $\varphi^* = 0.703$.

obtained with the swirling component (fig. 4.5). The center of the resulting vortex corresponds to the inflection point in the axial profile. It seems therefore that this point causes the main instability mechanism, following the classical Rayleigh criterion. The swirling component is hence only indirectly related to the appearance of the rotating helical vortex. It is the rotational motion that induces the trough in the axial velocity. An increase of the Reynolds number does not affect significantly the results, showing the inviscid nature of this instability.

IX

Summary and perspectives

Summary and perspectives

Summary

The numerical simulation of the unsteady turbulent flow in a draft tube is carried out with a commercial finite volume code solving the Reynolds averaged Navier-Stokes equations.

The flow in the draft tube is complex because of its unsteady three-dimensional and rotating nature. Time-dependent investigations have become feasible for industrial complex geometries; the limitations of this approach, however, are not well known. This work attempts to increase the understanding of the draft tube flow and to define the prediction capability of the model. Although the large-scale development of the hydroelectric resources on our continent is practically complete, the industrial interest lies in the considerable economical potential for refurbishment of the existing power plants.

Firstly, basic flows are addressed. Four reference cases testify the capability of the code to describe a laminar pulsating flow, a self-sustained vortex shedding behind a bluff body and the influence of swirl and adverse pressure gradients. However, these tests confirm that the model is not able to accurately predict swirling flows.

The attention is then focused on the mean flow field in the draft tube. Comparisons with detailed experimental data over an extended range of operating conditions reveal the limitations of the approach and the sensitivity on the inlet boundary conditions. After the parameters are calibrated, the mean flow field is however correctly captured with main trends. Quantitatively the static pressure recovery is reasonably well predicted while locally the flow details are partially missed. The numerical optimization of this component without measurements could be therefore hazardous. In spite of the detailed measurements, it is clear that insufficient data is present for the definition of the mean flow boundary conditions. A great effort is underway in the development of advanced turbulence models such as LES methods. These are today applicable to complex geometries. The use of advanced models however, requires even more detailed information at the boundaries, making this approach even more difficult to properly apply.

Visualization of scientific data sets plays an important role in understanding complex phenomena and data mining becomes more and more indispensable

with the acquisition of time-dependent high-resolution data by means of the numerical simulation. The topological study of the flow field is a useful tool in the synthesis and analysis of the data and has allowed the comprehension of the efficiency drop in the draft tube. The topological structure of the flow field shows a bifurcation with the flow rate as parameter leading to a Werlé-Legendre separation that reduces the performances over an operating range.

Time-dependent flow phenomena are then investigated. Steadiness is always a scale dependent characteristic in real flows. Measurements show regions with strong fluctuations, in particular for the operating points at higher flow rate or at part load, where oscillations are related to the onset of a periodic rotating fairly helical vortex. The runner rotation also introduces fluctuations at different frequencies. Firstly, possible self-sustained time-dependent phenomena are addressed. Even with steady boundary conditions two computations at different operating conditions predict self-sustained vortex shedding at a nondimensional frequency of about $St = 0.1$. Both cases are characterized by the existence of a backflow region and a focus located between two saddle points along the separatrix, defining the border of this region at the wall. The mean flow field is however only slightly affected by these phenomena.

Forced time-dependent phenomena are then considered. The code is apparently not able to describe the evolution of the oscillations introduced by the blade passage, which are characterized by a high frequency $St = 18$. A quick damping of the fluctuations, caused by an error in the prediction of the phase shift between velocity and pressure fluctuations, is observed. Experimentally these fluctuations are however recognized to disappear already at the cone outlet. On the other hand, at least in the first part of the draft tube, the rotating helical vortex seems to be qualitatively well predicted. The rotational frequency is $St = 0.4$. The computation of the operating point at part load by imposing the time averaged profile can predict, at least when an advanced turbulence model is applied, the onset of the instability without the necessity of any perturbation. It seems therefore that problems arise in the computation of time-dependent flows when the unsteadiness largely dominates the convective terms. Even if it is not excluded, there is no direct evidence that this is due to the turbulence modeling.

As a preliminary investigation a temporal linear stability analysis is carried out on experimental profiles with the objective to gain some insight of the basic instability mechanism at part load. Even if the frequency is not accurately predicted probably due to the influence of non-linear effects it seems that the instability has an inviscid nature and is attributable to the inflection point in the axial profile. The swirling component is hence only indirectly related to the appearance of the rotating helical vortex.

Perspectives

Complementary measurements should reduce the degrees of freedom in the inlet boundary definition and clarify the necessary level of detail. For instance the inlet turbulent kinetic energy profile is almost uninfluential on the prediction. The model is probably unable to correctly account for all the imposed information. The problem with the inlet boundary condition underlines the necessity for coupled runner-draft tube computations. Several research groups are currently investigating the capability of unsteady rotor-stator interface models. However the limitations of turbulence models, even for the prediction of relatively simple steady flows, are well known. The attempt to take into account more complex phenomena is questionable.

The capabilities of second-order closure schemes are still unclear. The employed RSM model performs poorly in the prediction of the steady state flow. The Reynolds' stress tensor at the inlet is however simply assumed isotropic and defined by the measured kinetic energy profile. On the other hand only this scheme is able to predict the onset of the self-sustained instability at part load. Investigations on the influence of the inlet Reynolds' stresses should definitively define the real potential of this turbulence model. LES computations are today feasible and it would be interesting to verify this approach in particular for the prediction of high frequency flow phenomena.

The analysis of the skin friction lines is found to be a very effective tool in the analysis of the numerical results. The interest of an automatic topological analysis is evident. This kind of investigation could also deliver valuable experimental data by means of the surface oil-flow visualization technique. Even if the investigation is more qualitative, it shows not only the main trends but also the localization of the critical regions in the flow. The global character of these measurements facilitates the interpretation of the comparison with the predicted flow.

Currently PIV measurements are carried out in the draft tube and will probably clarify the nature of the large scaled unsteadiness directly observable in the outlet region. This should indicate the physical or numerical nature of the predicted self-sustained vortex shedding phenomena.

In the near future, measurements will be available to quantitatively verify the prediction capability of the instability at part load. This capability will be useful for the conception of preventive measures that reduce dangerous fluctuations. A two-phase flow computation should be envisaged.

Unsteady computations still require several weeks of CPU time and this fact has limited the investigations. Additional, both experimental and numerical, studies are still necessary in order to clearly define the potential of the URANS approach.

Bibliography

- [Ack58] S. Ackeret. Grenzschichten in geraden und gekrümmten Diffusoren. In H. Grötler, editor, *IUTAM Symposium Freiburg*, pages 22–37, 1958. AIAA paper No. 87-0059.
- [AF89] S. W. Armfield and C. A. J. Fletcher. Comparison of $k - \epsilon$ and algebraic Reynolds stress models for swirling diffuser flow. *International Journal for Numerical Methods in Fluids*, 9:987–1009, 1989.
- [ARC88] M. Agouzoul, M. Reggio, and R. Camarero. A three-dimensional turbulent flow analysis in a draft tube. In *Hydraulic Machinery and Cavitation [Hyd88]*, pages 567–575. I5, Vol. 2.
- [ASM00] *Proceedings of ASME FEDSM'00*, Boston MA, 11-15 June 2000.
- [Ave01] F. Avellan. *Introduction aux turbomachines, notes de cours*. LMH-EPFL Lausanne, 2001.
- [Bat64] G. K. Batchelor. Axial flow in trailing line vortices. *J. Fluid Mech.*, 20:645–658, 1964.
- [Bat67] G. K. Batchelor. *An introduction to fluid dynamics*. Cambridge University Press, 1967.
- [BFM⁺99] R. Bader, J. Fritz, Y. Mochkaai, W. Knapp, and R. Schilling. Experimental and theoretical loss analysis in a Kaplan turbine. In *Turbine-99 Workshop on Draft Tube Flow [GGK99]*.
- [BG62] G. K. Batchelor and A. E. Gill. Analysis of the stability of axisymmetric jets. *J. Fluid Mech.*, 14:529–551, 1962.
- [BK81] G. Binder and J.-L. Kueny. Measurements of the periodic velocity oscillations near the wall in unsteady turbulent channel flow. In L. J. S. Bradbury, F. Durst, B.E. Launder, F. W. Schmidt, and J. H. Whitelaw, editors, *Turbulent Shear Flows 3*, pages 6–17, The University of California, Davis, September 9-11 1981. Springer.
- [Blo95] Gino Blommaert. Mesure du champ de vitesse instationnaire à la sortie d'une roue Francis avec anémométrie doppler à laser. Technical report, LMH-EPFL Lausanne, 1995.
-

- [Bos95] G. Bosch. *Experimentelle und theoretische Untersuchung der instationären Strömung um zylindrische Strukturen*. PhD thesis, Universität Friedericiana zu Karlsruhe, 1995.
- [BT71] P. W. Bearman and D. M. Trueman. An investigation of the flow around rectangular cylinders. *Aerodynamical Quarterly*, 23:1–6, 1971.
- [CEM96] E. Cabrera, V. Espert, and F. Martinez, editors. *Hydraulic Machinery and Cavitation*, volume 1, Dordrecht NL, 1996. Kluwer Academic Publishers. Proceedings of the XVIII IAHR Symposium.
- [Che95] X. Chen. *Multi-dimensional finite volume simulation of fluid flows on fixed, moving and deforming mesh systems*. PhD thesis, University of Minnesota, 1995.
- [Chi93] W. S. Chihab. *Experimentelle und theoretische Untersuchung des Saugrohres einer Kaplan turbine*. PhD thesis, Universität Stuttgart, 1993.
- [CKA00] G. D. Ciocan, J.-L. Kueny, and F. Avellan. Optical measurement techniques for experimental analysis of hydraulic turbines rotor-stator interaction. In ASME [ASM00]. Paper FEDSM2000-11084.
- [CKW93] P. D. Clausen, S. G. Koh, and D. H. Wood. Measurements of a swirling turbulent boundary layer developing in a conical diffuser. *Experimental thermal and fluid science*, 6(1):39–48, 1993.
- [CMAK01] G. D. Ciocan, S. Mauri, J. A. Arpe, and J.-L. Kueny. Étude du champ instationnaire de vitesse en sortie de roue de turbine. *La Houille Blanche*, 2:46–59, 2001.
- [CVD⁺90] J. F. Combes, A. Verry, M. Delorme, R. Philibert, and J. M. Vanel. Numerical and experimental analysis of the flow inside an elbow draft tube. In Hydraulic Machinery and Cavitation [Hyd90]. G5, Vol. 1.
- [DBSV90] S. Deniz, M. Bosshard, J. Speerli, and P. Volkart. Saugrohre bei Flusskraftwerken. Technical Report 106, VAW ETHZ, 1990.
- [DCH98] I. Delbende, J.-M. Chomaz, and P. Huerre. Absolute/convective instabilities in the Batchelor vortex: a numerical study of the linear impulse response. *J. Fluid Mech.*, 355:229–254, 1998.
- [Dél01] J. M. Délyery. Toward the elucidation of three-dimensional separation. *Annual Review of Fluid Mechanics*, 33:129–54, 2001.
-

-
- [DGS92] P. Drtina, E. Goede, and A. Schachenmann. Three-dimensional turbulent flow simulation for two different hydraulic turbine draft tubes. In C. Hirsch et al., editor, *Computational Fluid Dynamics 92*, pages 199–206. Von Karman Institute, Elsevier Science, 1992.
- [DHP88] D. F. G. Durao, M.V. Heitor, and J. C. F. Pereira. Measurements of turbulent and periodic flow around a square cross-section cylinder. *Exp. Fluids*, 6:298–304, 1988.
- [DR81] P. G. Drazin and W. H. Reid. *Hydrodynamic stability*. Cambridge University Press, 1981.
- [FP99] J. H. Ferziger and M. Perić. *Computational Methods for Fluid Dynamics*. Springer, 1999. Second ed.
- [Ge98] C. Godreche and P. Manneville (editors). *Hydrodynamics and Nonlinear Instabilities*. Cambridge University Press, 1998.
- [GGK99] B. R. Gebart, L. H. Gustavsson, and R. I. Karlsson. Proceedings of turbine-99 workshop on draft tube flow. Technical report, Lulea University of Technology, Department of Mechanical Engineering, Division of Fluid Mechanics, 1999. (Porjus, Sweden, June 20-23).
- [Hal72] M. G. Hall. Vortex breakdown. *Annual Review of Fluid Mechanics*, 4:195–218, 1972.
- [HG62] L. N. Howard and A. S. Gupta. On the hydrodynamic and hydro-magnetic stability of swirling flows. *J. Fluid Mech.*, 14:463–476, 1962.
- [HP84] H. Hornung and A. E. Perry. Some aspects of three-dimensional separation, part I: Streamsurface bifurcations. *Z. Flugwiss. Weltraumforsch.*, 8, Heft 2:77–87, 1984.
- [Hyd88] *Hydraulic Machinery and Cavitation*, Trondheim, 20-23 June 1988. Tapir Publishers. Proceedings of the XIV IAHR Symposium.
- [Hyd90] *Hydraulic Machinery and Cavitation*, Belgrade Yugoslavia, 1990. Proceedings of the XV IAHR Symposium.
- [Hyd94] *Hydraulic Machinery and Cavitation*, Beijing China, 1994. Proceedings of the XVII IAHR Symposium.
- [Ide69] I. E. Idelcik. *Memento des pertes de charge*. Eyrolles, Paris, 1969.
- [IEC99] *Hydraulic turbines, storage pumps and pump-turbines - Model acceptance tests*, 1999. International Standard IEC 60193.
-

- [Jac93] T. Jacob. *Evaluation on a scale model and prediction of the stability of operation of Francis turbines*. PhD thesis, EPFL No 1146, 1993.
- [JOe85] H.L Jordan, H. Oertel, and K. Robert (editors). *Nonlinear Dynamics of Transcritical Flows*. Springer, 1985.
- [KDS96] H. Keck, P Drtina, and M. Sick. Numerical hill chart prediction by means of CFD stage simulation for a complete Francis turbine. In Cabrera et al. [CEM96], pages 170–179. Vol. 1.
- [KHA96] T. Kubota, F. Han, and F. Avellan. Performance analysis of draft tube for gamm Francis turbine. In Cabrera et al. [CEM96], pages 130–139. Vol. 1.
- [Kho91] M. R. Khorrami. On the viscous modes of instability of a trailing line vortex. *J. Fluid Mech.*, 225:197–212, 1991.
- [KL93] M. Kato and B. E. Launder. The modelling of turbulent flow around stationary and vibrating square cylinders. In *Turbulent Shear Flows 9*, pages 6–17, Kyoto Japan, August 16-18 1993. Springer.
- [KM89] M. R. Khorrami and M. R. Malik. Application of spectral collocation techniques to the stability of swirling flows. *J. of computational physics*, 81:206–229, 1989.
- [KM00] S.-E. Kim and P. Malan. A numerical study of turbulent flow in a hydraulic turbine draft tube. In ASME [ASM00]. Paper FEDSM2000-11066.
- [Kov65] N. N. Kovalev. *Hydroturbines*. Israel Program for Scientific Translating, 1965. Design and construction.
- [LC98] E. Landrieux and J.F. Combes. Numerical flow analysis in the runner and the draft tube of a Kaplan turbine prior to a rehabilitation. In H. Brekke et al., editor, *Hydraulic Machinery and Cavitation*, pages 91–99, Singapore, 9-11 September 1998. World Scientific. Vol. 1.
- [Lee75] B. E. Lee. The effect of turbulence on the surface pressure field of a square cylinder. *J. Fluid Mech.*, 69:263–282, 1975.
- [Lei78] S. Leibovich. The structure of vortex breakdown. *Annual Review of Fluid Mechanics*, 10:221–246, 1978.
- [LERP95] D. A. Lyn, S. Einav, W. Rodi, and J.-H. Park. A laser-doppler velocimetry study of ensemble-averaged characteristics of the turbulent near wake of a square cylinder. *J. Fluid Mech.*, 304:285–319, 1995.
-

-
- [Les99] M. A. Leschziner. The computation of turbulent engineering flows with turbulence-transport closures. In R. Peyert and E. Krause, editors, *Advanced turbulent flow computations*, CISM Courses and Lectures No. 395, pages 209–277. Springer, 1999.
- [LP74] M. Lessen and F. Paillet. The stability of a trailing line vortex. Part 2. Viscous theory. *J. Fluid Mech.*, 65:769–779, 1974.
- [LR94] D. A. Lyn and W. Rodi. The flapping shear layer formed by flow separation from the forward corner of a square cylinder. *J. Fluid Mech.*, 267:353–376, 1994.
- [LS74] Launder and Spalding. The numerical computation of turbulent flows. *Comput. Methods Appl. Mech. Eng.*, 3:269–289, 1974.
- [LS75] B. E. Launder and D. B Spalding. Progress in the development of a Reynolds-stress turbulence closure. *J. Fluid Mech.*, pages 537–566, 1975.
- [LSP74] M. Lessen, P. J. Singh, and F. Paillet. The stability of a trailing line vortex. Part 1. Inviscid theory. *J. Fluid Mech.*, 65:753–763, 1974.
- [MP92] E. W. Mayer and K. G. Powell. Viscous and inviscid instabilities of a trailing vortex. *J. Fluid Mech.*, 245:91–114, 1992.
- [Nal87] N. Nallasamy. Turbulence models and their applications to the prediction of internal flows: a review. *Computer & Fluids*, 15-2:151–194, 1987.
- [NMaYS82] M. Nishi, S. Mutsunaga, and T. Kubota and Y. Senoo. Flow regimes in an elbow-type draft tube. In *Hydraulic Machinery and Cavitation*, Amsterdam, 1982. No. 38.
- [OH84] J. Osterwalder and L. Hippe. Guidelines for efficiency scaling process of hydraulic turbomachines with different technical roughnesses of flow passages. *J. of Hydraulic Research*, 22:77–102, 1984.
- [Oha91] H. Ohashi (editor). *Vibration and Oscillation of Hydraulic Machinery*. Avebury Technical, 1991.
- [Oka82] A. Okajima. Strouhal numbers of rectangular cylinders. *J. Fluid Mech.*, 123:379–398, 1982.
- [PC87] A. E. Perry and M. S. Chong. A description of eddying motions and flow patterns using critical-point concepts. *Ann. Rev. Fluid Mech.*, 19:125–155, 1987.
-

- [PDH⁺94] E. Parkinson, P. Dupont, R. Hirschi, J. Huang, and F. Avellan. Comparison of flow computation results with experimental flow surveys in a Francis turbine. In *Hydraulic Machinery and Cavitation* [Hyd94].
- [PGM96] M. Page, A.-M. Giroux, and B. Massé. Turbulent swirling flow computation in a conical diffuser with two commercial codes. In *4th annual conference of the CFD Society of Canada*, Ottawa, 1996.
- [Raa85] J. Raabe. *Hydro Power*. VDI-Verlag, 1985. The design, use and function of hydromechanical, hydraulic and electrical equipment.
- [RCG94] A. Ruprecht, W. Chihab, and F. Ginter. Experimental and numerical analysis of the three-dimensional flow in elbow draft tubes. In *Hydraulic Machinery and Cavitation* [Hyd94], pages 83–94. A5, Vol. 1.
- [RFBP97] W. Rodi, J. H. Ferziger, M. Breuer, and M. Pourquié. Status of large eddy simulation: Results of a workshop. *Journal of Fluids Engineering*, 119:248–262, 1997.
- [RGH89] M. J. Raw, P. F. Galpin, and B. R. Hutchinson. A colocated finite volume method for solving the Navier-Stokes equations for incompressible and compressible flows in turbomachinery: Results and applications. In *Thirty-Sixth Annual General Meeting Canadian Aeronautics and Space Institute*, pages 13.1–13, Ottawa, Ontario, 1989.
- [RHAS01] A. Ruprecht, T. Helmrich, T. Aschenbrenner, and T. Scherer. Simulation of pressure surge in a hydro power plant caused by an elbow draft tube. In *The Behaviour of Hydraulic Machinery under Steady Oscillatory Conditions* [The01]. Proceedings of the X International Meeting.
- [Roa93] P. J. Roache. Perspective: A method for uniform reporting of grid refinement studies. *Journal of Fluids Engineering*, 6(1):39–48, 1993.
- [Roa97] P. J. Roache. Quantification of uncertainty in computational fluid dynamics. *Annual Review of Fluid Mechanics*, 29:123–160, 1997.
- [Roa98] P. J. Roache. *Verification and Validation in Computational Science and Engineering*. Hermosa, 1998.
- [Rod84] W. Rodi. *Turbulence models and their application in hydraulics. State-of-the-art paper*. IAHR Experimental and Mathematical Fluid Dynamics. 1984. ISBN 90-212-7002-1.
-

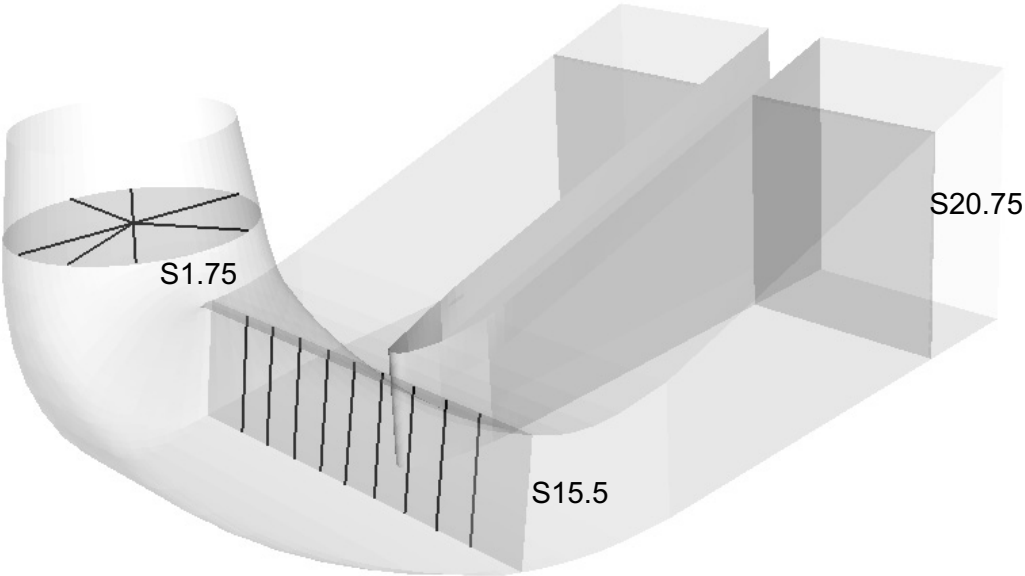
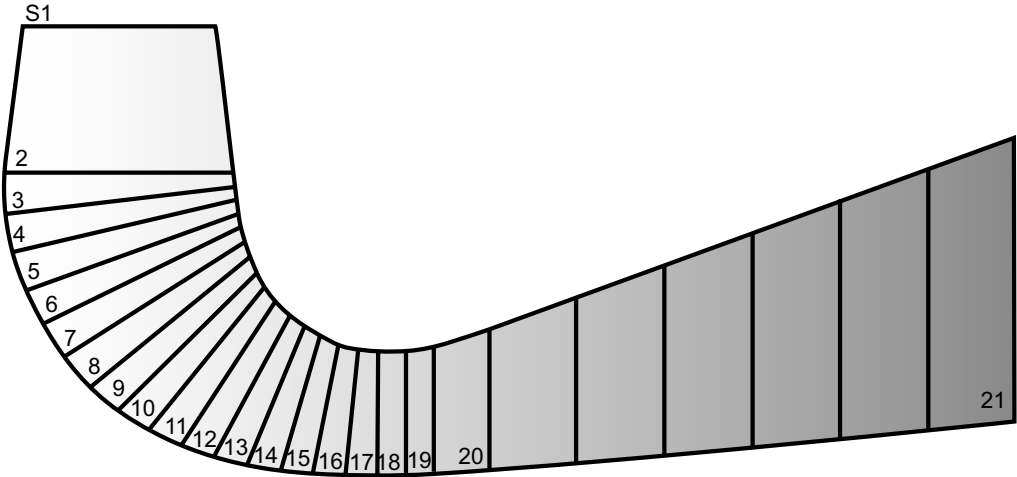
-
- [Rot00] M. Roth. *Automatic Extraction of Vortex Core Lines and Other Line-Type Features for Scientific Visualization*. PhD thesis, Diss. ETH No. 13673, 2000.
- [RS01] P. Rudolf and A. Skoták. Unsteady flow in the draft tube with elbow part b - numerical investigation. In *The Behaviour of Hydraulic Machinery under Steady Oscillatory Conditions* [The01]. Proceedings of the X International Meeting.
- [Rup89] A. Ruprecht. *Finite Elemente zur Berechnung dreidimensionaler, turbulenter Strömungen in komplexen Geometrien*. PhD thesis, Universität Stuttgart, 1989.
- [Rup90] A. Ruprecht. Numerical analysis of the flow in the elbow draft tube of a kaplan turbine. In *Hydraulic Machinery and Cavitation* [Hyd90]. G6, Vol. 1.
- [SB86] W. Shyy and M. E. Braaten. Three-dimensional analysis of the flow in a curved hydraulic turbine draft tube. *Int. Jou. for Num. Methods in Fluids*, 6:861–882, 1986.
- [SC94] M. Sabourin and M. Couson. Turbine rehabilitation - experience gained through systematic draft tube evaluation. In *Hydraulic Machinery and Cavitation* [Hyd94], pages 1379–1388. K7, Vol. 3.
- [Sch64] Schlichting. *Grenzschicht-Theorie*. Verlag G. Braun, Karlsruhe, 5th edition, 1964.
- [SH95] D. Sujudi and R. Haimes. Identification of swirling flow in 3-D vector fields. In *AIAA 95*, San Diego CA, June 1995. Paper 95-1715.
- [SR89] G. Sottas and I. L. Ryming, editors. *3D-Computation of Incompressible Internal Flows*, volume 39 of *Notes on Numerical Fluid Mechanics*, Lausanne, 13-15 September 1989. Proceedings of the GAMM Workshop.
- [SSG91] C. G. Speziale, S. Sarkar, and T. B. Gatski. Modelling the pressure-strain correlation of turbulence: an invariant dynamical system approach. *J. Fluid Mech.*, 227:245–272, 1991.
- [Ste95] W. Steenbergen. *Turbulent pipe flow with swirl*. PhD thesis, Eindhoven University of Technology, 1995. Webcatalogue TUE, <http://www.tue.nl/bib>.
- [TAS99] *CFX-TASCflow Theory Documentation Version 2.10*. Waterloo, Ontario, Canada N2L 5Z4, AEA Technology Engineering Software Limited edition, 1999.
-

- [The01] *The Behaviour of Hydraulic Machinery under Steady Oscillatory Conditions*, Trondheim, 26-28 June 2001. Proceedings of the X International Meeting.
- [TITS90] S. Tanabe, M. Ikegawa, T. Takagi, and J. Sato. Turbulent flow analysis in water turbine draft tube. In *Hydraulic Machinery and Cavitation [Hyd90]*. G2, Vol. 1.
- [TP82] M. Tobak and D. J. Peake. Topology of three-dimensional separated flows. *Ann. Rev. Fluid. Mech.*, 14:61–85, 1982.
- [VS88] T. C. Vu and W. Shyy. Viscous flow analysis for hydraulic turbine draft tube. In *Hydraulic Machinery and Cavitation [Hyd88]*, pages 915–926. Vol. 1.
- [VSP96] Y. Ventikos, F. Sotiropoulos, and V. C. Patel. Modelling complex draft-tube flows using near-wall turbulence closures. In Cabrera et al. [CEM96], pages 140–149. Vol. 1.
- [VTR87] J. P. Van Doormal, A. Turan, and G. D. Raithby. Evaluation of new techniques for the calculation of internal recirculating flows. In *AIAA 87*, Reno NV, January 1987. AIAA paper No. 87-0059.
- [Wil86] D. C: Wilcox. Multiscale model for turbulent flows. In *AIAA 86*, 1986.
- [WJX⁺00] L. Wenjun, Y. Jianming, T. Xuelin, W. Yulin, and W. Lin. Periodical unsteady turbulent flow computation through a draft tube by using LES. In ASME [ASM00]. Paper FEDSM2000-11216.
-

Nomenclature

- A_o Inlet section area
 A_{ref} Reference section area
 cv Control volume surface defined by mid-planes
 C Velocity vector
 C_n Normal velocity component
 C_o Mean local normal velocity
 C_r Radial velocity component
 C_t Circumferential velocity component
 D Diameter, runner outlet diameter $D = 0.4 [m]$
 $e_{k_i} = \frac{E_{k_i}}{E_{k_o}}$ Local mean specific kinetic energy coefficient
 $e_{p_i} = \frac{E_{p_i}}{E_{k_o}}$ Local mean specific static pressure energy coefficient
 $e_{t_i} = \frac{E_{t_i}}{E_{k_o}}$ Local mean specific energy coefficient
 $E_{k_o} = \frac{1}{Q} \int_{A_o} \frac{c^2}{2} \vec{c} \cdot \vec{n} dA$ Inlet mean kinetic specific energy
 $E_{k_i} = \frac{1}{Q_i} \int_{A_i} (\frac{c^2}{2}) \vec{c} \cdot \vec{n} dA$ Local mean kinetic specific energy
 $E_{p_i} = \frac{1}{Q_i} \int_{A_i} (\frac{p}{\rho}) \vec{c} \cdot \vec{n} dA$ Local mean static pressure specific energy
 $E_{t_i} = \frac{1}{Q_i} \int_{A_i} (\frac{p}{\rho} + \frac{c^2}{2}) \vec{c} \cdot \vec{n} dA$ Local mean specific energy
 k Turbulent kinetic energy
 $K = \omega L / U$ Reduced frequency
 L Characteristic length scale
 L_ϵ Turbulent (eddy, dissipation) length scale
 p Static pressure
 Q Flow rate
 r Radius
 $Re = \frac{U_o L}{\nu}$ Reynolds number
 $S = (\int_r C_n C_t r^2 dr) / (.5 D \int_r C_n^2 r dr)$ Swirl number
 $St = f L / U_o$ Strouhal number (nondimensional frequency)
 u_τ Wall tangential velocity
 U_o Characteristic velocity scale
 τ_w Wall shear stress
 y^+ Nondimensional distance from the wall
 $\chi = (\frac{1}{\rho} \Delta P_{dt}) / (.5 (\frac{Q}{A_{ref}})^2)$ Pressure recovery factor
 ΔP_{dt} Mean wall pressure difference between draft tube inlet and outlet
 ϵ Turbulent dissipation rate
 ω Angular frequency
 φ Flow rate coefficient

- φ^* Flow rate coefficient divided by the φ of the best efficiency point
 - ψ Head coefficient
 - ψ^* Head coefficient divided by the ψ of the best efficiency point
 - ν Specific speed, kinematic viscosity
 - ρ Water density
-



Curriculum vitae of the author

Date of Birth: 22nd April 1972

Nationality: Swiss

email: sebastiano.mauri@bluewin.ch

Education

- 97-01 Ph.D. thesis at the Swiss Federal Institute of Technology Lausanne, Laboratory for Hydraulic Machines. Numerical flow investigation of a hydraulic machine draft tube.
- 91-96 Diploma in mechanical engineering at the Swiss Federal Institute of Technology Zürich. Specialization in fluid dynamics and mathematics.
- 87-91 High school diploma at the Liceo Lugano (TI-CH). Scientific type.

Work Experience

- 6.96-5.97 Sulzer Hydro (VA TECH ESCHER WYSS) Zürich. Software development, runner design.
 - 4.96-6.96 Swiss Federal Institute of Technology Zürich Institute of Fluid Dynamics. Numerical investigation of laminar premixed flames instabilities.
 - 8.94-10.94 Mikron SA Agno. Optimization of internal production fluxes (European Norms ISO 9001).
-

